

The University of Oxford

St. Edmund Hall

Department of Engineering Science

Transpiration Cooling of Hypersonic Leading Edges

A thesis submitted for the degree of

Doctor of Philosophy

By

Raghul Ravichandran

2025

Abstract

This thesis presents the first full-cycle approach to the design, testing, and application of transpiration-cooled leading edges for hypersonic flight, addressing the trade-off between aerodynamic efficiency and heat loading on sharp leading edge geometries. Through integrated experimentation, numerical modelling, and performance analysis, results demonstrate that controlled transpiration cooling can reduce incoming heat fluxes without severely impacting the drag characteristics. The validated correlations, optimised injector designs, and multi-constraint analysis provide a framework for implementing transpiration cooling in future hypersonic vehicles.

In order to numerically model the effects of transpiration cooling on the flowfield in EILMER, the numerical method required experimental validation, especially of the mass flux boundary condition with distributed blowing. To achieve this, a novel leading edge injector was developed to achieve predictable and uniform coolant distribution through additive manufacturing of a porous ceramic. The porous ceramic and manufacturing process were developed in collaboration with Lithoz GmbH. This approach was compared with a commonly used off-the-shelf porous material, manufactured using conventional CNC machining methods. Both sets of injectors were designed with internal wall contouring to match prescribed target mass flux distributions which were based on the mass flux parameter B_h. A purpose-built benchtop characterisation rig measured the outflow velocity at the injector surface, with uniformity results compared to film cooling data collected in a hypersonic cross-flow. The results showed the mass flux of the machined injector had much higher spanwise variation than the additively manufactured one (56% versus 5%), which closely corresponded to film cooling variations (38% versus 9%). In addition to the superior injection uniformity, the additively manufactured design achieved mass fluxes 3 times higher due to material selection and designed structural reinforcement allowing larger plenum pressures.

Experimental validation of the numerical method was conducted in the Oxford High Density Tunnel at Mach 7 conditions. A transpiration-cooled model with 3 mm leading edge radius was tested across blowing parameters up to $B_h = 2.44$ using nitrogen and helium coolants. Heat flux, coolant concentration and surface pressure measurements were taken over the model surface using high-speed optical methods. All measurement quantities were compared against numerical simulations, which broadly showed agreement to within 10%. While helium was a more effective coolant per unit mass, nitrogen could achieve higher blowing condition, constrained

by the maximum internal pressure of the injector. At the highest blowing conditions of nitrogen, both coolant concentration and heat flux reduction was as high as 85%. Critically, when exceeding the conventional boundary layer blow-off parameter B^*, the surface pressure increase remained below 5% and the boundary layer remained laminar throughout the experimental domain.

A sweep of simulations was subsequently performed, covering flight-relevant, high enthalpy flow conditions with the aim of generating a reproducible, non-dimensional dataset for transpiration cooling performance. The data informed adaptations of existing transpiration cooling correlations to the case of a leading edge. A semi-empirical model of heat flux over the cooled leading edge geometry was constructed, only requiring flight condition and mass flux inputs. Cooling over the leading edge was correlated to within 9.8%. Deviation of the correlation increased further downstream, where heat fluxes and cooling requirements were significantly lower. At the point where heat flux was 4% of the stagnation point value, deviation was 30%.

A systems-level analysis was carried out to model the performance of a transpiration-cooled leading edge in steady flight, subject to material temperature and blowing constraints. A purpose-built finite element tool, PHIL, was developed to model the coupled two-dimensional thermal response and porous flow physics inside the leading edge injector. The tool incorporated the previously developed semi-empirical correlations as boundary conditions and included an optimisation algorithm to control the coolant distribution along the injector. Analysis across a matrix of conditions revealed that transpiration cooling significantly expanded the operational envelope compared to a passively re-radiating system. A blowing constraint of $B_h < 1.5B^*$ was implemented to coincide with the previously validated correlations, and to avoid excessive aerodynamic penalties. Tungsten leading edges with nitrogen coolant demonstrated the broadest operational range due to the high operational temperature of tungsten, and the high blowing limits of nitrogen. The modelling suggested that steady flight of a 1 mm blunted wedge at velocities up to 6 km/s at altitudes above 20 km fell within the blowing and thermal constraints. For a 10 minute flight, the highest blowing conditions required up to 10 kg of gas, requiring approximately 100 litres of storage. As found during experiments, helium was a more mass-efficient coolant, but nitrogen found to have higher blowing capabilities with lower volume and plenum pressure requirements.

Keywords

hypersonic, transpiration cooling, leading edge, thermal protection system, experimental, numerical simulation, systems modelling, short duration ground testing

Acknowledgements

It truly does take a village. I have been particularly fortunate to have come across so many different groups of such vibrant people throughout my time in this beautiful city.

First and foremost, I must express my deep thanks to my supervisors. Matt, thank you for giving me the chance to learn alongside such an impressive group of people, for making sure I didn't stay 'stuck in the weeds' of a problem, and for pushing me to deliver the best work that I could. Thank you also for not being *too* annoyed after blasting my first experimental model down the wind tunnel at Mach 7. I'm sure there is a gap in the literature for free-flight transpiration cooling that we could have a go at. Luke, thank you for always looking out for me, despite being drafted in partway through in a subject area you weren't familiar with. Your day-to-day guidance and reassurance has been immeasurable. Thank you for showing me the true meaning of attention to detail; it has truly made me a better engineer – though I'm a little afraid to ask which other aspects of my life now need to conform to engineering standards or require rigorous documentation. I am also appreciative of the funding provided by Trevor and DSTL that enabled this project.

The experiments in this thesis would not have been nearly as successful if it wasn't for Anthony. Your grit and infinite patience at the lowest points were invaluable. Sanding anodised aluminium for hours, breaking dowels, fixing models with car body filler, and trips to TPB were all in a day's work. I am also glad we have been able to become good friends. Invoking a cliché *standing-on-the-shoulders* moment, the contributions of Hassan, Marc, Imran, and PK can all be found at various points in this work – I am deeply grateful to all of you for helping me find my footing early on, and for taking the time to explain so many different aspects of experiments and simulations. Jack and Will, I have thoroughly enjoyed the way our friendship has developed over the past few years, from the tea breaks to the fresh memes and pub trips. The technical support during experiments in a highly complex facility has been outstanding; in particular Chris, Tristan, Wheels, and Andreea. Behind the chaotic scenes of the OTI, a massive thank you to Craig, Anna, Alex and Kathryn for keeping the lab on its feet. I have been

incredibly fortunate to be split between two colleges during my time in Oxford: at Teddy Hall as a student, and at Magdalen College as a Junior Dean. I would like to extend my gratitude to both sets of academic offices, catering staff, and porters that have all been so kind and accommodating. A special thank you to the Magdalen College decanal team, not only for giving me the chance to live at the heart of a gorgeous college for the past few years, but more importantly, for the access to the SCR espresso and wine machines that fueled thesis writing at all hours.

I could readily list everyone I know at Teddy Hall and SEHBC for their friendliness in making the Hall my second home. In particular, I am thankful to all those who helped throughout my MCR Presidency as we navigated the mix of pre- and post-COVID cohorts: Antonin, Natalie, Giovanni, Siddhant, Nancy, Jasper, Ronnie, Ben, Henry, Agata, Federico, and the rest of the MCR committee. From the exchange dinners to the long college meetings, you were all brilliant. I also feel very fortunate for the sense of camaraderie I found at SEHBC – Erika, India, Cyril, Rohit, Aleksei (Oleksii), Camille, Raghav and Anya. I will fondly remember the morning breakfasts and the giddy joy of bumping up to second on the river on the final day of Summer Eights.

Jack, you have been there almost every step of the way, keeping me grounded outside of the Oxford bubble: from lockdown video games to coffees down Cowley Road – thank you for being such a lively housemate and friend. Thank you also to Henry, Julie, and Julia each for your wonderful company, both in and out of lockdown. To my long-distance friends, Lea and Sally, I am incredibly grateful for your solidarity during turbulent times and am thankful that we have been able to share in life events from far away. I am also grateful to my earliest friends in Oxford, Jack G. and Alex Y., for helping me find my footing during a challenging first year. I can only apologise to some of my friends who haven't been able to get rid of me since the early days of undergrad: Isha, the Meme Team Extreme, and the Aero boys.

To Mr and Mrs W., for your eagerness in involving me in everything you knew I'd enjoy. I hope the donation of my sunglasses to Georgia's grass carp population is enough to cover my next round of Plum Porter.

It goes without saying that I have been incredibly fortunate to receive never-ending support and love throughout this process from my parents and Rohit. Mum, thank you for never letting me leave home without a fresh supply of home-cooked food, and for always looking after all of us. Dad, for your advice, pragmatism, and

always being there to encourage my love of science. This thesis is as much of a reflection on me as it is on you both.

Finally, to Phil, thank you for being a source of constant strength and support. During the intense experimental campaigns, I'd end up coming home in the early hours of the morning and going back to the lab again shortly after. While we barely got a chance to see each other during that time, you knew exactly how to look after me, and do your own experiments at the same time. Writing our theses side-by-side wasn't the original plan, but I couldn't have asked for a better writing partner. Every morning's cup of tea in bed has been an expression of never-ending care and love, and I am so very much looking forward to the future.

Transpiration Cooling of Hypersonic Leading Edges

A thesis
by

Raghul Ravichandran

July 2025

Supervisors:
Prof. Matthew McGilvray
Dr. Luke J. Doherty

Examiners:
Prof. David R. H. Gillespie
Prof. V. Wheatley

Examination date:
30th September 2025

This thesis adopts an integrated format, in which the core technical chapters are written as independent journal papers intended for submission, and are framed by an Introduction, Literature Review, and Conclusion. Each results chapter begins with a preface explaining its relevance to the overall research aims and detailing author contributions. Author contributions are credited according to the NISO Contributor Roles Taxonomy (CRediT).

The document was typeset using a custom-built LaTeX template. Both the template and a corresponding user guide are available via Git[1] and may also be requested by email. Two layout formats are offered: a single-page, centre-aligned version optimised for digital reading, and a two-sided (recto–verso) version designed for print and binding. This document is the single-page version.

Where possible, figures are fully vectorised, created using MATLAB 2024b and Inkscape v1.4. Figures are optimised for compatibility across digital viewing platforms, particularly for consistent rendering. Contour plots use uniformly perceptible colourmaps from Fabio Crameri's Scientific Colourmaps v8.0.

© Raghul Ravichandran

The University of Oxford
Department of Engineering Science

[1] https://github.com/RaghulRavichandran0

To Mum and Dad.
Thank you for giving me everything
I needed for this journey.

1 Introduction · page 1

2 Background and Literature · page 17

3 Design of a Transpiration-Cooled Leading Edge · page 46

4 Experiments on a Transpiration-Cooled Leading Edge in Hypersonic Flow · page 75

5 Numerical Simulations of Leading Edge Transpiration Cooling at Flight Conditions · page 114

6 Performance of a Transpiration Cooled Leading Edge · page 149

7 Conclusion and Final Remarks · page 192

Contents

Abstract ii

Acknowledgements iv

List of Figures xiv

List of Tables xix

Nomenclature xxi

1 Introduction 1
- 1.1 The Pursuit of Hypersonic Flight 2
- 1.2 Thermal Protection Systems 6
- 1.3 Transpiration Cooling Heat Balance 11
- 1.4 Research Objectives 14

2 Background and Literature 17
- 2.1 Porous Media Flow 19
- 2.2 Heat Flux Correlations 30
- 2.3 Coolant Concentration Correlations 38
- 2.4 Systems-Level Modelling 41
- 2.5 Non-Intrusive Measurement Techniques 42

3 Design of a Transpiration-Cooled Leading Edge 46
- 3.1 Introduction 48
- 3.2 Target Mass Flux 51
- 3.3 Material Selection 53
- 3.4 Design Methodology 57
- 3.5 Geometry 59
- 3.6 Experimental Setup 63
- 3.7 Performance Comparison 69
- 3.8 Conclusion 74

4 Experiments on a Transpiration-Cooled Leading Edge in Hypersonic Flow 75
- 4.1 Introduction 77
- 4.2 Experimental Setup 82
- 4.3 Post-Processing 95

4.4 Numerical Modelling 98
4.5 Results 100
4.6 Conclusion 112

5 Numerical Simulations of Leading Edge Transpiration Cooling at Flight Conditions 114
5.1 Introduction 116
5.2 Simulation Setup 122
5.3 Aerodynamic Results 130
5.4 Heat Flux and Concentration Results 138
5.5 Conclusion 146

6 Performance of a Transpiration Cooled Leading Edge 149
6.1 Introduction 151
6.2 Study Setup 158
6.3 Model Setup 163
6.4 Passive TPS Results 170
6.5 Transpiration Cooling Results 172
6.6 The Effect of Input Parameters 177
6.7 Further Constraints 183
6.8 Conclusion 188

7 Conclusion and Final Remarks 192
7.1 Summary of Presented Work 193
7.2 Key Results 195
7.3 Further Work and Recommendations 197
7.4 Final Remarks 200

References 201

Appendices

A Supplementary Experimental Material 215
A.1 Additional Leading Edge Outflow Simulations 216
A.2 Additional Experimental Photographs 218
A.3 Post-Processing of Experimental Optical Data 222

B Eilmer Simulation Setup 239
B.1 Solver Description 240
B.2 Mesh Independence Study 244

C Heat Flux Modelling 248

C.1 Uncooled Heat Flux Modelling 249
C.2 Film Cooling Correlation Formulation 252
C.3 Semi-empirical Transpiration Cooling Model 254

D Supplementary CFD Data 257
D.1 Effect of Input Parameter on Blowing 258
D.2 Drag Augmentation 260
D.3 Boundary and Shock Layer Augmentation 261
D.4 Heat Flux Reduction 263

E Internal Geometry Optimisation 266

F Steady-State Systems Analysis Data 269
F.1 Operating Limits 270
F.2 Surface Heat Flux and Temperature Reduction 271
F.3 Mass Flux 272

List of Figures

Chapter 1: Introduction

1.1 Stagnation point cold wall heat flux versus velocity. 4
1.2 Sketches of thermal protection system concepts. 6
1.3 Velocity-altitude trajectory maps for historical and conceptual missions. 9
1.4 Peak stagnation point heat fluxes and heat loads of historical missions. 10
1.5 Minimum required surface temperature for local thermal equilibrium with mass injection. 13

Chapter 2: Background and Literature

2.1 A sketch of a transpiration-cooled leading edge. 18
2.2 Pressure differential against coolant inlet velocity. 21
2.3 Microporous features of CMC and sintered ceramic. 22
2.4 Measured velocity outflow distributions and corresponding cooling performance of two flat plate injectors. 27
2.5 Outflow (dynamic pressure) of a CMC porous cone. 27
2.6 Internal structures of numerically-designed leading edge injectors. 29
2.7 Internal structures of two manufactured conical nosetip injectors. 29
2.8 Comparison of stagnation point cooling correlations from the 1960s. 32
2.9 Review of regimes where flat plate transpiration cooling is most effective. 33
2.10 Coordinate system used by Ifti et al. 34
2.11 Experimental data collapse of flat plate results by Ifti et al. 34
2.12 Sketch of the model and surface pressure results by Pappas & Lee. 36
2.13 Diagram of the hemispherical model used by Kaattari. 36
2.14 Experimental and correlation results of downstream concentration. 40
2.15 Spectral radiance of a black body for a range of temperatures. 43
2.16 Two types of surface preparation for PSP application. 45

Chapter 3: Design of a Transpiration-Cooled Leading Edge

3.1 Example heat and mass flux distributions in Eilmer simulations. 52
3.2 Leading edge injector orientation and print direction. 56
3.3 Wall thickness parameterisation for mass flux optimisation. 58
3.4 Annotated sketch of the outer mould line of the leading edge. 59
3.5 Calculated porous wall shapes. 60
3.6 Wall thickness distributions. 60
3.7 Simulated mass flux for the optimised internal geometries. 61

3.8 Internal geometry of leading edge final configurations. 62
3.9 Calibration curve of the CTA and hot-wire sensor for outflow. 64
3.10 Annotated sketch of the POT rig for outflow velocity measurements. 65
3.11 Annotated photograph of the transpiration-cooled wedge model. 67
3.12 Top view sketch of the optical setup for HDT experiments. 68
3.13 Measured mass flux distributions of the leading edges. 69
3.14 Heat transfer results from HDT testing of the two leading edge injectors. 73

Chapter 4: Experiments on a Transpiration-Cooled Leading Edge in Hypersonic Flow

4.1 Annotated sketch of a transpiration-cooled leading edge. 77
4.2 Annotated exploded view of the experimental model. 82
4.3 Annotated photographs of the optical measuremnt surfaces. 84
4.4 Cross-sectional view of the transpiration-cooled model. 85
4.5 Internal structure of the transpiration-cooled leading edge. 87
4.6 Results of the mass flux benchtop characterisation using hot-wire anemometry. 88
4.7 Estimated distributions of B_h for a range of test conditions. 89
4.8 Annotated sketch of the HDT. 90
4.9 Traces of measured $P_{0,\infty}$ and $T_{0,\infty}$ for the two conditions tested in HDT. 91
4.10 Top view of optical arrangements used during the experimental campaign. 92
4.11 A sketch of the boundary conditions used in the Eilmer simulations. 99
4.12 Experimental contours of downstream film cooling. 102
4.13 Spanwise-averaged distributions of thermal and concentration efficiencies. 103
4.14 Thermal and concentration efficiency decay distributions. 105
4.15 IR camera view of the leading edge surface temperature change. 107
4.16 Transient surface heat flux on the injector as evaluated by FER. 108
4.17 Leading edge heat fluxes for experiment, correlation, and CFD. 108
4.18 Surface pressure augmentation measured by PSP. 110

Chapter 5: Numerical Simulations of Leading Edge Transpiration Cooling at Flight Conditions

5.1 Annotated sketch of a transpiration-cooled leading edge. 116
5.2 Annotated sketch of a transpiration-cooled flat plate. 120
5.3 Curves of predicted flux reduction at the stagnation point. 123
5.4 Sketch of the leading edge geometry definition for the numerical tests. 124
5.5 Sketch of the domain shape and boundary conditions for simulations. 125
5.6 Prescribed mass flux distributions. 127
5.7 A selected mesh following the mesh independence study. 129
5.8 Contour plot of the temperature and total enthalpy fields. 131

5.9 Contour plot of the nitrogen mass fraction and static pressure. 131
5.10 Detected shock and boundary layer shapes with and without blowing. 132
5.11 Boundary layer (BL) thicknesses. 133
5.12 Shock layer (SL) thickness augmentation. 134
5.13 Distributions of surface pressure and skin friction for different B_h values. 135
5.14 Drag contributions demonstrating the relative effects of B_h and R_{LE}. 136
5.15 Relative effect of B_h on drag contributions. 137
5.16 Stagnation point cooling compared to Yoshikawa's correlation. 138
5.17 Heat flux distribution normalised by the cooled stagnation point. 139
5.18 Downstream thermal efficiency, showing the effect of radius and B_h. 140
5.19 Coordinate system for the film cooling correlation over the leading edge. 141
5.20 Normalised thermal efficiency against the correlation parameter. 142
5.21 Cooling distributions predicted by the current correlation and CFD data. 142
5.22 Concentration and velocity profiles within the boundary layer. 144
5.23 Concentration parameter versus film concentration efficiency. 145
5.24 Film cooling concentration efficiency parameter versus surface coordinate. 146
5.25 A comparison of modelled and CFD heat flux distributions. 148

Chapter 6: Performance of a Transpiration Cooled Leading Edge

6.1 Peak cold wall stagnation point heat flux and heat loads of historical missions. 152
6.2 A sketch of a transpiration-cooled leading edge. 153
6.3 Sketch of the porous injector, with the internal wall contouring highlighted. 159
6.4 Flowchart of the steady state study. 161
6.5 Flow of variables between the optimiser and the finite element simulation. 163
6.6 A sketch of the 2D outer mould line for external boundary conditions. 165
6.7 Annotated sketch of the domain and boundary conditions. 168
6.8 Passive TPS boundary conditions. 170
6.9 Stagnation point temperature contours T_{w0} for a passive TPS. 171
6.10 B_h-based performance map for a transpiration-cooled TPS. 172
6.11 Temperature field T_s of the permeable leading edge. 174
6.12 Temperature and velocity fields of coolant through the porous material. 174
6.13 Surface profiles of T_s, $\dot{q}$, B_h and $\dot{m}_{\text{inj}}$, for a 1 mm tungsten leading edge. 175
6.14 Porous wall shape and thickness distribution for three flight conditions. 176
6.15 Effect of varying material. 177
6.16 Effect of varying coolant. 178
6.17 Heat flux reduction correlation by Yoshikawa. 179
6.18 Effect of varying radius. 180
6.19 Effect of h_v on surface temperature and surface mass flux. 182

6.20 First principle linear stress contributions of the pressure-induced and thermal stresses on the porous leading edge. 184
6.21 Mass budget for a 10 minute steady-state flight. 187
6.22 Volume budget for a 10 minute steady-state flight. 187
6.23 Contour of blowing parameter with overlaid trajectories. 189

Chapter 7: Conclusion and Final Remarks

7.1 Abstract sketch of the set of conditions and assumptions spanned by each stage of the thesis. 198

Appendix A: Supplementary Experimental Material

A.1 Lower Reynolds number (Condition B in Table 4.2). 216
A.2 Higher blowing (B_h=1.6) N_2 injection. 217
A.3 Helium coolant (at $B_h = 0.4$) 217
A.4 Annotated photograph of the underside of the surface pressure tappings. 218
A.5 Downstream view of the optical layout and infrastructure for HDT testing. 219
A.6 TCLE model in the HDT test section. 220
A.7 TCLE model rotated by 90° in the HDT test section. 221
A.8 IR calibration data points and curve fits. 224
A.9 Images of the spatial calibration procedure for directional emissivity correction. 226
A.10 Annotated diagram of the boundary conditions used by the FER method. 229
A.11 Transient temperature distributions used as an input to the FER model. 230
A.12 3D temperature field of the FER model. 230
A.13 Flowchart of heat flux processing of the experiments. 231
A.14 Calibration contour plots for the downstream IR measurements. 232
A.15 Calibration contour plots for the leading edge IR measurements. 233
A.16 PSP calibration data points and curve fits. 235
A.17 Contour plots of the PSP calibration curve coefficients. 238

Appendix B: Eilmer Simulation Setup

B.1 Sketch of the transpiration cooling boundary condition in Eilmer. 242
B.2 Diagram of grid for mesh independence study. 245
B.3 Surface heat flux distribution for each level of grid refinement. 246
B.4 Stagnation point surface heat flux convergence for all three R_{LE} domains. 246
B.5 Distributions of Re_c for $s/R < 10$. 247

Appendix C: Heat Flux Modelling

C.1 Comparison of theoretical and numerical heat flux distributions. 251
C.2 Leading edge coordinate system for film cooling correlation. 252

C.3 Leading edge coordinates for heat flux correlations. 254

Appendix D: Supplementary CFD Data

D.1 Curves of predicted stagnation point heat flux reduction, Ψ, against B_h. 258
D.2 Mass flux distributions calculated from uncooled simulations. 259
D.3 Detected shock and boundary layer shape over the leading edge. 260
D.4 Effect of B_h on drag contributions. 260
D.5 Boundary layer thickness distributions. 261
D.6 Shock layer thickness augmentation. 262
D.7 Heat flux reduction along the leading edge injector for constant B_h. 263
D.8 Downstream heat flux reduction. 264
D.9 Film cooling spatial distributions for a range of conditions. 265

Appendix E: Internal Geometry Optimisation

E.1 Internal geometry parameterisation for injector optimisation. 267
E.2 Flow of variables between programs during geometry optimisation. 268

Appendix F: Steady-State Systems Analysis Data

F.1 B_h/B^* for different coolant gases. 270
F.2 Heat flux reduction at the stagnation point due to blowing. 271
F.3 Temperature reduction at the stagnation point due to blowing. 271
F.4 Uncooled stagnation point heat flux. 271
F.5 Contour of B^*, used as the system limit parameter. 271
F.6 Mass flux at the stagnation point. 272
F.7 F at the stagnation point. 272

List of Tables

Chapter 1: Introduction

1.1 Parameters used for the heat balance shown in Figure 1.5. 12

Chapter 2: Background and Literature

2.1 Porous material values used in previous transpiration cooling studies. 24

Chapter 3: Design of a Transpiration-Cooled Leading Edge

3.1 HDT freestream conditions used as the porous injector design point. 51
3.2 Properties of porous materials for transpiration cooling experiments. 54
3.3 List of boundary conditions for the comsol model. 58
3.4 List of components of the Porous Outflow Traverse. 66
3.5 Experimentally measured injector performance relative to design. 71

Chapter 4: Experiments on a Transpiration-Cooled Leading Edge in Hypersonic Flow

4.1 LithaLox 1347-P30 porosity and permeability coefficients. 86
4.2 Freestream conditions during HDT testing. 90
4.3 IR acquisition parameters for the two configurations shown in Figure 4.10. 93
4.4 PSP acquisition parameters. 94
4.5 Key Eilmer settings. 99
4.6 A list of inputs required for each heat flux reduction prediction method. 106
4.7 Experimental and CFD results of pressure drag augmentation. 111

Chapter 5: Numerical Simulations of Leading Edge Transpiration Cooling at Flight Conditions

5.1 List of freestream conditions and maximum blowing parameters tested. 123
5.2 List of boundary conditions labelled in Figure 5.5. 125
5.3 Key Eilmer settings used in this numerical work. 125
5.4 Selected mesh parameters for each domain size dictated by R_{LE}. 129
5.5 List of adapted models for a heat flux model of leading edge transpiration cooling. 147

Chapter 6: Performance of a Transpiration Cooled Leading Edge

6.1 Comparison of existing numerical tools for assessing transpiration-cooled vehicles, including the present work. 157
6.2 Solid material properties evaluated at 300 K. 162

6.3 Assumed porous properties and volumetric HTC. 162
6.4 Coolant fluid properties evaluated at 300 K. 162
6.5 Assumptions required by the coupled modelling used in PHIL. 164
6.6 Governing equations of coupled heat transfer and porous flow processes in PHIL. 168
6.7 List of boundary conditions in PHIL. 169
6.8 List of internal pressures and mechanical stresses. 185

Chapter 7: Conclusion and Final Remarks

7.1 Span of conditions and assumptions for each of the three stages of investigation (experiment, numerical, systems). 198

Appendix A: Supplementary Experimental Material

A.1 Nominal thermal properties used for IR data processing. Values of the PEEK were provided in [119], measured by NETZSCH GmbH Application Laboratory. Values for the LithaLox were provided by Lithoz GmbH. 222

Appendix B: Eilmer Simulation Setup

B.1 Key parameters for the mesh independence study. 245
B.2 Selected mesh resolution parameters following the mesh independence study. 247

Appendix C: Heat Flux Modelling

Appendix D: Supplementary CFD Data

Nomenclature

Latin

B^*	Boundary layer blow-off parameter	[-]
B_h	Blowing parameter	[-]
$\overline{B_h}$	Mean blowing parameter	[-]
C_p	Specific heat capacity	$\mathrm{J\,kg^{-1}\,K^{-1}}$
D	Drag	N
D_{12}	Binary diffusion coefficient	$\mathrm{m^2\,s^{-1}}$
F	Blowing ratio	[-]
h	Specific enthalpy	$\mathrm{J\,kg^{-1}}$
h_v	Volumetric heat-transfer coefficient	$\mathrm{W\,m^{-3}\,K^{-1}}$
I	Intensity	[-]
k	Thermal conductivity	$\mathrm{W\,m^{-1}\,K^{-1}}$
K_D	Darcy coefficient	$\mathrm{m^2}$
K_F	Forchheimer coefficient	m
L/D	Lift-to-drag ratio	[-]
Le	Lewis number	[-]
M	Mach number	[-]
$\dot{m}$	Mass flux	$\mathrm{kg\,m^{-2}\,s^{-1}}$
Pr	Prandtl number	[-]
p	Pressure	Pa
$p\mathrm{O}_2$	Partial pressure of oxygen	Pa
Re_u	Unit Reynolds number	$\mathrm{m^{-1}}$
Re_s	Surface-coordinate Reynolds number	[-]
Q	Heat load	$\mathrm{J\,m^{-2}}$
$\dot{q}$	Heat flux	$\mathrm{W\,m^{-2}}$
R_{LE}	Leading edge radius	m
St	Stanton number	[-]
s	Surface coordinate	m

s_0	Surface coordinate at injector end	m
T	Temperature	K
u	Fluid velocity	$\mathrm{m\,s^{-1}}$
v	Flight / freestream velocity	$\mathrm{m\,s^{-1}}$
W	Molecular weight	$\mathrm{kg\,kmol^{-1}}$
x	Streamwise coordinate	m
y	Transverse coordinate	m
z	Spanwise coordinate	m

Greek

ϵ	Surface emissivity	[-]
η_c	Concentration efficiency	[-]
η_{th}	Thermal efficiency	[-]
μ	Dynamic viscosity	$\mathrm{Pa\,s}$
ϕ	Porosity	[-]
Ψ	Heat-flux reduction ratio	[-]
ρ	Density	$\mathrm{kg\,m^{-3}}$
σ	Stefan–Boltzmann constant	$\mathrm{W\,m^{-2}\,K^{-4}}$
θ	Subtended angle around surface	rad
τ_w	Wall shear stress	Pa
ξ_c	Concentration correlation parameter	[-]
ξ_{th}	Thermal correlation parameter	[-]

Superscripts

0	Uncooled
aw	Adiabatic wall
c	Coolant property
cw	Cold-wall conditions
e	Boundary-layer edge
ext	External surface
f	Fluid (within porous material)
FP	Flat plate
FR	Fay–Riddell correlation
∞	Freestream

inj	Injection quantity
int	Internal (plenum)
re-rad	Surface re-radiation
s	Solid (porous material)
SP	Stagnation point
T	Total
w	Wall conditions

Abbreviations

C/C	Carbon–carbon
CEA2	Chemical Equilibrium with Applications v2
CFD	Computational fluid dynamics
CMC	Ceramic matrix composite
CNC	Computer numerical control
CTA	Constant-temperature anemometer
DAQ	Data acquisition
FER	Finite element reconstruction
HDT	High-Density Tunnel
HGV	Hypersonic glide vehicle
IR	Infra-red
LCM	Lithography-based manufacturing
LE	Leading edge
LTE	Local thermal equilibrium
LTNE	Local thermal non-equilibrium
MWIR	Mid-wave infra-red
PHIL	Porous Flow and Heat Transfer in Leading Edges
POT	Porous Outflow Traverse
PSP	Pressure-sensitive paint
TCLE	Transpiration-cooled leading edge
TPS	Thermal protection system
UHTC	Ultra-high-temperature ceramic

CHAPTER 1

Introduction

1.1 The Pursuit of Hypersonic Flight 2

1.2 Thermal Protection Systems 6

1.3 Transpiration Cooling Heat Balance 11

1.4 Research Objectives 14

1.1 The Pursuit of Hypersonic Flight

As a flight vehicle accelerates from subsonic to supersonic speeds, it begins to travel faster than the air in front can move aside. Shock waves form ahead of the body, compressing the air rapidly and marking the onset of supersonic flow. In the reference frame of the vehicle, the high-speed incoming air is slowed down by the shock wave, converting kinetic energy into internal and thermal energy, heating the air behind the shock wave. Accelerating further still, the post-shock gas increases in temperature with the square of velocity, leading to thermochemical effects within the gas. The onset of hypersonic flow is loosely defined as the regime where these effects begin to dominate the flowfield and heat transfer to the vehicle, which becomes significant at and above Mach 5 [1].

While re-entry vehicles have achieved manned and unmanned hypersonic flight since the 1960s, practical hypersonic flight has not quite been realised. An excellent example of this is the conceptual single-stage-to-orbit spacecraft: a cheap, reusable means of accessing space from a vehicle that does not discard any components. These concept vehicles have captivated engineers for decades, from NASA's NASP programme in the 1960s [2] to Reaction Engine's Skylon in the 2020s[1]. These concept vehicles are typically long, slender bodies that require good glide and manoeuvrability characteristics, but crucially must survive hypersonic flow conditions on ascent and descent.

After a period of relative dormancy, the pursuit of hypersonic flight has re-emerged as a major area of technological and geopolitical focus. The U.S. Department of Defense's budget request for hypersonics development has been steadily rising, increasing from USD 4.7 billion to USD 6.9 billion from FY2023 to FY2025 [3]. Within American academia, the University Consortium for Applied Hypersonics (UCAH) unites over 120 institutions working on hypersonic aerothermodynamics [4]. The UK has launched initiatives such as the Hypersonic Air Vehicle Experimental (HVX) programme for reusable hypersonic vehicles [5] and the Hypersonic

[1] Reaction Engines Ltd. entered administration in October 2024.

Technologies & Capability Development Framework (HTCDF) with the aim of improving UK hypersonic capability [6]. The strategic appeal of hypersonic systems lies in their speed and manoeuvrability at low altitudes.

A number of high-profile experimental programmes have demonstrated the potential and complexity of sustained hypersonic flight. NASA's X-43 and the X-51 programmes provided landmark demonstrations of air-breathing propulsion at hypersonic speeds. The European Space Agency have more recently considered a series of design studies of hypersonic passenger flight: LAPCAT-II, STRATOFLY and HEXAFLY-INT. ESA's continued efforts toward this goal have included the SHEFEX, STORT and HIFLIER flight experiments, contributing data on sharp leading edge reentry configurations that aim to balance aerodynamic efficiency with survivability during atmospheric return. Despite decades of experience, tackling the challenges of aerothermal heating and thermal protection system (TPS) durability remains an area of active research. This has been more recently aided by recent developments in manufacturing capabilities, computational power, and experimental techniques.

1.1.1 Aerothermal Heating

At the leading edge of a hypersonic vehicle, conversion from kinetic energy (which scales with the square of velocity) to thermal and chemical energy can raise the post-shock temperatures to thousands of kelvin within millimetres of the surface. At sufficiently high speed, the superheated gas behind the shock wave can dissociate and ionise, leading to a themochemically complex plasma. Heat flux (the incoming thermal power per unit area) is dependent on the temperature gradients at the wall. For a shock layer with gas temperatures above 3000 K, aerodynamic heat fluxes are often measured in MW/m^2. As a result, vehicle survivability in hypersonic flight depends heavily on the design of the TPS. For low to moderate hypersonic speeds (1.5–9 km/s), convective heat transfer dominates the thermal loading. Beyond 9 km/s, radiative heat flux from excited species in the shock layer begins to dominate the heating.

Stagnation point heat flux is a common starting point for a quick calculation

on the survivability of a vehicle. Equation 1.1 shows the stagnation point heat flux for non-catalytic equilibrium flow using Fay & Riddell's semi-analytic correlation. The equation shows adaptions for axisymmetric (e.g. concial nosetip) or 2D planar (e.g. wing leading edge) geometries [7]. The computation process of Equation 1.1 is demonstrated in Appendix C. Figure 1.1 illustrates the relationship between altitude and velocity to heat flux by plotting Equation 1.1 for a 2D planar leading edge of radius $R_{LE} = 10$ mm at a cold wall temperature of $T_w = 300$ K.

$$\dot{q}_{FR} = \frac{A}{Pr_w^{0.6}}(\rho_e\mu_e)^b(\rho_w\mu_w)^c(h_{T,e} - h_w)\left(1 + (Le^{0.52} - 1)\frac{h_d}{h_{T,e}}\right)\left(\frac{dv_e}{dx}\right)^{0.5} \tag{1.1}$$

where

$$\begin{cases} \text{Axisymmetric:} & A = 0.759, \quad b = 0.4, \quad c = 0.1 \\ \text{Planar:} & A = 0.537, \quad b = 0.44, \quad c = 0.06 \end{cases}$$

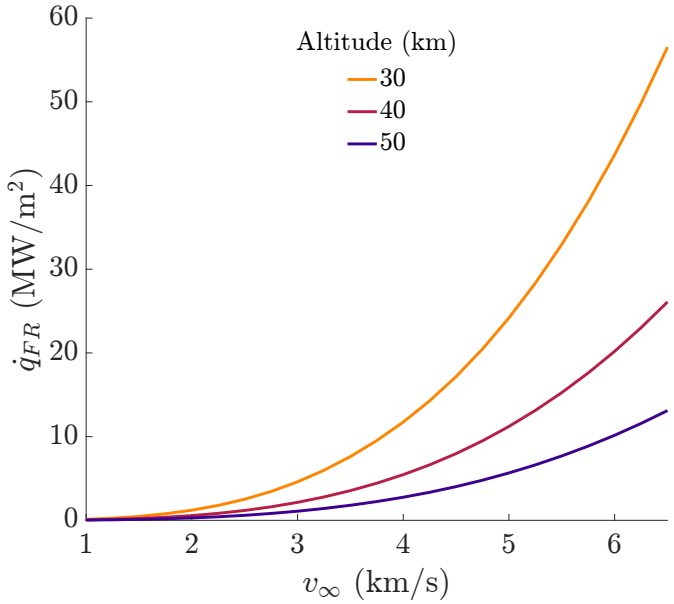


Figure 1.1: Stagnation point cold wall heat flux versus velocity for three different altitudes for a 10 mm leading edge radius.

1.1.2 Aerodynamic Efficiency

Improving cross-range and manoeuvrability characteristics have become increasingly desirable for mission profiles such as sustained hypersonic flight [2, 5, 8], single-stage-to-orbit (SSTO) re-entry [9, 10], and boost-glide vehicles [11]. These capabilities depend heavily on the vehicle's lift-to-drag ratio (L/D), with sharper leading edges widely recognised as a means to improve L/D [12–14].

Numerical studies have shown that increasing a glide vehicle's leading edge bluntness from 2 mm to 10 mm reduces L/D by around 8% [14], and from 10 mm to 30 mm by a further 16% [13, 15]. Since hypersonic glide cross-range roughly scales with L/D [16], these aerodynamic losses can significantly constrain mission profiles.

On the other hand, heat flux scales inversely with the square root of the radius[2], meaning a reduction from 10 mm to 2 mm more than doubles the incoming heat flux. In addition, infinitely sharp leading edges are highly sensitive to machining tolerances and are vulnerable to damage [12].

A balance must therefore be struck between aerodynamic performance and thermal protection. Where sharp leading edges are required, the increased heating must be mitigated through the selection of an appropriate TPS.

[2]The velocity gradient term in Equation 1.1, dv_e/dx, is often estimated using Newtonian flow theory where $dv_e/dx \propto 1/R_{LE}$, and therefore $\dot{q}_{FR} \propto 1/\sqrt{R_{LE}}$. This is further discussed in Appendix C.

1.2 Thermal Protection Systems

Figure 1.2 shows how thermal protection systems broadly fall into three categories: passive, semi-passive, and active. Historically TPS designs have employed passive and ablative (semi-passive) systems, while active systems have not been fully realised into vehicle design outside of flight experiments. The designs in the figure are discussed further below.

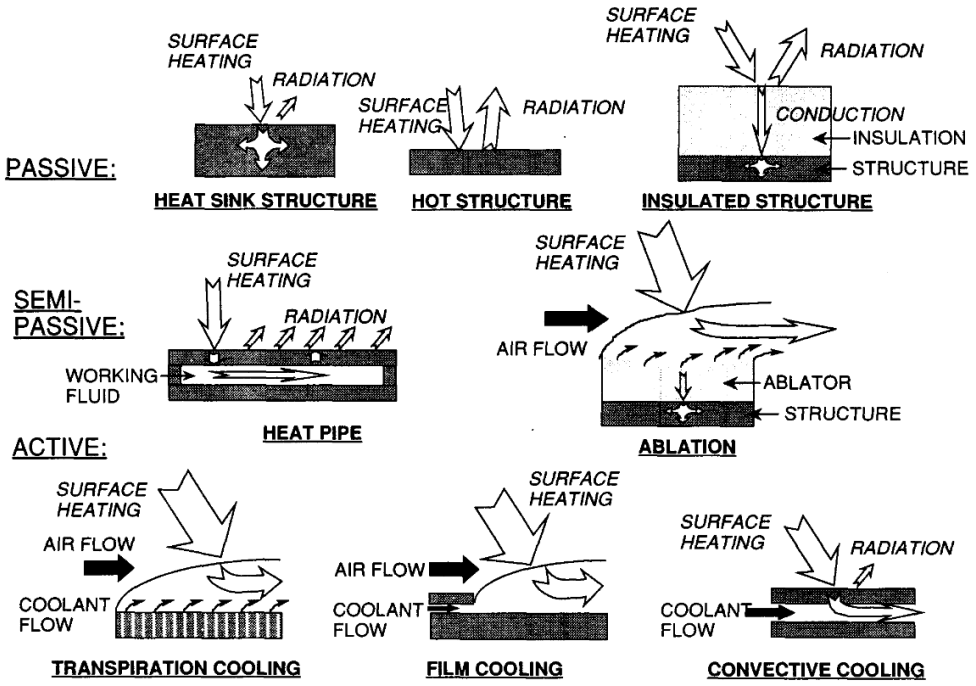


Figure 1.2: Sketches of thermal protection system concepts, taken from [2].

1.2.1 Passive Systems

Heat sinks and insulated structures rely on thermal mass to protect the substructure, so high heat fluxes may still lead to material failure if the system cannot reject local heat fluxes quickly enough. A key facet of the passive TPS design is using high temperature, high emissivity materials to enable heat flux rejection via thermal re-radiation. This is described by the Stefan–Boltzmann law, shown in Equation 1.2. The equation shows how re-radiative heat flux rejection increases with the

surface temperature to the fourth power. In the equation, $\sigma = 5.67 \cdot 10^{-8}$ W/m^{2}K^4 is the Stefan–Boltzmann constant, ε is the surface emissivity between 0 and 1, and T_w is the wall surface temperature.

$$\dot{q}_{\text{re-rad}} = \varepsilon \sigma T_w^4 \tag{1.2}$$

Even with radiative heat rejection, a long duration glide trajectory at low heat fluxes would still require appropriate thermal management to effectively operate in steady-state. The heat flux accumulated over a trajectory is the heat load: a measure of the total energy transfer. Provided the heat load can be managed, passive systems are generally are suited for these low heat flux trajectories at low cost.

1.2.2 Semi-passive Systems

Ablative TPSs have been used since the 1960s, having been proven on multiple mission programmes spanning decades. Ablators reduce heat flux through endothermic decomposition (pyrolysis, oxidation, sublimation) and convective cooling from pyrolysis gas ejection [17]. These sacrificial mechanisms restrict ablators to single-use missions, driving up costs where reusability seeks to reduce them. The sacrificial nature of an ablator also leads to (possibly non-uniform) surface recession, which alters the aerodynamic shape and can lead to degradation in aerodynamic performance. Additionally, ablative TPS mass fraction increases linearly with heat load [18], reaching up to 50% for the Galileo probe. Ablative TPS strategies are therefore employed for single-use vehicles that undergo very high heat fluxes.

Additional qualitative drawbacks include surface roughness and uncontrolled blowing that may promote boundary layer transition [19]. Boundary layer transition increases heat flux via entrainment of the hot post-shock gas into the boundary layer. Pyrolysis and spallation products can also increase radar signature and block optical sensors [20].

Heat pipes have also been proposed as semi-passive solutions for hypersonic leading edges [21, 22]. These two-phase systems redistribute heat internally via

vapour transport and capillary action, requiring no external energy. Heat pipes are embedded beneath the vehicle skin transporting thermal energy from the stagnation region. Upper heat flux limits for 3 mm leading edges have been shown to be around 2-3 MW/m^2 [22].

1.2.3 Active Systems

Active TPS strategies are typically reusable but require an energy input and a controller. The most common active cooling technologies are film cooling and transpiration cooling. Film cooling injects coolant gas over the vehicle surface through discrete slots or holes in the vehicle wall to form a coolant film. Transpiration cooling injects coolant through a porous material, providing a means of distributed injection as well as internal cooling via convective heat transfer within the porous matrix. Recent studies have shown transpiration cooling to be significantly more mass-efficient than film cooling [23].

Components such as pipework, flow control, and storage are associated with a mass and volume penalty. The inherent complexity of such a system adds risk, and active systems do not have the flight heritage of passive and semi-passive systems. As such, the study of active cooling for hypersonic vehicles has been limited to fundamental ground testing, simulations, and sounding rocket tests.

For applications where heat fluxes are too high for passive systems, and ablative systems cannot provide re-usability or shape stability over the whole mission, an active TPS could be employed in a targeted manner to the hottest regions of the vehicle.

1.2.4 TPS Selection

Figure 1.3 shows the trajectories of several historical and conceptual missions on an altitude–velocity map. Overlaid is a rough dividing line [17] between passive and ablative systems, based on heat fluxes encountered by historical, highly blunted

re-entry bodies with radii on the order of metres[3]. While some trajectories of interest (HGV glide, Shuttle return, and IXV) lie within the passive region, this classification is not applicable for the much higher heat fluxes if a sharper leading edge were to be used. For a change in radius from 1 m to 10 mm, the heat flux is nominally 10 times higher and would require ablative materials.

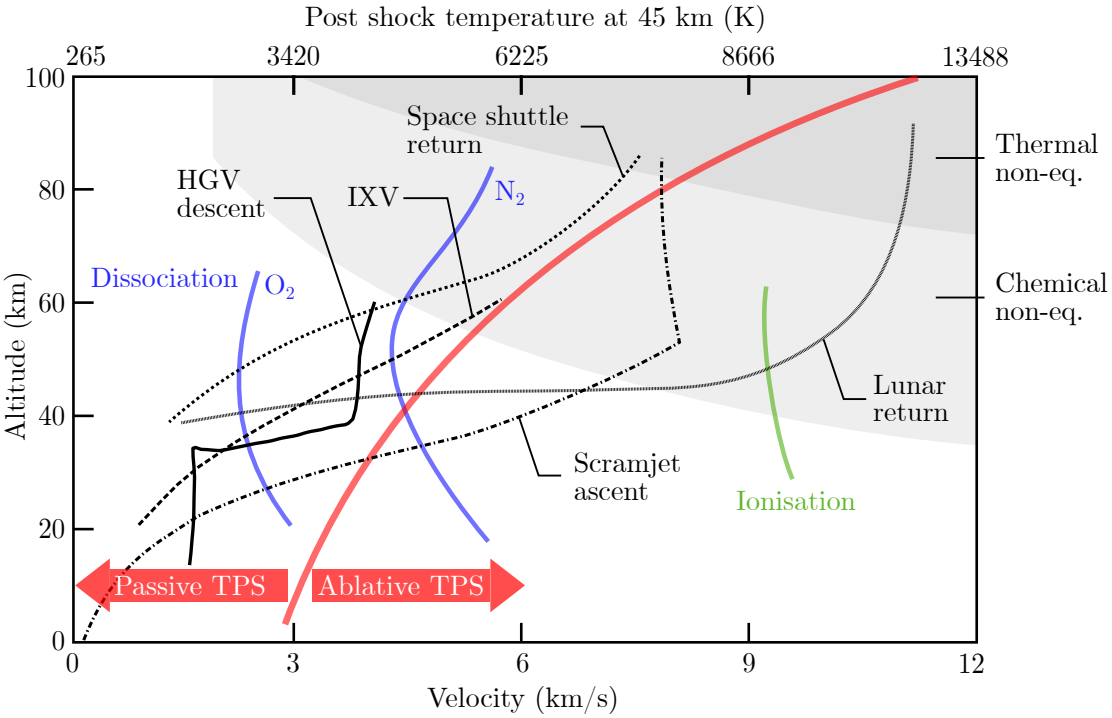


Figure 1.3: Velocity-altitude trajectory maps for a series of historical and conceptual missions. The historical division of passive and ablative TPS strategies, and regions of thermochemical interest (dissociation, ionisation, non-equilibrium) are overlaid. This plot is compiled and adapted from data in [17, 24, 25].

Along with trajectory analysis, examining the stagnation point heating provides additional insight for TPS selection. Figure 1.4 presents cold wall heat fluxes and integrated heat loads at the stagnation points of historical missions, alongside a high L/D glide trajectory. Among the missions, only the Space Shuttle orbiter used a passive, insulative TPS; all others relied on ablative systems. It follows that the sharp leading edge glide trajectories experience moderate heat fluxes, but very high heat loads due to the length of time spent in the hypersonic regime.

[3]For example, the Space Shuttle had a leading-edge radius of approximately 1 m, and the Apollo command module was around 2 m.

While an ablative TPS could mitigate the high heat flux, and a passive TPS could mitigate the effects of the extended duration, an active TPS could be considered to manage both.

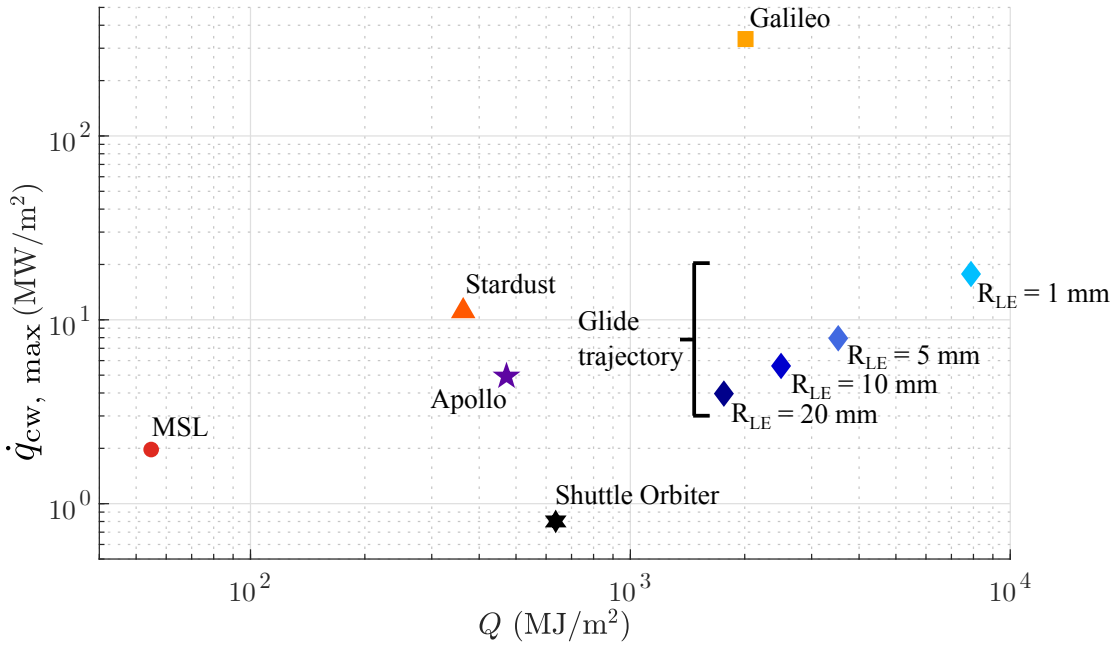


Figure 1.4: Peak cold wall stagnation point heat fluxes and heat loads of historical missions [17, 26–28] versus that of a generic glide trajectory [11] at different R_{LE} values.

1.3 Transpiration Cooling Heat Balance

1.3.1 Blowing Parameter

At the stagnation point, a heat balance can show the approximate regions where transpiration cooling may be viable. In [29], Yoshikawa developed a semi-analytic correlation for the heat flux reduction at a transpiration cooled stagnation point, blowing at a non-dimensional mass injection parameter B_h. The blowing parameter is the blowing ratio, F, normalised by the uncooled Stanton number, St_0. Mass injection in literature is often characterised by the non-dimensional blowing parameter, as shown in Equation 1.5. Here, ρu is mass flux, $\dot{q}$ is heat flux, and h_{aw} is adiabatic wall enthalpy. Subscripts 0, c, and ∞ correspond to uncooled, injected coolant, and freestream quantities respectively.

$$F = \frac{\rho_c u_c}{\rho_\infty u_\infty} \tag{1.3}$$

$$St_0 = \frac{\dot{q}_0}{\rho_\infty u_\infty (h_{aw} - h_w)} \tag{1.4}$$

$$B_h = \frac{F}{St_0} = \frac{\rho_c u_c (h_{aw} - h_w)}{\dot{q}_0} \tag{1.5}$$

In Equation 1.5, it can be seen that B_h has the form of an inverse Stanton number. In actuality, B_h represents the ratio of the thermal capacity carried by the injected coolant mass to the convective heat transfer capability of the external flow. It therefore characterises the ability of the coolant to 'block' heating by thickening the boundary layer and preventing the hot shock layer gases from reaching the surface. At $B_h = 1$, this cooling capacity is balanced by the heating of the external flow, achieving the maximum heat flux reduction per unit coolant mass.

1.3.2 Thermal Equilibrium at a Stagnation Point

Equation 1.6 shows the local thermal equilibrium of a transpiration cooled stagnation point, found by balancing the incoming heat flux (Equation 1.1) with re-radiation (Equation 1.2) and transpiration cooling. In the below heat balance,

$\dot{q}_{FR}$ and $\dot{q}_{\text{re-rad}}$ are the same as parameters as the previous equations, and $\dot{q}_{TC}$ is the heat flux reduction due to transpiration cooling.

$$\begin{aligned} \dot{q}_{\text{tot}} = 0 = &\dot{q}_{FR} - \dot{q}_{\text{re-rad}} - \dot{q}_{\text{TC}} \\ \text{where,}\quad &\dot{q}_{FR} = \dot{q}_{FR}(R_{LE}) \\ &\dot{q}_{\text{re-rad}} = \dot{q}_{\text{re-rad}}(T_{\text{op}}) \\ &\dot{q}_{\text{TC}} = \dot{q}_{\text{TC}}(B_h) \end{aligned} \tag{1.6}$$

The equation shows a trade-off between the radius (R_{LE}), the operating wall temperature (T_{op}) and the required blowing parameter (B_h). Higher operating temperatures increase heat flux rejection through re-radiation, decreasing the required blowing rates. When the maximum blowing rate is constrained to B^*[4], there is an equilibrium point at which the maximum allowable blowing condition corresponds to a minimum allowable operating wall temperature T_{op,B^*} for local thermal equilibrium.

A heat balance is calculated at the conditions shown in Table 1.1, for a series of R_{LE}. The results of this calculation are presented in Figure 1.5. The figure shows that within the B^* constraint, a material must be selected that can withstand T_{op,B^*}. A smaller radius must re-radiate more, leading to a higher temperature limit, requiring a more resilient material.

Table 1.1: Parameters used for the heat balance shown in Figure 1.5.

Coolant	B_h	v_∞	Altitude	ε
N_2	1.7 ($= B^*$)	2.1 km/s	35 km	0.9

[4]Yohshikawa also correlated a B^* parameter where the coolant layer displaces the boundary layer and affects the flowfield. Typically, $B_h = B^*$ or $1.5B^*$ is taken as a blowing limit, after which aerodynamic penalties may occur, which is also a topic of interest in this thesis.

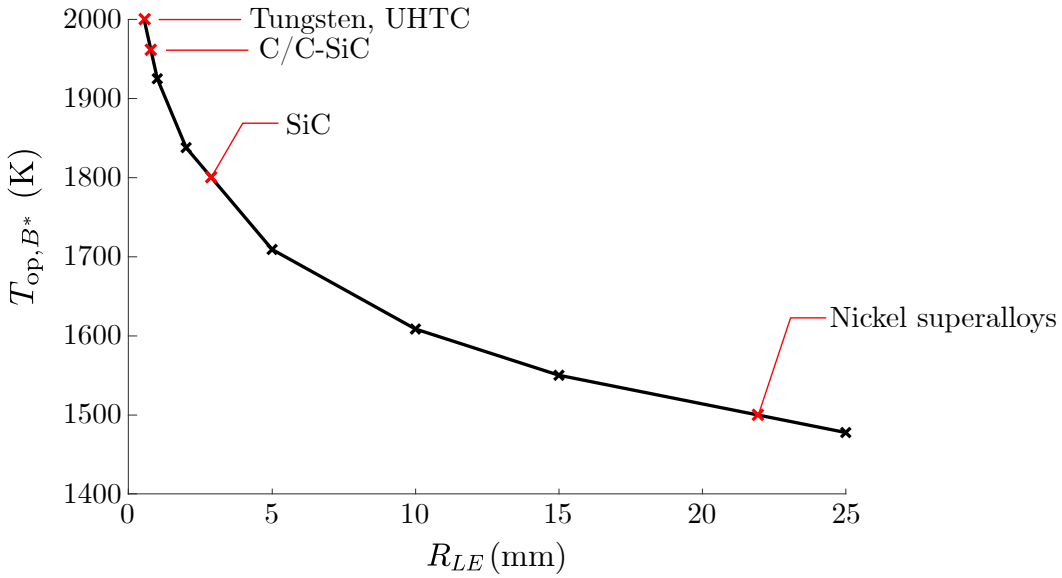


Figure 1.5: Minimum required surface temperature for local thermal equilibrium at the stagnation point for nitrogen blowing at $B_h = B^*$. Operating limits of common high-temperature materials are overlaid to indicate the minimum radius at which each material could operate under transpiration cooling.

1.4 Research Objectives

The work in this thesis aims to investigate the viability of transpiration cooling for hypersonic leading edges. To achieve this, this research is split into three primary objectives.

Determine the range of flight conditions and geometries for which transpiration cooling is both applicable and beneficial.

Active cooling would not be considered for a given trajectory if a passive system could survive. Conversely, there is likely a region where the required mass injection would be excessive, effectively blunting the leading edge and negating the aerodynamic advantage that transpiration cooling was employed for. This thesis will look at where these two constraints lie, effectively providing an envelope of viable performance. In the prior stagnation point heat balance, the trade-off between three input parameters was considered for a stagnation point. Examination of other input parameters will help map a more detailed design space.

Develop experimentally validated engineering correlations for leading edge transpiration cooling.

Currently, no correlations exist for leading edge injectors that capture key transpiration cooling parameters, specifically surface heat flux reduction and coolant concentration. This work seeks to establish such correlations by generating high-fidelity data through validated numerical simulations.

Design and characterise a transpiration-cooled leading edge.

Bridging the gap between numerically optimised and experimentally manufactured leading edge injectors is critical to generating reproducible experimental datasets. This would also include the first known test of a sharp transpiration-cooled leading edge in a hypersonic flow environment. To achieve this, a

novel design and manufacturing approach is required to leverage advanced fabrication methods to deliver precisely targeted mass flux distributions.

1.4.1 Thesis Outline

This thesis investigates these research objectives using a 'bottom-up' approach. The chapters of the thesis are as follows:

- **Chapter 2: Background and Literature**
  A review of the literature is carried out to understand the relevant studies that cover aspects of the above research objectives, helping to frame the scope and direction of this thesis.

- **Chapter 3: Design of a Transpiration-Cooled Leading Edge**
  Transpiration-cooled leading edges are designed and manufactured according to two different manufacturing methods. The uniformity and accuracy of the mass flux compared to the numerical designs are measured by a bespoke benchtop rig. These measurements are used to interpret the cooling performance observed in hypersonic wind tunnel tests. This chapter also presents the first additively manufactured injector tested in a hypersonic flow, which enabled more precise mass flux control.

- **Chapter 4: Experiments on a Transpiration-Cooled Leading Edge in Hypersonic Flow**
  Wind tunnel experiments are carried out following development of the injector. Optical methods (infra-red thermography, pressure-sensitive paint) are used to capture the heat flux and coolant concentration both on the injector, and downstream of it. The datasets are compared to laminar CFD simulations to validate the numerical method and blowing boundary condition. Surface pressure measurements are taken downstream of the injector, in the context of examining the drag effects of larger blowing parameters for sharp leading edges.

- **Chapter 5: Numerical Simulations of Leading Edge Transpiration Cooling at Flight Conditions**

  Following validation of the numerical method, simulations are conducted at flight conditions to investigate the effects of mass injection on heat flux, coolant concentration and drag. The data for a range of conditions, geometries, and coolants is collapsed by semi-empirical correlations, providing a foundation for low-order modelling.

- **Chapter 6: Performance of a Transpiration Cooled Leading Edge**

  The validated correlations and design tools developed in the previous chapters are brought together in a multiphysics modelling tool to simulate the thermal response of a leading edge in flight. Aerothermal limits of the system are implemented to calculate steady flight envelopes where transpiration cooling may be beneficial. The effect of different input parameters (material, gas, and radius) are also considered.

- **Chapter 7: Conclusion and Final Remarks**

  A final conclusion of the key results of the thesis is presented. Reflections on the methodology are made and the scope for further work is explored.

CHAPTER 2

Background and Literature

2.1 Porous Media Flow 19

2.2 Heat Flux Correlations 30

2.3 Coolant Concentration Correlations 38

2.4 Systems-Level Modelling 41

2.5 Non-Intrusive Measurement Techniques 42

Transpiration cooling injects coolant into the crossflow, sketched in Figure 2.1. Understanding the internal and external flow processes informs the approach of the literature review. High external heat fluxes are mitigated through three mechanisms:

1. Solid to coolant gas convective heat transfer as the gas passes through the porous material [30].

2. Film cooling, where coolant gas and boundary layer thickening reduce the incoming heat flux by decreasing thermal gradients at the wall [31].

3. Reduction of catalytic wall heating and protection from material oxidation, the latter of which may allow vehicles to operate at higher temperatures through re-radiation [32].

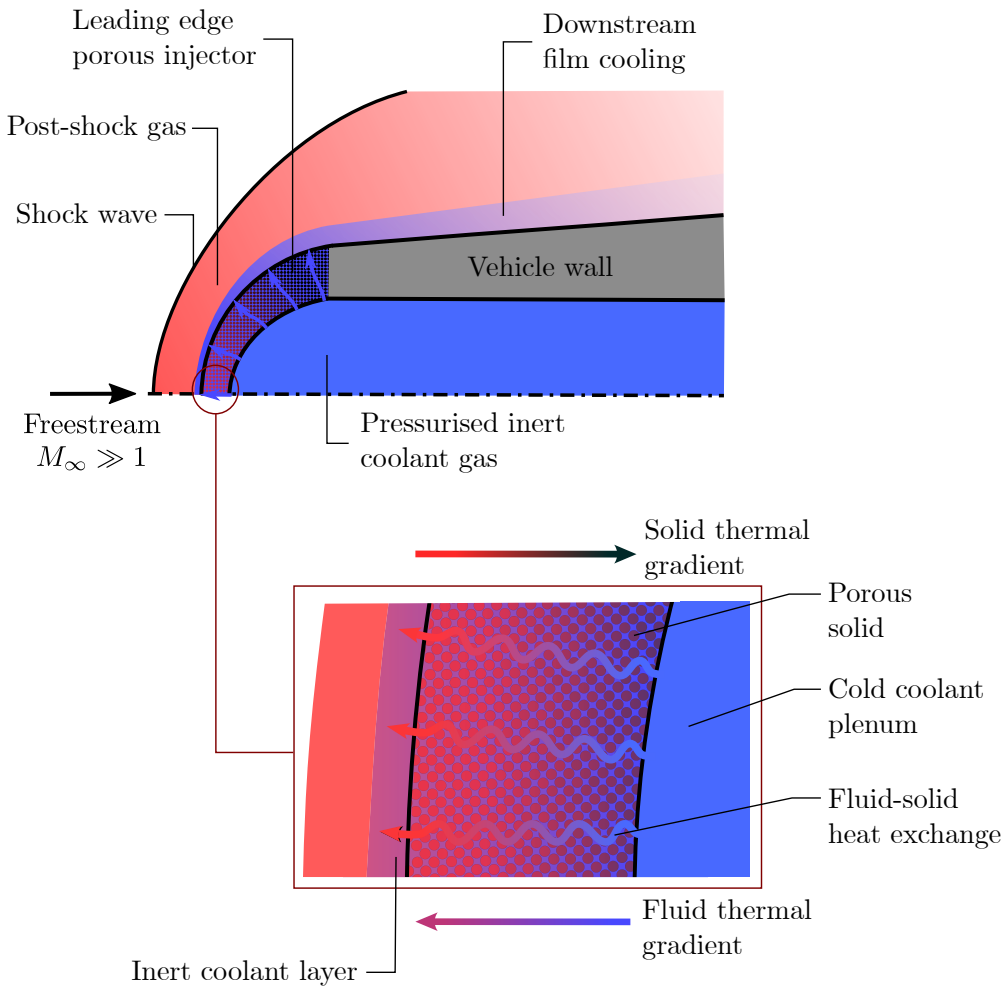


Figure 2.1: A sketch of a transpiration-cooled leading edge.

2.1 Porous Media Flow

Understanding how coolant moves through the porous structure is critical for predicting and optimising system performance. Porous media are often characterised by their porosity and permeability. The porosity, ϕ, is the volume fraction of void (also known as pore space) within the material. Here, open porosity is the volume fraction of interconnected pores that permit fluid flow from inlet to outlet. Most relevant literature, including this thesis, assumes the porous medium is fully open and saturated with coolant. Pore sizes in sintered materials for transpiration cooling are typically on the order of 10-100 μm [33, 34], therefore injecting coolant in bulk rather than discontinuous jets. Rather than modelling the flow through each individual pore (a computationally expensive task), macroscopic modelling of the volume-average fluid velocity is carried out using the Darcy-Forchheimer equation, shown in Equation 2.1. The equation describes the pressure losses in porous media due to viscous and inertial flow resistances. Inertial losses become significant when the pore-scale Reynolds number exceeds $Re_{\text{pore}} \gtrsim 10$ [34, 35].

$$-\nabla p = \underbrace{\frac{\mu_c}{k_D}\underline{\boldsymbol{u_c}}}_{\text{viscous}} + \underbrace{\frac{\rho_c u_c}{k_F}\underline{\boldsymbol{u_c}}}_{\text{inertial}} \tag{2.1}$$

Here, ∇p is the pressure gradient; μ_c, ρ_c, u_c and $\underline{\boldsymbol{u_c}}$ are the fluid viscosity, density, velocity magnitude and velocity vector respectively. k_D and k_F are the Darcy and Forchheimer coefficients: material-specific permeability terms that describe how the tortuosity of the network of pores resists the fluid flow. Permeabilities are highly dependent on the material and manufacturing techniques. Due to the random nature of pore formation (discussed below), porous samples often exhibit variation between identically-manufactured samples. Sintered materials are generally considered isotropic with scalar k_D and k_F values [33], whereas porous composites have been documented to be highly orthotropic due to the nature of fibre layup [36, 37], both of which are discussed further in Section 2.1.1.

The 1D Darcy-Forchheimer equation may be integrated from inlet to outlet

to characterise the porous mass flux in terms of the boundary conditions only. Equation 2.3 shows this for an isothermal case, where subscripts int and ext correspond to the internal plenum and external wall conditions respectively.

$$-\frac{\mathrm{d}P}{\mathrm{d}x} = \frac{\mu}{k_D}u + \frac{\rho}{k_F}u^2 \tag{2.2}$$

$$\frac{P_{\text{int}}^2 - P_{\text{ext}}^2}{2P_{\text{int}}L} = \frac{\mu_{\text{int}}}{k_D}u_{\text{int}} + \frac{\rho_{\text{int}}}{k_F}u_{\text{int}}^2 \tag{2.3}$$

In high-temperature applications, the gas is heated as it passes through the hot porous matrix, increasing μ_c and therefore reducing local mass flux. This is known as *viscous blockage*. Langener et al. [38] devised a 1D analytic solution (Equation 2.4) for an assumed linear coolant temperature distribution in a flat plate injector. Figure 2.2 shows the effect of gas temperature on viscous blockage and coolant velocity. For a two-dimensional leading edge, localised heating in one area of the injector may reduce the local mass flux, further increasing the local heating in a positive feedback loop.

$$\frac{P_{\text{int}}^2 - P_{\text{ext}}^2}{2P_{\text{int}}L} = \frac{\mu_{\text{int}}}{k_D}Au_{\text{int}} + \frac{\rho_{\text{ext}}}{k_F}Bu_{\text{ext}}^2 \tag{2.4}$$

$$A = \frac{\beta}{(n+2)}\left[(1+\beta)^{n+2} - 1\right] \tag{2.4a}$$

$$B = (1+\beta) \tag{2.4b}$$

$$\beta = \frac{b}{T_{\text{int}}} \tag{2.4c}$$

$$\mu = \mu_{\text{ref}}\left(\frac{T}{T_{\text{ref}}}\right)^n \tag{2.4d}$$

$$T = T_{\text{int}} + (T_w - T_{\text{int}})\frac{x}{L} = T_{\text{int}} + b\frac{x}{L} \tag{2.4e}$$

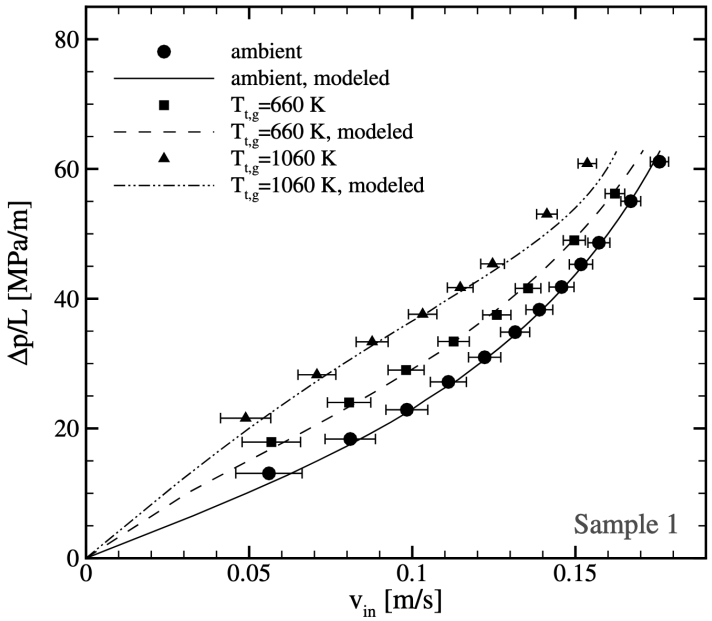


Figure 2.2: Pressure differential against coolant inlet velocity, measured by Langener et al. [38] at high total temperature supersonic conditions.

An analytic solution for 2D porous flow by Hermann & McGilvray was developed for an isothermal, incompressible Darcy flow using potential flow theory. To account for an unknown coolant temperature distribution and compressibility effects, finite difference calculations have been carried out [34, 36, 39].

Material permeability is directly linked to internal thermal energy exchange: greater pore tortuosity reduces material permeability but enhances interfacial heat transfer between solid and fluid [40]. Internal thermal exchange is characterised by the volumetric heat transfer coefficient, h_v, which quantifies the internal convective heat exchange. At local thermal equilibrium (LTE), fluid and solid temperatures are equal. For the millimetre-scale wall thicknesses under consideration, this only occurs as $h_v \to \infty$. Otherwise the porous domain is considered to be in local thermal non-equilibrium (LTNE).

Equations 2.5 and 2.6 show the coupled energy exchange within a porous medium for the porous solid and fluid, derived by Glass et al. [41]. In the equations, subscripts s and f represent solid and fluid respectively. Equation 2.5 considers con-

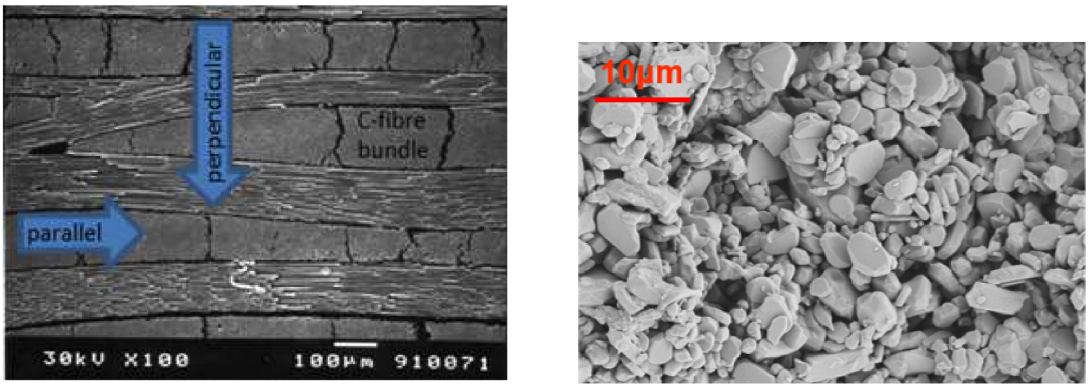
duction only within the solid, and Equation 2.6 considers convection via fluid flow.

$$(1-\phi)\rho_s C_{p,s}\frac{\partial T_s}{\partial t} = k_{y,s}(1-\phi)\frac{\partial^2 T_s}{\partial x^2} + h_v(T_f - T_s) \tag{2.5}$$

$$\phi\rho_f C_{p,f}\frac{\partial T_f}{\partial t} = \phi\rho_f C_{p,f}\frac{u_f}{\phi}\frac{\partial T_f}{\partial x} + h_v(T_s - T_f) \tag{2.6}$$

2.1.1 Porous Materials

Pore formation on the micron level for transpiration cooling has been studied in two classes of materials: composites and sintered materials. In porous composites, micro-scale porosity arises from interconnected cracks or voids within the resin matrix during thermal cycling, which are often oriented by the fibre direction. Porosity in sintered materials is introduced either by partial sintering or by adding pore-forming agents that decompose during thermal processing to create a pore network. Figure 2.3 shows the microstructures of both material classes that enable permeability.



(a) Porous CMC [42] (b) Porous alumina [43]

Figure 2.3: Microstructure of CMC and sintered ceramic, with visible microporous features.

Porous carbon-carbon, a type of carbon matrix composite (CMC), has been extensively characterised by DLR over the past decade as a candidate material for transpiration cooling due to its high operating temperatures (approx. 1800 K) and good mechanical strength [36, 37, 39, 42, 44]. A key milestone was the AKTIV experiment, which demonstrated a flat CMC injector on the SHEFEX-II flight

experiment [10, 45], supported by extensive ground tests in plasma facilities [46], shock tube tests [47, 48], and numerical modelling [49]. The flight experiment showed cooling efficiencies up to 58% at the injector and 42% downstream, and matched numerical modelling to within 14%.

Sintered stainless steel was one of the first materials considered for transpiration cooling [50–52]. More recent studies have considered porous tungsten, [34, 53, 54], known for its high operating temperatures (approx. 2000 K [55]) and good mechanical properties.

Another class of sintered materials are porous ultra-high temperature ceramics (UHTCs) such as ZrB_2. They are able to operate at extremely high temperatures, with a melting temperature of over 3000 K [56] and good volumetric heat transfer lending itself to high internal cooling [57]. UHTCs have recently been developed for transpiration cooling applications at Imperial College London [58–61] and tested at The University of Oxford [23, 31, 33, 62].

Both CMCs and UHTCs have a large passive cooling potential through re-radiation, which is proportional to the surface temperature to the fourth power. Increasing the operating temperature from 1000 K to 2000 K yields a 16 times greater heat flux rejection. However, both materials are susceptible to oxidation which leads to surface recession, formation of impermeable oxide layers, and embrittling [62, 63]. This behaviour broadly begins at 1000 K for both materials, delayed temporarily by SiC barrier coatings [64, 65]. Transpiration cooling has therefore also been investigated as a form of oxidation barrier which may enable high-temperature re-radiation [32].

For prototyping purposes, other porous materials have been employed for low temperature experimental transpiration cooling studies. Reasons for material substitution include machinability, and enabling optical diagnostics for non-intrusive measurements. Metapor is an off-the-shelf product line of sintered materials often selected for experiments [66–68] due to their ease of machining, which enables fabrication of complex injector geometries. Ewenz Rocher [43, 69] employed porous alumina as its pore size was sufficiently small to enable pressure-sensitive paint

measurements. Naved et al. [66, 70] used porous alumina and zirconia on separate occasions due to their emissivities and low thermal diffusivities that enabled infra-red (IR) thermography measurements. Optical techniques for transpiration cooling experiments are discussed further in Section 2.5.

While the exact permeabilities and heat transfer properties will be different between prototyping materials and flight-relevant materials, matching the pore size and mass fluxes permits reconstruction of the bulk coolant film to analyse transpiration cooling effects. Table 2.1 shows a summary of materials employed in transpiration cooling studies, noting their permeabilities and volumetric heat transfer coefficients where available.

Table 2.1: Intrinsic porous material values used in previous transpiration cooling studies. Where a range of values were presented in the literature, a median was taken.

Material	Studies	ϕ	k_D (m^2)	k_F (m)	h_v (Wm^{-3}K^{-1})
ZrB_2	[30, 33, 71]	0.41	$2.3 \cdot 10^{-14}$	$1.54 \cdot 10^{-7}$	$2.7 \cdot 10^4$
Bronze (SIKA-B)	[33]	0.30	$2.16 \cdot 10^{-12}$	$1.02 \cdot 10^{-6}$	
C/C CMC [*]	[36, 42]	0.11	$3.57 \cdot 10^{-13}$	$2.08 \cdot 10^{-8}$	$1.15 \cdot 10^5$
Al_2O_3 (Metapor CE70)	[66]	0.40	$2.51 \cdot 10^{-13}$	$1.08 \cdot 10^{-8}$	
Al (Metapor BF100Al)	[67]	0.17	$8.26 \cdot 10^{-14}$	$5.3 \cdot 10^{-10}$	
ZrO_2	[62, 66]	0.20	$1.60 \cdot 10^{-14}$	$1.98 \cdot 10^{-10}$	$5 \cdot 10^5$
Alumina	[43, 69]	0.39	$3.48 \cdot 10^{-15}$	$0.72 \cdot 10^{-9}$	

[*] Properties are highly orthotropic due to fibre direction layup. Values shown are for flow direction parallel to layup.

2.1.2 Measurement of Properties

Permeability coefficients have been measured experimentally using standardised engineering methods for a range of porous materials [33, 72] by comparing pressure and temperature changes to the mass flow rate across a sealed porous sample subject

to a pressure differential. Ifti et al. [33] also compared measured permeability coefficients of sintered spherical bronze beads (mean diameter 69 μm) against a predictive model by Ergun [73] that uses particle diameter and porosity only. The modelling equations are given below in Equations 2.7 and 2.8, where d_p is the particle diameter. The experimental results matched k_D to within 9.7%, however a larger discrepancy of 37% was found for k_F, attributed toward non-uniform particle diameter distribution.

$$k_{D,\text{ Erg.}} = \frac{\phi^3 d_p^2}{150(1-\phi)^2} \tag{2.7}$$

$$k_{F,\text{ Erg.}} = \frac{\phi^3 d_p}{1.75(1-\phi)} \tag{2.8}$$

Due to the complex setup, experimental data for volumetric heat transfer coefficient, h_v, is limited. h_v has been previously measured by heating either the porous matrix [30, 74] or heating the fluid upstream of injection [71] and measuring the corresponding change in solid or fluid temperature at a fixed flow rate. As with permeability, h_v depends on the porous microstructure, which changes with material processing and exhibits a degree of randomness [71].

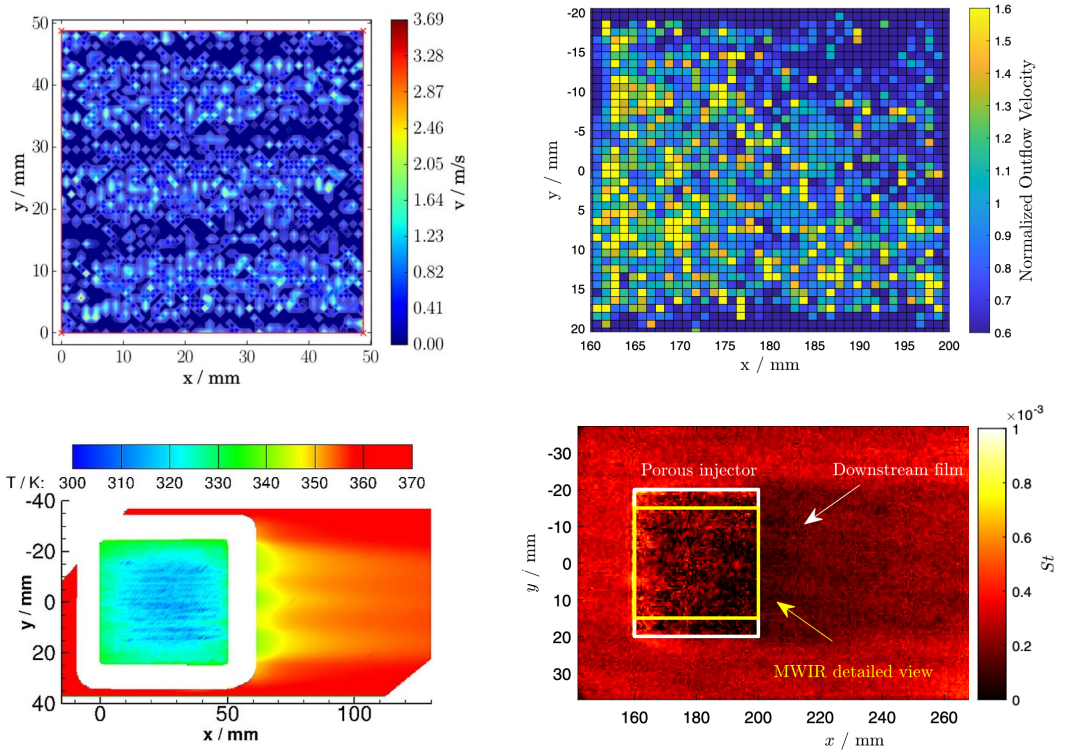
2.1.3 Measurement and Effects of Inhomogeneities

Homogeneous outflow from the injector is essential for uniform coolant coverage. With uniform outflow, the local blowing conditions align more closely with the assumed average, improving confidence in data based on mass flux values [23, 66]. Kerth et al. [75] also highlighted that local jetting from inhomogeneous injectors could promote boundary layer transition, although this effect remains unquantified.

Measurement of outflow homogeneity has been carried out by articulating velocity sensors over the surface of an injector, usually performed as a benchtop test under atmospheric conditions. These sensors can be hot-wires [33, 35, 67] or pitot tubes [36, 37, 76]. While flat injector shapes are more straightforward, conical injectors have used 4-axis [36] or 5-axis [67] traverse systems to ensure appropriate probe positioning and orientation.

The outflow from sintered metals and ceramics has generally been shown to be more uniform than that of CMC injectors. Figure 2.4 compares the velocity outflow from two flat plate injectors: Metapor and CMC, and includes corresponding IR thermography results from wind tunnel tests. Note the narrower velocity scale for the Metapor than the CMC in the uniformity maps. The CMC injector has a clearly patterned outflow distribution (attributed to the directionality of the fibre layup [37]) which leads to uneven film cooling. In comparison, the Metapor has more uniform blowing and therefore produces a more even coolant layer[1]. The effect of fibre layup direction is even more apparent for more complex injectors, such as the CMC cone in Figure 2.5, where the outflow dynamic pressure varies by an order of magnitude depending between fibre orientations, as marked in the figure. Another CMC cone tested in an arc-jet facility by Gulli et al. [77] showed relatively poor performance during tests, where local hot-spots are visible in the IR thermography images due to uneven coolant coverage.

[1]The Metapor sample used by Naved et al. [66] is less homogeneous than most other ceramic materials they tested but is the only result where the film effect is visualised.



(a) CMC injector performance, taken from König et al. [37].

(b) Metapor CE170 injector performance, taken Naved et al. [66].

Figure 2.4: Measured velocity outflow distributions and corresponding cooling performance of two flat plate injectors.

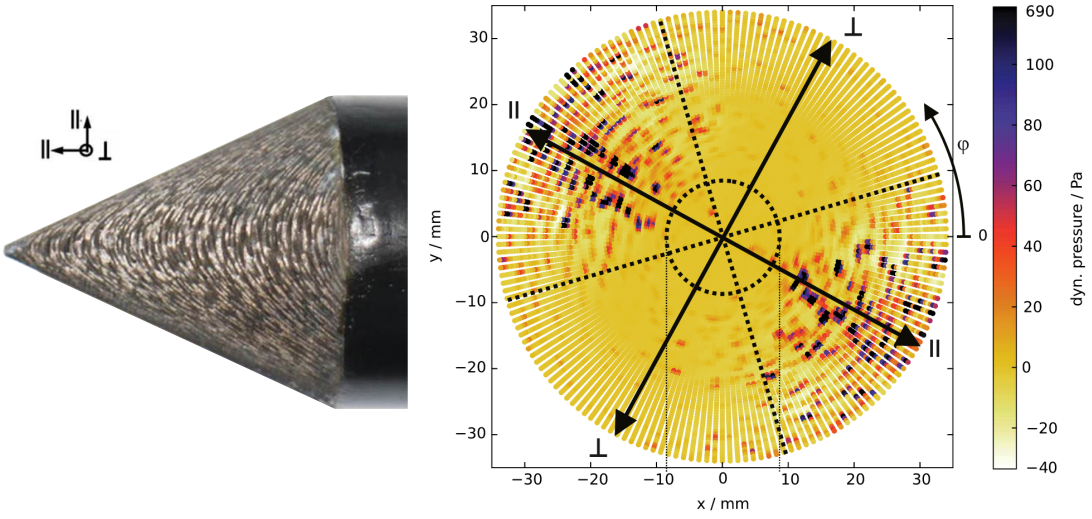


Figure 2.5: Outflow (dynamic pressure) of a CMC porous cone measured by Dittert et al. [36]. The direction of fibre layup is marked on the diagram and corresponds closely to the large measurement variations.

2.1.4 Coolant Fluids

Water has been considered in numerical [34, 52] and experimental arc-jet [78–80] studies due to its high heat capacity and additional energy transport potential associated with phase change from liquid to vapour. However water is a heavy coolant, and is more challenging to pressurise. Arc-jet tests have also found that large ice dendrites formed around injectors due to the low pressure test environment, though it was put forward that ice formation is less likely on a flight vehicle.

A range of coolant gases has been investigated, most commonly helium, nitrogen, and air [31, 50, 51]. Inert gases are often favoured for oxidation protection [32], while nitrogen offers improved availability with some protective capability. Refrigerants such as freon-12 were found experimentally to provide no additional cooling benefit over light gases [81], a result attributed to chemical effects. More recent numerical studies suggest that even reactive coolants undergo limited reaction in the shock layer and may still provide oxidation protection [82].

It has been shown extensively that helium achieves better cooling than nitrogen at the same mass flow rate, due to its high heat capacity aiding thermal transport, and low density which thickens the boundary layer and reduces thermal gradients [31, 46, 50, 51, 66, 81, 83–85]. As a result of its cooling efficiency and inert nature, helium is widely regarded as the coolant of choice.

2.1.5 Design of Injectors

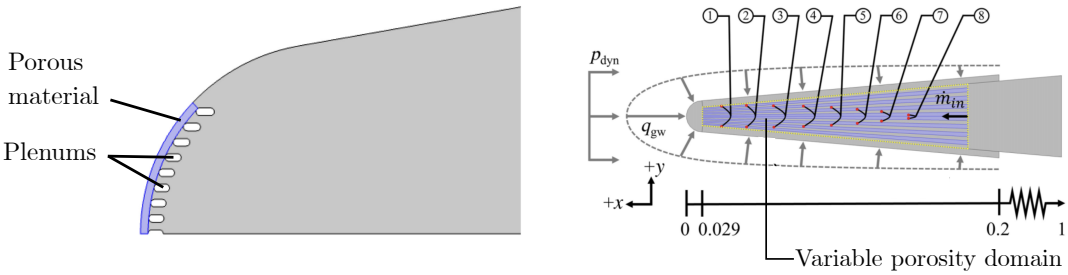
Most current transpiration cooling studies have focused on constant-thickness injectors applied to regions with minimal external pressure variation, such as flat plates, stagnation points, and frustums. Consequently, experiments and systems studies [49, 86] have typically modelled the porous flow in 1D.

On a leading edge or nosetip, the highest mass flux is expected at the stagnation point to overcome the highest heat flux. As the heat flux decreases over the surface, the mass flux would correspondingly diminsh. Since the mass flux distribution is a pressure-driven problem, the injector architecture must also account for the

variation in the external surface pressure. Figures 2.6 and 2.7 illustrate the complexity gap between numerically-designed leading edges with variable mass flux, and experimentally achieved injector designs.

In general, numerical design studies have produced highly targeted mass fluxes by controlling the material permeability distribution [34], using multiple plenums [87], or designing a structure with variable wall thickness [52]. Two examples are illustrated in Figure 2.6.

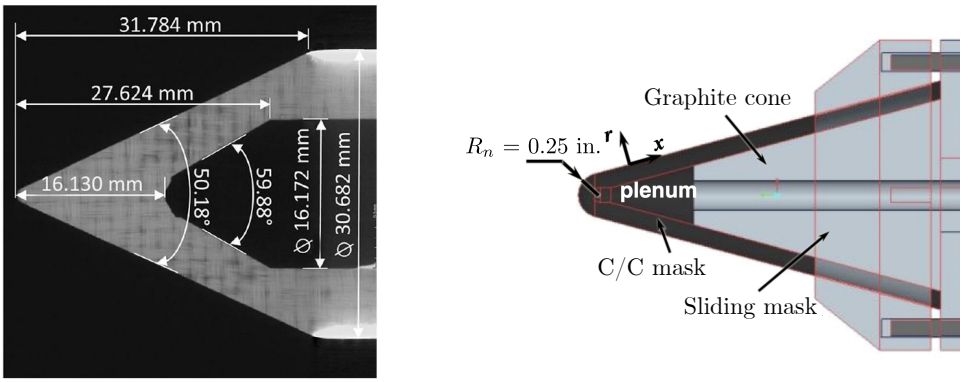
In contrast, manufactured injectors for experiments have directed mass flux toward the stagnation point, but without precise targeting or calculation. While the outflow mass flux distributions were measured, their uniformity and the overall outflow distribution were not considered further when analysing wind tunnel data [36, 77]. Two manufactured CMC cones are shown in Figure 2.7.



(a) Multi-plenum design from [87].

(b) Multi-plenum design from [34].

Figure 2.6: Internal structures of numerically-designed leading edge injectors.



(a) Sharp CMC cone from [36].

(b) Blunt CMC cone from [35].

Figure 2.7: Internal structures of two manufactured conical nosetip injectors.

2.2 Heat Flux Correlations

Several correlations exist for transpiration cooling of fundamental geometries such as stagnation points and flat plates, however to the author's knowledge, there are no correlations for modelling the heat flux on a leading edge injector. A key goal of this thesis is to build up empirical models for low-cost rapid modelling, beginning with assessing the applicability of previous models for fundamental geometries. This section discusses transpiration cooling correlations for stagnation points, flat plates, and leading edges.

Research on cooling due to mass injection has been carried out in the context of ablation studies since the 1950s, forming key engineering correlations for a range of parameters and geometries. The conversion of ablation outgassing correlations to transpiration cooling has occurred gradually over the past 15 years, which are grouped by injector geometry in this section. In the studies presented below, the blowing parameter and blowing ratio are two key parameters of interest. The blowing ratio, F, is simply a mass flux ratio of injection to freestream. The blowing parameter, B_h, is a non-dimensional mass flux; defined as the blowing ratio scaled by the uncooled Stanton number, St_0. These parameters are given in Equation 2.9 – 2.11.

$$F = \frac{\rho_c u_c}{\rho_\infty u_\infty} \tag{2.9}$$

$$St_0 = \frac{\dot{q}_0}{\rho_\infty u_\infty (h_{aw} - h_w)} \tag{2.10}$$

$$B_h = \frac{F}{St_0} = \frac{\rho_c u_c (h_{aw} - h_w)}{\dot{q}_0} \tag{2.11}$$

Where ρu is mass flux, $\dot{q}$ is heat flux, and h_{aw} is adiabatic wall enthalpy. Subscripts 0, c, and ∞ correspond to uncooled, injected coolant, and freestream quantities respectively. B_h is an especially useful mass flux correlation parameter due to the incorporation of freestream conditions and heat flux.

2.2.1 Stagnation Points

Correlating the heat flux reduction with mass flux at the stagnation point was first carried out by Swann & Pittman [88] during the modelling of a recessing ablative char layer. Numerical modelling of the boundary layer equations for air injection into air led to the blowing parameter correlation, shown in Equation 2.12.

$$\Psi = \frac{\dot{q}}{\dot{q}_0} = 1 - 0.72B_h + 0.13B_h^2 \tag{2.12}$$

Marvin & Pope [89] analytically extended the correlation to account for binary mixtures (where the injected gas is different to the coolant gas) by changing the correlation parameter from B_h to $B_h \left(\frac{W_\infty}{W_c}\right)^n$, where W is molecular weight. Tauber [90] suggested a value of $n \approx 0.25$ from a collection of available experimental data.

A different semi-analytic approach was devised by Yoshikawa [29] through linearisation of the shock layer energy equation. The correlation is shown below in Equation 2.13, and also accounts for binary gas mixtures through the molecular weight ratio.

$$\Psi = \frac{\dot{q}}{\dot{q}_0} = \sqrt{\pi\Lambda}\frac{\exp\{-\Lambda B_h^2\}}{1 + \mathrm{erf}\{\Lambda\}^{0.5} B_h} \tag{2.13}$$

$$\Lambda = \begin{cases} \frac{1}{\pi}\frac{\Delta}{\Delta_0}\lambda^{B_h/B^*} & (B_h \leq B^*) \\ \frac{1}{\pi}\frac{\Delta}{\Delta_0}\lambda & (B_h > B^*) \end{cases} \tag{2.13a}$$

$$B^* = 1.82\frac{\sqrt{\pi\epsilon(W_c/W_\infty)}}{k_b(\chi'_w)^*} \tag{2.13b}$$

$$(\chi'_w)^* = \frac{1.187\sqrt{(8\epsilon(1-\epsilon)}}{(1+\sqrt{8/3\epsilon}) - \epsilon)(1 + 0.225\sqrt{\epsilon})} \tag{2.13c}$$

$$\lambda = \sqrt{\frac{W_\infty}{W_c}} N_c \tag{2.13d}$$

$$\frac{\Delta}{\Delta_0} = 1 + k_b\sqrt{\frac{1}{\epsilon}\frac{W_\infty}{W_c}} F \tag{2.13e}$$

$$\epsilon = \frac{\rho_\infty}{\rho_1} \tag{2.13f}$$

Here, $N_c = 1$ or $5/9$ for diatomic or monatomic coolant gases respectively. The shape factor, k_b, equals unity for axisymmetric stagnation points. The parameter Δ/Δ_0 represents the change in shock layer thickness due to blowing. B^* is the *boundary layer blow-off parameter*, defined by Yoshikawa as the point at which the shock layer thickness increases by the original boundary layer thickness. At this threshold, the coolant layer sufficiently displaces the boundary layer, dominating the wall flow and altering the cooling behavior, as per Equation 2.13a. Implications of boundary layer blow-off on the broader flowfield have not been considered in depth for transpiration cooling.

Figure 2.8 demonstrates the comparison between Yoshikawa's correlation to that of Swann & Pittman and Marvin & Pope, showing excellent consistency between the predictions, along with experimental data of Howe & Sheaffer [91].

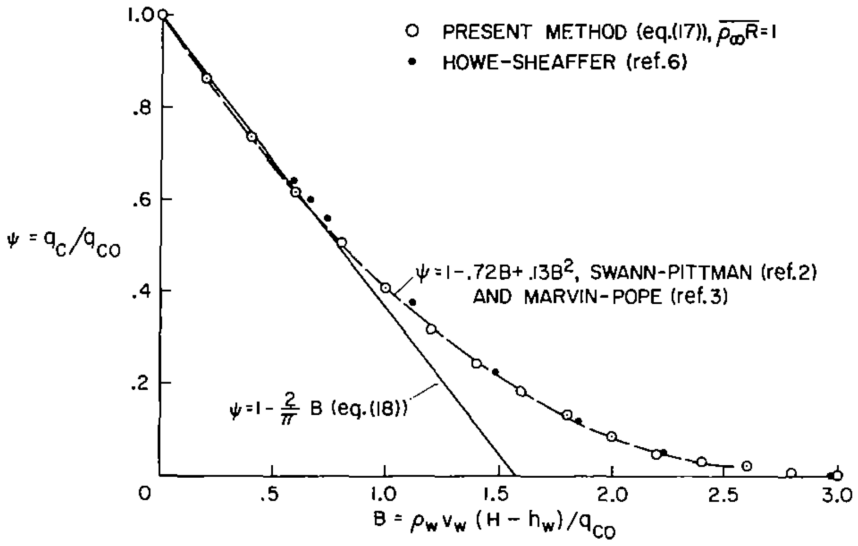


Figure 2.8: Comparison of stagnation point cooling correlations from the 1960s, taken from [29].

In the 1970s, further experimental datasets [81, 92] verified Equations 2.12 and 2.13 at the stagnation point of hemispherical ablator geometries. More recent experimental [70] and numerical [93] studies have verified the applicability of Yoshikawa's correlation to transpiration cooling.

2.2.2 Flat Plates and Film Cooling

The cooling both on and downstream of a flat plate injector has been studied extensively, with correlations formed for a wide range of flow conditions. Cooling and mixing has been investigated analytically [94] numerically [86, 95], and experimentally [38, 66]. Film cooling downstream of a flat injector is particularly relevant to the present work, as the surface downstream of a leading edge or nosetip could be considered analogous to an inclined flat plate.

Film cooling has been the subject of extensive study for over 50 years. Goldstein [96] reviewed a wide range of theoretical and experimental film cooling correlations, many involving control volume analyses of hot gas entrainment into the coolant film layer. Fujiwara [97] more recently suggested that formulation of a unified film cooling theory would be exceedingly difficult due to the sheer number of variables involved.

In Figure 2.9, Hermann et al. [57] showed that laminar transpiration cooling conditions are maintained by moderate blowing at moderate $Re_{u,\infty}$. Laminar cooling is more effective compared to turbulent conditions, as turbulent entrainment and mixing draw hot gases into the film layer.

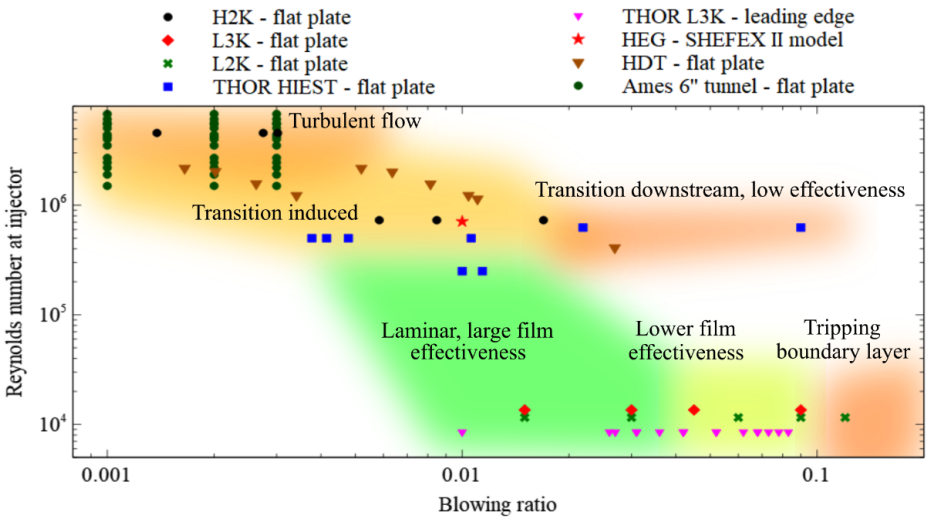
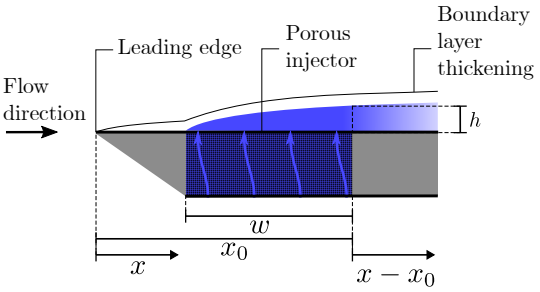


Figure 2.9: Review of regimes where flat plate transpiration cooling is most effective, taken from [57].

A correlation developed by Heufer & Olivier [98] for laminar film cooling from a slot injector was modified by Ifti et al. [31, 86] for a porous injector. The modification to the correlation parameter ξ_{th} used an updated coordinate system for a porous injector, shown in Figure 2.10.

Ifti's experimental results in Figure 2.11, show that the modified correlation (Equation 2.14) gives good agreement downstream of the injector for moderate blowing ratios of helium and nitrogen. In the equation, η_{th} is the thermal efficiency: $1 - \dot{q}/\dot{q}_0$, and C^* is the Chapman-Rubesin factor at the Eckert reference temperature.



$$\eta_{th} = \begin{cases} 1 & (\xi_{th,FP} \leq \beta) \\ [1 + \alpha(\xi_{th} - \beta)]^{\gamma} & (\xi_{th} > \beta) \end{cases} \tag{2.14}$$

$$\xi_{th} = \frac{1}{Fw}\sqrt{\frac{x - x_0}{x_{ref}}\frac{C^* x}{Re_{u,\infty}}} \tag{2.14a}$$

Figure 2.10: Coordinate system used by Ifti et al. [86] for Equation 2.14.

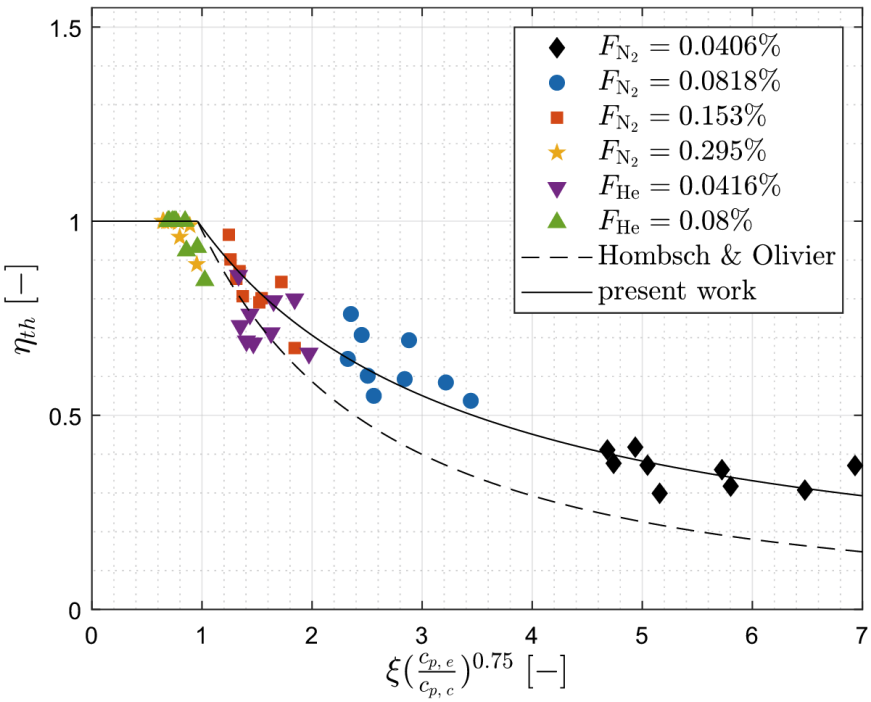


Figure 2.11: Experimental data collapse of flat plate results by Ifti et al. [86].

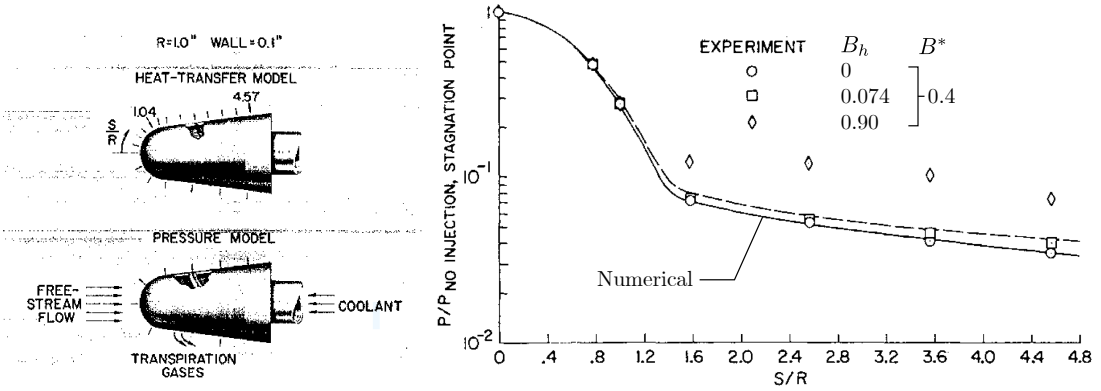
2.2.3 Leading Edges and Nosetips

Many of the studies with mass injection on cones between 1950 and 1980 were carried out with porous outgassing downstream of a solid nosetip [50, 83, 99–102]. During this period, only two experiments were carried out with measurements taken directly on a porous leading edge injector.

Pappas & Lee [81] tested a 25 mm blunted cone with a short porous afterbody, shown in Figure 2.12a. Seven coolant gases were tested at $M_\infty = 13.4$ and $Re_{u,\infty} = 1.0 \cdot 10^5$ /m. Figure 2.12b shows the surface pressure augmentation due to helium injection, with B_h and B^* values overlaid for the present context. Across all gases and blowing conditions in the study, stagnation point pressure remained constant but increased at downstream locations for high blowing conditions. For some gases, the downstream surface pressure was 3 times larger with cooling than without. In the context of a nosetip, this would lead to a significant rise in pressure drag.

Kaattari [92] tested hemispherical models of radius 89 mm with 6.4 mm-thick porous skin at $M_\infty = 7.32$ and $Re_{u,\infty} = 3.4 - 29.2 \cdot 10^6$ /m. Air was injected into an air freestream for blowing parameters up to $B_h \approx 2.4$. After verifying the stagnation point heat flux matched Swann & Pittman's correlation, reasonable agreement was also achieved when applying the correlation to locations other than the stagnation point. To achieve this, the blowing parameter was redefined using local uncooled heat flux, and a mass flux averaged over the entire injector surface.

Figures 2.12 and 2.13 show that the studies by Pappas & Lee and Kaattari employed discrete sensors embedded within the porous material, with sensor radius between 1.6 and 2.5 mm. While the sensor radius was significantly less than the model radius, it was of similar size to the thickness of the porous material. It is possible that sensors mounted in such a way disrupted the coolant flow within the porous material, however this effect was not quantified.



(a) Model and sensor locations. (b) Surface pressure results with helium.

Figure 2.12: Sketch of the blunted porous cone and surface pressure results by Pappas & Lee [103]. B_h and B^* values are overlaid to show the effect of large B_h on surface pressure.

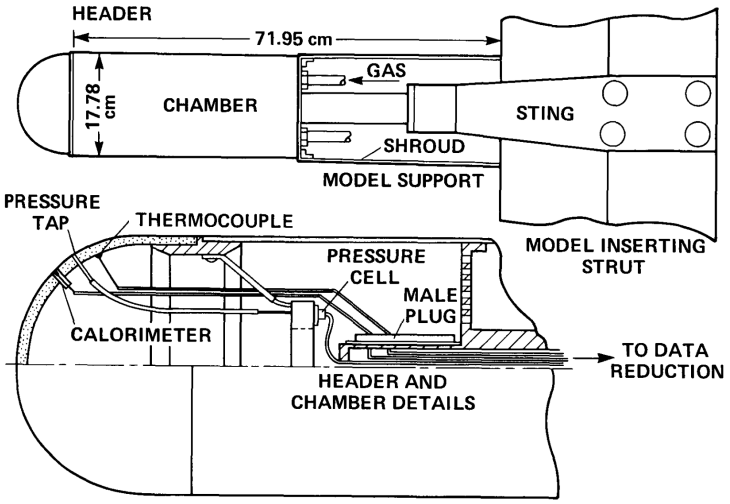


Figure 2.13: Diagram of the hemispherical model used by Kaattari, showing the method of instrumenting the porous injector, taken from [92].

More recent experimental studies have focused on manufacture and testing of sharper leading edges (between 0.1 and 10 mm) in the context of transpiration cooling. Examples of injectors were shown earlier in Figures 2.6 and 2.7. Experiments have been conducted in subsonic heated flow facilities [104] or arc-jets [44, 77, 80], with most studies employing IR thermography for temperature measurements. The results of these studies are often presented as temperature or heat flux fields. While heat flux is more robust for comparison, these studies lacked

generalised correlations or dimensionless parameters linking heat flux to the mass flux distributions, limiting their applicability to other cases.

The flowfields around a leading edge with transpiration cooling have been modelled numerically using finite volume simulations with prescribed mass flux boundary conditions [105–108]. The results of these studies showed minimal shock layer perturbation from leading edge injection, and effective film cooling when the downstream flow remained laminar. Again, no correlation between local cooling performance and local mass flux was established.

2.3 Coolant Concentration Correlations

While heat flux modelling due to gas injection has been studied for decades in the context of ablation and more recently applied to transpiration cooling, the modelling of surface coolant concentration lacks this historical foundation. The distribution of surface coolant concentration is of interest as it indicates how effective transpiration cooling may be for oxidation protection and mitigating surface catalytic heating.

2.3.1 Stagnation Point

Ewenz Rocher [109] used a self-similar laminar boundary layer solution and film theory to develop a correlation for the coolant mass fraction at the wall, c_w, against the mass blowing parameter, B_m. The correlation is shown in Equation 2.15, where W is the coolant molecular weight, Sc is the Schmidt number, and D is the binary diffusion coefficient between the coolant and freestream. In [109], the finite volume code Eilmer was used to verify the correlation across a broad range of mass fluxes, freestream conditions, and gases.

$$c_w = 1 - \frac{B_m}{e^{B_m} - 1} \tag{2.15}$$

$$B_m = \sqrt{\frac{8}{\rho_e \mu_e \frac{\mathrm{d}u_e}{\mathrm{d}x}}} Sc_{w;\mathrm{ext}}^{0.6}\ \dot{m} \left(\frac{W_\infty D_{\infty-\infty}}{W_c D_{c-\infty}} \right) \tag{2.15a}$$

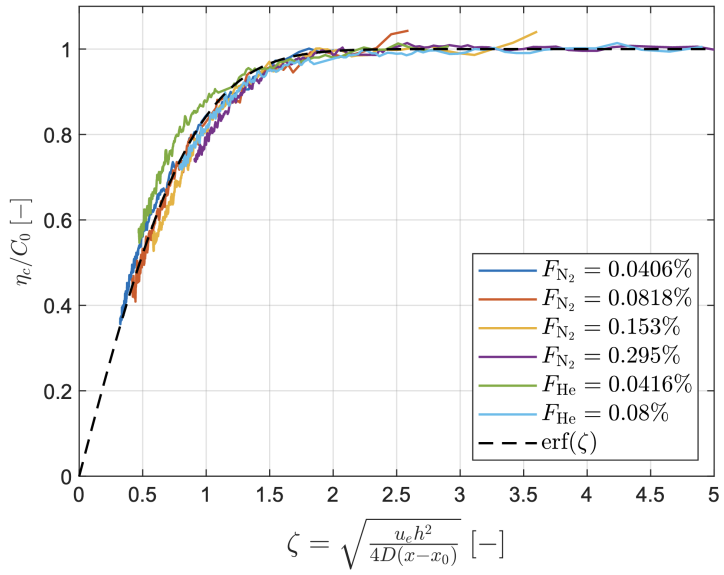
2.3.2 Flat Plates and Film Cooling

Downstream of a flat plate injector, Ifti [110] developed a semi-analytic correlation for the concentration efficiency of a laminar coolant film being swept downstream. The concentration efficiency, η_c, was defined based on the reduction in partial pressure of oxygen (pO_2) at the wall between cooled and uncooled cases. The correlation is shown in Equation 2.16, referencing the coordinate system in Figure 2.10, and an advection-diffusion model to model the dissipation of the film along the length of a flat plate. In the correlation, u_e is the boundary layer edge velocity,

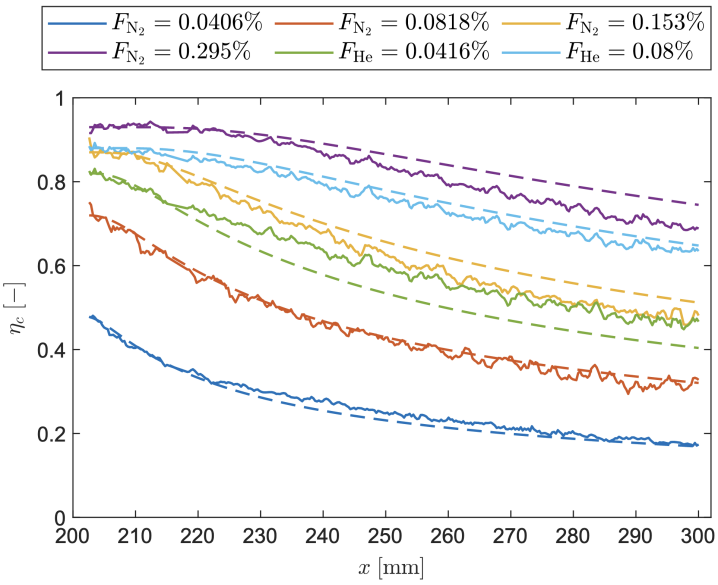
h is the coolant slab height immediately after the injector, and D is the binary diffusion coefficient. In [110], h was calculated using a control volume analysis around the injector to model the boundary layer entrainment into the coolant film layer. Figure 2.14 shows the comparison of the semi-analytic theory against experimental data, with spatial distributions of η_c within 17% of the experiment.

$$\eta_c = 1 - \frac{pO_2}{pO_{2,0}} = \mathrm{erf}(\xi_c) \tag{2.16}$$

$$\xi_c = \sqrt{\frac{u_e h^2}{4D(x - x_0)}} \tag{2.16a}$$



(a) Concentration efficiency against correlation parameter.



(b) Concentration efficiency against surface coordinate.

Figure 2.14: Experimental [31] and semi-analytic correlation [110] results of surface concentration downstream of a flat plate injector. Figures taken from [110].

2.4 Systems-Level Modelling

Two previous numerical tools have been developed to assess the performance of transpiration-cooled vehicles, both using generalised correlations similar to those presented above.

Böhrk et al. [49], developed a finite-difference code, HEATS, to calculate the mass flux requirements of a constant-thickness, transpiration-cooled flat plate in the context of the flight experiment SHEFEX-II [45]. The solid and fluid temperatures were solved using a finite difference scheme for the thermal exchange equations in 2D (Equations 2.5 and 2.6) and the porous flow in 1D (Equation 2.2). Aerodynamic heating models [111, 112] for flat plates were used to calculate the uncooled surface heat flux distribution, and film cooling was modelled using Goldstein's [96] correlation. Blowing limits of $F < 0.144$ were imposed to avoid triggering downstream turbulence, a limit taken from slot injection experiments [98]. When compared to the SHEFEX-II flight data, agreement of the transient wall temperature to that predicted by HEATS was within 14%.

Another code, PIRATE, was developed by Hermann et al. [113] by deriving the thermal impulse response to the thermal exchange equations, enabling rapid temperature calculations without a finite difference scheme. PIRATE, discretised both flat plate and blunt body domains into 1D slices. Again, semi-empirical correlations for aerodynamic heat flux and cooling efficiencies were used, both for flat plates [111, 112, 114] and blunt bodies [29, 115–117]. System limits of $F < 0.04$ were imposed to avoid boundary layer transition. For blunt body calculations, PIRATE assumed that the body radius was significantly greater than the wall thickness to justify the 1D porous flow and heat transfer assumption. PIRATE was used to assess the performance of a transpiration-cooled heat shield on a conical nosetip with $R_{LE} = 0.5$ m under both steady and transient flight conditions [57]. The required mass fluxes were prescribed as boundary conditions based on the thermal requirements of the model. In the study, transpiration cooling was shown to be beneficial for velocities of 5.5 to 8 km/s and altitudes of 30 to 55 km.

2.5 Non-Intrusive Measurement Techniques

The majority of the correlations presented above have been experimentally validated, with increasingly complex geometries requiring more sophisticated measurement techniques. As previously mentioned, experimental studies in the 1970s used discrete sensors embedded within large (50-100 mm) blunt-body experimental models. For experiments on sharp leading edges (1-10 mm) made from porous materials, non-intrusive methods are essential to avoid blocking pores with sensors, to accommodate model space constraints, and to provide sufficient measurement resolution. Such measurements include heat flux, coolant concentration and surface pressure. While some contemporary studies have employed discrete sensors on the backside of injectors [44, 118], most recent experiments mentioned above have used optical techniques for heat flux and concentration measurements.

2.5.1 Heat Flux

All physical bodies emit electromagnetic radiation over a range of wavelengths, with emission power from a black body described by Planck's Law (Equation 2.17). Here, $I(\lambda, T)$ is the spectral intensity: the radiative power per unit area per unit at a given wavelength, λ, and temperature, T. h is the Planck constant, c is the speed of light in a vacuum, and k_B is the Boltzmann constant.

$$I(\lambda, T) = \frac{2\pi hc^2}{\lambda^5} \left[\exp\left\{ \frac{hc}{\lambda k_B T} - 1 \right\} \right]^{-1} \tag{2.17}$$

Spectral radiance (which relates to spectral intensity by incorporating directional dependence), is detected by infra-red thermography: a form of surface temperature measurement based on emitted radiation which is sensitive to a specific band of the infrared spectrum. These temperature measurements can then be processed to determine transient heat flux distributions.

Figure 2.15 shows the typical bands of IR thermography cameras and the corresponding black body radiance at different temperatures. For real materials

(known as grey bodies), the peak radiance occurs at different wavelengths depending on the material. Material selection is therefore a critical component of experimental design when using IR thermography: materials must have good emissivity in the wavelengths corresponding to the camera's sensitivity. By additionally selecting materials with low thermal diffusivity, processing may be conducted on a pixel-wise basis, allowing each pixel to act as an individual temperature sensor. In previous experiments, IR thermography has been employed for measurements on porous ceramics (e.g. Metapor, alumina) [31, 66] or porous CMCs [77, 78] and on PEEK downstream of injectors [66].

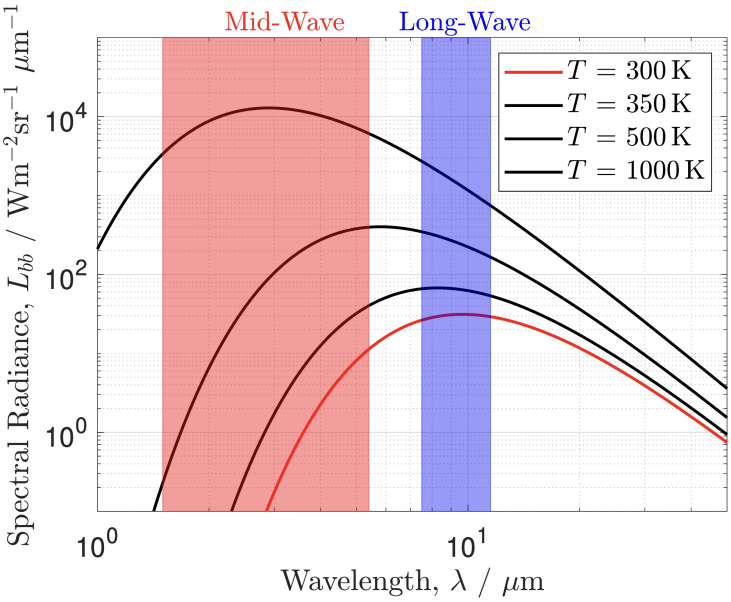


Figure 2.15: Spectral radiance of a black body for a range of temperatures, taken from [119].

IR thermography has been used extensively to measure heat fluxes both on and downstream of transpiration cooled injectors, with detailed studies focusing on stagnation points and flat plate injectors [37, 46, 66, 70, 78, 120].

Studies employing IR thermography on nosetip or wedge injectors have lacked detailed calibration procedures or spatially calibrated heat flux distributions [77, 80, 104]. A critical requirement for such geometries is accounting for the influence of highly curved surfaces on the emissivity [121]. Condren et al. [68, 120] addressed

this by applying an in-situ calibration technique [122] for patterned blowing surfaces by calculating the global camera position relative to the model. Details on the IR post-processing techniques employed in this thesis can be found in Appendix A.3.

2.5.2 Coolant Concentration

Pressure-sensitive paint (PSP) has been employed to measure coolant concentration at the wall in transpiration cooling studies. PSP contains a luminophore, a molecule that fluoresces with a high Stokes shift. The luminophore exhibits repeatable sensitivity to oxygen quenching, producing reduced emission intensity at higher oxygen partial pressure as modelled by the Stern-Volmer equation in Equation 2.18, where 'ref' corresponds to a reference condition, usually just before freestream flow arrival. When processing intensity-based PSP measurements, the ratio of intensities directly describes the ratio of partial pressures and is applied to each frame of high-speed camera recordings [123].

$$\frac{I}{I_{\text{ref}}} = A\left(\frac{pO_{2,\text{ref}}}{pO_2}\right)^n + B \tag{2.18}$$

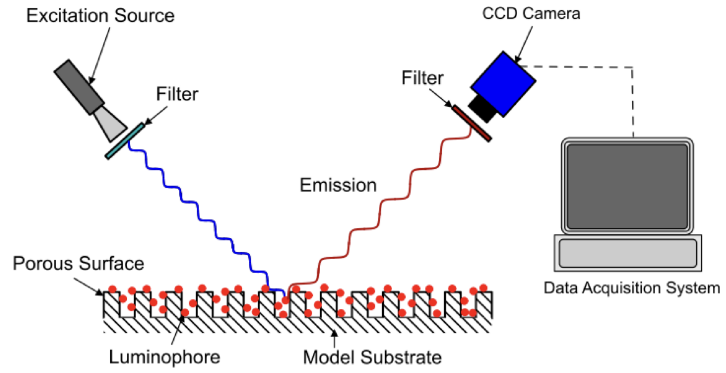
When local pressure is known, oxygen concentration may be determined from partial pressure measurements assuming static pressure remains constant with blowing. Coolant concentration at the wall may then be inferred by injecting oxygen-free gas and measuring the resulting oxygen reduction.

In [43, 69], a $Ru(dpp)_3$ porous PSP was applied directly on a porous injector to measure the surface coolant concentration without blocking the material pores. In [23, 31], ISSI TurboFIB PSP (a commercially available PSP formulation) was successfully deployed to take measurements downstream of flat plate injectors.

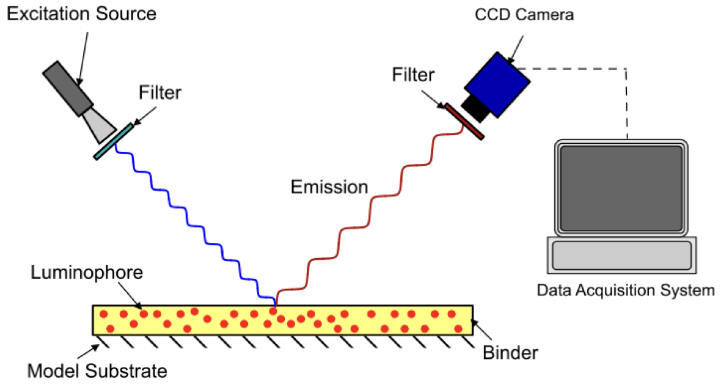
For short-duration facilities, the response time of PSP is critical and is largely dictated by surface preparation, with two methods illustrated in Figure 2.16. Spraying onto a porous surface (e.g. an injector or anodised metal) can achieve response times below 1 ms [124, 125], though anodisation is an intrusive process that may not be suitable for some models. Spraying onto a surface primed with a binder or base layer is also feasible. However the associated response

time has been estimated to be around 0.1 s [125], which would be unsuitable for short-duration facilities.

PSP intensity is also affected by surface temperature. The temperature sensitivities of the $Ru(dpp)_3$ and ISSI PSPs are similar, at 0.64 %/K and 0.5 %/K respectively [124, 126]. When measuring concentrations at the stagnation point, Ewenz Rocher [69] accounted for surface heating effects using additional nitrogen freestream tests for calibration. By contrast, the temperature rise on the flat plate used by Ifti [31] was considerably smaller, and no such calibration was performed.



(a) Porous surface



(b) Surface with binder

Figure 2.16: Two types of surface preparation for PSP application, taken from [126].

CHAPTER 3

Design of a Transpiration-Cooled Leading Edge

3.1 Introduction 48

3.2 Target Mass Flux 51

3.3 Material Selection 53

3.4 Design Methodology 57

3.5 Geometry 59

3.6 Experimental Setup 63

3.7 Performance Comparison 69

3.8 Conclusion 74

Preface

The first chapter of this research explores the design requirements of a transpiration-cooled leading edge. Manufacturing leading edge injectors capable of delivering consistent mass flux boundary conditions is key for a reproducible dataset that provides the means to validate numerical methods. Two manufacturing processes for porous leading edges are developed and compared, with each method numerically designed for a targeted blowing distribution and evaluated through benchtop testing and hypersonic wind tunnel experiments.

Parts of this chapter was presented at the High-Speed Vehicle Science and Technology (HiSST) conference [127].

Author Contributions

- Raghul Ravichandran: Conceptualisation, methodology, investigation, data analysis, and writing.
- Luke Doherty: Supervision as secondary supervisor.
- Matthew McGilvray: Supervision as principal investigator and funding acquisition.
- Anthony Finnerty: Engineering design support.
- Lithoz GmbH: Resources and manufacturing of 3D-printed porous leading edge.
- Serkan Nohut (Lithoz GmbH): Review & editing of material development and manufacturing.

Acknowledgements

The authors would like to thank Nathan Donaldson for his advice on programming the 5-axis outflow traverse system. This research was funded by DSTL.

3.1 Introduction

As hypersonic missions and vehicle designs impose greater aerodynamic heating demands, mitigating extreme thermal environments becomes increasingly challenging. In extreme environments where passive thermal protection systems (TPSs) are insufficient and aerodynamic shape or reusability requirements exclude ablative solutions, active cooling systems potentially provide an effective method for managing high heat fluxes. Despite mass and complexity penalties, active systems could be applied in a targeted manner, such as at vehicle leading edges. Transpiration cooling is a promising active TPS candidate whereby coolant gas is injected into the hypersonic boundary layer via a porous injector on the vehicle surface. Transpiration cooling reduces external heat fluxes through the coolant layer and thickened boundary layer, reducing thermal gradients at the wall [31]. Flow through a porous medium also actively cools the vehicle structure, by means of thermal exchange between the hot porous matrix and the coolant gas [30].

Rather than modelling the fluid flow through individual microscopic channels, flow through a porous medium is often described using bulk flow properties and homogenised material properties. The pressure gradient of coolant within the porous medium is commonly expressed by the Darcy-Forchheimer equation:

$$-\nabla p = \frac{\mu_c}{k_D}\underline{\boldsymbol{u_c}} + \frac{\rho_c u_c}{k_F}\underline{\boldsymbol{u_c}} \tag{3.1}$$

Here, ∇p is the pressure gradient; μ_c, $\rho_c u_c$ and $\underline{\boldsymbol{u_c}}$ are the coolant flow viscosity, mass flux and velocity vector respectively. In a hot re-entry vehicle, heat transfer from the hot porous solid to the coolant can increase local coolant temperature, increasing μ_c, and decreasing mass flux to the hottest regions of the injector [53]. This effect is known as *viscous blocking*. For flat injectors, such as flat plates and stagnation points, lateral pressure gradients are negligible, allowing Equation 3.1 to be treated in 1D. In contrast, highly curved leading edge injectors require 3D modelling to account for 3D pressure gradients and coolant flow turning within the porous structure, which influence the mass flux boundary condition.

During the Apollo missions, numerical and theoretical studies [29, 88, 90, 91] were carried out to understand the effect of mass injection on heat flux reduction for stagnation points, in the context of an ablative TPS. More recent studies have considered the applicability of the results of these studies to transpiration cooling [70, 78, 79]. A common correlation parameter across these results was the blowing parameter, B_h, defined as the ratio of blowing ratio, F, to uncooled Stanton number, St_0, shown in Equation 3.2.

$$B_h = \frac{F}{St_0} \tag{3.2}$$

$$F = \frac{\dot{m}_{inj}}{\rho_\infty u_\infty} = \frac{\rho_{inj} u_{inj}}{\rho_\infty u_\infty} \tag{3.3}$$

$$St_0 = \frac{\dot{q}_0}{\rho_\infty u_\infty (h_{aw} - h_w)} \tag{3.4}$$

Here $\dot{m}$ is mass flux, $\dot{q}$ is heat flux, and h_{aw} is adiabatic wall enthalpy. Subscripts 0, inj, and ∞ correspond to uncooled, injected coolant, and freestream quantities respectively.

Historical experiments have considered the effect of moderate blowing on heat flux and pressure augmentation directly on an injector surface using discrete surface sensors embedded within the porous materials [81, 92]. The effect of embedded sensors on the porous flow through the material has not been considered, although the results align well with the semi-analytic correlations. More contemporary studies have employed non-intrusive measurement techniques, including IR thermography [70, 77, 78] and sensors on the injector backside [44] for measurement of heat transfer.

The targeted design of injectors to achieve a specific mass flux distribution for leading edge transpiration cooling has been confined to numerical studies. In [87], multiple plenum architectures are used to minimise the probability of thermal shock failure in an ultra-high temperature ceramic (UHTC) leading edge, whilst in [34], the permeability of porous tungsten was varied discretely along the leading edge to target mass flux toward the regions of highest heat flux. In experimental studies on transpiration-cooled leading edges, there has been some

focus on directing coolant toward the stagnation point, however the explicit design and manufacture for a target distribution has not yet been carried out.

Experimental studies have also considered the characterisation of manufactured porous materials for mass injection. Ifti et al. [33] outlined a methodology to characterise the velocity uniformity and distribution of a flat plate injector using a hot-wire anemometer probe for UHTC injectors. This setup was used in subsequent porous ceramic characterisation [31, 66, 67, 69]. Porous carbon-carbon (C/C) conical nosetips were similarly characterised by Dittert et al. [36] using a pitot probe, and Gulli et al. [35] using a hot film anemometer. For conical geometries, multi-axis traversing systems were developed to position the sensors in space to ensure perpendicularity from the surface and consistent spacing between the sensor and surface.

Studies on porous ceramic matrix composite (CMC) cones [35, 36] have revealed that due to the orthotropic nature of the fibre layup in a carbon-carbon composite, the injection mass flux in the direction parallel to the fibre layup was several times more than that perpendicular to the fibre layup. Non-uniform outflow led to inconsistent cooling during arc-jet testing, revealed by the IR thermography results. In ceramic injectors, Naved et al. [66] similarly showed that outflow uniformity of a flat plate injector significantly affected the two-dimensionality of the coolant film, and therefore restricted the ability to draw conclusions from the heat transfer data.

The present work aims to optimise, manufacture and characterise a porous leading edge injector for heat transfer measurements in a wind tunnel. A target mass flux distribution is assigned based on the non-dimensional blowing parameter, B_h, and the internal architecture of the leading edge is optimised for this condition. Two leading edge materials and corresponding designs are manufactured, the uniformity of which are then characterised using a hot-wire anemometer articulated on a 4-axis traversing system. Heat flux measurements are carried out on each injector in a wind tunnel, to assess the effect of the outflow on the quality of heat flux data.

3.2 Target Mass Flux

3.2.1 Freestream Design Conditions

The leading edges were tested in the University of Oxford's High Density Tunnel (HDT) [128]: a cold-flow Ludweig tube facility that can operate over a range of Mach ($M_\infty = 4$ to 7) and Reynolds numbers ($Re_{u,\infty} = 2 \cdot 10^6$ to $53 \cdot 10^6$ /m). The design point for leading edge injection was the facility test flow condition given in Table 3.1.

Table 3.1: The HDT freestream conditions used as the porous injector design point. The conditions were characterised prior to wind tunnel tests using Kulite pressure sensors and aspirated thermocouples on a Pitot rake, as described in [129].

M_∞	$P_{0,\infty}$ (Pa)	$T_{0,\infty}$ (K)	P_∞ (Pa)	T_∞ (K)	$Re_{u,\infty} \cdot 10^{-6}$ (/m)	Equiv. altitude (km)
7.0	1280	481.9	309.4	44.6	7.09	≈ 23.7

3.2.2 Target Parameter

Variations in the uncooled surface heat flux along the leading edge require corresponding changes in coolant mass flux: higher heat flux at the stagnation point requires more coolant. The blowing parameter, B_h, is directly proportional to surface heat flux and has been used to correlate heat flux reduction with injection mass flux. In this work, the injector was designed to distribute mass flux to achieve a constant B_h value. A design point of constant $B_h = 1.2$ for nitrogen coolant was selected. The required mass flux is given in Equation 3.5, by rearranging Equations 3.2 to 3.4. Equation 3.5 extends the definition beyond the stagnation point, using local properties along the leading edge surface to calculate a mass flux distribution.

$$\dot{m}_{inj}(\theta) = \frac{B_h \cdot \dot{q}_0(\theta) \cdot \rho_\infty v_\infty}{(h_{aw}(\theta) - h_w)} \tag{3.5}$$

To determine the required heat flux and boundary layer variables in this equation, the numerical code Eilmer was used to simulate the flowfield around an uncooled model. $\dot{q}_0$ and h_{aw} were extracted from simulation data, while h_w was taken at room temperature. The predicted uncooled heat flux and corresponding

target blowing distributions are plotted in Figure 3.1. Further details of the numerical method and validation are given in Chapters 4 and 5.

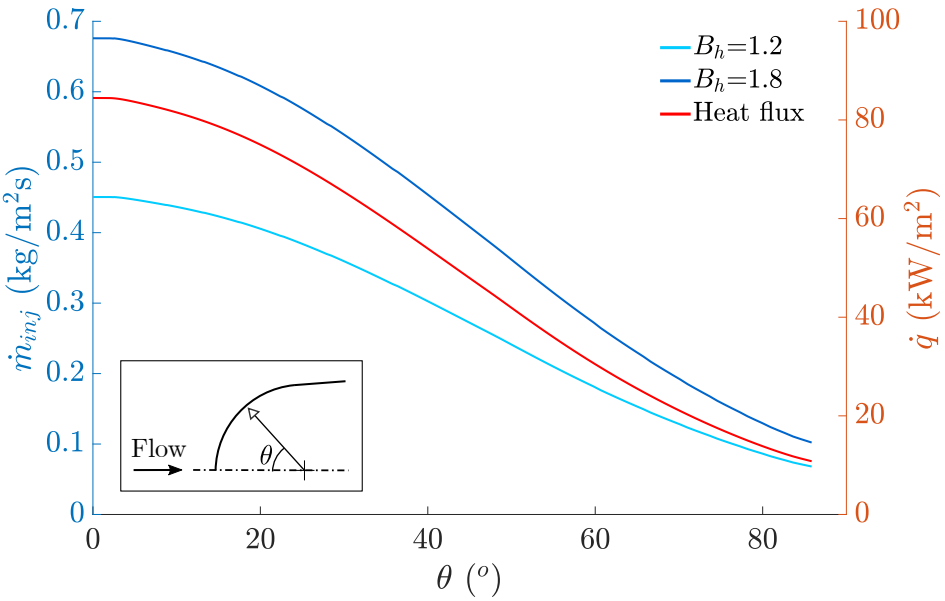


Figure 3.1: Heat flux distribution predicted in Eilmer, and the calculated mass fluxes required for different B_h values. For this experiment, $B_h = 1.2$ was the design point when used with nitrogen coolant.

3.3 Material Selection

IR thermography was selected as a non-intrusive technique for measuring heat flux on the injector surface. Porous material selection prioritised good mid-wave IR (MWIR) emissivity (wavelengths of $1.5 - 5.4$ μm, corresponding to the available MWIR camera), and low thermal diffusivity for pixel-wise heat flux analysis. Typically, ceramic materials are suitable for this purpose.

Two candidate materials and manufacturing methods were selected. Metapor CE100 is an off-the-shelf porous aluminium hydroxide manufactured in blocks by Portec AG. Metapor is easily shaped through CNC machining, and has been employed in a range of transpiration cooling experiments [66–68]. In this study, it serves as an accessible benchmark for material development. LithaLox 1347-P30 is a porous aluminium oxide (alumina) slurry developed by Lithoz GmbH for ceramic 3D printing. LithaLox components were manufactured on a CeraFab S65 printer using lithography-based ceramic manufacturing (LCM). Part of the present work focuses on refining the LithaLox processing for transpiration cooling applications, presented below. To the authors' knowledge, the use of additively manufactured microporous injectors (of any geometry) has not yet been employed in hypersonic transpiration cooling studies.

Nominal material properties for both porous ceramics are listed in Table 3.2. k_D and k_F were measured experimentally on constant-thickness samples with a mass flow controller, using the setup described in Section 3.6.1. The properties of ρ, k, C_p are provided by the manufacturers and use Landauer's relation to account for the effect of material porosity [130].

Table 3.2: Properties of candidate porous materials for transpiration cooling experiments. Peak emissivity is provided for the MWIR wavelength range.

	Variable	Metapor CE100	LithaLox 1347-P30
Porosity	ϕ	0.2	0.4
Darcy coefficient (m^2)	k_D	$6.42 \cdot 10^{-13}$	$2.26 \cdot 10^{-14}$
Forchheimer coefficient (m)	k_F	$2.12 \cdot 10^{-8}$	$1.72 \cdot 10^{-8}$
Density (kg m^{-3})	ρ	1710	3990
Thermal conductivity (W m^{-1} K^{-1})	k	1.662	29.0
Specific heat capacity (J kg^{-1} K^{-1})	C_p	1177	880
Thermal diffusivity (m^2 s^{-1})	$\alpha = \frac{k}{\rho C_p}$	$8.26 \cdot 10^{-7}$	$7.69 \cdot 10^{-6}$
Thermal product (J m^{-2} K^{-1} $s^{-0.5}$)	$rrck = \sqrt{\rho C_p k}$	1829	9735
Emissivity	ε	0.95	0.45

3.3.1 Development of Porous Alumina

LithaLox 1347 is a photocurable alumina slurry, developed by Lithoz GmbH and formulated from a pure α-Al_2O_3 powder content of 47% by weight to produce a dense, impermeable ceramic once fully sintered at 1650 °C [131]. Two methods were used to introduce porosity in the LithaLox. First, a pore-forming agent (PFA) of polymethylmethacrylate (PMMA) microbeads was incorporated into the slurry. Voids form in the ceramic structure following the thermal decomposition of the PMMA (occurring between 200 °C and 400 °C) during thermal post-processing [132, 133]. Second, partial sintering at a temperature lower than 1650 °C to promote pore interconnectivity.

Flat coupons of different LithaLox formulations were characterised to determine the material processing parameters (sintering temperature, PMMA content) and geometric factors (layer thickness, support structure) that promoted open porosity and uniform coolant outflow. To introduce a multi-modal pore size distribution, two types of PMMA microbeads were utilized: PMMA-1, with a particle size distribution of d_{50}[1] $\approx 8 - 11$ μm, and PMMA-2 ($d_{50} \approx 4 - 6$ μm).

Each mixture was stirred in a speed mixer at 1600 rpm for 2 minutes, followed by 1750 rpm for 1 minute to ensure a homogeneous distribution of the PMMA particles within the slurry. The multi-layered coupons were printed by the CeraFab

[1] Median particle diameter.

Multi 2M30, equipped with dual-vat systems to enable the use of porous and dense alumina slurries during a single printing process.

The most promising formulation that provided open porosity and uniformity was achieved by the LithaLox 1347-P30 slurry that was produced by combining LithaLox 1347 with 10 wt% of PMMA-1 and 20 wt% of PMMA-2, and sintering at a temperature of 1600 °C for 2 hours.

3.3.2 Manufacture of Porous Injectors

The Metapor leading edge was machined and cleaned in-house, in accordance with the recommendations of the material supplier [134]. Metapor CE100 has open porosity throughout, and so the machined leading edge required sealing on all surfaces (internal and external) except the injection area, accomplished using Dowsil 3140 RTV silicone. The flowable nature of the RTV allowed the silicone to penetrate into the pores without significant impact on the outer mould line. Outflow testing (see Section 3.6.1) confirmed no outgassing occurred over these surfaces.

For the LithaLox leading edge injector, a CeraFab S65 printer was used, where permeable and impermeable regions were printed consecutively. Shown in Figure 3.2, the base and support structure of the leading edge was printed from LithaLox 1347, and the porous leading edge from LithaLox 1347-P30. Print layers are built-up through photopolymerisation: each 50 μm layer was exposed to 180 mJ/cm^2 with a projector power of 50 mW/cm^2 and print resolution of approximately 40 μm per pixel.

After printing, the components, known as *green bodies*, were cleaned using a LithaSol 80 solution[2] and compressed air to eliminate excess surface slurry. Following the debinding process at 1100 °C to remove PFA particles and polymer binder, the components were sintered at 1600 °C for 2 hours under atmospheric conditions at a heating rate of 1 K/min. Sintering was found to shrink the components, requiring a stretching factor of 1.24 to be applied to the print (z) direction, and a factor of 1.20 was applied to the other two (xy) directions.

[2] Lithoz GmbH proprietary [135].

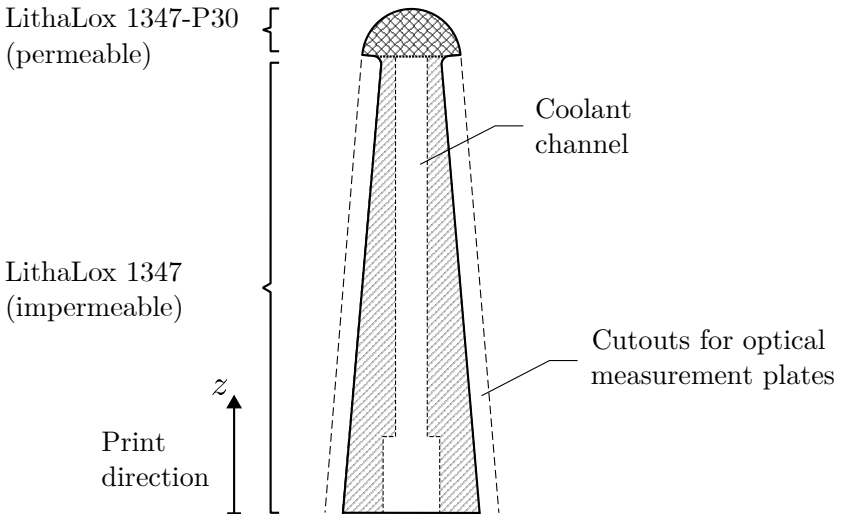


Figure 3.2: Leading edge injector orientation and print direction for the multi-material print.

3.4 Design Methodology

A targeted mass flux distribution can be achieved by varying local material permeability, porous wall thickness, or the inclusion of multiple plenums. This study focused on varying wall thickness, due to the simpler manufacturing and characterisation of a single plenum with the available constant-permeability materials. To vary the wall thickness under the constraint of a fixed outer mould line, the internal wall shape was varied.

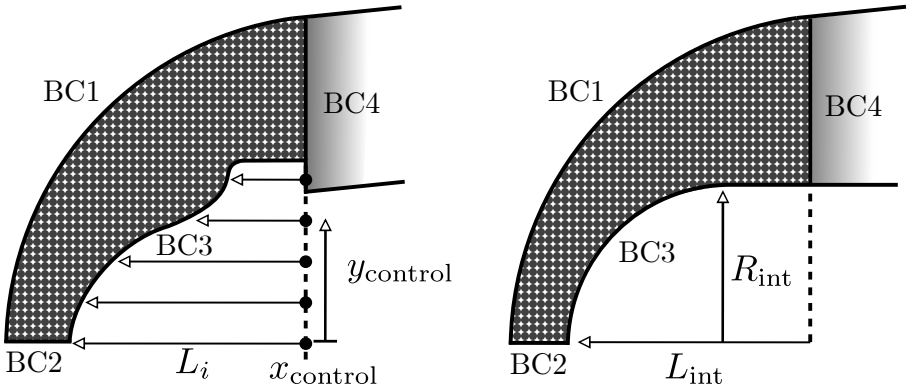
Parametrisation of the internal geometry for CNC machining and 3D printing is shown in Figure 3.3. The internal wall of the 3D printed leading edge is defined by a fourth-order Bézier curve, constrained to prevent a self-intersecting or otherwise non-physical geometry. The CNC machined leading edge was more heavily constrained as the internal wall face was restricted to the available tooling diameters and mill end shapes: (ball-nosed and flat-end mills).

The finite-element software, COMSOL MULTIPHYSICS, was used to simulate the internal coolant flow within the porous injector, driven by the internal pressure from a single plenum. The applied boundary conditions are sketched in Figure 3.3 and listed in Table 3.3. For each injector type, the internal wall shape was determined by varying the wall thickness to optimise agreement with a prescribed target mass flux distribution (shown earlier in Figure 3.1). A Nelder–Mead minimisation algorithm, implemented via COMSOL's LIVELINK FOR MATLAB, was used to adjust the geometry of the internal wall. The optimisation drove the simulated mass flux toward the target distribution formulated in Section 3.2, using an R^2 objective function.

The porous domains were modelled as isothermal 2D planar half-bodies. This was considered appropriate as the leading edge was a symmetric wedge tested at zero angle of attack in a cold flow facility[3]. The external pressure boundary was modelled using the modified Newtonian distribution and was assumed to be

[3]The short duration test time and cold flow facility mean that while the model surface temperature would rise sufficiently for data collection, the effect of viscous blockage would be negligible.

unaffected by the injection mass flux at the moderate target blowing parameters used in the study, an assumption supported by previous works [81, 136].



(a) LithaLox (3D printed) (b) Metapor (CNC machined)

Figure 3.3: Wall thickness parameterisation for mass flux optimisation. The numerical boundary conditions, BC1 to BC4, are described in Table 3.3.

Table 3.3: List of boundary conditions for the COMSOL model shown in Figure 3.3. $\mathbf{n}$ is the surface normal direction, P_{int} & P_{ext} are the internal & external pressure boundary conditions.

Boundary	Description	Equation
BC1	Outlet: pressure distribution	$P = P_{\text{ext}}$
BC2	Symmetry	$\mathbf{n} \cdot \rho\mathbf{u} = 0$
BC3	Inlet: plenum pressure	$P = P_{\text{int}}$
BC4	No flow	$\mathbf{n} \cdot \rho\mathbf{u} = 0$

3.5 Geometry

3.5.1 Outer Mould Line

Both leading edge injector types were designed to fit into the same 5° half-angle wedge model, cylindrically blunted with a 3 mm external radius. The resulting external injector geometry is shown in Figure 3.4. Small cutouts were added to the injector outer mould line to account for PEEK insert plates used for IR thermography. Injectors were required to span a sufficient width to form an effective coolant film and interface with a plenum for coolant gas delivery. For sealing, the impermeable backside face of each material was sanded and smoothed for O-ring contact. Sealing integrity was verified by outflow testing (Section 3.6.1) across the entire interface.

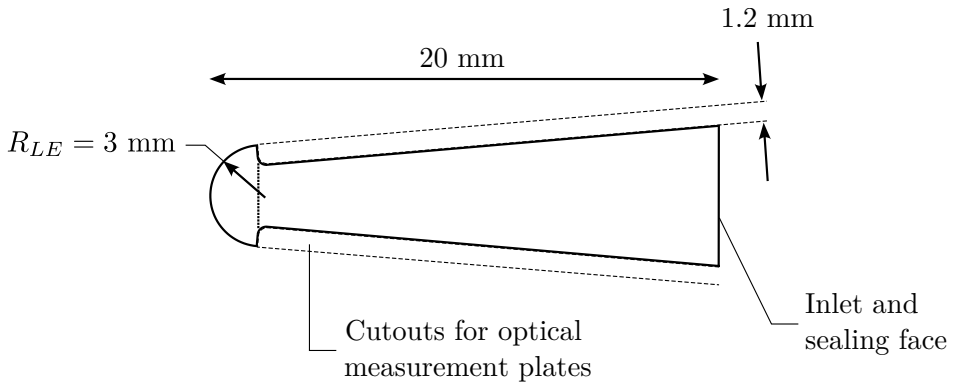
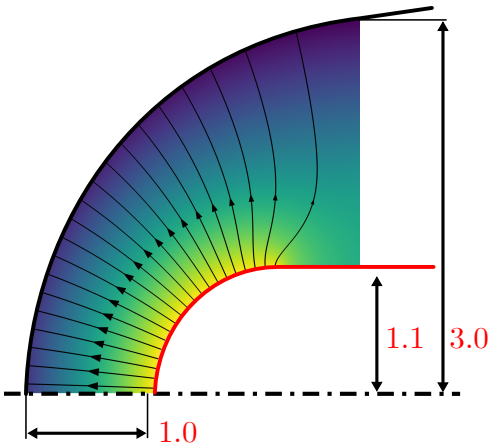


Figure 3.4: Annotated sketch of the outer mould line of both types of leading edge, constrained by the wind tunnel model and sealing.

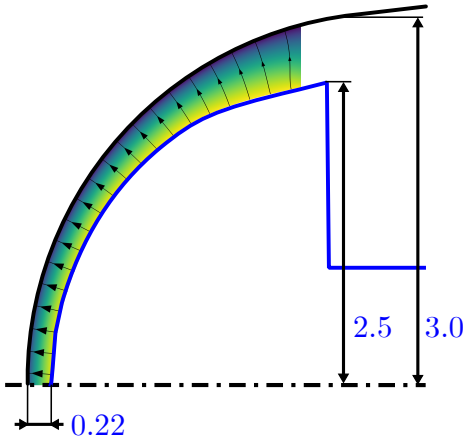
3.5.2 Injector Wall Design

Following the optimisation sequence described in Section 3.4, the optimised internal wall geometries and the corresponding mass flux outputs are shown in Figures 3.5 and 3.6. The LithaLox injector was additionally constrained to a maximum wall thickness of 0.5 mm due to challenges in maintaining open porosity when printing thicker samples. Both design methodologies converged on a solution where the porous wall was thinnest at the stagnation point. This design feature was

driven by a two-fold effect of requiring the highest mass flux at the stagnation point, and overcoming the highest external pressure.



(a) Metapor (CNC machined)



(b) LithaLox (3D printed)

Figure 3.5: Calculated porous wall shapes superimposed with the coolant pressure field and velocity streamlines. Diagram to scale, dimensions in mm.

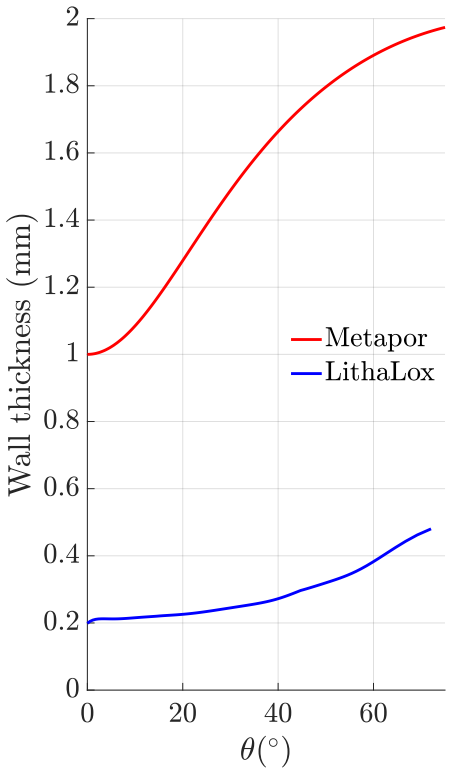
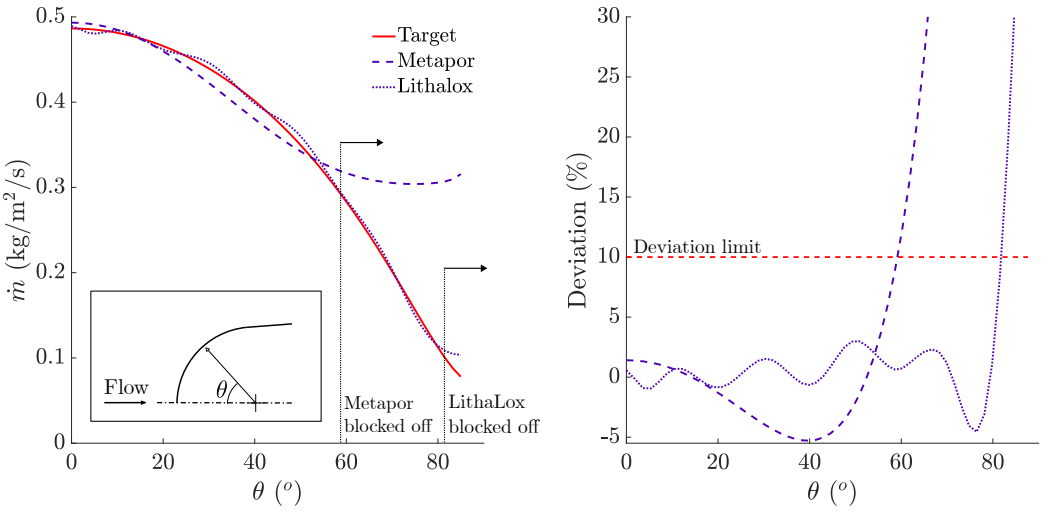


Figure 3.6: Wall thickness distributions.

Figure 3.7 shows the simulated mass fluxes of the optimised injectors compared to the target distribution. The figure shows that the more flexible parametrisation of the LithaLox injector meant that the optimisation procedure could match the target much more closely. The porous flow was highly two-dimensional in both injectors. In the downstream regions (higher θ), the mass flux overshoots the target

to varying degrees. It was found that impermeable backside boundary condition led to the flow re-directing from the backside to the nearest permeable outflow. The flexible parameterisation of the LithaLox injector could compensate for this more easily, leading to significantly smaller overshoot.



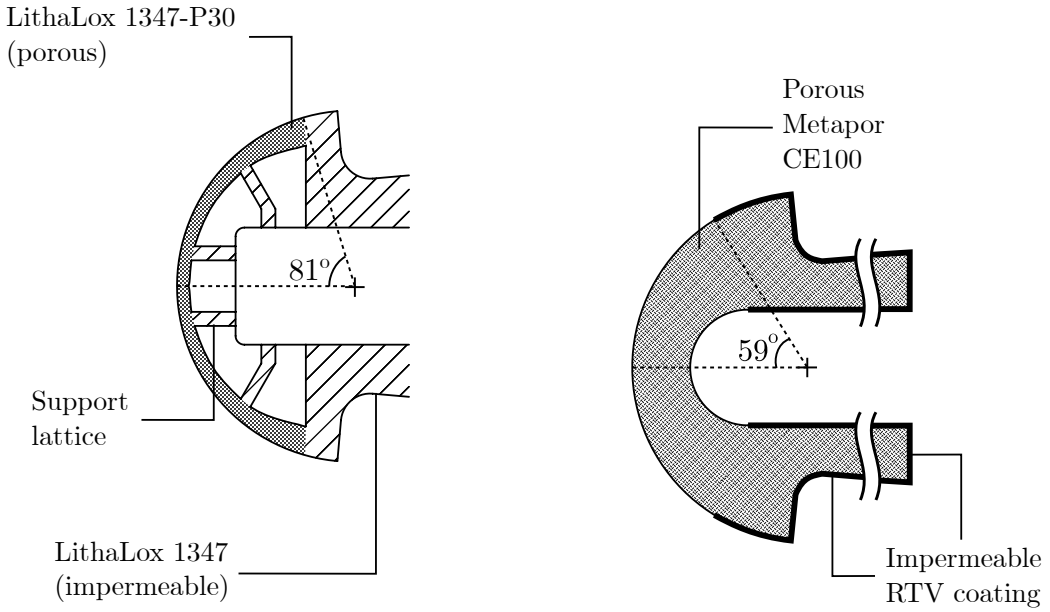
(a) Simulated mass fluxes.

(b) Mass flux deviation.

Figure 3.7: Simulated mass flux for the optimised internal geometries, and percentage deviation from the target condition.

An acceptable limit of 10% was set for the deviation of the simulated mass flux from the target. This was to guarantee a reasonably constant-B_h blowing condition, and to avoid adverse effects of excessive local blowing resulting from the overshoot at high θ. As such, the region of injection of the Metapor injector was limited to $\theta \leq 59°$, and the LithaLox to $\theta \leq 81°$. This required the blocking of injection surfaces up to the specified angles. Shown in Figure 3.8, this was achieved slightly differently for each material.

The LithaLox injector employed the dual-material printing capabilities of the manufacturing process. Utilising the print direction capabilities shown in Figure 3.2, the impermeable material was printed up to the porous limit and the remainder was printed from porous alumina. The porous region was reinforced with an internal support lattice due to the thin porous layer. Additional simulations and outflow



(a) LithaLox (3D printed)

(b) Metapor (CNC machined)

Figure 3.8: Internal geometry drawings of each leading edge showing final configuration after manufacturing modifications. Drawings to scale.

testing confirmed that the support lattice did not affect the mass flux distribution.

The Metapor injector employed the same RTV silicone as before to block outflow beyond 59°. A small 3D printed jig set at the appropriate angle was employed to apply the RTV precisely.

To understand the off-design performance of the injectors, the designs were simulated at different blowing parameters, coolants, and freestream conditions. For each case, plenum pressure was adjusted to best match the required mass flux distribution. Broadly, the mass flux was consistent and remained within 10% of the target for most of the injector surface. Violation of the 10% deviation limit occurred at similar angles as the on-design performance, and changed only marginally with condition. Plots of the simulated off-design performance may be found in Appendix A.1.

3.6 Experimental Setup

3.6.1 Outflow Characterisation

Uniform outflow is crucial for high-quality wind tunnel data and vehicle performance. Due to the random nature of microscopic pore formation during sintering, the outflow of coolant gas may vary locally within a single sample and across identically manufactured samples. The motivation for outflow characterisation was therefore two-fold: (1) to map the uniformity of the injector mass flow rate; and (2) to measure the mass flux distribution of the manufactured injector against the numerical design.

A 5-axis benchtop traverse, the Porous Outflow Traverse (POT), was developed to enable surface mass flux measurements of three-dimensional injectors. This measures the uniformity of local injection as well as to verify the manufactured components conform to the numerical design. For outflow velocity measurements, a constant temperature anemometer (Dantec StreamLine Pro) with hot-wire probe (Dantec 55P11 miniature straight wire) was used. The wire was calibrated in-situ using a Dantec StreamLine Pro Automatic Calibrator to relate hot-wire output voltage, E, to calibrator setpoint velocities v_{cal} between 0.08 and 0.63 m/s. The calibration data for an individual sensor is shown in Figure 3.9. As per King's Law [137], a fourth-order polynomial was fitted to the data points.

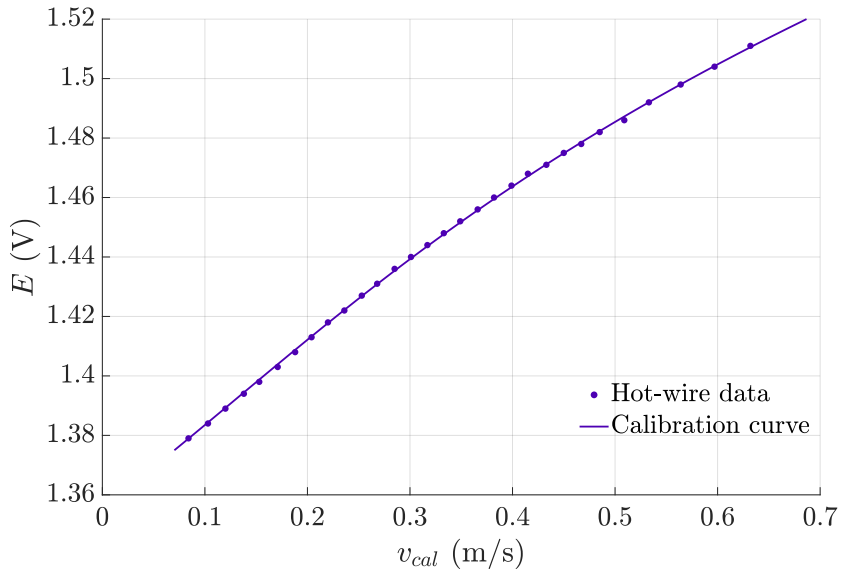


Figure 3.9: Calibration curve of the CTA and hot-wire sensor used in outflow measurements.

The 4-axis version of the POT setup is shown in Figure 3.10, consisting of three linear stage axes (x, y, z) with 110 mm range of motion, and one rotational stage (θ) with 90° range[4]. The hot-wire was articulated around the injector surface, maintaining a perpendicular orientation at a distance of approximately 1 mm. This was the minimum distance that ensured probe safety during articulation in three dimensions whilst also preserving near-wall spatial resolution of the jetting. Jet development at other wall-normal distances was not examined here but could be investigated in future work.

The stages were driven by off-the-shelf components, listed in Table 3.4. Assembly and calibration were carried out by Micromech Ltd. to provide positional resolution of 1.25 μm and 9 $\cdot 10^{-4}$ degrees. A custom LabVIEW script controlled both the traversal and data acquisition, and avoided collision of the hot-wire sensor with the model through staged movements. A buffer time of 2 seconds in between measurement points was included to ensure sensor movement did not influence the measured outflow velocity. The hot-wire 3D position was calibrated relative to the model using a precisely positioned dowel hole near the injector as a reference point.

[4]Another rotational axis was implemented, but not required for leading edge measurements. It has been deployed for 5-axis measurements on transpiration cooled cones [67].

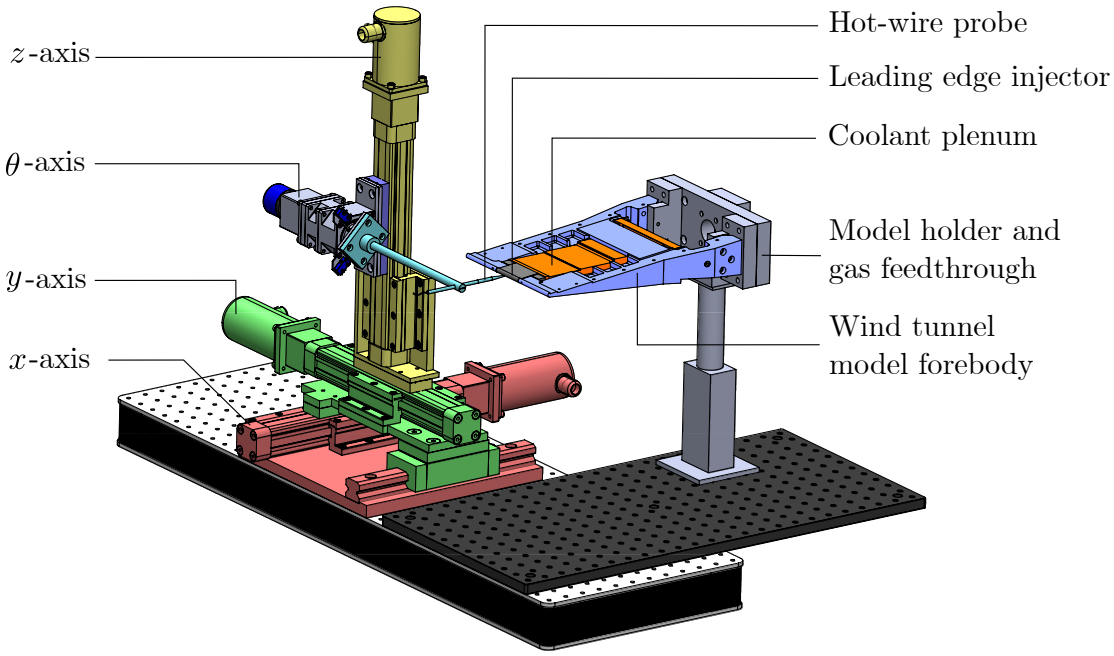


Figure 3.10: Annotated sketch of the POT rig for outflow velocity measurements.

Mass flow rate through the plenum and into the injector was kept at a constant value of 0.15 g/s throughout the duration of the test using a digital mass flow controller (Omega FMA-2609-A) connected to a 100 psi dry air supply line. The model plenum was instrumented to measure gas pressure and temperature (GEMS 3100 series pressure transducer and RS Pro K-type thermocouple). The output voltages of the StreamLine Pro signal conditioner and plenum pressure sensor were captured by an NI-9223 ADC card, while the thermocouple was connected to an NI-9211 card. Both cards were recorded by a NI cDAQ-9174. The results of the outflow characterisation are presented in Section 3.7.

Table 3.4: List of components of the Porous Outflow Traverse.

Component	Model	Range
Linear stage driver	Parker XL50	
Linear stage motor	Stogra SM56.2 stepper motor	0 - 110 mm
Rotational stage driver	Leadshine M752	
Rotational stage motor	Soyo NEMW SY42STH47 stepper motor	0 - 90°
Motor Controller	Micromech MC508 8-channel	
Gas inlet supply	Laboratory 100 psi dry air line	0 - 100 psi
Mass flow controller	Omega FMA-2609A	0 - 50 SLM
Hot-wire probe	Dantec 55P11 Miniature straight wire	0.2 - 200 m/s
Hot-wire signal conditioner	Dantec StreamLine Pro CTA	
Hot-wire calibrator	Dantec StreamLine Pro Automatic Calibrator	0.02 - 300 m/s
Plenum pressure sensor	Gems 3100R0025 pressure sensor	0-25 barG
Plenum temperature sensor	RS Pro K-type thermocouple	213 - 623 K
ADC cards	NI-9223, NI-9211	1MS/s/ch, 14S/s
DAQ	NI cDAQ-9174	

3.6.2 Wind Tunnel Experiment

To translate the outflow maps to the performance in a hypersonic crossflow, the characterised leading edges were tested in the University of Oxford's High Density Tunnel (HDT) at the flow conditions described earlier in Table 3.1. Further information on the operation and facility instrumentation are given in [128, 129]. Due to structural failure of the Metapor leading edge at higher internal pressures, both leading edges were tested at a mass flow rate of 0.065 g/s of nitrogen coolant. This corresponded to a $B_h \approx 0.54$, less than the design condition.

An annotated photograph of the wind tunnel model is shown in Figure 3.11. It includes PEEK plates for IR thermography measurements. A MWIR Telops FAST M3k infra-red camera was used with a 13 mm wide-angle lens to capture heat transfer data at a resolution of 1.085 pix/mm. Sketched in Figure 3.12, the camera was positioned outside the test section with optical access provided through a ∅100 mm sapphire window. IR image frames were acquired at 1200 Hz with a 150 μs exposure time.

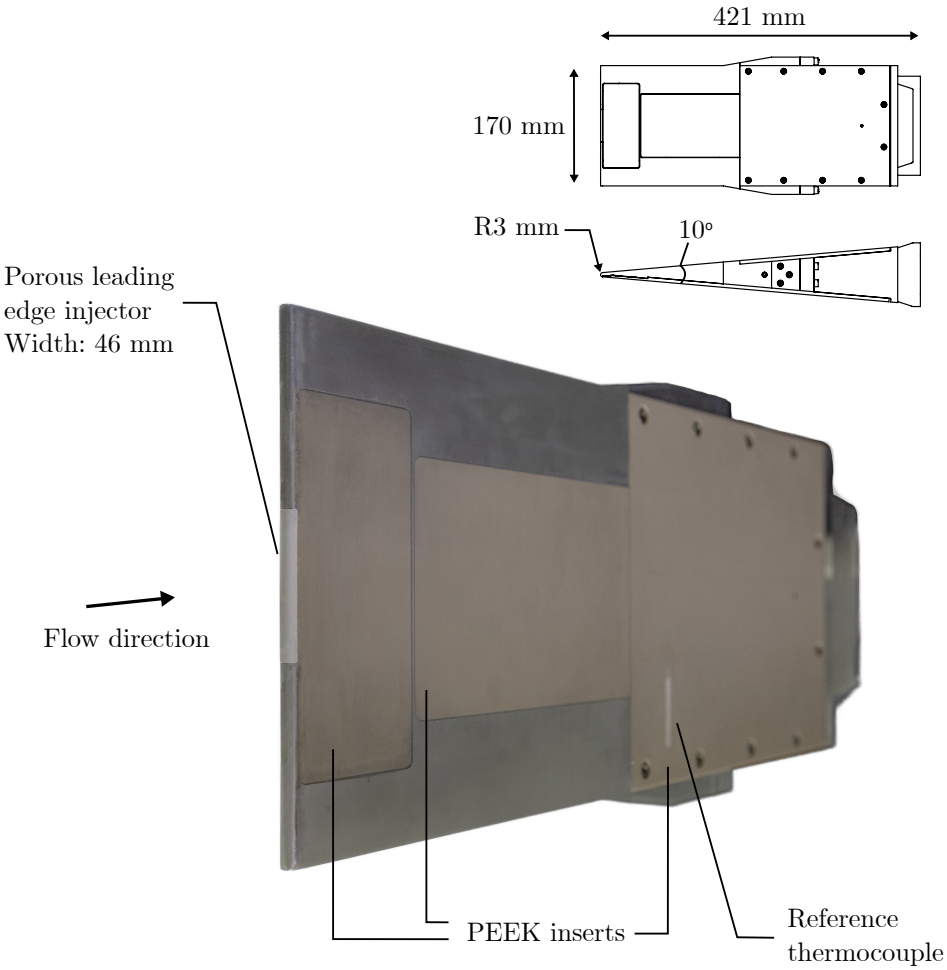


Figure 3.11: Annotated photograph of the transpiration-cooled wedge model.

In-situ calibration was carried out using a portable black body calibrator (CI-Systems SR-33-7), to correct sensor non-uniformities and relate raw pixel counts to black body temperatures, as described in [66]. After applying a PEEK material emissivity correction, transient surface temperature maps could be obtained from the raw infra-red signal. Using the calibrated surface temperature rise, ΔT, the transient surface heat flux was reconstructed using Oldfield's impulse response method [138]. Both the calibration and impulse response deconvolution were carried out on a pixel-wise basis, providing 2D surface heat flux maps right up to the injector surface. Further details on IR thermography calibration and data processing on PEEK surfaces in the HDT may be found in [66, 139].

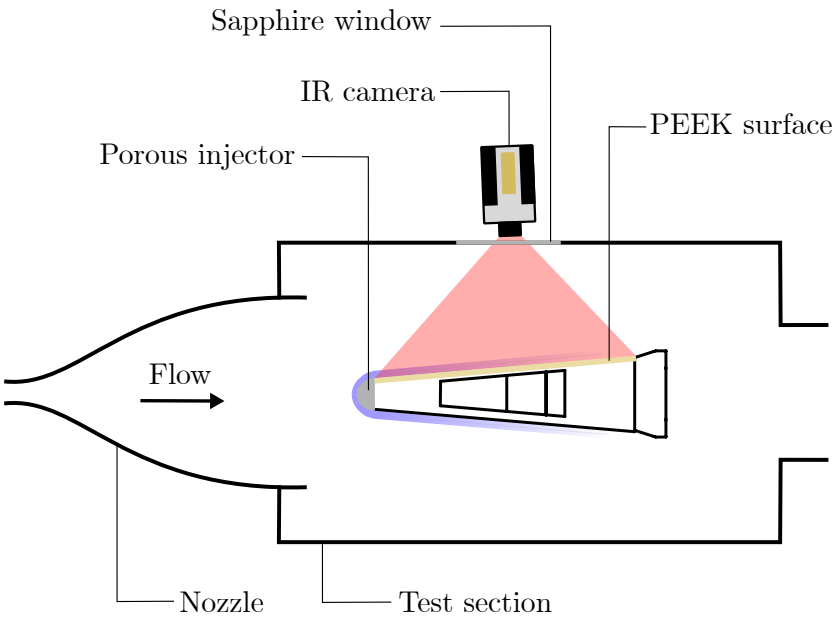


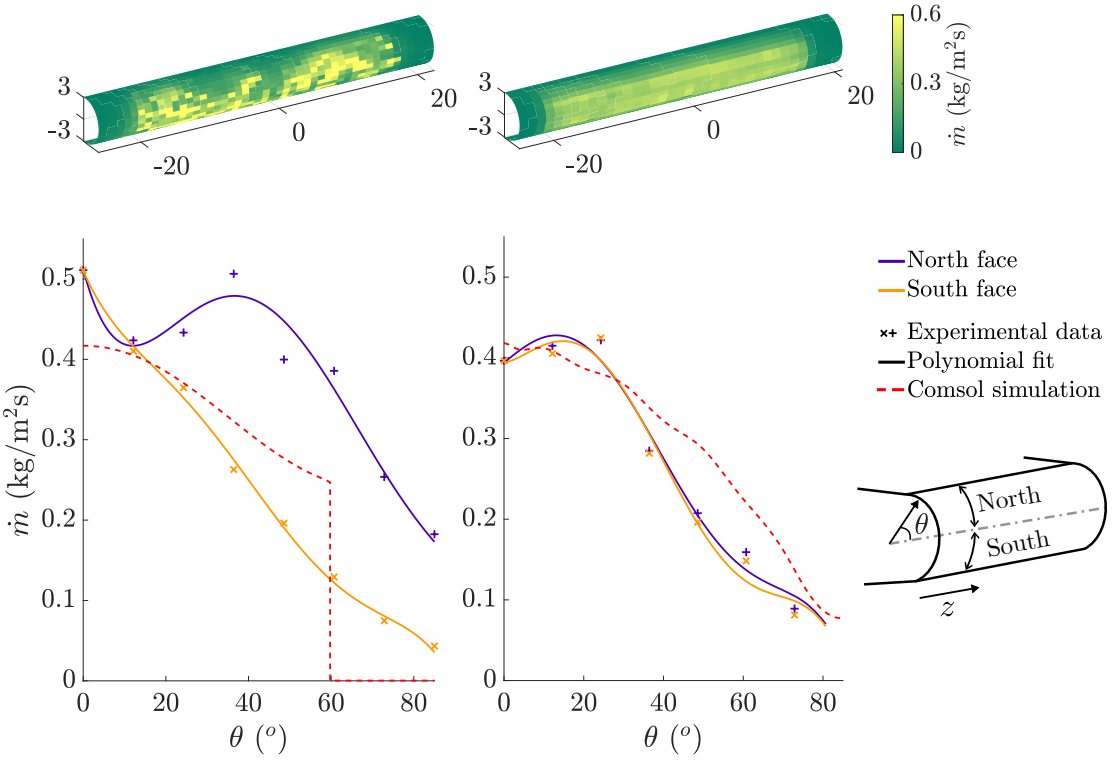
Figure 3.12: Top view sketch of the optical setup for HDT experiments. Sketch not to scale.

3.7 Performance Comparison

3.7.1 Outflow Results

Mass flux and B_h distributions cannot be measured directly along the injector surface during wind tunnel tests, though can be inferred from the measured mass flow rate and plenum pressure. Estimating the mass flux distribution during wind tunnel tests involves simulating the porous flow using experimental data of the pressure boundary conditions, using the same COMSOL modelling as before.

To validate the COMSOL modelling approach, outflow measurements were conducted at atmospheric conditions and compared against the model results. Experimental mass flux was calculated by multiplying atmospheric density by the measured velocity distribution, assuming isothermal porous flow. The results of the test are shown in Figure 3.13.



(b) Metapor (a) LithaLox

Figure 3.13: Whole surface and spanwise-averaged mass flux distributions of the Metapor and LithaLox leading edges, tested at a mass flow rate of 0.15 g/s.

In the figure, measured spanwise-average distributions of each half of the injector are presented against the simulation of the designed injector under the same atmospheric conditions. A fifth-order polynomial is fitted to the experimental data points. The low velocity regions on both sides ($z = \pm 19$) are impermeable side walls. Direct conversion from benchtop mass flux to an equivalent B_h distribution is not possible since the pressure boundary conditions and resulting 2D porous flow differ from wind tunnel testing conditions.

The LithaLox injector demonstrates high symmetry, with spanwise-averaged mass flux distributions differing by less than 10% between its north and south injection faces. In contrast, the Metapor injector shows a difference of up to 150% between faces. The LithaLox injector exhibits a slight undershoot at the stagnation point and an overshoot just downstream. Two possbile manufacturing artefacts may have contributed to this effect. The first is incomplete slurry removal process from the stagnation line. This was also observed on coupon specimens during material development. The second is a print layer overlap between the north and south faces producing a locally thicker wall. The latter effect may be qualified by surface profilometry of the leading edge.

Table 3.5 provides other statistical metrics along the stagnation line ($\theta = 0$, denoted SP) and the maximum values on each of the north and south faces. σ is the mean profile-normalised standard deviation, indicating local uniformity and Δ is the percentage deviation from the numerical design, reflecting manufacturing accuracy.

Overall, the LithaLox injector achieves a consistent outflow distribution that aligns reasonably well with numerical predictions: the stagnation point mass flux is to within 5.8% of the design. On the other hand, the Metapor's performance is uneven, with poor uniformity. Also, the accuracy of the south face is comparable to the LithaLox, however the north face deviates significantly more.

Table 3.5: Experimentally measured injector uniformity (measured by spanwise standard deviation, σ) and deviations relative to the numerical method (measured by percentage difference Δ).

Injector	σ_{SP} (%)	σ_{max} (%)		Δ_{SP} (%)	Δ_{max} (%)	
		N	S		N	S
LithaLox	4.7	6.1	10.6	5.8	37.9	44.2
Metapor	56.4	67.2	69.1	21.9	64.7	44.8

3.7.2 Range of Blowing Conditions

Additional leading edges were manufactured and pressure tested to find their operating limits from the maximum plenum pressure. Both leading edge materials failed in repeatable manners at consistent pressures, indicating the consistency of the manufacturing processes. At the point of mechanical failure, the LithaLox leading edge could withstand a higher pressure differential ($P_{\text{internal}} - P_{\text{external}}$) of 2.6 bar compared to 1.2 bar for Metapor, despite the LithaLox's thinner wall.

In an evacuated test section (ambient pressure of 180 Pa), the LithaLox injector could achieve a maximum mass flow rate of 0.290 g/s of nitrogen, corresponding to $B_{h,SP} \approx 3.0$. In contrast, the Metapor leading edge failed at a maximum nitrogen flow rate of 0.085 g/s, giving $B_{h,SP} \approx 0.9$. The Metapor could therefore only deliver around 29% of the mass flux than the LithaLox, despite the Metapor's higher material permeability.

3.7.3 Wind Tunnel Results

To understand how the leading edge mass flux distributions affected the film cooling performance of the injector, heat flux measurements were captured downstream of the south face of each injector. The parameter of interest was the thermal efficiency, η_{th}, defined in Equation 3.6 in terms of cooled versus uncooled heat flux ratio, $\dot{q}/\dot{q}_0$.

$$\eta_{th} = 1 - \frac{\dot{q}}{\dot{q}_0} \tag{3.6}$$

Figure 3.14 shows the experimental contour map of η_{th} downstream of the

injectors, captured by IR thermography. The plot also shows the corresponding spanwise-averaged distributions of $\overline{\eta_{th}}$ (bottom side), and profiles of η_{th} along the span at different streamwise locations (right side). The spanwise uniformity of the cooling distribution is quantified by σ_η. In the figure, this is provided as an absolute value due to downstream measurement noise. In the analysis below, σ_η is discussed as a mean mean-normalised value, using percentages.

For the Metapor injector, local coolant jetting at $z = 5$ mm can be seen. As the film propagates downstream, the jet spreads laterally, providing a more uniform spanwise cooling distribution. The Metapor injector delivered 56% spanwise variation in outflow mass flux leading to 38% standard deviation in film cooling just after the injector. In contrast, the LithaLox injector delivered only 5% variation in mass flux, with corresponding film cooling standard deviation of 9%. For the Metapor, the effect of the coolant jetting on σ_η is apparent immediately downstream of the Metapor injector, but recovers to within a similar range of the LithaLox injector after around $s/R_{LE} = 33$. Both spanwise variations are relatively large downstream due to the low signal-to-noise ratio as the coolant dissipates.

For the streamwise distributions, both injectors show similar initial thermal efficiency, however the cooling rate of decay is much higher for the Metapor than that of the LithaLox. Despite the same mass flow rate setting, the film decay rate appears to be influenced by the injector uniformity. The validity of the mass injection boundary condition for experiments should therefore be carefully considered when interpreting the experimental data.

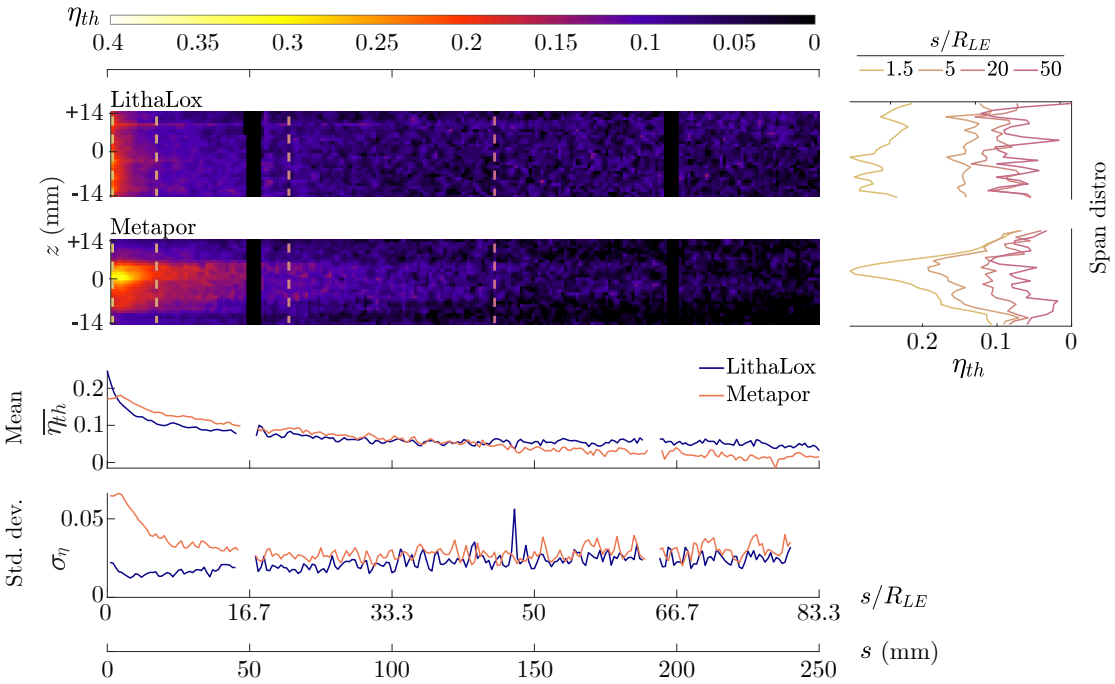


Figure 3.14: Heat transfer results from HDT testing of two porous leading edge injectors. **Top**: contour plots of η_{th} for the two injectors. **Right**: spanwise distributions of η_{th}. **Bottom**: spanwise-mean ($\overline{\eta_{th}}$) and normalised standard deviation (σ_η) along the model. The gaps in the contours and streamwise distributions are spaces between the PEEK inserts, required for model assembly.

3.8 Conclusion

This study demonstrated an integrated approach to the design, manufacture, and testing of a transpiration-cooled leading edge. The novel implementation of additive manufacturing of porous ceramic (LithaLox) leading edges was investigated. A direct comparison was made to a CNC-machined counterpart made from a commercially available porous material (Metapor) used in recent studies. Due to the highly two-dimensional porous flow in the small radius injector, the internal wall was contoured to match a B_h-based mass flux distribution target. During the numerical design phase, the design flexibility afforded by additive manufacturing enabled a closer match to the target distribution than the CNC-machined geometry. Benchtop hot-wire tests revealed that the Metapor injector exhibited non-uniform outflow, leading to localised coolant jetting. In a hypersonic cross-flow, this led to substantial spanwise variation in thermal film effectiveness. In contrast, the LithaLox injector delivered a more uniform mass flux and a correspondingly more uniform film. Despite testing at the same total coolant mass flux, the film cooling decay rate differed between the two injectors, demonstrating that film cooling performance is sensitive to both the integrated mass flux but also to its spatial distribution. Experiments that intend to fully interrogate the flow physics and validate numerical models must therefore match the design mass flux boundary condition. In this case, the more uniform LithaLox injector provides a closer approximation to the intended boundary condition.

Overall, the results demonstrate that additive manufacturing is a viable method to manufacture injectors with a reasonably well-tailored mass flux with good uniformity, as well as the required strength to achieve high blowing conditions. Further work is required to diagnose and refine the manufacturing process to correct the reduced mass flux along the stagnation line.

CHAPTER 4

Experiments on a Transpiration-Cooled Leading Edge in Hypersonic Flow

4.1 Introduction 77

4.2 Experimental Setup 82

4.3 Post-Processing 95

4.4 Numerical Modelling 98

4.5 Results 100

4.6 Conclusion 112

Preface

Following the development and characterisation of a leading edge injector, this chapter presents an experimental investigation into the effects of transpiration cooling on heat transfer, coolant concentration, and aerodynamics over a sharp leading edge in a hypersonic cross-flow. Infra-red thermography and pressure-sensitive paint were employed for non-intrusive optical diagnostics. Confidence in the mass flux boundary condition enabled direct comparison with numerical simulations. The validated numerical method is carried forward in the next chapter.

Parts of this chapter was presented at the High-Speed Vehicle Science and Technology (HiSST) conference [127].

Author Contributions

- Raghul Ravichandran: Conceptualisation, experimental design, investigation, analysis, and writing.
- Anthony Finnerty: Assistance with experimental design and investigation.
- Luke Doherty: Supervision as secondary supervisor.
- Matthew McGilvray: Supervision as principal investigator and funding acquisition.
- Lithoz GmbH: Resources and manufacturing of the porous leading edge.

Acknowledgements

The authors would like to acknowledge Terry Benfield (TPB Precision Engineering) for his time and expertise on machining the model; and Harry Kachika for in-house machining. Thank you to Andreea Dabija and Gabriel Tansley for instrumenting the model. Thanks also to Chris Hambidge and Tristan Crumpton for operating the HDT and for their infrastructural support. This work was funded by DSTL.

4.1 Introduction

Sharp leading edges on hypersonic vehicles are becoming increasingly desirable for sustained hypersonic flight [2, 8] and re-entry missions [9], due to their improvement in lift-to-drag ratio [12]. Studies considering leading edges of radius $R_{LE} = 0.1 - 30$ mm for flight vehicle geometries have been carried out numerically [12, 13], as well as on flight test vehicles [8, 10]. Sharper leading edges are associated with increased heat flux and higher localised temperatures, requiring appropriate thermal protection system (TPS) selection. A passive TPS may not provide sufficient protection at very high heat flux conditions [53]; and an ablative TPS may be precluded for sharp leading edges if shape stability or reusability is required. While active cooling systems involve mass and complexity penalties, they offer an effective approach for high heat fluxes and can be strategically implemented, such as at a vehicle leading edge. Transpiration cooling is a promising active TPS candidate whereby coolant gas is injected into the hypersonic boundary layer via a porous injector on the vehicle surface, as sketched in Figure 4.1.

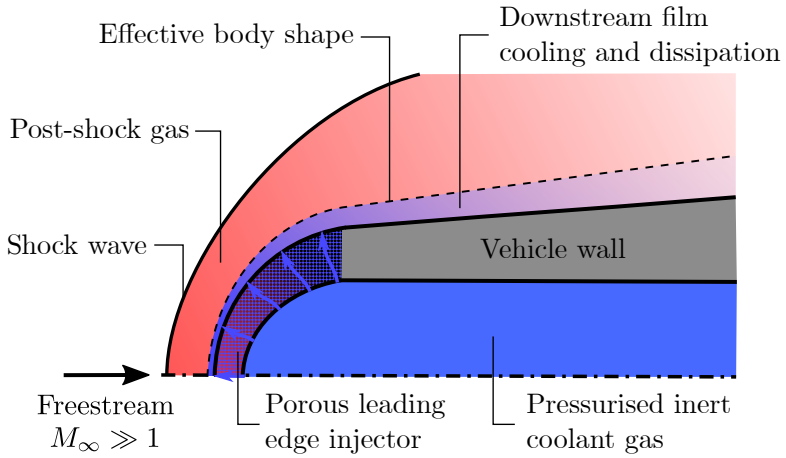


Figure 4.1: Annotated sketch of a transpiration-cooled leading edge.

Transpiration cooling actively mitigates the effects of high external heat fluxes by means of three mechanisms:

1. Convective heat transfer from the solid to the coolant gas flowing through the porous material [30].

2. Film cooling, where the coolant gas and boundary layer thickening lowers the heat flux by reducing thermal gradients at the wall [31].

3. Mitigation of catalytic wall heating and protection from material oxidation, potentially enabling higher temperature operation through re-radiative heat rejection [32].

In the 1960s, numerical and theoretical studies [29, 88–90] were carried out to investigate the effect of mass injection on the stagnation point heat flux reduction in the context of outgassing ablative materials. A common correlation parameter in these studies is the blowing parameter, B_h, a non-dimensional mass flux parameter. The blowing parameter is defined as the ratio of blowing ratio, F, to uncooled Stanton number, St_0, as shown in Equation 4.1. Here, ρu is mass flux, $\dot{q}$ is heat flux, and h_{aw} is adiabatic wall enthalpy. Subscripts 0, inj, and ∞ correspond to uncooled, injected coolant, and freestream quantities respectively. Since B_h accounts for local heat flux, it provides a rational basis for distributing coolant around the leading edge surface according to thermal loading.

$$B_h = \frac{F}{St_0} \tag{4.1}$$

$$F = \frac{\dot{m}_{inj}}{\rho_\infty u_\infty} = \frac{\rho_{inj} u_{inj}}{\rho_\infty u_\infty} \tag{4.2}$$

$$St_0 = \frac{\dot{q}_0}{\rho_\infty u_\infty (h_{aw} - h_w)} \tag{4.3}$$

In the 1970s, these stagnation point correlations were experimentally verified on large radius porous hemispheres instrumented with heat flux and pressure sensors embedded within the porous material [81, 92]. The effect of the sensors on the porous flow was not quantified. In experiments involving air injection into an air freestream, Kaattari [92] observed that heat flux reduction over the large-radius injector followed Swann & Pittman's stagnation point correlation [88] when the terms were redefined using local rather than stagnation point properties.

Yoshikawa's correlation [29] is shown in Equation 4.4, correlating B_h to the

stagnation point heat flux ratio, $\dot{q}_{SP}/\dot{q}_{0,SP}$ where subscript 0 is the uncooled quantity. It accounts for the effect of dissimilarity between coolant and freestream gases by considering their molecular weight (W_f, W_∞). $N_f = 1$ or $5/9$ for diatomic or monatomic coolant gases respectively. The shape factor, k_b, equals unity for axisymmetric stagnation points. The parameter Δ/Δ_0 represents the change in shock layer thickness due to blowing. More recently, experimental [70] and numerical [93] studies investigated Yoshikawa's [29] correlation for its applicability to transpiration cooling at a stagnation point, with good agreement.

$$\Psi = \frac{\dot{q}_{SP}}{\dot{q}_{0,SP}} = \sqrt{\pi\Lambda}\frac{\exp\{-\Lambda B_h^2\}}{1+\mathrm{erf}\{\Lambda\}^{0.5}B_h} \tag{4.4}$$

$$\Lambda = \begin{cases} \frac{1}{\pi}\frac{\Delta}{\Delta_0}\lambda^{B_h/B^*} & (B_h \leq B^*) \\ \frac{1}{\pi}\frac{\Delta}{\Delta_0}\lambda & (B_h > B^*) \end{cases} \tag{4.4a}$$

$$B^* = 1.82\frac{\sqrt{\pi\epsilon(W_f/W_\infty)}}{k_b(\chi_w')^*} \tag{4.4b}$$

$$(\chi_w')^* = \frac{1.187\sqrt{(8\epsilon(1-\epsilon)}}{(1+\sqrt{8/3\epsilon})-\epsilon)(1+0.225\sqrt{\epsilon})} \tag{4.4c}$$

$$\lambda = \sqrt{\frac{W_\infty}{W_f}}N_f \tag{4.4d}$$

$$\frac{\Delta}{\Delta_0} = 1 + k_b\sqrt{\frac{1}{\epsilon}\frac{W_\infty}{W_f}}F \tag{4.4e}$$

$$\epsilon = \frac{\rho_\infty}{\rho_1} \tag{4.4f}$$

The correlation also defined a *boundary layer blow-off* parameter, B^*, where the increase in shock-layer thickness due to blowing is equal to the thickness of the original uncooled boundary layer. At this point, the coolant dominates the wall flow, altering the cooling behavior. Implications of boundary layer blow-off on the broader flowfield have not been fully characterised for transpiration cooling. Pappas & Lee [81] showed that excessive blowing on a conical nosetip can substantially increase the surface pressure, and therefore drag. In their case, surface pressure over the nosetip remained relatively constant for all gases and

blowing parameters, but helium injection at $B_h \approx 2.25B^*$ caused the downstream pressure to nearly double compared to the uncooled case. The experiment used a 25 mm cone with uniform mass flux that extended downstream of the nosetip. This work investigates the use of tailored mass flux at a sharp leading edge only.

More recent experimental studies on leading edges have focused on manufacturing of sharper geometries and were tested in subsonic heated flow facilities or arc-jets [44, 77, 80, 104]. However, many of the results are not reduced to transferable forms, lacking generalised correlations or dimensionless parameters linking heat flux to mass flux that enable application to other scenarios.

The design of transpiration-cooled leading edges to achieve a target mass flux distribution has been limited to numerical studies, either through multiple plenums [87], or variable permeability [34]. While previous experimental studies have directed higher mass fluxes toward the stagnation point, they have not explicitly designed target distributions or correlated local mass flux with heat flux measurements.

Experimental studies have successfully measured the coolant outflow from injectors using benchtop rigs. Porous sintered flat plate injectors [33], and porous carbon-carbon (C/C) conical nosetips [35, 36] have been previously characterised using hot-wire anemometry and pitot probes. These studies demonstrated that the anisotropic layup of C/C composites leads to highly directional mass fluxes that correspond to the fibre layup. In [35], the highly non-uniform outgassing from a conical nosetip injector was shown to lead to irregular cooling in the IR thermography measurements during arc-jet testing in [77]. In [33], the sintered microstructure provided reasonably uniform outgassing, however it was further shown that even small non-uniformities can affect film cooling experiments [70].

Studies have also employed non-intrusive measurement techniques to measure heat fluxes directly on injectors, either by mounting transducers on the backside of injectors [44, 118], or by employing infrared (IR) thermography [70, 77, 78].

Material selection is a critical component of experimental design when using IR thermography, as the materials must have good emissivity in the infrared spectrum,

and suitable thermal properties for the heat flux processing techniques. Often, porous ceramics [31, 66] or ceramic composites [77, 78] are used.

In [43], pressure-sensitive paint (PSP) is used to measure the surface concentration of coolant downstream of an injector. PSP intensity is directly affected by partial pressure of oxygen, which in turn is proportional to oxygen concentration. Coolant concentration may therefore be calculated by measuring the relative absence of oxygen at the surface in an air freestream, if the surface pressure remains consistent between the cooled and uncooled tests.

This study aims to carry out wind tunnel tests to experimentally quantify the heat flux, coolant concentration, and surface pressure effects of foreign gas injection on a leading edge injector in a hypersonic cross-flow. A porous leading edge injector with internal contouring was manufactured to produce a spanwise-uniform, well-defined mass flux under external pressure boundary conditions. Heat transfer and coolant concentration measurements were taken downstream and on the injector, and were compared against laminar CFD for numerical method validation. The heat flux along the injector surface was also compared to Yoshikawa's [29] correlation, to investigate if it could be extended to further geometries. Lastly, at high injection blowing conditions, pressure measurements were taken to examine the aerodynamic penalties of transpiration cooling and identify where significant drag penalties could occur.

4.2 Experimental Setup

4.2.1 Wind Tunnel Model and Instrumentation

Wind tunnel experiments were conducted using a 5° half-angle blunted wedge with 3 mm leading edge radius, and an injector width of 38 mm, shown schematically in Figure 4.2. Experiments were carried out at 0° angle of attack and yaw. Model alignment with the freestream was achieved using four pressure sensors (Honeywell HSC-DANN-015PA) located on each of the four windward wedge faces. The model assembly is described below.

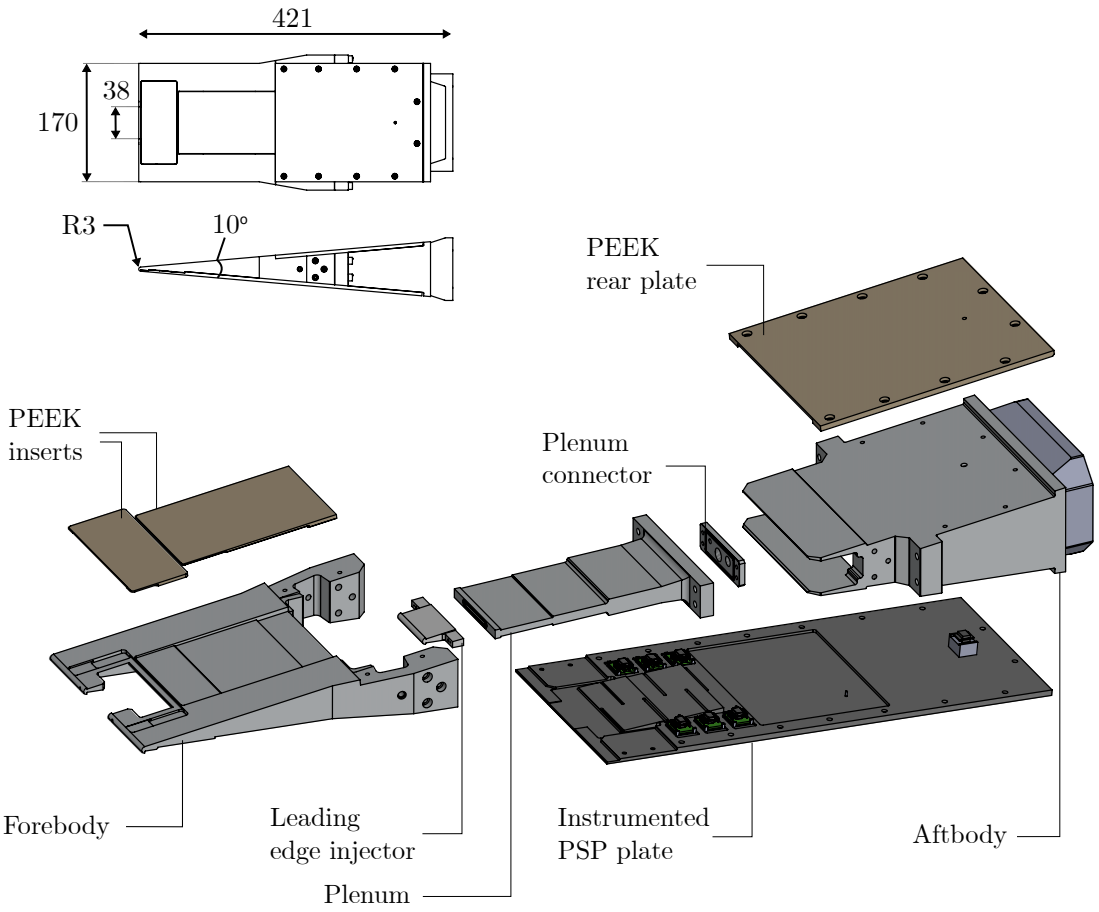


Figure 4.2: Annotated exploded view of the experimental model with outer dimensions in mm.

The leading edge injector and plenum were housed in a central cutout in the forebody. Photographs of the external surfaces are shown in Figure 4.3, and a cross-sectional view of the model and coolant delivery is shown in Figure 4.4. The coolant gas was fed into the model from a mass flow controller (Omega FMA-2609-A) situated outside of the wind tunnel test section. The plenum was instrumented with an RS Pro K-type thermocouple and XT-190SM-35BARA Kulite for transient coolant temperature and pressure measurements. In the forebody, space constraints due to the coolant plenum and small leading edge radius ruled out the use of discrete sensors. Consequently for surface measurements, non-intrusive optical methods were adopted: IR thermography for heat transfer and PSP for coolant concentration and pressure measurements. Specialised optical insert plates were mounted each side of the wedge to obtain simultaneous measurements during an experiment.

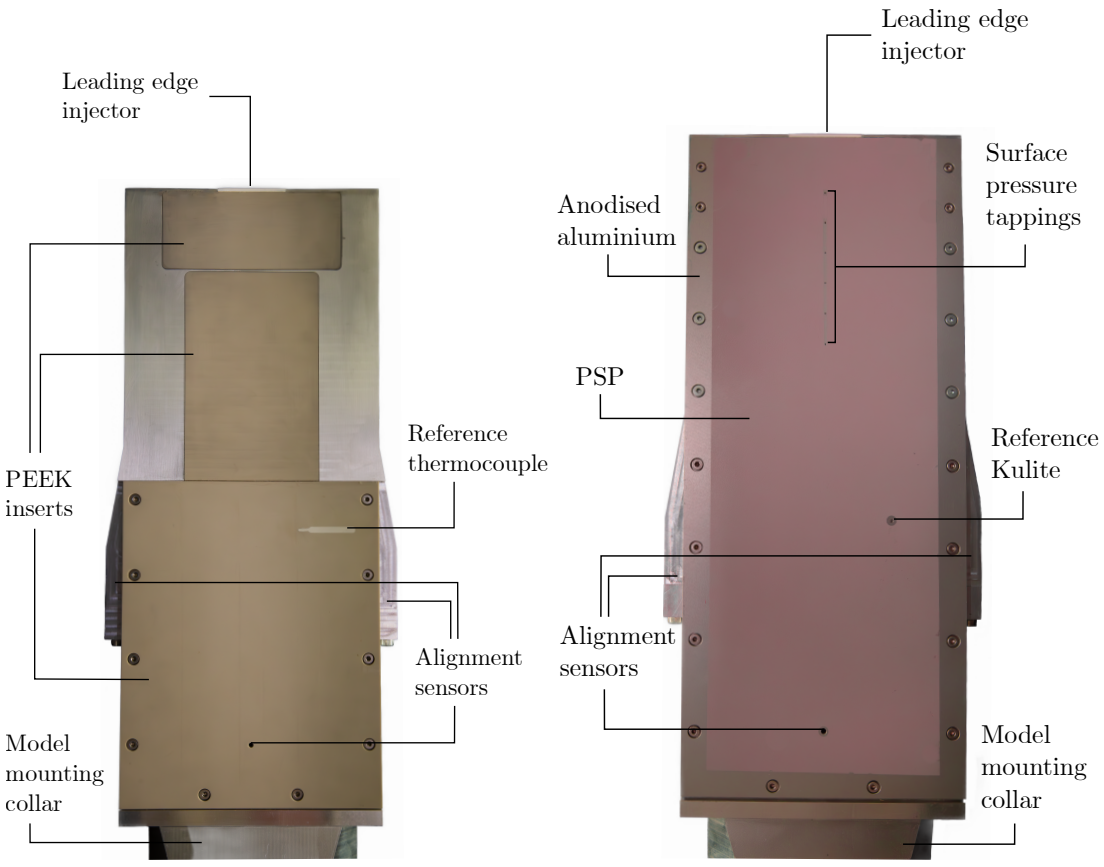
The forebody, plenum, connection plate and aftbody were machined from Al 7075. The PEEK inserts and plate for IR thermography were made from Victrex PEEK 450G. The thermal properties of the PEEK grade have previously been characterised [66, 140]. The inserts were glued into the model forebody using 3M DP8005 structural plastic adhesive[1], and machined as a glued assembly to ensure a smooth, continuous surface finish. The downstream PEEK plate was bolted in place, with a fast response surface-mount thermocouple (Omega CO2-K) was installed as a reference temperature sensor. An annotated photograph of the heat transfer measurement surface is shown in Figure 4.3a. Further discussion on the optical measurement methodologies is provided in Section 4.2.5.

The PSP measurement plate was machined from anodised, rolled Al 5053, selected for its ability to remain flat during machining. The anodisation creates a porous aluminium oxide surface layer that promotes binding of PSP luminophores without the need for a basecoat, improving response time for transient measurements [126]. ISSI TurboFIB PSP (quoted response time < 1 ms) was sprayed onto the anodised plate in accordance to the painting guidelines [141]. A downstream

[1]The adhesive, recommended after correspondence with the manufacturer, is specialised for low surface energy plastics such as PEEK. Adhesive around and underneath the inserts filled gaps that would otherwise allow the external flow to enter the gaps and lift up the plate away from the model.

flush-mounted Kulite (XCS-062-10A) was mounted in the plate as a reference sensor for the PSP data during calibration and pressure measurements. An annotated photograph of the PSP surface is shown in Figure 4.3b.

To directly measure pressure augmentation downstream of the injector, six Honeywell sensors (HSC-MRNN-015PA) were mounted to the underside of the aluminium plate. Due to the space limitation toward the leading edge, thin-walled pressure tubing was installed flush to the plate surface, and routed to the sensors housed further downstream. An annotated photograph of the surface pressure measurement sensors is shown in Appendix A.2. An annotated cross-sectional diagram of the model assembly and coolant delivery system and are shown in Figure 4.4, channels in the plate for the pressure tappings are also shown in the section view.



(a) IR thermography surface (b) PSP surface

Figure 4.3: Annotated photographs of the surfaces used for IR thermography and PSP measurements.

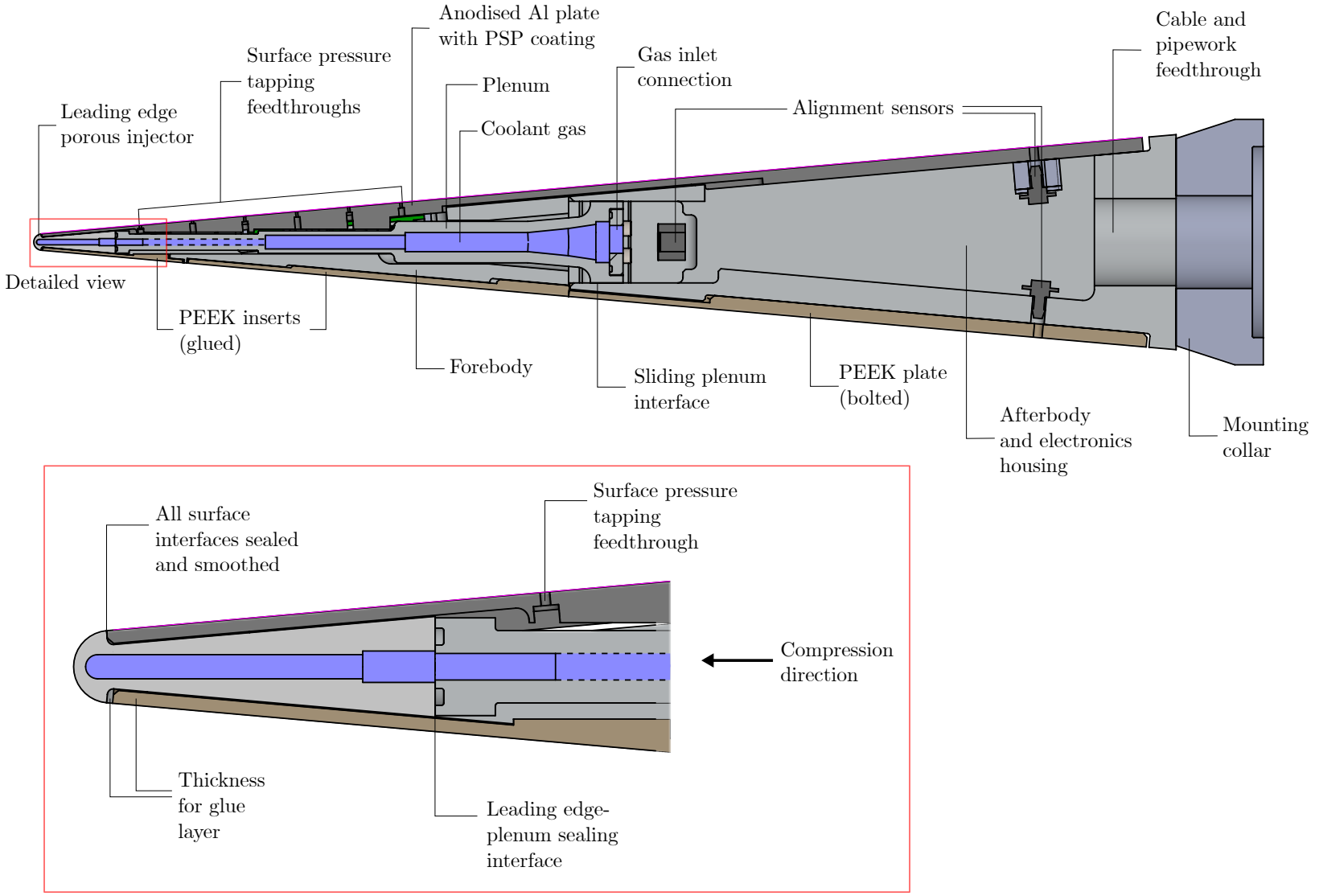


Figure 4.4: Cross-sectional view of the transpiration-cooled model. The coolant flow is highlighted in blue. The plenum was sealed to the leading edge by sliding along the model forebody, with four bolts pulling it toward the fixed leading edge. This compressive interface was suitable for O-ring sealing.

4.2.2 Leading Edge Injector

A highly non-uniform surface heat flux distribution necessitates a corresponding spatially distributed mass flux. The leading edge was designed to have a constant B_h distribution, aligning coolant mass flux with local heat flux.

The leading edge was manufactured by Lithoz GmbH from LithaLox 1347, a photocurable alumina slurry suitable for 3D printing developed by Lithoz. Alumina was selected as due to its compatibility with transient IR thermography measurements. LithaLox 1347 is impermeable after sintering. For the injection region, open porosity was introduced through a modified slurry, LithaLox 1347-P30. The modified slurry contained PMMA microbeads of diameter approximately between 4 and 11 μm, which thermally decomposed during the high temperature debinding process, leaving voids in their place. Porosity was also promoted through lower temperature sintering at 1600 °C. The porosity and permeability coefficients are given in Table 4.1. The leading edge was manufactured using a CeraFab S65 printer, a lithography-based system permitting permeable and impermeable regions to be printed consecutively. Geometric scaling factors of 1.24 in the print direction and 1.20 in the orthogonal axes were applied to account for shrinkage during sintering.

Table 4.1: LithaLox 1347-P30 porosity and permeability coefficients.

Porosity	ϕ	0.3
Approx. Darcy coefficient (m^2)	k_D	$2.26 \cdot 10^{-14}$
Approx. Forchheimer coefficient (m)	k_F	$1.72 \cdot 10^{-8}$

The coolant flow within the porous material was modelled in comsol, using known freestream condition data and material permeability. The internal wall shape was optimised to yield a target mass flux condition corresponding to $B_h = 1.2$ using N_2 coolant at freestream condition A (see Table 4.2). Overall, it was estimated that the distribution provided a constant B_h distribution over the injection area to within 10%. For subtended angles of $> 81°$, the highly two-dimensional porous flow led to an overshoot past the target mass flux. These

regions were therefore manufactured from impermeable alumina instead, as shown in Figure 4.5. An impermeable structural support lattice was also added behind the relatively thin porous surface, also shown in the figure. The lattice walls were very thin: between 0.11 and 0.24 mm and designed to avoid blocking the stagnation line outflow: modelling and outflow measurements with and without the lattice showed that it did not affect the outflow. The lattice ends were attached to the impermeable side-walls of the injector.

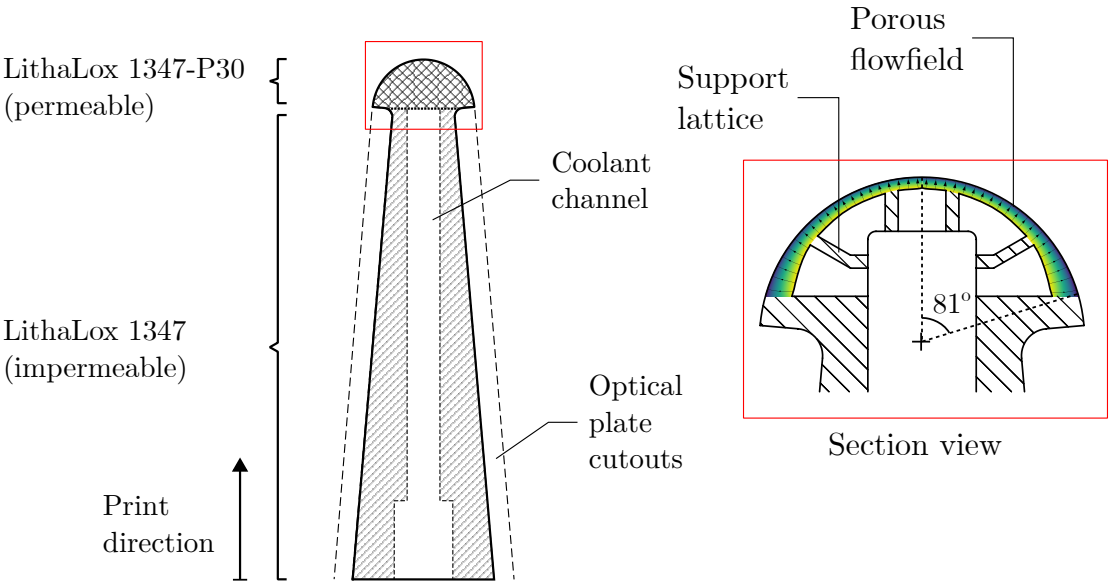


Figure 4.5: Internal structure of the 3D-printed transpiration-cooled leading edge used in wind tunnel testing. The simulated pressure field and velocity streamlines are overlaid in the section view.

Following manufacturing, a constant temperature anemometer (CTA) with hot-wire probe was used to measure the surface mass flux distribution of gas under atmospheric conditions. The measured mass flux was compared against the COMSOL simulation of the designed geometry at the same conditions, to verify accuracy of the manufactured component in matching the numerical design. The results are shown in Figure 4.6. The measurements show that the stagnation line mass flux is within 5.8% of the simulated mass flux. They also show uniformity of the mass flux: along the injection region the spanwise standard deviation of mass flux is less than 3% and the north and south face mean distributions are within 10% of each other.

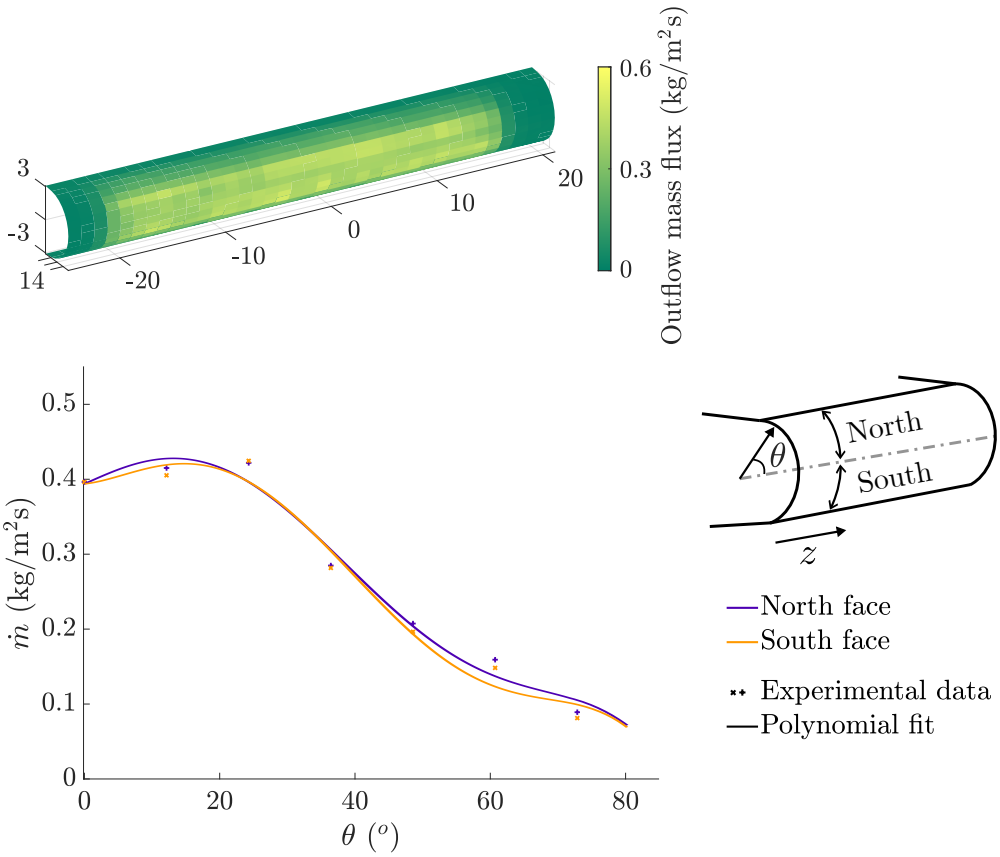


Figure 4.6: Results of the mass flux benchtop characterisation using hot-wire anemometry.

4.2.3 Local Blowing Parameter Calculation

In the present study, the test conditions are defined by the freestream condition (defined as conditions A & B in Section 4.2.4), the coolant gas, and the blowing parameter. While the mass flow rate was set by the mass flow controller, mass flux and B_h distributions cannot be measured directly during a test. Instead, B_h was estimated using Equation 4.5, in which B_h and the other variables have been redefined to use local values along the injector surface.

$$B_h(\theta) = \frac{F(\theta)}{St_0(\theta)} = \frac{\dot{m}_{\text{inj}}(h_{aw} - h_w)}{\dot{q}_0} \tag{4.5}$$

For each test, the mass flux distribution was estimated using the validated comsol porous-flow model with experimentally informed pressure boundary conditions: a Newtonian surface-pressure distribution derived from the characterised

freestream, and the measured internal plenum pressure. The heat flux and enthalpies were estimated numerically using Eilmer (Section 4.2.4). The estimated B_h distributions are shown in Figure 4.7, and the blowing condition for each test is defined as the mean B_h: $\overline{B_h}$.

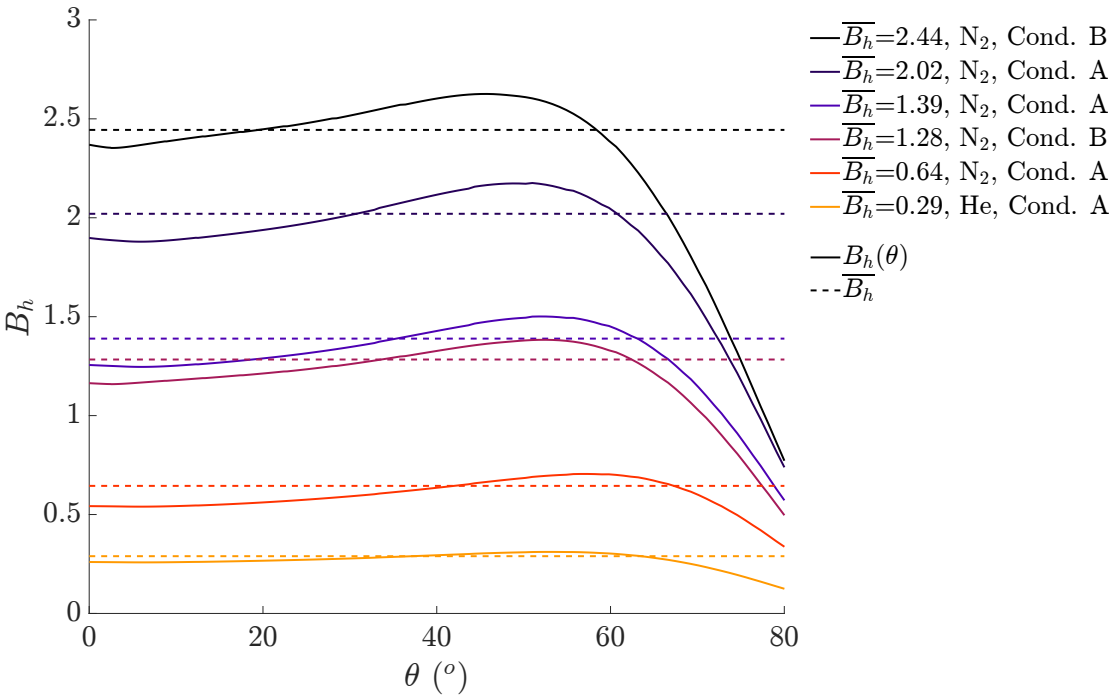


Figure 4.7: Estimated distributions of B_h for a range of test conditions.

4.2.4 Facility and Test Conditions

Experiments were conducted at the University of Oxford's High Density Tunnel (HDT) at the Oxford Thermofluids Institute. Tests were carried out using a Mach 7 nozzle at two freestream conditions, selected to match the freestream unit Reynolds number of Mach 7 flight at 23.7 and 27.4 km altitude using the 1976 U.S. Standard Atmosphere [142]. The freestream gas was a synthetic air mixture of nitrogen and oxygen only, selected to avoid IR interference from carbon dioxide and water. The freestream flow properties, given in Table 4.2, were characterised beforehand using a sting-mounted rake equipped with pitot probes and aspirated thermocouples for freestream pressure and temperature measurements.

Table 4.2: Freestream conditions during HDT testing, typically specified by the test gas fill pressure and temperature (P_{fill}, T_{fill}). The conditions are based on the second quasi-steady region shown in Figure 4.9.

Condition	A	B
Freestream gas	Air	Air
M_∞	7.0	7.0
P_{fill} (kPa)	1510	840
T_{fill} (K)	550	550
$P_{0,\infty}$ (Pa)	1280	715
$T_{0,\infty}$ (K)	481.9	480.6
P_∞ (Pa)	309.4	186.3
T_∞ (K)	44.6	45.3
$Re_{u,\infty}$ / 1e6	7.09	4.05
Equiv. altitude (km)	$\approx$ 23.7	$\approx$ 27.4

A schematic diagram of the HDT is shown in Figure 4.8. The HDT was operated in Ludweig mode, where pre-heated and pressurised test gas is stored in a barrel and expanded through a Laval nozzle into an evacuated test section via a fast-acting plug valve. Test time is characterised by expansion waves originating from the plug valve, propagating upstream, and reflected downstream. When a wave reaches the valve plenum, there is a drop in total freestream temperature and pressure ($P_{0,\infty}$, $T_{0,\infty}$), as can be seen in Figure 4.9. The quasi-steady test conditions are highlighted in grey. All HDT conditions referenced in this paper use the second quasi-steady condition (t = 0.115 - 0.143 s), unless otherwise stated. Further information on the operation of the HDT can be found in [128, 143].

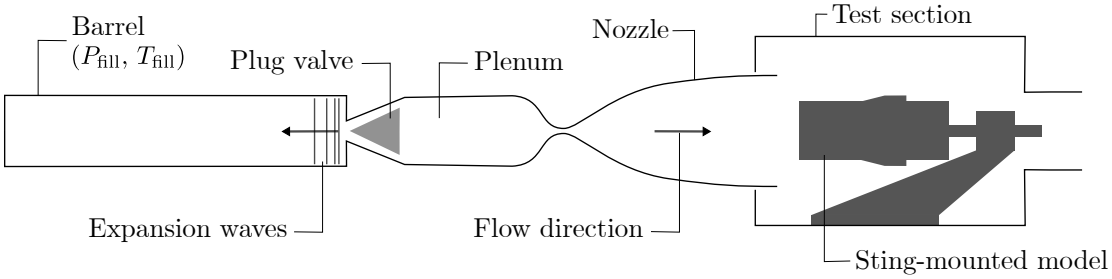


Figure 4.8: Annotated sketch of the HDT, adapted from [143], not to scale.

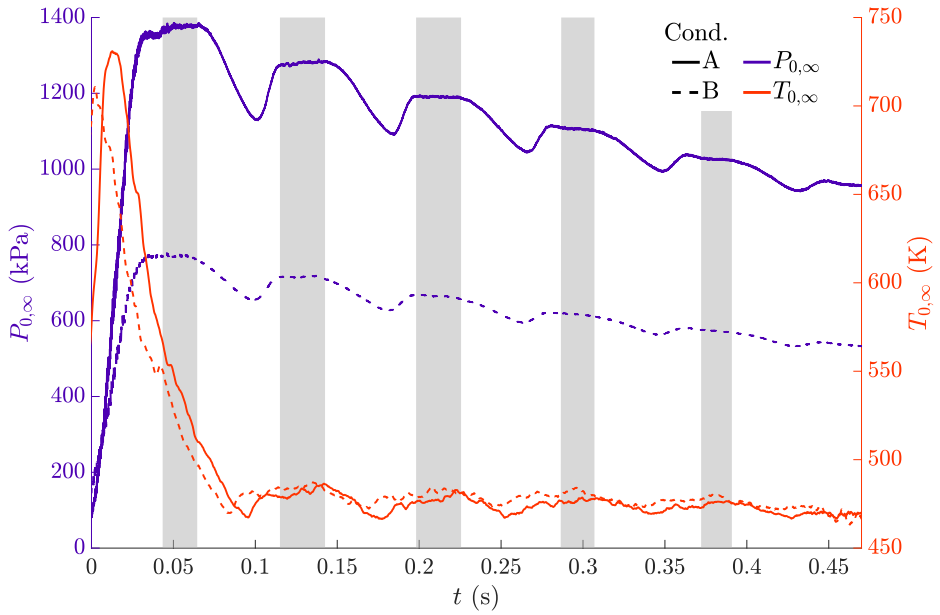


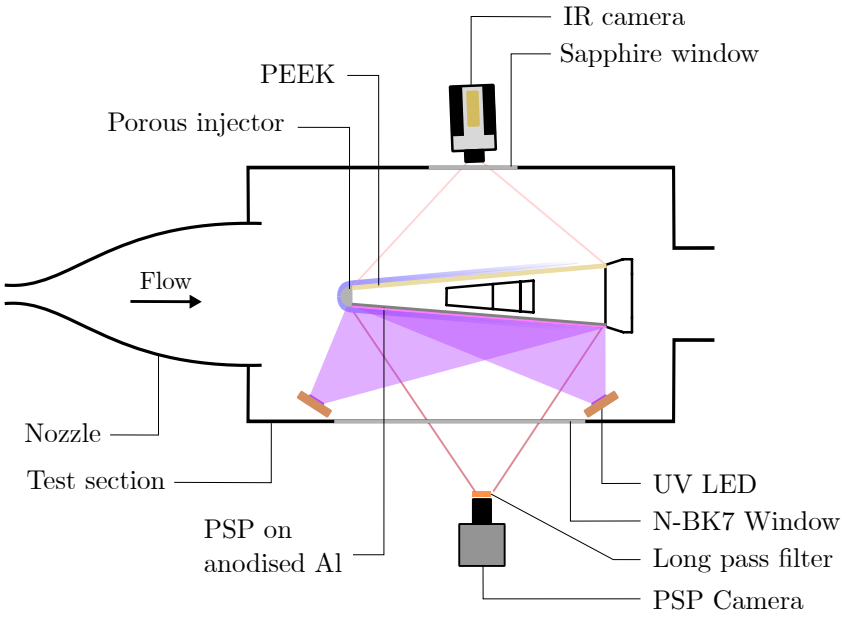
Figure 4.9: Traces of measured $P_{0,\infty}$ and $T_{0,\infty}$ for the two conditions tested in HDT.

The model sensors, rake sensors (when installed), and tunnel infrastructure sensors were connected to amplifiers and a data acquisition (DAQ) card. All Kulites were connected to Fylde FE-H379TA amplifiers, thermocouples to Fylde 351UA amplifiers, and the Honeywell sensors had their own integrated amplifiers. During operation, the mass flow controller provided a continuous 0–5 V analogue signal, corresponding to the achieved mass flow rate. All signals were recorded by a NI PXIe-6368 data acquisition system at a sample rate of 100 kHz during testing, including the duration where coolant gas was injected for 7 seconds prior to flow arrival to stabilise plenum pressure and reach thermal equlibrium. Data acquisition was triggered by the pressure signal inside the HDT plenum. The digital output functionality of the DAQ was utilised to simultaneously trigger the high-speed cameras to enable time-accurate optical data.

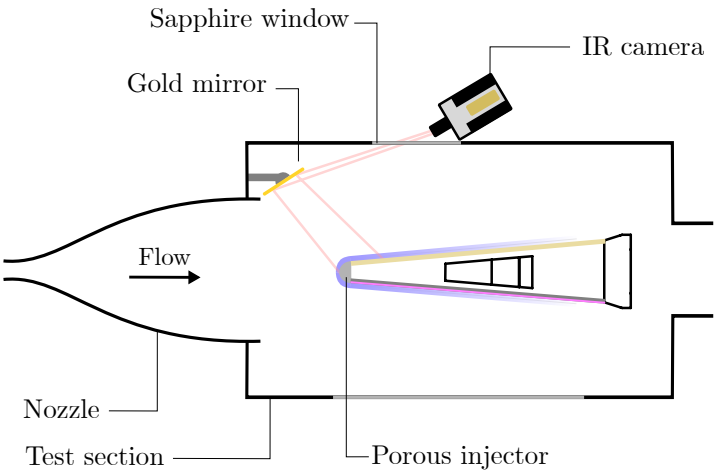
4.2.5 Optical Arrangement

The optical arrangement consisted of two techniques: IR thermography and PSP. These were arranged in two different configurations, shown in Figure 4.10. Configuration 1 was employed to simultaneously measure the heat flux and concentration

of the downstream coolant film. Configuration 2 was employed to measure heat flux directly on the leading edge.



(a) Configuration 1



(b) Configuration 2

Figure 4.10: Top view of optical arrangements used during the experimental campaign.

Heat flux measurement

A Telops FAST M3k infra-red camera was used, with sensitivity in the mid-wave infra-red (MWIR) part of the spectrum (1.5 -5.4 μm). All tests were recorded at 1200 Hz with an exposure time of 150 μs. The camera was positioned outside of the test section, with optical access provided through a ∅100 mm sapphire window insert that could be positioned within the test section wall at different streamwise locations. For downstream measurements (config. 1), a 13 mm wide-angle lens was used for a wide field-of-view along the model length. For leading edge measurements (config. 2), a 100 mm lens was used to maximise resolution on the leading edge surface. Further parameters on each optical configuration are given in Table 4.3.

Table 4.3: IR acquisition parameters for the two configurations shown in Figure 4.10.

Optical configuration	1	2
Model view	Downstream	Leading edge
Approx. optical path length (mm)	470	950
Telops lens model	TEL-10013	TEL-6915
Lens focal length (mm)	13	100
Lens f/number	f/2.5	f/2.5
Lens wavelength range (μm)	1.5 – 5.15	1.5 – 5.15
Exposure time (μs)	150	150
Frame rate (Hz)	1200	1200
Field of view (mm)	347 × 278	55.1 × 44.1
Resolution (pix/mm)	1.085	5.81

Concentration and pressure measurements

Concentration and pressure measurements using PSP were taken using an intensity-based approach. The PSP formulation used was ISSI Turbo-FIB, a commercial fast-response PSP with a quoted response time of of < 1 ms [124], suitable for measurements within the pseudo-steady test periods of the HDT. The PSP was mixed and sprayed onto the anodised aluminium plate according to the manufacturer's instructions [141].

The PSP was excited using two high power UV LEDs (Luminus CBT-90-TE

UV), which were mounted inside the test section, outside of the mainstream flow. The LEDs were connected in series to a PeakTech 1580 power supply, driving each LED at approximately 30W. The PSP emission was captured by a Photron Fastcam Mini AX200 900K high-speed camera with a Tamron SP AF 70-200mm F/2.8 zoom lens, and a 550 nm long-pass filter to block the UV excitation light. The camera operated at 2000 Hz, with a 0.5 ms exposure time. Further parameters are given in Table 4.4.

Table 4.4: PSP acquisition parameters. The wavelength ranges presented are full-width at half maximum (FWHM) values provided by the manufacturers.

Model view	Downstream
Exposure time (μs)	500
Frame rate (Hz)	2000
Field of view (mm)	454 × 454
Resolution (pix/mm)	2.267
LED emission wavelength range (nm)	408 - 422
PSP excitation wavelength range (nm)	380 - 500
PSP emission wavelength range (nm)	620 - 750
Lens filter wavelength range (nm)	550 - 750

To limit photodegradation, LED operation was restricted to a few seconds per test, and the PSP surface was shielded from ambient light whenever possible. Some photodegradation was still unavoidable, so daily calibrations were performed to correct for this and maintain measurement accuracy.

4.3 Post-Processing

The conversion from raw camera signals to 2D maps of physical surface parameters such as heat flux and concentration requires a calibration procedure and assumptions on the aerothermodynamic processes. With the exception of leading edge heat transfer, these assumptions enable processing on a pixel-wise basis, where each pixel acts as an individual measurement sensor. A short outline of the postprocessing procedures is given here. A detailed step-by-step description including calibration contours and photographs is provided in Appendix A.3.

4.3.1 IR Thermography

Heat flux processing for IR thermography in the HDT was pioneered by Naved et al. [66, 70]. This work follows the processing that was further developed by Ivison [140], outlined below. The processing for optical configurations 1 and 2 follow a common framework. Additional steps required for configuration 2 are also indicated below.

1. **Black Body Calibration:** This calibration converts known temperatures to raw pixel counts by using a portable calibrator with variable temperature settings. The calibration was carried out in-situ to ensure ambient reflections and emissions were accounted for. Calibration curves were generated on a pixel-wise basis.

2. **Calibration corrections:** Differences in gas composition between calibration (atmospheric air) and testing (synthetic air) affected transmissivity. The material emissivity also varied between the portable calibrator and the model surface. Both effects were accounted for in applying the calibration to the experimental data. Emissivity values have been measured in [70], and transmissivity in [140].

3. **Dewarping:** Precisely manufactured calibration plates were placed over the model surface in-situ and aligned using locating features. Images of the

plates were used to calculate distortion correction transforms and map image pixels to a physical 2D coordinate system.

4. **Directional emissivity correction (Config. 2):** The leading edge is a highly curved surface and the effect of view angle on the measured emissivity, known as *directional emissivity*, is well-documented [121]. The calibration procedure developed by Condren et al. [120] for IR measurements in the HDT was followed to generate a map of directional emissivity within the images.

5. **Temperature:** Applying the black body calibration (including emissivity and transmissivity corrections) to the experimental data yields a time-accurate trace of the model surface temperature.

6. **Heat flux calculation:**

   (a) For the view of the PEEK surface (Configuration 1), heat flux processing of temperature data was accomplished using Oldfield's impulse response method [138]. This method fundamentally assumes 1D semi-infinite conduction, enabling processing on a per-pixel basis.

   (b) The porous leading edge was too thin for the above approach in Configuration 2, and so was processed using a finite element reconstruction (FER) method. COMSOL MULTIPHYSICS with the *heat transfer in solids* module was employed to model the conduction and temperature rise of an imported CAD geometry. An optimisation algorithm was used to best match the experimentally measured transient surface temperature by varying the transient input heat flux. The distribution was characterised by a Bezier curve with 4 control points over the leading edge, and 4 control points downstream, up to $x/R = 3$.

4.3.2 Pressure-Sensitive Paint

PSP processing for both the surface coolant concentration and surface pressure followed nearly identical steps. PSP intensity is inversely related to the partial pressure of oxygen (pO_2) at the surface, which depends on the local static pressure and the mole fraction of oxygen. These effects cannot easily be disentangled, and separate experiments must be carried out to measure each effect in isolation. The optical arrangement for both sets of measurements were identical, and the processing diverged only at the final step.

1. **Intensity Calibration:** The PSP is calibrated in-situ by allowing an evacuated wind tunnel test section to increase in pressure to atmosphere over a few seconds while the PSP is illuminated. The camera is synchronised with the model's surface-mounted kulite to produce a time-accurate trace of intensity ratio versus pressure ratio for each pixel.

2. **Measurement:** During a test, PSP luminophore emission intensity was measured by a high speed camera. The calibration curve is applied to the 2D transient intensity map to yield pO_2.

3. **Conversion to concentration or pressure:** Determining the coolant concentration or surface pressure from the PSP data depends on the coolant.

   (a) Coolant concentration is effectively processed as the absence of oxygen. Oxygen concentration is converted from the measured pO_2 using Dalton's law of partial pressures and the ideal gas law. This processing assumes surface static pressure does not change between the cooled and uncooled tests [103, 136], and that the coolant is oxygen-free.

   (b) Surface pressure is calculated by converting the oxygen partial pressure to static pressure by dividing by the mole fraction of oxygen in the air, taken to be 0.21. This requires the injected coolant to have the same concentration as the freestream, so synthetic air is also used in the gas injection system.

4.4 Numerical Modelling

One aim of the present study is to determine whether numerical methods can capture the correct flow physics for leading edge and downstream film cooling. Each experimental test was accompanied by a corresponding numerical simulation. Simulations were carried out using Eilmer4: a finite-volume solver specialising in compressible flow simulations [144, 145]. This section describes the setup of the numerical simulations, and the next section presents a comparison of the experimental and numerical results.

4.4.1 Boundary Conditions

Flow was simulated over a 2D planar half-body at zero angle of attack with leading edge transpiration cooling. The boundary conditions of the simulations are shown in Figure 4.11, and are described below.

A key challenge was to align the mass flux boundary condition of the numerical solver with the experimental mass fluxes. As previously described in Section 4.2.3, the leading edges were designed to produce a constant-B_h blowing distribution. The target mass fluxes were calculated using uncooled Eilmer simulations to estimate heat flux and boundary layer properties. For simulations with cooling, the target mass flux distributions were prescribed into the Eilmer simulations using a custom mass flux boundary condition, which is discussed in further detail in Chapter 5 of this thesis.

The inflow conditions were based on the experimental freestream data provided in Table 4.2. Both the porous injector and solid wall were set to no-slip conditions, and coolant outflow was assumed to be normal to the surface. The wall and injected coolant temperatures were uniformly set to the ambient temperature of the respective test.

4.4.2 Solver Settings

Simulations were configured to solve laminar, non-reacting flows of dry synthetic air at the quasi-steady test conditions of the HDT. Table 4.5 shows the key solver settings.

Table 4.5: Key Eilmer settings used in this numerical work.

Flow characteristic	Assumption
Mass injection distribution	Constant blowing parameter
Timestepping	Steady state
Turbulence model	Laminar
Wall temperature	Cold wall, T_{amb}
Gas model	Perfect gas
Diffusion model	Fick's first law with binary diffusion

Steady-state solutions were achieved using a time-implicit scheme and a Newton-Krylov method to accelerate convergence, developed in [146]. Following a grid convergence study for surface heat flux, the shock-fitted domain was populated with 250 streamwise and 200 surface normal cells. Cell clustering was applied to the shock-fitted inflow, wall, and symmetry boundaries. A cell stretching parameter defined by Roberts [147], was set to 1.01 for these boundaries. Further details of the numerical method, blowing boundary condition, and grid convergence procedure is provided in Appendix B.

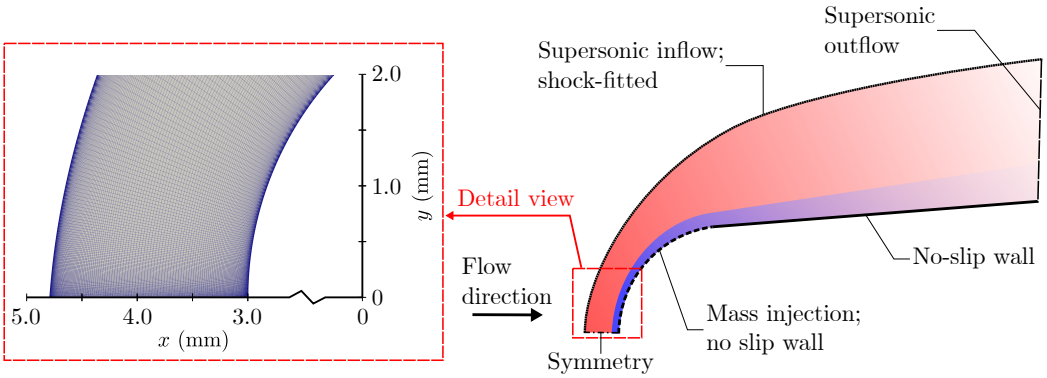


Figure 4.11: A sketch of the boundary conditions used in the Eilmer simulations, not to scale. A detailed view of the to-scale mesh around the symmetry line is shown, for freestream condition A with N_2 coolant.

4.5 Results

This section presents the experimental and numerical results, grouped into three parts. Each test case is defined by the freestream condition, coolant gas, and mean blowing parameter ($\overline{B_h}$). The three key result sets are:

1. Downstream film cooling and coolant concentration measurements.
2. Leading edge heat flux and comparison to stagnation point correlations extrapolated across the surface.
3. Downstream surface pressure measurements to assess the effect of higher blowing parameters on drag.

4.5.1 Downstream Film Cooling and Concentration

Figure 4.12 shows selected experimental contours of the measured surface heat flux and partial pressure of oxygen, where the effect of the coolant film is clearly observable at the centre of the model. The coolant film shows excellent spanwise uniformity, with spanwise heat flux variation within 8.9% for low blowing ($\overline{B_h} = 0.64$) and 10.7% for high blowing ($\overline{B_h} = 2.02$) immediately downstream of the injector. Partial pressure of oxygen measurements observed spanwise variations within 6.0%, irrespective of the blowing parameter. As the coolant is swept downstream, spanwise variation diffuses laterally, smoothing both quantities about the mean.

Often associated with film cooling [31], parameters of interest were the thermal efficiency (η_{th}) and the concentration efficiency (η_c), defined in Equations 4.6 and 4.7. Here, subscript 0 represents quantities measured without cooling applied.

$$\eta_{th} = 1 - \frac{\dot{q}}{\dot{q}_0} \tag{4.6}$$

$$\eta_c = 1 - \frac{pO_2}{pO_{2,0}} \tag{4.7}$$

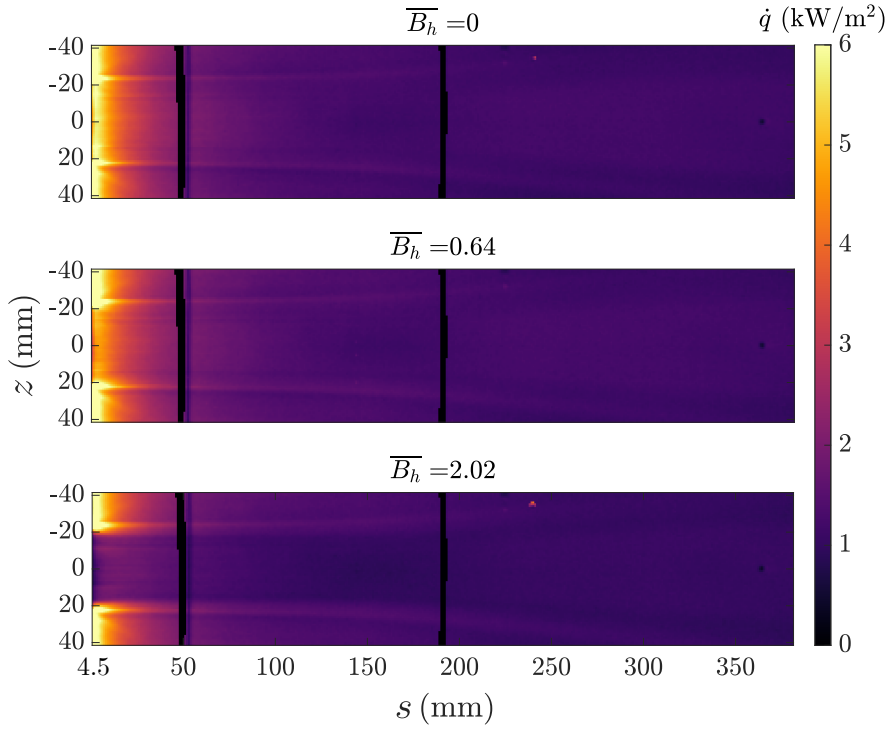
1D streamwise distributions of η_{th} and η_c were obtained by averaging across the injection region ($z = \pm 19$ mm). Figure 4.13 presents these experimental results

(solid lines) compared to the 2D laminar CFD (dashed lines). Most results presented below correspond to nitrogen blowing. Helium injection proved challenging because its high compressibility required plenum pressures that exceeded the injector's allowable limit except at very low mass fluxes.

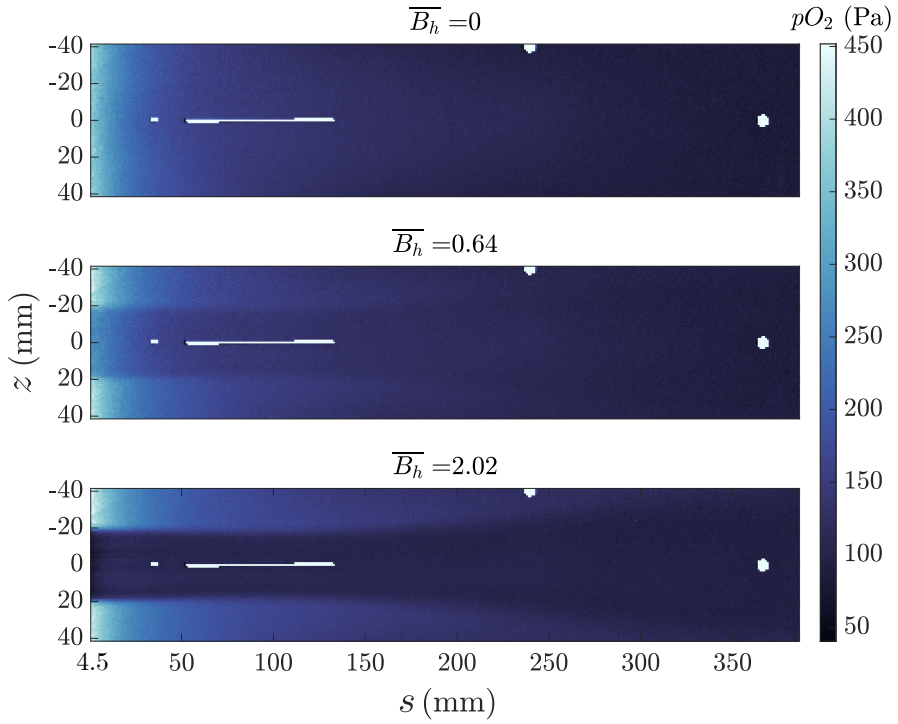
It was found that a weak wave from the HDT nozzle impinged on the model surface at $x = 220$ mm, and so the comparative results are truncated up to this point[2].

The results show good agreement between the CFD and experiment. The thermal efficiency has better agreement at higher $\overline{B_h}$ values than at lower values: at the highest blowing conditions ($\overline{B_h} > 2$), the CFD remains within 10% of the experimental distribution throughout the measurement region, whereas for lower $\overline{B_h}$, agreement is within 20%. Concentration efficiency agreement does not have this $\overline{B_h}$ dependence, and all the presented η_c CFD distributions agree to within 10%.

[2]While not particularly visible in Figure 4.12, there effect is clear in the 1D distributions past $x = 220$ mm. This is not thought to be boundary layer transition due to the insensitivity to blowing.

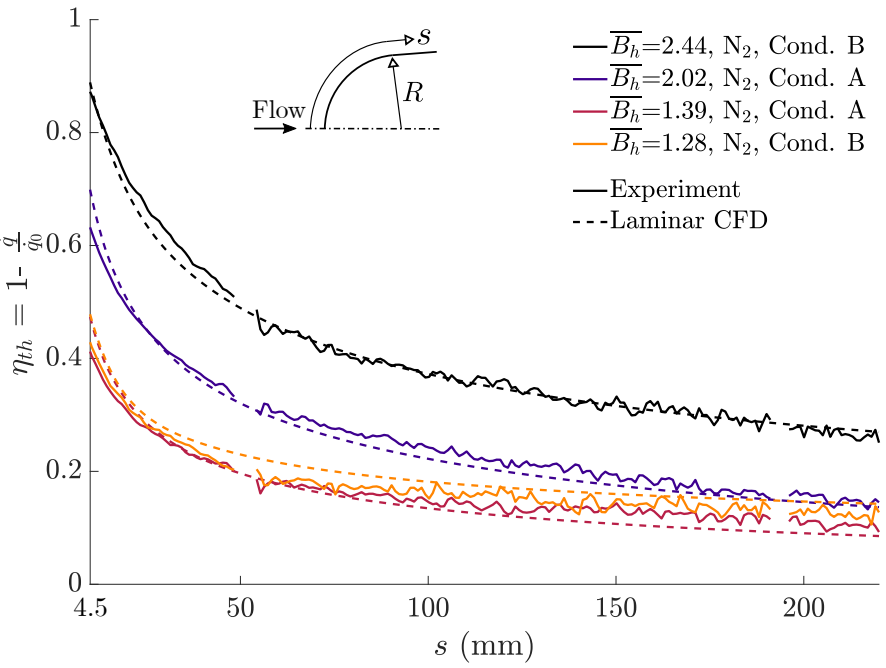


(a) Heat flux

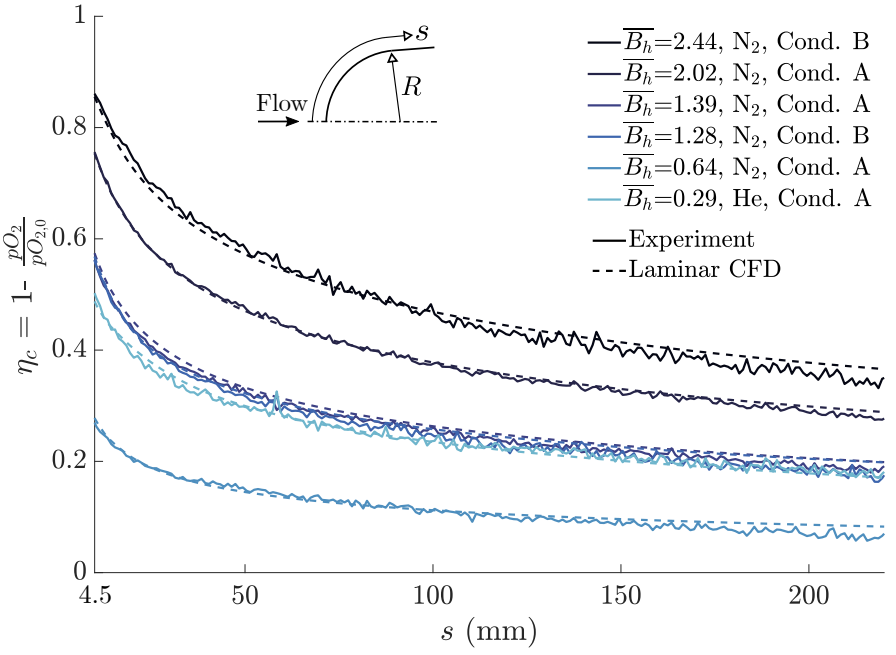


(b) Partial pressure of oxygen

Figure 4.12: Experimental contours of downstream film cooling as measured simultaneously by IR thermography and PSP. These results were obtained at freestream Condition A with nitrogen coolant. Artificial masks are applied in between PEEK panels, and at sensor locations. s is the surface coordinate starting at the stagnation point, with the downstream region beginning at $s = 4.5$ mm.



(a) Thermal efficiency



(b) Concentration efficiency

Figure 4.13: Spanwise-averaged distributions of thermal and concentration efficiencies. A range of experimental conditions are presented and compared to laminar CFD simulations.

Effect of Coolant Gas

From Figure 4.13b, it is clear that helium is able to achieve similar concentration efficiencies to nitrogen at a much lower mass flux: η_c for helium at $\overline{B_h} = 0.29$ shows similar performance to that of nitrogen at 4.8 times higher mass flux ($\overline{B_h} = 1.39$). The performance of helium compared to nitrogen has been attributed toward its lower molecular mass (therefore higher molar flow rate) and higher specific heat capacity, which commonly leads to the suggestion that helium is a better coolant gas candidate [57, 148]. However, this conclusion does not account for operating limits of the injector itself. In this experiment, mass flux was limited by the maximum differential pressure that the injector could withstand (2.6 bar). Due to helium's lower molecular mass, the same driving pressure produced a mass flux approximately six times lower than that of nitrogen. This effect outweighed helium's increased efficiency, and so a greater range of cooling conditions could be achieved with nitrogen.

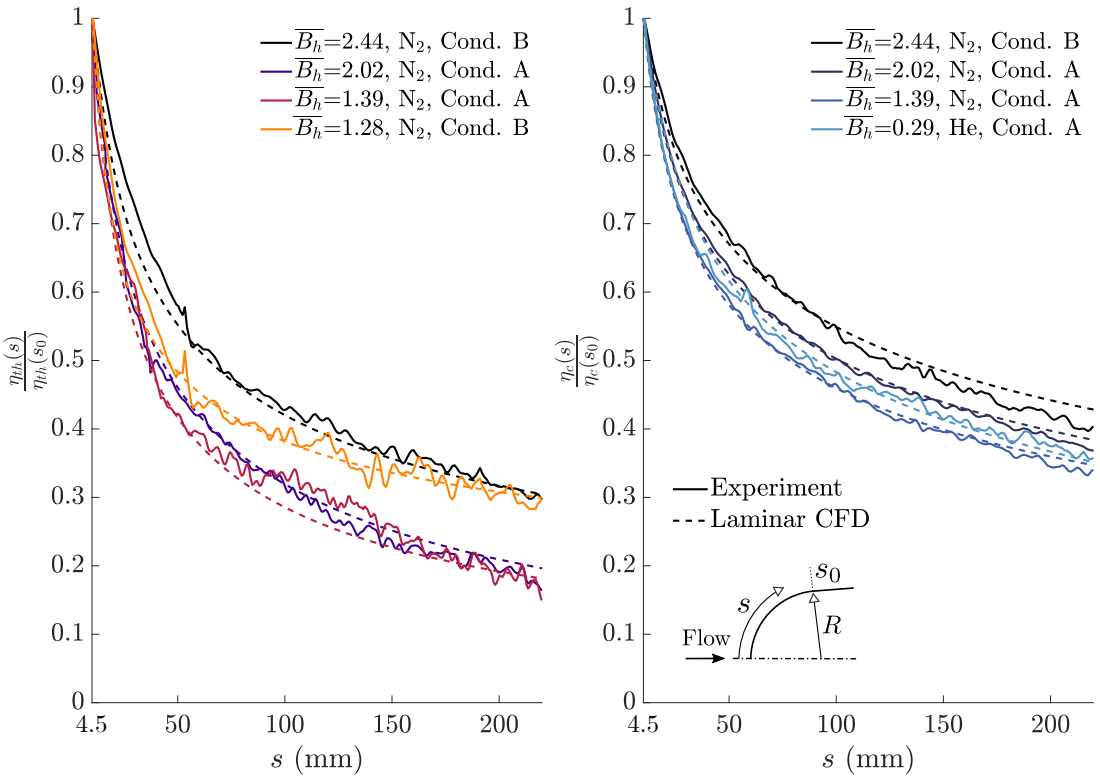
Effect of B^*

For nitrogen injection, the blow-off parameter was calculated to be $\overline{B_h} \approx 1.8$ for conditions A & B. The experimental results at $\overline{B_h} > B^*$ show that operating at these conditions does not affect the ability of the laminar CFD to predict the concentration and heat flux augmentations. It can be concluded that the coolant film and boundary layer remain laminar at these high blowing conditions.

Further results in Section 4.5.2 and Chapter 5 suggest that at these blowing conditions, the coolant layer does achieve boundary layer blow-off due to the change in cooling behaviour. However, this behaviour does not lead to significant loss in aerodynamic or cooling performance of the leading edge. This may be due to the blowing beginning at the stagnation point, allowing the boundary layer to form over the coolant film, which acts as an effective modified body contour.

Effect of $\mathbf{Re_{u,\infty}}$

Figure 4.14 shows the decay rates of the coolant film efficiencies, visualised by normalising the distributions by the values at the end of the injector: $\eta_{th}(s_0)$ and $\eta_c(s_0)$. Once more, the CFD and experimental data match well across the range of Reynolds numbers presented. It can be seen that higher B_h leads to a slower decay, and the higher freestream Reynolds number condition (cond. A) leads to faster film decay. Shown in the following chapter, modelling the decay rate successfully provides the means to collapse the data to form correlations.



(a) η_{th} decay rate

(b) η_c decay rate

Figure 4.14: Thermal and concentration efficiency decay visualised by normalising the distributions of η_{th} and η_c by the efficiencies at the end of the injector (at location s_0).

4.5.2 Leading Edge Heat Flux Reduction

One aim of the experiment was to assess whether stagnation point injector correlations could predict heat flux reduction along the surface of a leading-edge

injector, based on the local blowing parameter $B_h(s)$. The injector was designed to produce a constant B_h distribution.

As well as the comparison of the experimental results against the laminar CFD, heat flux reduction along the leading edge was also compared to Yoshikawa's correlation. Local $B_h(s)$ was estimated as per Section 4.2.3 and fed into Equation 4.4. Table 4.6 presents a comparison of the different methods employed to evaluate leading edge heat flux for the expected blowing conditions. It shows the required inputs for each stage, indicating the relative cost of each method.

Table 4.6: A list of inputs required for each heat flux reduction prediction method on the leading edge injector, in decreasing order of cost.

<table>
<tr><th></th><th>Mass flux distribution</th><th>Flow and plenum conditions</th><th>Heat flux reduction processing method</th></tr>
<tr><td>Experiment</td><td>Not required</td><td>Not required</td><td>Finite element reconstruction of IR data</td></tr>
<tr><td>CFD</td><td rowspan="2">Calculated by COMSOL porous flow modelling</td><td rowspan="2">Experimentally measured</td><td>Cooled & uncooled CFD data</td></tr>
<tr><td>Correlation</td><td>Uncooled CFD data only</td></tr>
</table>

Figure 4.15 shows the experimental contours of the leading edge temperature rise, dT, due to the hypersonic cross-flow. The contours are presented at $t = 0.13$ s, where $dT = 0$ K at $t = 0$ s (at flow arrival). The temperature field is calculated after applying the pixel-wise non-uniformity calibration and emissivity correction for the curved surface. For highest B_h case, it can be seen that the injector did not change temperature, leading to effectively zero (or even negative) heat flux: an effect that has been well-documented [29, 31, 70]. In this work, heat flux analysis on the leading edge of such *over-cooled* cases was not performed, though their downstream results remain relevant.

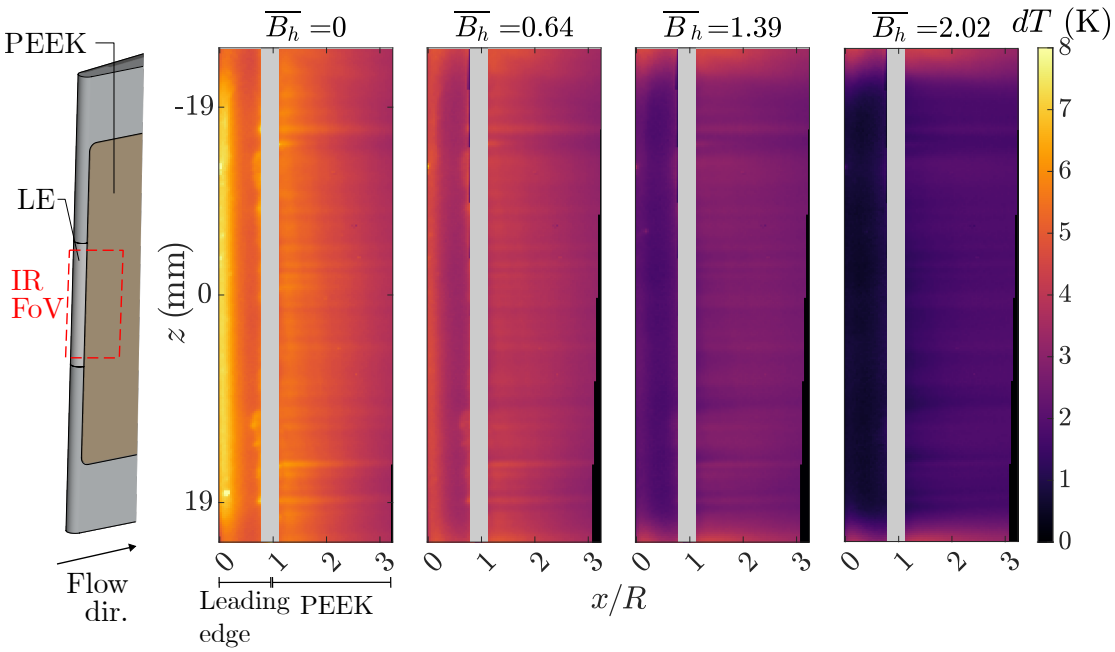


Figure 4.15: IR camera view of the leading edge showing experimental contours of surface temperature change, dT at $t = 0.13$ s. The grey bars mask the interface between the leading edge and PEEK panel where accurate temperature measurement could not be taken. These tests used N_2 coolant at freestream Condition A.

The IR data was averaged across the injector span ($z = \pm 19$ mm) yielding transient 1D temperature distributions, which was used as an input to the FER method. Appendix A.3 presents details on using the FER method to convert transient dT profiles to heat fluxes.

Figure 4.16 shows the calculated transient heat flux profiles. The method calculates a spanwise-uniform 1D heat flux profile, so the result in the Figure is also in 1D. The total temperature spike associated with tunnel start-up can be seen at around $t = 0.03$ s. As labelled in the figure, the transient profiles were averaged over the second steady plateau and normalised by the uncooled data to give profiles of heat flux reduction over the injector surface, shown in Figure 4.17.

The figure shows that the injectors, designed for a approximately constant B_h, produced reasonably uniform heat flux reduction along the surface. The broad agreement between experimental and numerical data suggests that the mass flux boundary conditions were successfully implemented in the experiment. The consistency of both datasets with Yoshikawa's correlation demonstrates, for the first time,

that this correlation is applicable over the injector surface with foreign gas injection.

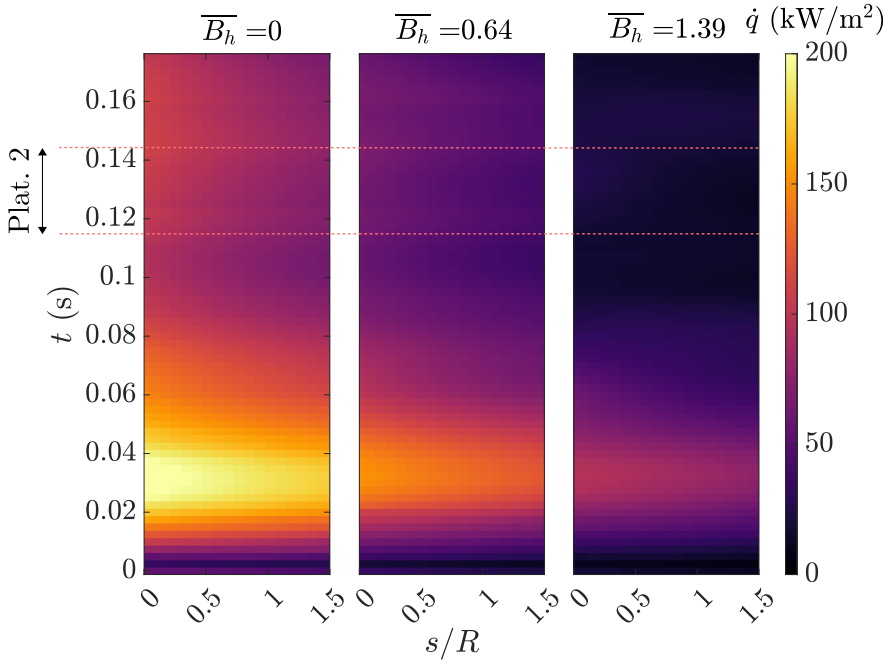


Figure 4.16: Transient surface heat flux distribution on the injector as evaluated by finite element reconstruction. These test cases used N_2 coolant at Condition A.

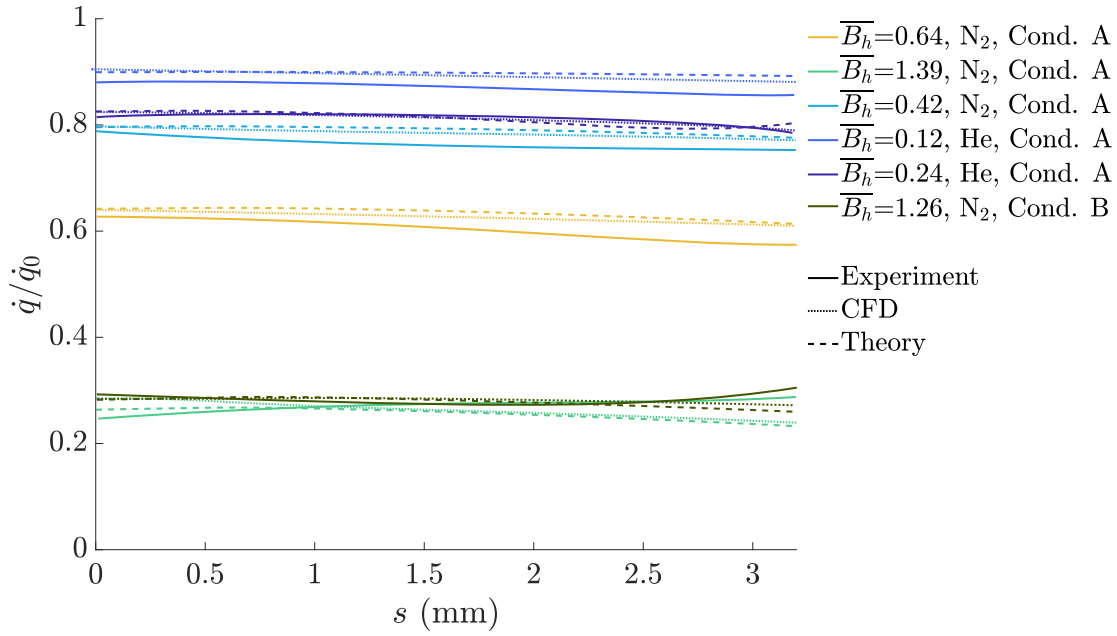


Figure 4.17: 1D heat flux reduction distributions for a range of conditions, compared to the Yoshikawa correlation and to laminar CFD. The injectors were designed to provide a constant B_h along the surface.

The utility of the correlation is significant: it provides a design tool for transpiration-cooled vehicles. Leading edge heat flux reduction was accurately predicted using only uncooled CFD, eliminating the need for computationally expensive cooled simulations across multiple blowing conditions. This approach enables rapid performance assessment during preliminary design phases.

4.5.3 Pressure Augmentation

To investigate the change in surface pressure due to transpiration cooling, air was employed as a coolant gas at high mass fluxes at the two freestream conditions.

The downstream pressure field was measured by PSP and verified by the pressure tappings. Figure 4.18 shows the ratio of cooled to uncooled surface pressure, $\Delta P = P/P_0$ at the highest mass fluxes achievable for air injection. By averaging over the active injection area ($z = \pm 19$ mm), 1D distributions of ΔP are also presented in the figure. These distributions are compared with the laminar CFD results, showing excellent agreement.

The pressure field can be divided into two regions: near the leading edge ($s/R < 10$) and further downstream ($s/R > 10$). Near the leading edge, the flow overexpands, possibly due to the increased effective bluntness of the leading edge, and ΔP drops below 1 for a short distance downstream of the injector. Higher $\overline{B_h}$ increased this overexpansion in the experimental results, though the numerical results did not predict this well. Further downstream, experimental results showed elevated surface pressures (about 2–3%) that gradually relaxed toward the uncooled surface pressure ($\Delta P = 1$) but did not fully reach it within the domain. The CFD values agreed much more closely in this region. In the figure, the results of the pressure tappings are shown to agree with the PSP data. The pressure tapping data for helium and nitrogen injection remained within the same range.

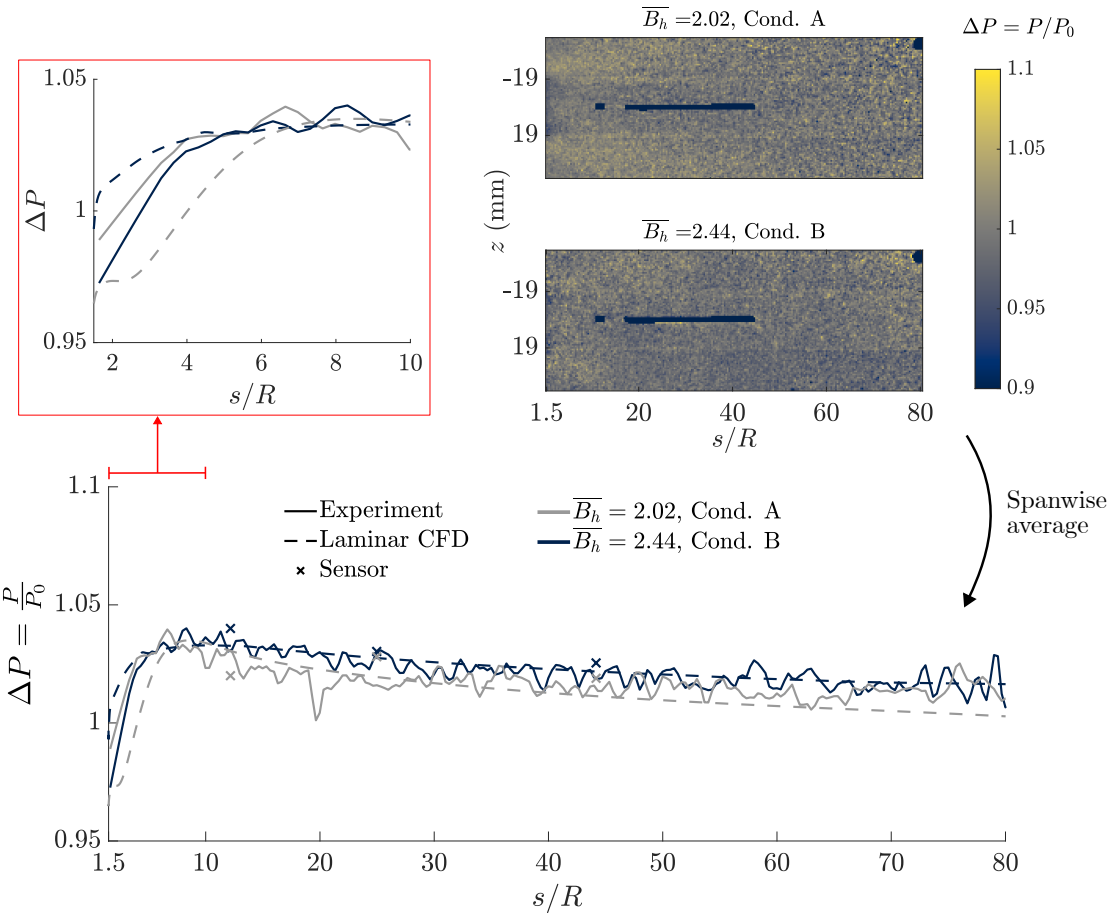


Figure 4.18: 2D (upper right) and span-averaged (bottom) surface pressure augmentation measured by PSP and pressure tappings for the maximum attainable B_h using air as a coolant. The experimental results are compared to CFD results at the same conditions.

Noting that pressure augmentation is of interest due to its drag implications, the 1D pressure distribution was resolved in the streamwise direction and integrated along the surface to give the downstream pressure drag per unit span. While this calculation is geometry-specific, it provides some insight into blowing-induced pressure drag.

The pressure drag augmentation, denoted ΔD_P, is defined as the cooled pressure drag normalised by the uncooled case. Table 4.7 shows the measured and simulated pressure drag augmentation due to blowing. Good agreement is observed between the integrated pressure values from experiment and CFD, as the discrepancy in the low-pressure region near the injector ($s/R < 10$) affects only a small portion of the surface.

Table 4.7: Experimental and CFD results of pressure drag augmentation due to blowing. The CFD results are presented with and without leading edge pressure drag contributions.

	ΔD_P (%)		
	Experiment (downstream only)	Simulation (downstream only)	Simulation (incl. leading edge)
$\overline{B_h} = 2.02$, cond. A	2.69	2.45	1.89
$\overline{B_h} = 2.44$, cond. B	3.24	3.50	3.40

Limitations in the PSP measurements meant that only the augmentation downstream of the injector ($s/R > 1.5$) could be captured, though literature indicates that the pressure changes would be most significant downstream of the injector [92], and pressure on the injector itself is relatively insensitive to blowing [136].

It should be carefully noted that only the pressure drag is considered here. Momentum drag due to injection and skin friction augmentation were not measured (the latter is well-known to decrease due to injection [149, 150]). It is seen in both Chapter 5 and in [136] that these other contributions are small relative to the effect of pressure drag.

Overall, these results show very small (<5%) changes in pressure due to moderately high blowing parameters ($B_h/B^* \approx 1.5$). In comparison, the only other dataset of pressure augmentation [92] shows 200-300 % increase in downstream pressure for $B_h/B^* \approx 2.25$, suggesting that the limit of feasibility of transpiration cooling may lie in-between these blowing conditions.

4.6 Conclusion

This study presents the first experimental demonstration of a transpiration-cooled leading edge at hypersonic conditions using a highly optimised mass flux distribution. It is also the first to assess the viability of such an active TPS by jointly measuring heat flux, coolant concentration, and the potential drag implications of blowing. All results were non-dimensionalised across freestream and blowing conditions to generate reproducible data, addressing a key gap in the literature.

The experimental model consisted of a $R_{LE} = 3$ mm leading edge injector, with surfaces designed for optical diagnostics. Flight-relevant freestream conditions were tested at Mach 7 using moderate blowing parameters ($B_h = 0 - 2.44$). Despite literature suggesting helium as a preferred coolant, nitrogen allowed for a wider operational range of B_h, and higher cooling performance due to constraints imposed by the injector pressure limits.

The conventional constraint of the boundary layer blow-off parameter, B^* was shown not to be a significant limit as the cooling and aerodynamic performance were not degraded when exceeding this parameter, and the boundary layer remained laminar within the experimental domain. At the highest blowing parameters, concentration and cooling efficiencies of almost 90% were reached, but only resulted in small surface pressure and pressure drag increases ($< 5\%$). The combination of these results suggests that sharper leading edges could be flown at these conditions.

The experimental results were compared to low-cost laminar CFD simulations, showing excellent agreement (within 10%) across key parameters. This validates not only the numerical method but, critically, the accuracy of the applied mass flux boundary condition. To achieve this, a novel additively manufactured injector was designed and manufactured, providing a predictable mass flux output with spanwise uniformity. With appropriate boundary condition treatment, CFD could generate broader datasets for developing engineering correlations to support design studies.

One such correlation was adapted in this study. Yoshikawa's stagnation point model [29], was adapted to the leading edge geometry using local blowing and

heat flux distributions. Spatially resolved heat transfer measurements showed that both the adapted correlation and CFD could predict heat flux reduction along the surface. This validated correlation enables rapid design assessment using only uncooled flow solutions and mass flux distributions, eliminating the need for expensive cooled CFD runs.

CHAPTER 5

Numerical Simulations of Leading Edge Transpiration Cooling at Flight Conditions

5.1 Introduction 116

5.2 Simulation Setup 122

5.3 Aerodynamic Results 130

5.4 Heat Flux and Concentration Results 138

5.5 Conclusion 146

Preface

Building on the validation of the numerical method in the previous chapter, this chapter presents numerical simulations of a transpiration-cooled leading edge under high-enthalpy flight conditions. Eilmer4 was used to investigate heat flux and drag across a range of flight conditions, geometries, and blowing conditions. The data is collapsed by adapting existing correlations for fundamental geometries, enabling direct comparison across the different test conditions.

The majority of this chapter is composed of a conference paper published at AIAA SciTech [136], extended to include additional freestream conditions and gases for this thesis.

Author Contributions

- Raghul Ravichandran: Conceptualisation, investigation, analysis, and writing.
- Luke Doherty: Supervision as secondary supervisor.
- Matthew McGilvray: Supervision as principal investigator and funding acquisition.
- Kyle Damm: Support with numerical setup and review of the description of Eilmer.
- Rowan Gollan: Support with numerical setup.

Acknowledgements

The authors would like to acknowledge the use of the University of Oxford Advanced Research Computing (ARC) facility [151] and for their technical support. The authors also gratefully acknoweledge the help of Aaron Kennedy by providing HPC access at short notice. This research was funded by DSTL.

5.1 Introduction

Sharp leading edges are becoming increasingly favourable in hypersonic vehicle design for both re-entry [9] and sustained hypersonic flight [2, 8], due to increased lift-to-drag ratio leading to enhanced aerodynamic performance [12, 13]. Studies investigating the effect of blunting have typically explored a leading edge radius (R_{LE}) ranging from 0.1 mm to 30 mm. The reduction in leading edge radius is also associated with an increase in heat flux [17], the mitigation of which is a topic of active research [10, 85, 152].

For missions and geometries where passive systems do not provide sufficient protection, and where ablative systems are ruled out by shape stability or reusability requirements, active cooling systems are an effective means to mitigate high heat fluxes. While active cooling systems carry mass and complexity penalties, they may be employed in a targeted manner, such as at a vehicle leading edge. Transpiration cooling is a promising active thermal protection system (TPS) candidate whereby coolant gas is injected into the hypersonic boundary layer via a porous injector on the vehicle surface. A transpiration-cooled leading edge is sketched in Figure 5.1.

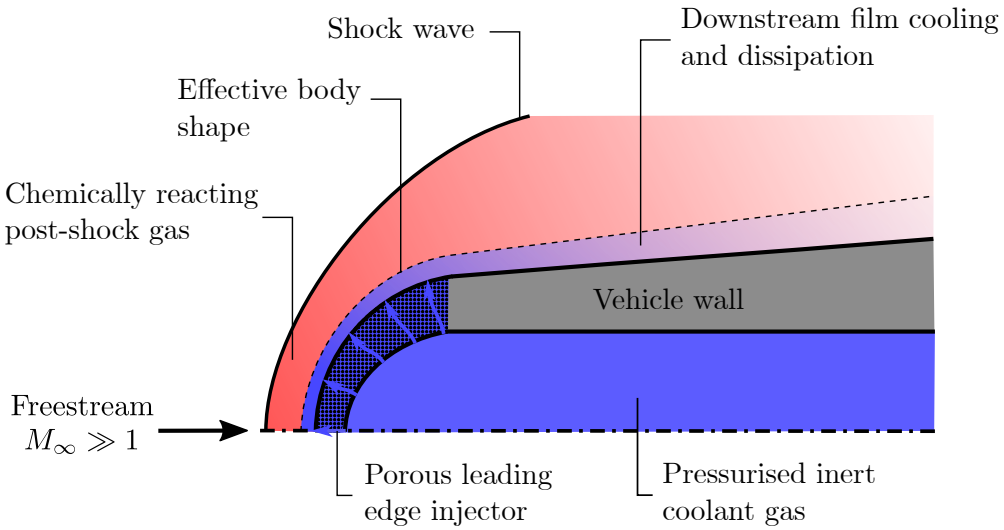


Figure 5.1: Annotated sketch of a transpiration-cooled leading edge in high speed, high total enthalpy flow.

Transpiration cooling actively reduces the temperature of the local structure by means of three mechanisms:

1. Solid to coolant gas convective heat transfer as the gas passes through the porous material [30].

2. Film cooling, where the coolant gas and thickened boundary layer reduce the surface heat flux by reducing thermal gradients at the wall [86].

3. Reduction of catalytic wall heating and material oxidation, the latter of which may allow materials to operate at higher temperatures [62].

In the 1960s and 70s, the effect of mass injection on heat flux and pressure was studied as a means of isolating the effect of outgassing in an ablative TPS for stagnation points [29, 51, 84, 88, 153], and around blunt bodies [81, 92, 154, 155]. These studies showed that moderate mass fluxes could yield significant heat flux reduction without significant changes to the surface pressure [81, 92]. In contrast, high mass fluxes or extended downstream injection thickened the effective body shape, increasing downstream pressure. These results imply that if moderate injection is limited to the leading edge, drag penalties could be minimised whilst providing effective cooling. These studies were conducted on large radius injectors (50 to 100 mm).

More recent numerical studies on transpiration cooling [105, 107, 108, 156] have explored heat flux reduction on small radius injectors (0.1 to 10 mm), but lack formal correlation between heat flux reduction and injection distribution. Literature has also not yet explored the trade-off between heat flux reduction and drag, where effective blunting may possibly negate the aerodynamic advantage of a sharp leading edge. Connelly [108] qualitatively showed that injection applied at the leading edge only slightly increased the effective leading edge radius, and that wedge angle had no effect on cooling performance.

Studies of blowing at the stagnation point have correlated heat flux reduction against non-dimensional blowing parameter, B_h [29, 88]. Shown in Equation 5.1, B_h is defined as the ratio of uncooled local Stanton number, St_0, to the blowing

ratio, F. Here, h_{aw} and h_w are the adiabatic wall enthalpy and the wall enthalpy, $\dot{m}_c$ is the coolant mass flux, $\dot{q}_0$ is the uncooled heat flux; subscripts c, ∞, and 0 refer to injected coolant, freestream, and uncooled quantities respectively. Since B_h accounts for local heat flux, it provides a means for distributing coolant around the leading edge surface according to thermal loading distribution.

$$B_h = \frac{F}{St_0} \tag{5.1}$$

$$F = \frac{\dot{m}_c}{\rho_\infty u_\infty} = \frac{\rho_c u_c}{\rho_\infty u_\infty} \tag{5.2}$$

$$St_0 = \frac{\dot{q}_0}{\rho_\infty u_\infty (h_{aw} - h_w)} \tag{5.3}$$

Yoshikawa [29] correlated B_h to the stagnation point heat flux using Equation 5.4. Yoshikawa also defined a critical blowing parameter, B^*, where the cooling behaviour changes. In the previous chapter, it was found that exceeding this parameter up to $1.5B^*$ did not lead to massive aerodynamic penalties or boundary layer transition, and that cooling performance could still be accurately simulated.

$$\Psi = \frac{\dot{q}}{\dot{q}_0} = \sqrt{\pi\Lambda}\frac{\exp\{-\Lambda B_h^2\}}{1 + \mathrm{erf}\{\Lambda\}^{0.5} B_h} \tag{5.4}$$

$$\Lambda = \begin{cases} \frac{1}{\pi}\frac{\Delta}{\Delta_0}\lambda^{B_h/B^*} & (B_h \leq B^*) \\ \frac{1}{\pi}\frac{\Delta}{\Delta_0}\lambda & (B_h > B^*) \end{cases} \tag{5.4a}$$

$$B^* = 1.82\frac{\sqrt{\pi\epsilon(W_c/W_\infty)}}{k_b(\chi'_w)^*} \tag{5.4b}$$

$$(\chi'_w)^* = \frac{1.187\sqrt{(8\epsilon(1-\epsilon)}}{(1+\sqrt{8/3\epsilon}) - \epsilon)(1 + 0.225\sqrt{\epsilon})} \tag{5.4c}$$

$$\lambda = \sqrt{\frac{W_\infty}{W_c}} N_c \tag{5.4d}$$

$$\frac{\Delta_{SP}}{\Delta_{SP,0}} = 1 + k_b\sqrt{\frac{1}{\epsilon}\frac{W_\infty}{W_c}} F \tag{5.4e}$$

$$\epsilon = \frac{\rho_\infty}{\rho_1} \tag{5.4f}$$

Here, $N_c = 1$ or $5/9$ for diatomic or monatomic coolant gases respectively; k_b

is a shape factor equal to unity; and W is molecular weight. Δ/Δ_0 is the predicted shock standoff augmentation due to blowing, where subscript 0 references uncooled quantities.

Downstream of an injector, film cooling on flat plates in supersonic flow has been studied since the 1960s, originally using slot injectors [157], where performance was quantified by the thermal efficiency, η_{th} (Equation 5.5). Heufer & Olivier [98] showed that for an isothermal case where $T_{\text{inj}} \approx T_{\text{ambient}}$ (i.e. in short duration facilities and in cold wall, cold coolant simulations), the heat flux ratio may be equivalently used, which is shown below.

$$\eta_{th}(s) = 1 - \frac{\dot{q}(s)}{\dot{q}_0(s)} \tag{5.5}$$

Heufer & Olivier [98] also correlated numerical and experimental thermal effectiveness for laminar slot injection for different injection parameters and freestream conditions. A film cooling correlation parameter, $\xi_{th,FP}$, shown in Equation 5.6, was constructed and used in further studies [86, 158, 159]. The correlation was adapted by Ifti et al. [31] for a porous injector with an updated coordinate system, shown in Figure 5.2.

$$\eta_{th,FP} = \begin{cases} 1 & (\xi_{th,FP} \leq \beta) \\ [1 + \alpha(\xi_{th,FP} - \beta)]^{\gamma} & (\xi_{th,FP} > \beta) \end{cases} \tag{5.6}$$

$$\xi_{th,FP} = \frac{1}{Fw}\sqrt{\frac{x - x_0}{x_{ref}}\frac{C^* x}{Re_u}} \tag{5.6a}$$

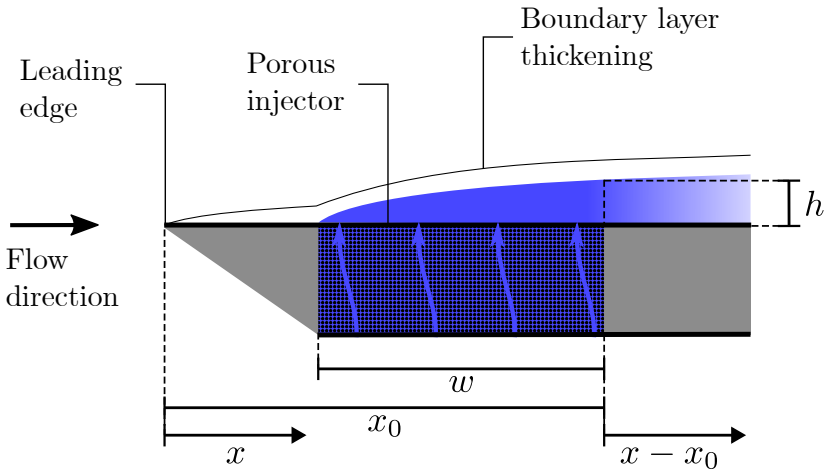


Figure 5.2: Annotated sketch of a transpiration-cooled flat plate with coordinates and dimensions relevant to the cooling correlation in Equations 5.6 and 5.8.

In the correlation, C^* is the Chapman-Rubesin factor, where $C^* = (\rho^*\mu^*/\rho_e\mu_e)^{0.5}$, evaluated at the Eckert reference conditions [160]. Re_u is the boundary layer edge unit Reynolds number, and x_{ref} is a reference length to account for the boundary layer formation upstream of the injector, empirically deduced as $x_{\text{ref}} = x_0^{1.16}$. The empirical geometry-dependent coefficients $\alpha = 0.4$, $\beta = 0.96$, and $\gamma = -1$ were used for the porous injector study.

The concentration efficiency, η_c, has been used as a performance metric of the coolant distribution, and is defined as the coolant concentration at the wall ($C_{c,w}$) relative to that in the freestream gas ($C_{c,\infty}$), shown in Equation 5.7.

$$\eta_c = \frac{C_{c,w} - C_{c,\infty}}{1 - C_{c,\infty}} \tag{5.7}$$

Ifti et al. [110] formulated a semi-analytic correlation for a flat plate by considering the diffusion-advection problem of a coolant gas slug injected into the boundary layer. Shown in Equation 5.8, the model predicted the concentration decay rate downstream of the injector, correlated by parameter $\xi_{th,FP}$. For the decay rate, η_c is normalised by the concentration at the end of the injector $C_0 = C(x_0)$; D_{12} is the binary diffusion coefficient of coolant into air, estimated using the Lennard-Jones diffusion parameters [161]; and u_e is the coolant velocity, assumed to be equal to the boundary layer edge velocity. Finally h is the height of

the coolant slab at the end of the injector, estimated by a control volume analysis.

$$\eta_{c,FP} = C_0 \left(\text{erf}\{\xi_{c,FP}\}\right) \tag{5.8}$$

$$\xi_{c,FP} = \sqrt{\frac{u_e h^2}{4D_{12}(x - x_0)}} \tag{5.8a}$$

In the present study, numerical simulations were carried out for a selection of flight conditions and geometries with the aim of formulating correlations and constraints for low-cost modelling of a transpiration-cooled system. As such, the purpose of the current study is two-fold:

1. This study aims to understand how leading edge mass injection affects the flowfield and whether high blowing parameters impose a drag penalty on sharp leading edges. This includes examining the effects of blowing and radius on the augmentation of the boundary layer, shock layer, and the drag. A comparison of the induced drag effects with various blowing parameters and leading edge radii are made. This analysis will determine whether transpiration cooling provides sufficient aerodynamic benefit to justify its complexity, or whether a larger radius with passive thermal protection would achieve equivalent drag performance with greater simplicity.

2. This study also aims to provide cooling correlations that may be employed without high fidelity CFD inputs for direct comparison across a range of conditions. For modelling purposes, these correlations are presented in terms of surface heat flux reduction for thermal modelling, and coolant concentration at the wall that would enable oxidation and material modelling.

5.2 Simulation Setup

Eilmer [162], part of the GDTk [163] gas dynamics toolkit developed at the University of Queensland, was used for flowfield computation in this study[1]. Eilmer is a general-purpose hypersonic simulation program that can solve the Euler, Navier-Stokes or Reynolds-Averaged Navier-Stokes equations on either structured or unstructured, two- or three-dimensional body-fitted grids using explicit time integration or Newton-Krylov acceleration for steady-state problems. For this work, Eilmer was used to solve the Navier-Stokes flow equations for a multi-species reacting gas in thermodynamic equilibrium on a two-dimensional structured quadrilateral grid.

This section outlines the boundary conditions and simulation settings employed in this study. Further details of the governing equations, Newton-Krylov accelerator and spatial discretisation applied in this study are provided in Appendix B.1. General literature containing details of the Eilmer solver may be found in [144, 145, 162–164].

5.2.1 Test Conditions

Simulations were carried out at three freestream conditions in steady flight, given in Table 5.1, with three inert coolant gases: helium, nitrogen, and argon. Previously noted, the numerical method was validated up to $1.5B^*$, which was adopted as the blowing limit in this study. The maximum B_h values corresponding to this limit are listed in the table. B^* depends on the coolant gas and freestream conditions, but is independent of radius.

[1] Specifically, Eilmer4 with MPI, Newton-Krylov accelerator, and complex numbers build options enabled.

Table 5.1: List of freestream conditions and maximum blowing parameters tested.

Condition	M_∞	Altitude (km)	v_∞ (km/s)	P_∞ (Pa)	T_∞ (K)	$Re_{u,\infty}$ (10^6/m)	$B_{h,\,\max} = 1.5B^*$ He	N_2	Ar
A	7	35	2.16	559	237	1.16	0.94	2.50	2.98
B	7	25	2.09	2511	222	5.69	0.95	2.51	2.99
C	5	25	1.43	2511	222	4.07	0.99	2.62	3.12

Using Yoshikawa's correlation (Equation 5.4), Figure 5.3 shows the predicted heat flux reduction for a stagnation point injector at a fixed flight condition and radius ($R_{LE} = 1$ mm, condition B). Here, each B_h value corresponds to a fixed mass flux, independent of the coolant species. The coolant gas molecular weight has a significant influence on the degree of cooling for a given mass flux, and on the B^* parameter: lower molecular weight coolants are more effective per unit mass, but also reach the $1.5B^*$ limit much sooner. When considering vehicle design, there would be a trade-off between cooling efficiency, range of operable B_h, and mass budget, which is considered in the next chapter.

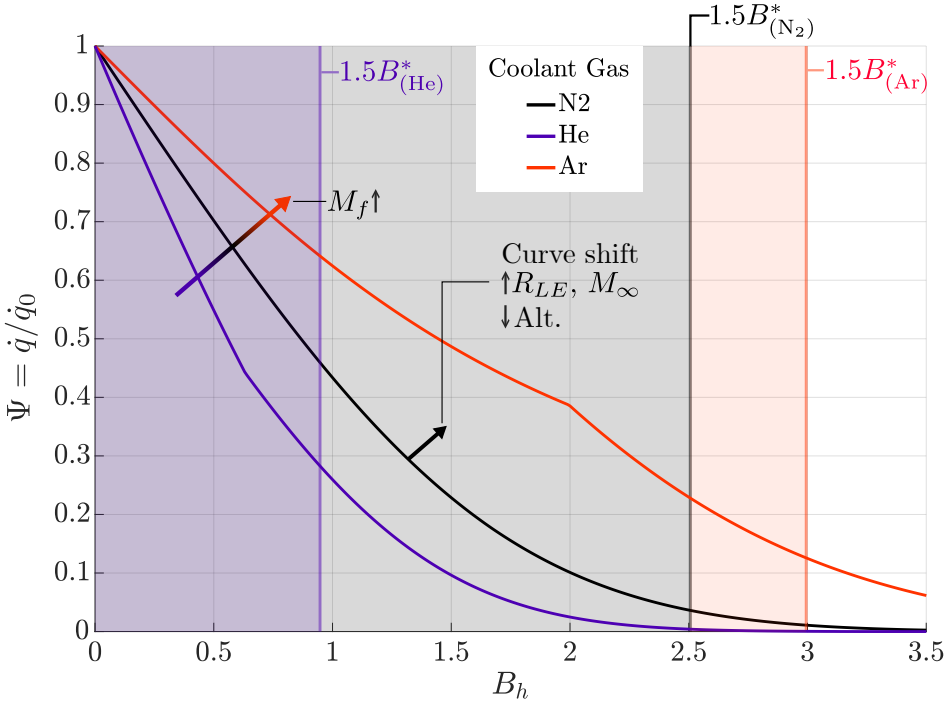


Figure 5.3: Curves of predicted flux reduction at the stagnation point against B_h for the three coolant gases. Data for $R_{LE} = 1$ mm at condition B. The direction of curve shift for other inputs is labelled in the figure, however the effects are small.

An array of cooling curves is presented in Appendix D.1, showing that the curves and onset of B^* are weakly sensitive to altitude, freestream Mach number and radius. Further discussion on the effect of input parameters for stagnation points is presented by Yoshikawa [29].

5.2.2 Geometry

The leading edge and downstream geometry was modelled as a 5-degree wedge, cylindrically blunted with leading edge radius R_{LE} between 1 and 25 mm. To compare the drag implications of leading edge cooling, the base length of an equivalent sharp 5-degree wedge was fixed and truncated according to the leading edge bluntness, as sketched in Figure 5.4. Simulations were performed for a leading edge at zero pitch and yaw, and could therefore be modelled as a 2D planar half-body. Transpiration cooling was applied only at the blunted leading edge.

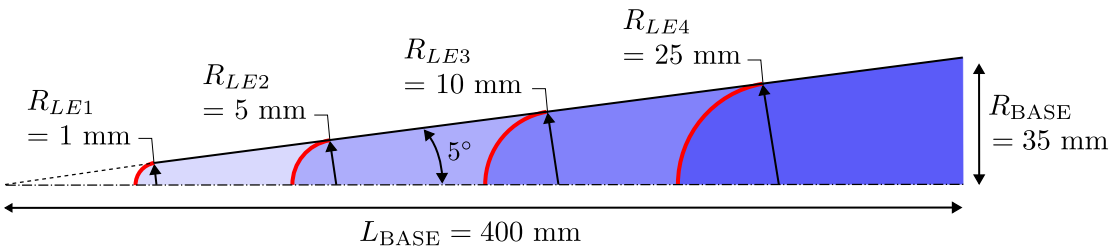


Figure 5.4: Sketch of the leading edge geometry definition for the numerical tests, with base dimensions set by an idealised sharp wedge. The leading edge injection region is highlighted in red.

5.2.3 Boundary Conditions

A sketch of the domain with labelled boundary conditions is shown in Figure 5.5 and described in Table 5.2. The inflow boundary shape, BC1, was obtained by a shock-capturing approach: the shock shape was obtained by an initial inviscid shock-fitted solution; this shape was displaced outward and used as a supersonic inflow boundary in the subsequent viscous domain. This approach provided an initial solution to the viscous steady-state solver and ensured a high-quality shock-aligned grid without the extra computational cost of a moving mesh. A boundary

displacement of $0.7\Delta_{SP}$ (where Δ_{SP} is the stagnation point shock standoff) was applied, to avoid intersection of the shock and inflow boundary and to provide space in the domain for boundary layer formation.

The mass flux boundary condition (BC3) set a prescribed mass flux, implemented as a 5th-order polynomial over the surface coordinate to maintain a smooth distribution. The calculation of the target mass flux distribution is discussed below in the next section. A description of the implementation of the mass flux boundary condition is provided in Appendix B.1, based on the work by Ewenz Rocher [109].

Table 5.2: List of boundary conditions labelled in Figure 5.5.

BC1	Supersonic inflow
BC2	Symmetry
BC3	Mass injection, no-slip
BC4	No-slip
BC5	Supersonic outflow

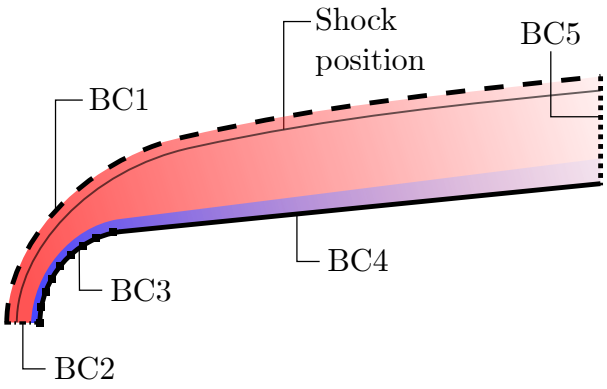


Figure 5.5: Sketch of the domain shape and annotated boundary conditions for the Eilmer simulations. Sketch not to scale.

5.2.4 Solver Settings

The primary settings of the simulation are listed in Table 5.3, and are discussed in the text below.

Table 5.3: Key Eilmer settings used in this numerical work.

Flow characteristic	Assumption
Mass injection distribution	Constant blowing parameter
Timestepping	Steady state
Turbulence model	Laminar
Wall temperature	Cold wall, 300K
Chemical reactions	Chemically reacting, 5 species air, 1 temperature
Diffusion model	Fick's First Law using binary coefficients

Mass injection distribution

It is more meaningful to target regions of high heat flux with greater coolant flow rates: heat flux tapers off quickly around the curvature of the leading edge [116], and so coolant mass flux should decrease around the surface. It is therefore important to distribute the local mass flux in a targeted manner that still provides reproducible local heat flux reduction. In this study, B_h was used to set the mass flux as it scales directly with heat flux. Originally defined for a stagnation point, B_h along the injector surface was defined using local flow properties, shown in Equation 5.9, where s is the local surface coordinate.

$$B_h(s) = \frac{F(s)}{St_0(s)} = \frac{\dot{m}_c(s) \cdot (h_{aw}(s) - h_w)}{\dot{q}_0(s)} \tag{5.9}$$

Leading edge simulations without cooling were carried out first, to find the uncooled surface heat flux and boundary layer properties. These variables were required to convert a target B_h to a mass flux distribution. The calculated mass flux was then implemented into the corresponding cooled simulation. Figure 5.6 shows an example uncooled heat flux distribution and the calculated mass flux for a 1 mm leading edge at condition B. As with the cooling curves in Figure 5.3, freestream and geometry input parameters affect the mass flux distribution with varying sensitivities. Additional mass flux distributions are provided in Appendix D.1, to highlight the effect of these each input parameters.

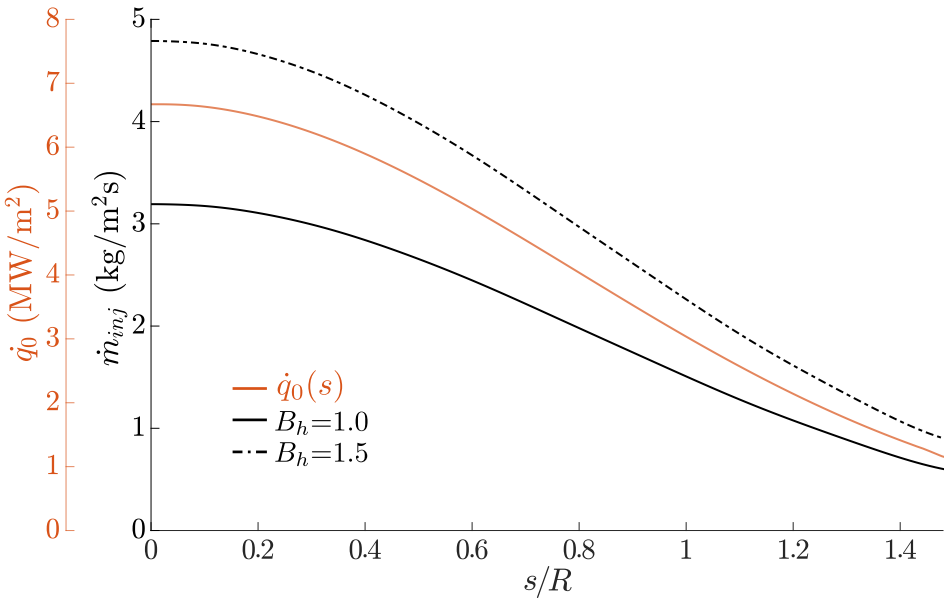


Figure 5.6: Prescribed mass flux distributions calculated from the results of the uncooled simulations at condition B, $R_{LE} = 1$ mm.

Laminar flow

A turbulent boundary layer encourages mixing of the hot post-shock gas with the coolant, limiting the effectiveness of transpiration cooling. In the previous chapter, experiments that were conducted at similar Mach and Reynolds numbers to the present study showed no evidence of transition, and laminar CFD followed the measured heat transfer. The effect of transpiration cooling on transition onset for cylindrically or spherically blunted bodies remains an area of active research [67].

Steady state solver

A Newton-Krylov method was utilised in Eilmer to accelerate the convergence of the solution to the steady state. A short description of the numerical implementation may be found in Appendix B.1, and further reading can be found in [146].

Wall Temperature

The injector was considered to be in local thermal equilibrium, assuming cold injection gas and a cold wall. Modelling of a hot wall and cold coolant would require modifications to the Eilmer code, outside of the current scope.

Chemical reactions

A thermally perfect 5-species air model (N_2, O_2, NO, N, O) was used for the calculations in this study. Reaction rate coefficients were determined using the scheme of Gupta et al. [25], and chemical source terms were evaluated via a finite-rate chemistry model. Thermodynamic and transport properties for each species were obtained via curve-fits from the NASA Glenn thermodynamic database [165]. Mixture thermodynamic state variables were computed using mass fraction-weighted averages, and mixture transport properties were calculated using the scheme devised by Gordon and McBride [166], which uses a modified form of Wilke's mixing rule. Diffusion was modelled by Fick's first law, with coefficients computed through binary collision integrals for each species pair. These calculations were all performed internally by Eilmer.

5.2.5 Mesh Independence

A mesh independence study was carried out to ensure that the domain was sufficiently discretised to capture the flow physics, while avoiding excessive refinement that would lead to unnecessary computational cost. A full description and set of results of the mesh independence study is provided in Appendix B.2, a short description of which is provided below.

Domain size scaled approximately linearly with radius, making it the primary factor affecting mesh requirements. While freestream and blowing conditions caused minor domain variations, these were considered negligible compared to the radius effect. Mesh independence studies were therefore conducted only for radius variations at freestream condition B (highest $Re_{u,\infty}$), with convergence assessed using surface heat flux and wall cell Reynolds number. The resulting mesh parameters for each radius are shown in Table 5.4.

These mesh parameters were then applied to all freestream and blowing conditions for each respective radius. While each simulation required unique mesh generation due to slight domain shape variations from shock fitting, the underlying resolution parameters were held constant for a given radius.

In the table, parameter β is a cell stretching parameter defined by Roberts [147], which increases cell density towards a specified boundary as β approaches 1. Figure 5.7 shows the body surface normal and tangential directions, η and ξ, as well as the cell clustering directions. Symmetric cell clustering in the ξ direction was employed to resolve the shock near the western boundary, and the boundary and coolant film layers at the eastern boundary.

Table 5.4: Selected mesh parameters for each domain size dictated by R_{LE}.

R_{LE} (mm)	n_{cells}	n_η	n_ξ	β_η	β_ξ
1	203k	450	450	1.001	1.01
5	203k	450	450	1.001	1.01
10	457k	676	676	1.001	1.01

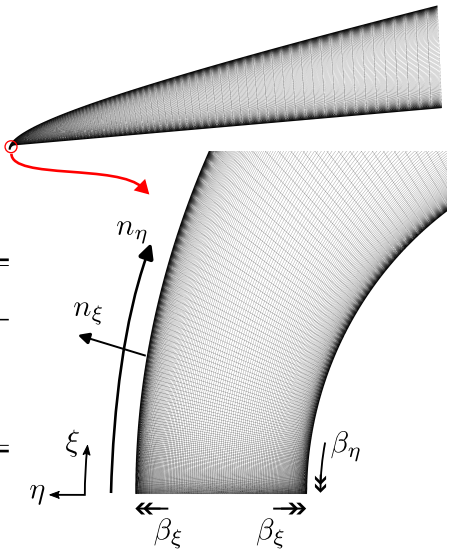


Figure 5.7: The selected mesh for $R_{LE} = 5$ mm following the mesh independence study. Annotations show the cell number (n) and clustering directions (β).

5.3 Aerodynamic Results

The results of this study are presented in two halves. In this first half, the effects of mass injection on the 2D flowfield and drag are considered. For brevity, selected conditions are presented below. For each plot below, additional data is presented in Appendix D. Each data point in this section is specified by the four input parameters: R_{LE}, coolant gas, B_h, and freestream condition in Table 5.1.

5.3.1 Flowfield

Contour plots of the 2D flowfield are shown in Figures 5.8 and 5.9 for the case of $R_{LE} = 1$ mm at freestream condition A, using nitrogen coolant at $B_h = 1$. In each figure, two contours are shown as mirrored half-bodies with corresponding colourmaps.

Figure 5.8 shows the static temperature and total enthalpy fields. In this study, an enthalpy boundary layer was specified with edge condition defined by Equation 5.10, where H_T and H_w are the total and wall static enthalpies respectively. The figure highlights the detected boundary layer as a blue line.

$$H(\delta) = 0.99(H_T - H_w) \tag{5.10}$$

Toward the stagnation region, Figure 5.9 shows the mass fraction of nitrogen and the static pressure with overlaid velocity streamlines. The effective body shape can be inferred from the dividing streamline just off the body surface, marked in the figure. The coolant contour shows that the dividing streamline occurs right at the diffuse edge of the coolant layer but the overall change in the 2D flowfield is small. The plot of nitrogen mass fraction also shows negligible changes in gas composition as the gas passes through the shock, indicating very small changes in chemical species within the heated shock layer, except at the coolant layer.

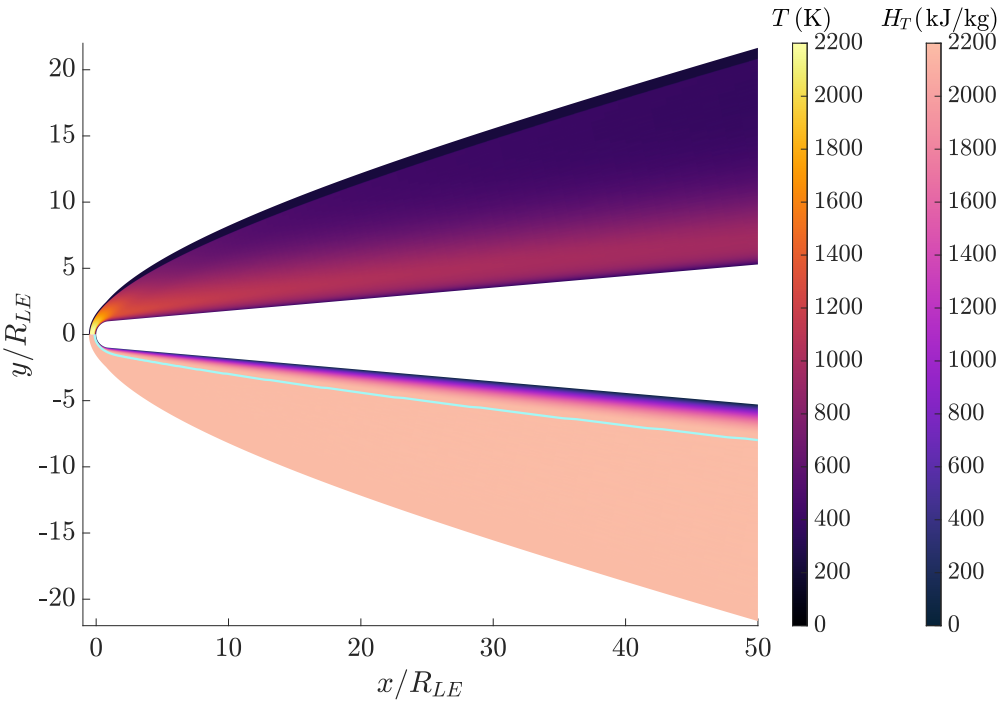


Figure 5.8: Contour plot of the temperature and total enthalpy fields. The detected boundary layer is highlighted in blue on the enthalpy field. $R_{LE} = 1$ mm, Cond. A, coolant: N_2, $B_h = 1$.

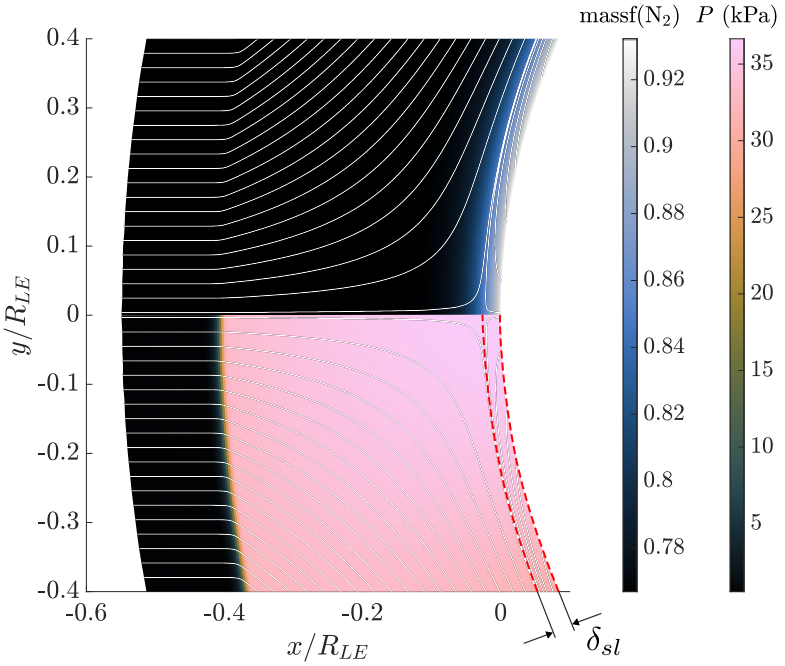


Figure 5.9: Contour plot of the nitrogen mass fraction and static pressure fields around the stagnation region. The velocity streamslines are overlaid in white. The formation of the dividing stream line offset from the body surface is marked in red, with thickness denoted δ_{sl}. $R_{LE} = 1$ mm, Cond. A, coolant: N_2, $B_h = 1$.

5.3.2 Shock layer and boundary layer thickness

Changes in boundary layer thickness provide insight into the flow gradients at the wall that dictate heat transfer and skin friction. Similarly, changes in shock layer thickness provide insight into changes in the pressure field that affect pressure drag. Using the boundary layer edge definition in Equation 5.10, and Eilmer's in-built shock-detector, the boundary layer and shock positions are shown below.

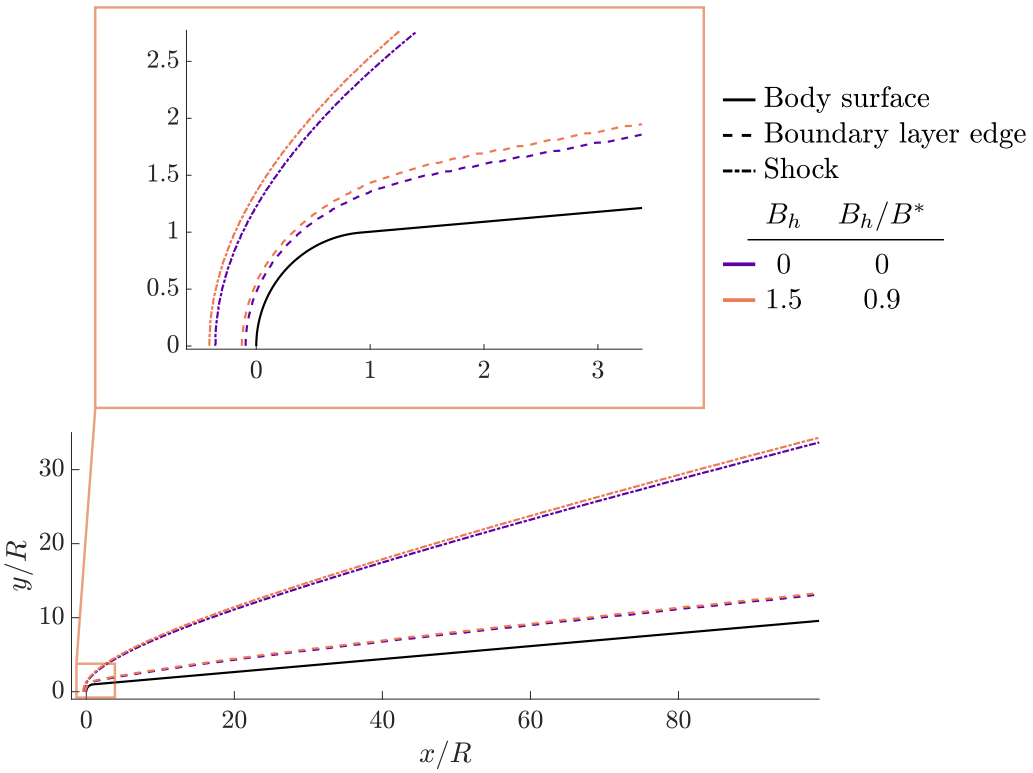
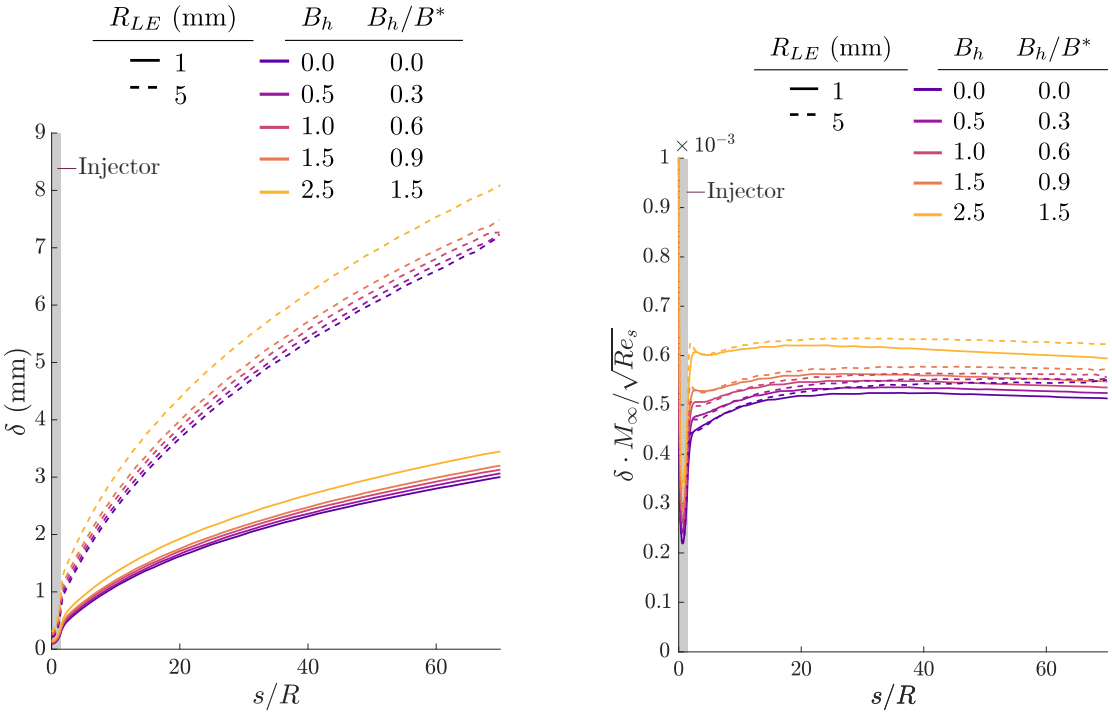


Figure 5.10: Detected shock and boundary layer shapes with and without blowing. Plot to scale. $R_{LE} = 1$ mm, Cond. A, coolant: N_2.

The boundary layer and shock layer thicknesses, measured in the surface normal direction, are shown in Figures 5.11 and 5.12.

Figure 5.11 shows that boundary layer thickness, δ, increases with leading edge radius and blowing parameter as expected. Normalising by the laminar compressible boundary layer growth rate factor, $\sqrt{Re_s}/M_\infty$, provides two key observations. Firstly, the curves for different R_{LE} collapse, indicating that boundary layer thickness scales linearly with radius while preserving its shape. Secondly, the

post-injection curves are governed by B_h but remain flat, suggesting that blowing linearly displaces the boundary layer without altering its growth rate. By looking further downstream of the injector ($s/R > 50$), the cooled boundary layers are permanently offset from the uncooled case. This would lead to a permanently reduced heat flux far downstream due to small thermal gradients, regardless of whether the coolant is still present.

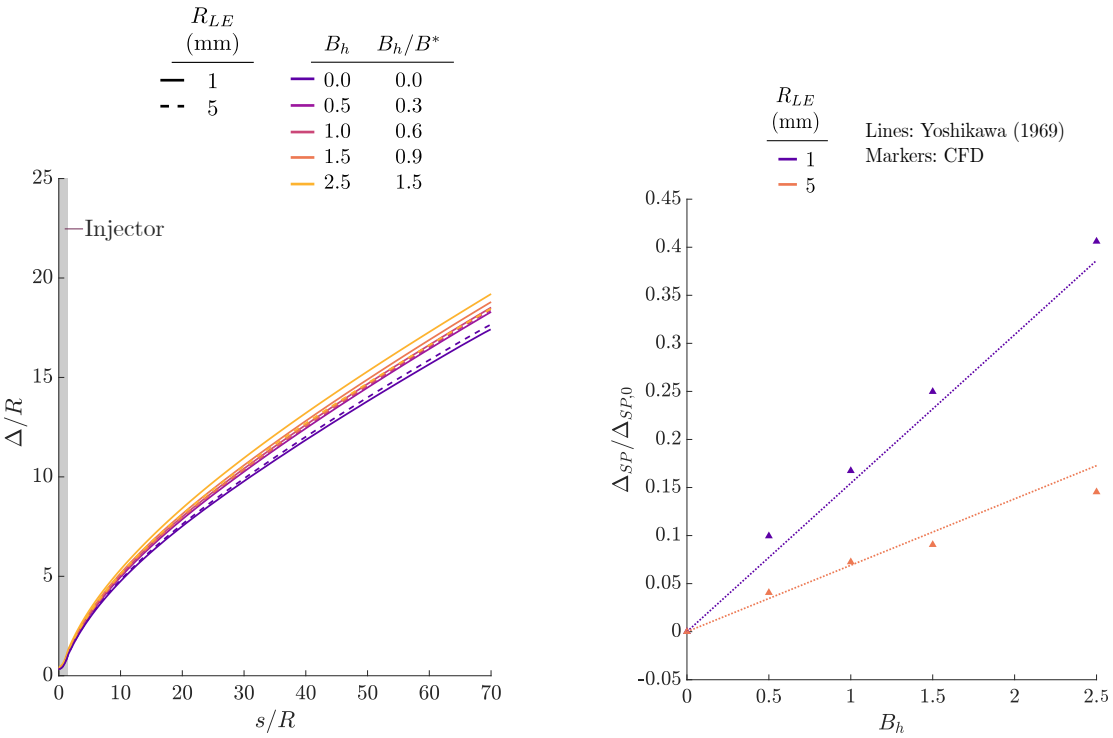


(a) Absolute BL thickness

(b) BL thickness normalised by laminar growth factor.

Figure 5.11: Boundary layer (BL) thicknesses for $R_{LE} = 1$ and 5 mm at condition A, coolant N_2.

Figure 5.12 shows that the effect of blowing on the shock layer thickness, Δ, is small. On the stagnation line, the shock standoff augmentation, $\Delta_{SP}/\Delta_{SP,0}$, is compared in Figure 5.12 to the semi-analytical prediction: Δ/Δ_0 in Equation 5.4e. The CFD and theory agree on the relative effects of B_h and freestream condition, however the accuracy of the semi-analytical theory here is not sufficient.



(a) SL thickness normalised by R_{LE}.

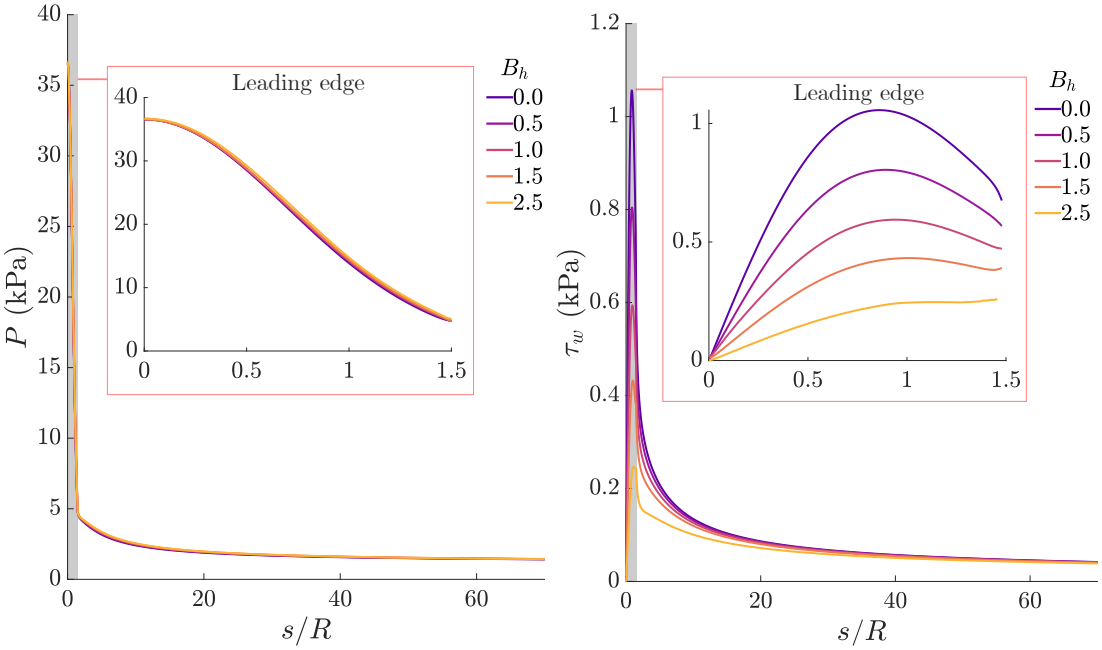
(b) Stagnation point standoff augmentation versus semi-analytical theory.

Figure 5.12: Shock layer (SL) thickness augmentation for $R_{LE} = 1$ and 5 mm at condition A, coolant: N_2.

5.3.3 Drag

If transpiration cooling increases leading edge drag to that of a larger-radius geometry (one that could instead use a simpler passive TPS), the aerodynamic benefit is negated while retaining the complexity of an active system. Although the present results are specific to the tested geometries and conditions, the trends offer insight into the relative aerodynamic impact of different blowing rates and radii relevant to flight.

Figure 5.13 shows the effects of B_h on pressure and skin friction at the body surface. Mass injection led to a slight increase in surface pressure, attributed to the modest shock layer thickening. Conversely, skin friction decreased, likely due to the thicker boundary layer and the diminished velocity gradients at the wall.



(a) Pressure (b) Skin friction

Figure 5.13: Distributions of surface pressure and skin friction for different B_h values. $R_{LE} = 1$ mm at condition A, N_2 coolant.

These distributions were resolved in the axial direction and integrated over the surface to obtain the drag contributions. Figure 5.14 shows the combined effect of radius and blowing in a stacked bar chart. The values here are normalised by the total drag of the uncooled 1 mm case, $D_{0,1\text{mm}}$, as a baseline. Axial momentum flux due to injection was included, however its contribution was negligible.

Figure 5.15 isolates the effect of blowing by normalising pressure and shear drag components by their uncooled equivalent. The normalised pressure drag is denoted $(D/D_0)_P$, and the normalised skin friction drag is denoted $(D/D_0)_\tau$. This is plotted as a line graph to more precisely examine the trends in pressure and skin friction drag.

In the bar chart (Figure 5.14), the dominant factor in drag variation was the leading edge radius: total drag increased by a factor of 2.2 from 1 mm to 5 mm, and by 7.7 from 1 mm to 25 mm. In terms of drag contributions, pressure drag contribution clearly dominates: for the 1 mm case without injection, pressure drag contributes around 85% of the total force. Pressure drag increases marginally with blowing. For the 1 mm case, the maximum range of blowing (from $B_h = 0$

to $B_h = 1.5B^*$) increases pressure drag by 3.5%. However, skin friction drag, despite contributing only 15% of total drag, dropped by nearly 45% due to blowing. In total, there is a decrease in drag by 1.4% over the maximum blowing range. Overall, it is clear that transpiration cooling, even past the boundary layer blow-off parameter, does not contribute to significant drag penalties.

In the line plot (Figure 5.15), pressure and shear drag augmentations are both reasonably linear for $B_h < B^*$. Past this limit, skin friction drag maintains this relationship, however pressure drag increases beyond the linear trend, indicating higher B_h may lead to more severe drag penalties more quickly.

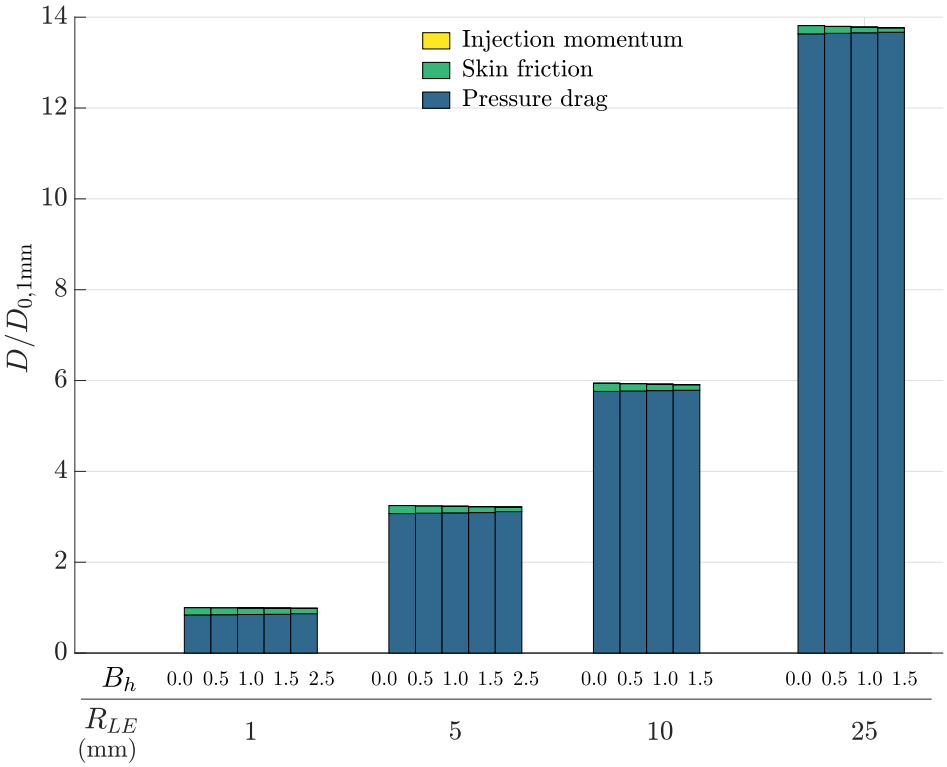


Figure 5.14: Drag contributions demonstrating the relative effects of B_h and R_{LE}. Values normalised by a baseline case of a 1 mm leading edge without cooling, $D_{0,1\text{mm}}$. N_2 coolant, freestream condition A.

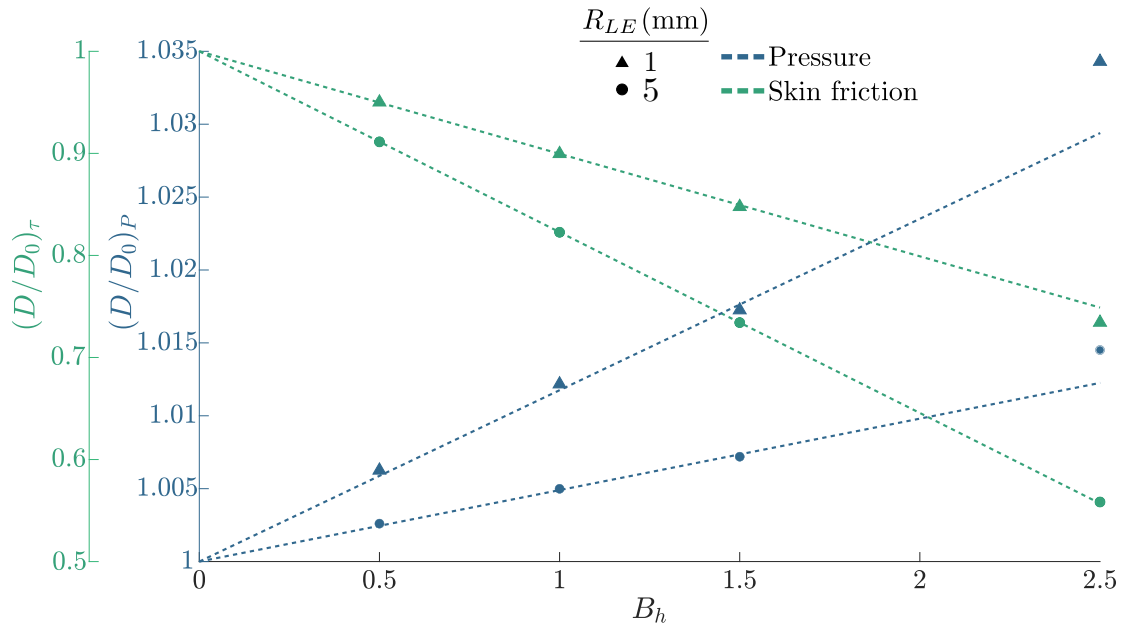


Figure 5.15: Relative effect of B_h on drag contributions: cooled drag normalised by uncooled drag for pressure and skin friction. N_2 coolant, freestream condition A.

5.4 Heat Flux and Concentration Results

In this second part of the results, key transpiration cooling parameters: heat flux and concentration are examined, with the intent to formulate semi-empirical correlations.

Once again, selected points are presented below with full datasets presented in Appendix D. Each test and result in this section is specified by the four input parameters: R_{LE}, coolant gas, B_h, and freestream condition in Table 5.1.

5.4.1 Leading edge heat flux

This section considers the effect of heat flux reduction on the leading edge, and how the data may be collapsed. To do this, results in this section are normalised by uncooled quantities (subscript 0) or cooled stagnation point quantities (subscript SP).

Figure 5.16 plots the simulated heat flux reduction at the stagnation point (markers) compared against Yoshikawa's correlation (lines) for a range of conditions, radii and coolants. These results show agreement to within 11%.

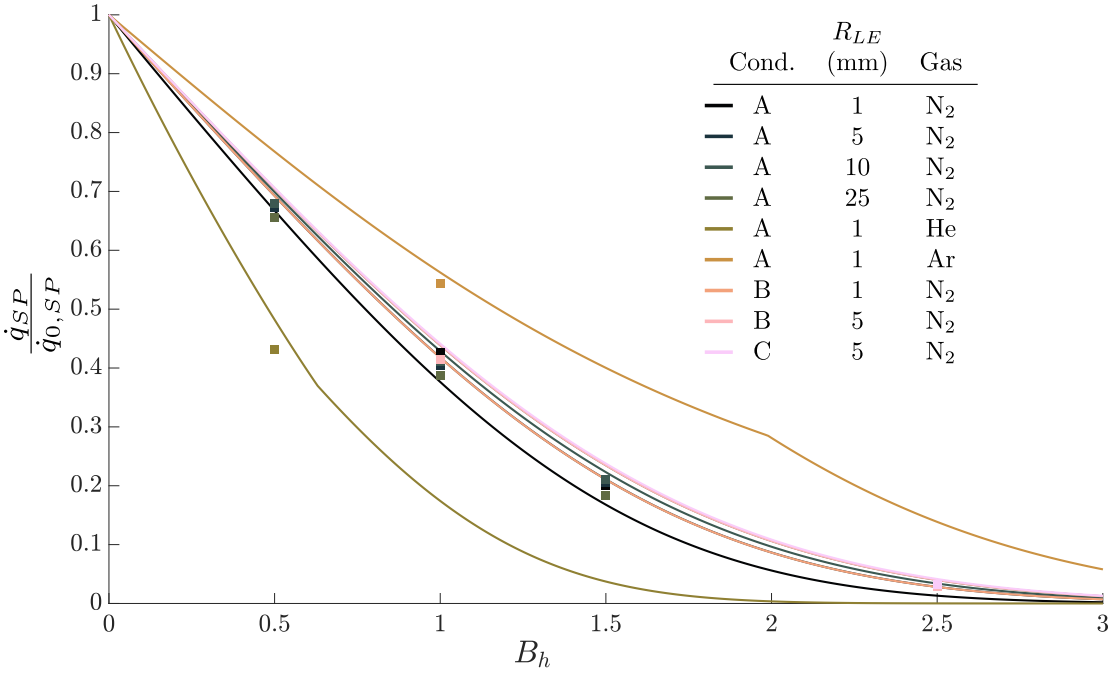


Figure 5.16: Stagnation point cooling compared to Yoshikawa's correlation (Equation 5.4) for a range of conditions.

This analysis was extended to the whole leading edge. Figure 5.17 shows cooled heat flux distribution, $\dot{q}(s)$, normalised by the cooled stagnation point heat flux, $\dot{q}_{SP}$. The figure shows that this collapses the cooled and uncooled distributions onto a single profile. For $B_h < B^*$, the mass flux corresponding to a constant local blowing parameter leads to a uniform heat flux reduction. This is shown explicitly as constant spatial distributions of $\dot{q}/\dot{q}_0$ showing uniform values in Appendix D.4. Thus, for $B_h < B^*$, heat flux on a leading edge injector can be reliably modelled for small radii by extending Yoshikawa's stagnation point correlation to the whole injector surface by using localised $B_h(s)$ as a correlation parameter.

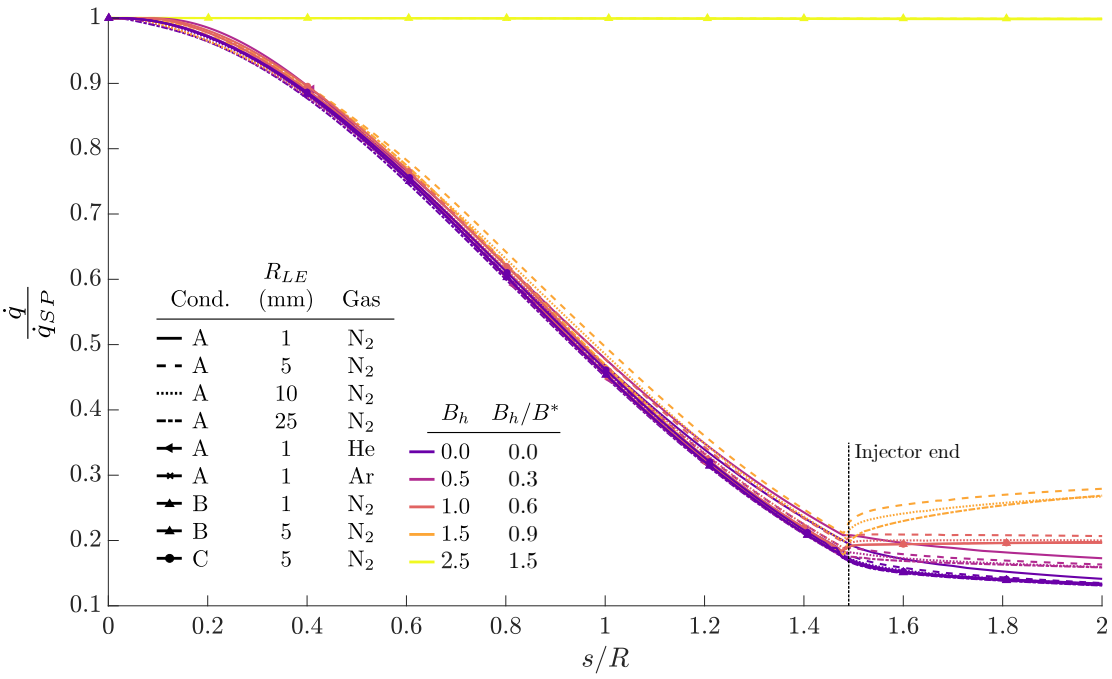


Figure 5.17: Heat flux distribution normalised by the cooled stagnation point for a range of input parameters.

For the high blowing ($B_h > B^*$) cases, while the stagnation point heat flux can still be reliably predicted by Yoshikawa's theory, the heat flux distribution changes from the lower blowing cases. Figure 5.17 shows that over the injector surface, absolute heat flux, rather than heat flux ratio, remains nearly constant.

Exceeding the boundary layer blow-off leads to a very thick coolant layer, where all points along the injector experience uniform coolant-layer conditions,

and therefore local heat transfer is driven to a nearly uniform value. In Chapter 4, it was shown experimentally that this behaviour does not destroy the laminar boundary layer. In both the current work and the previous experiments, it also does not lead to significant downstream pressure losses. Since injection is applied from the stagnation point, the boundary layer may instead form over the coolant film acting as a slightly modified body contour. This leads to the small pressure rise seen previously, rather than the sudden shape change associated with an already established boundary layer on a flat plate passing over an injector (see Figure 5.2).

5.4.2 Downstream Heat Flux Reduction

The thermal efficiency is re-stated below in Equation 5.11, where, $\eta_{th} = 1$ represents full film cooling (i.e. heat flux is zero) and $\eta_{th} = 0$ represents no film cooling (i.e. heat flux is equal to the uncooled heat flux; $\dot{q} = \dot{q}_0$). Figure 5.18 shows η_{th} for a range of B_h and R_{LE}.

$$\eta_{th}(s) = 1 - \frac{\dot{q}(s)}{\dot{q}_0(s)} \tag{5.11}$$

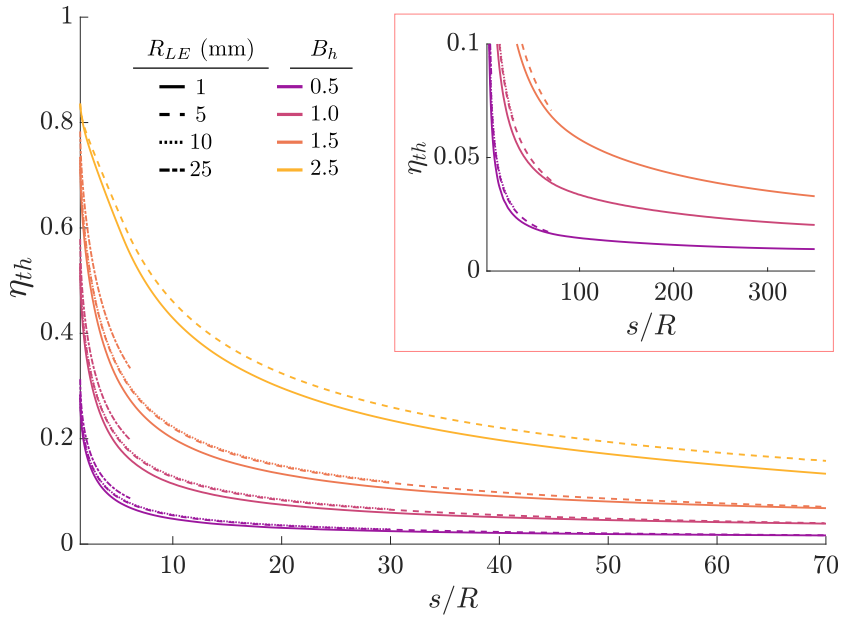


Figure 5.18: Downstream thermal efficiency, showing the effect of radius and B_h. The inset plot shows the film cooling persistence over $s/R \leq 350$ for $R_{LE} = 1$ mm at moderate B_h. Freestream condition A, coolant: N_2.

Immediately downstream of the injector, cooling effects rapidly decrease as the coolant dissipates. Far downstream, heat flux remained below that of the uncooled case even beyond the length of the domain. With reference to the effect of blowing on boundary layer thickness (Figure 5.11), it is possible that heat flux reduction far downstream of the injector is dominated by the constant offset in boundary layer height rather than residual foreign gas.

By considering the downstream region as an inclined flat plate, the film cooling correlation in Equation 5.6 was adapted to account for the injector shape and non-uniform mass flux. The updated correlation parameter is shown in Equation 5.12, using the coordinate system in Figure 5.19. In the correlation, $\overline{F}$ is the area-averaged blowing ratio, s is the surface coordinate, and $f(B_h)$ is an empirically-fitted quadratic function in B_h. The step-by-step approach of adapting the coordinate system from the flat plate to leading edge is presented in Appendix C.2.

$$\xi_{th} = \frac{f(B_h)}{\overline{F}w}\sqrt{\frac{s - s_0}{s_{\text{ref}}}\frac{s}{Re_{u,\infty}}} \tag{5.12}$$

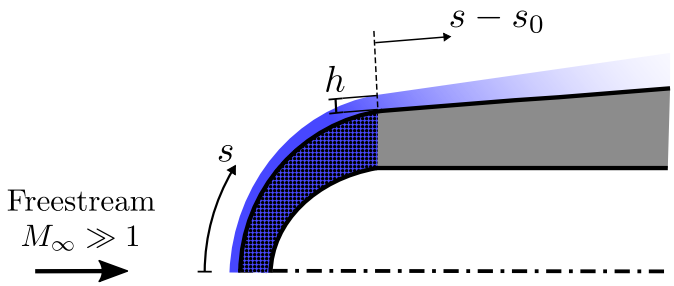


Figure 5.19: Coordinate system for the film cooling correlation over the leading edge in Equations 5.12 and 5.13.

Figure 5.20 shows the thermal efficiency decay data, $\eta_{th}(s)/\eta_{th}(s_0)$, collapsed by ξ_{th}. Equation 5.6 was fitted through a selected dataset ($R_{LE} = 1$ mm, $B_h = 1$, N_2 coolant at condition A) giving coefficients $a = 2.05$, $b = 0.0476$, $c = -0.907$. Figure 5.21 plots the correlation prediction in physical coordinates against the 5 mm dataset.

$$\eta_{th} = \eta_{th}(s_0)\ [1 + a\xi_{th}]^c + b \tag{5.13}$$

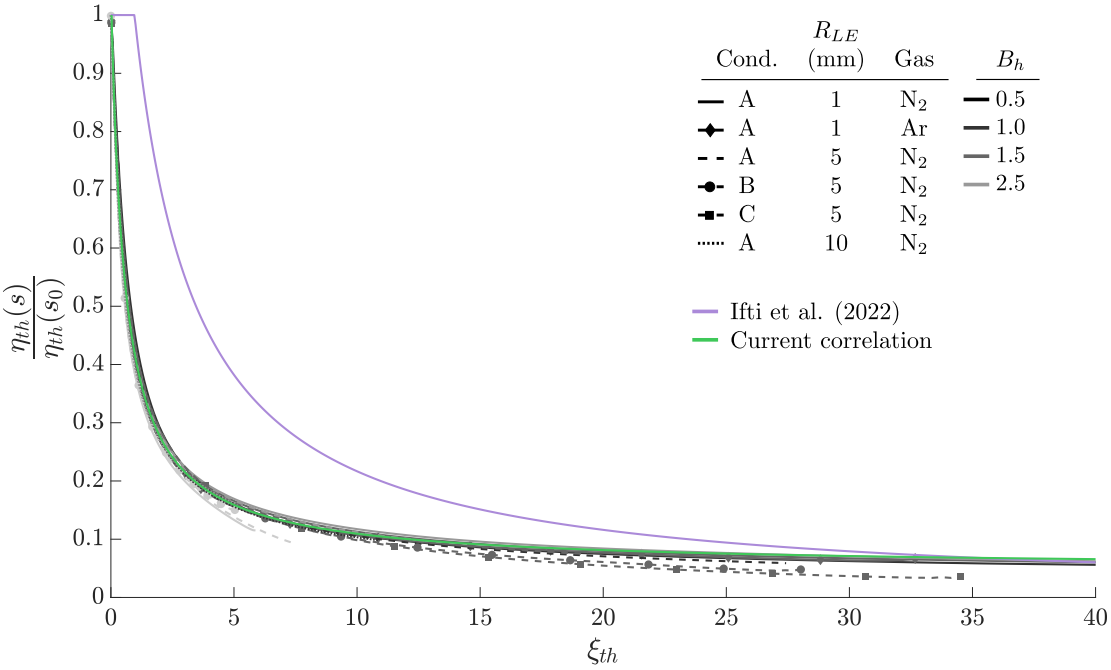


Figure 5.20: Normalised thermal efficiency against the correlation parameter, including a correlation curve fit, updated for the leading edge and compared to the original flat plate correlation.

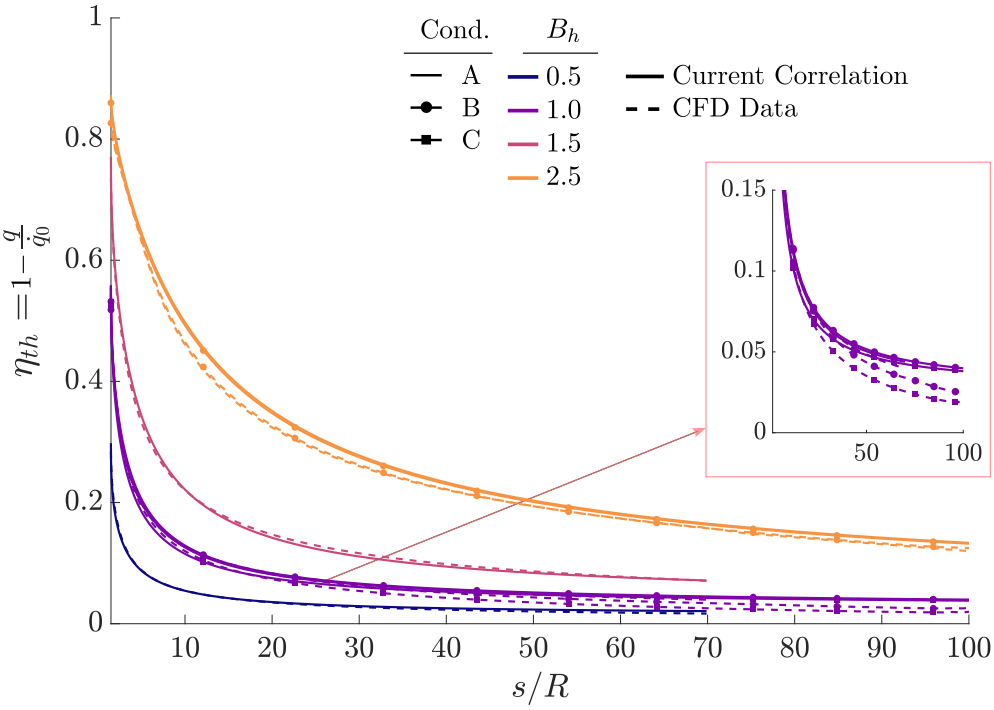


Figure 5.21: Comparison of spatial cooling distributions predicted by the current correlation and CFD data for a 5 mm leading edge using nitrogen coolant.

The correlation parameter plotted in Figure 5.20 accounts for varying radius, gas, and blowing condition well. However, there is more variation with freestream conditions.

When mapped to physical coordinates (Figure 5.21), the film cooling at condition A is well-predicted, where the correlation is within 8.7% of CFD data for $s/R < 40$ and within 12.0% over each domain. Even at high blowing ($B_h = 2.5$), the predicted cooling is still within this range, but is more systematically offset.

For conditions B and C, the correlation parameter captures the cooling behavior well for $\xi_{th} < 10$, but deviates at larger values ($\xi_{th} > 25$). In physical coordinates, accuracy is maintained within 10% only for $s/R < 27$, deteriorating to 80% deviation further downstream for moderate blowing. This degradation suggests that ξ_{th} does not fully capture the effect of freestream conditions on far downstream boundary layer thickening.

In general, the film cooling modelling was most accurate just downstream of the injector, where the heat flux is highest. For all cases except those with the highest blowing, the cooling efficiency had decayed to $\eta_{th}(s)/\eta_{th}(s_0) \leq 16\%$ by $s/R = 30$. Modelling the far downstream cooling is important for estimation of the heat loading and lateral conduction within the substructure. However, accurately modelling the heat fluxes close to the injector is more critical for a first-cut systems analysis.

5.4.3 Coolant Film Concentration

Characterisation of the inert coolant concentration at the wall provides further input to scenarios where the material oxidation can be mitigated through transpiration cooling [62]. By once more considering the downstream region as an inclined flat plate, Ifti's advection-diffusion model (Equation 5.8) for concentration was recast for a leading edge geometry. Equation 5.14 shows the modified concentration correlation parameter, ξ_c. Here, u_h is the coolant slug velocity. All other symbols are the same as in Equation 5.8.

$$\xi_c = \sqrt{\frac{u_h h^2}{4D_{12}(s - s_0)}} \tag{5.14}$$

In [110], a control volume analysis was used to establish the coolant layer height, assuming $u_h = u_e$. Figure 5.22 presents the numerical coolant concentration and velocity profiles across the boundary layer for nitrogen injection. By defining the coolant layer edge as 95% of the coolant concentration at the wall ($h = y(0.95C_w(s))$), it is evident that $u_h \neq u_e$ for most of the downstream region. However, the figure also shows that coolant layer height remains relatively independent of B_h, relative to the boundary layer thickness, consistent with the earlier finding that blowing linearly displaces the boundary layer. These results suggest that a control volume analysis remains applicable, but requires modification from the analyses in the literature.

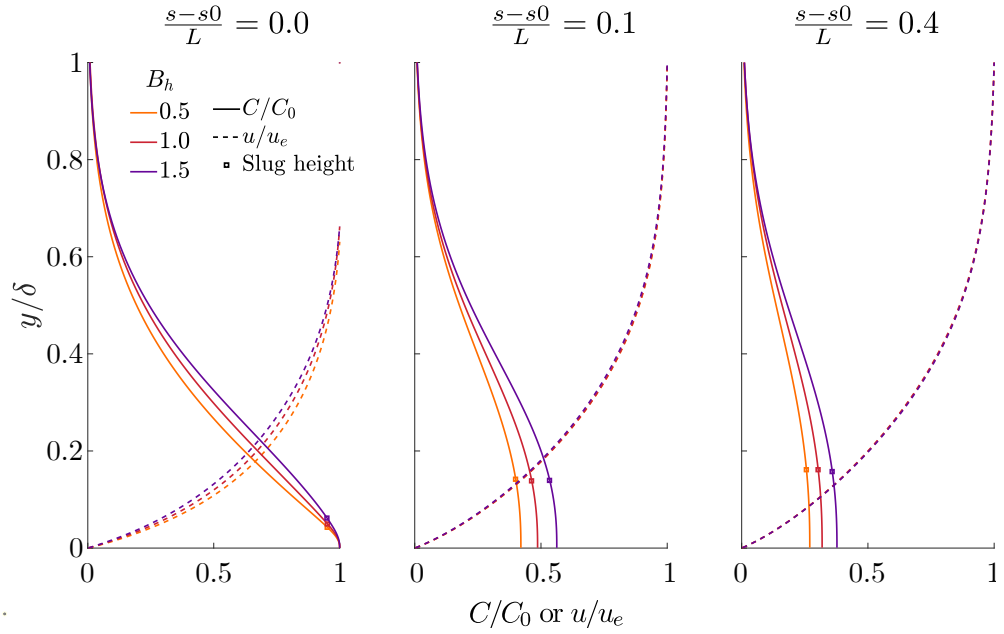


Figure 5.22: Concentration and velocity profiles within the boundary layer for B_h values at condition A, $R_{LE} = 1$ mm, N_2 coolant. The detected concentration-based coolant slug height and the corresponding slug velocity are also shown.

Figure 5.23 shows the concentration efficiency decay, $\eta_c(s)/\eta_c(s_0)$, plotted against correlation parameter ξ_c for nitrogen coolant at condition A. The effect of R_{LE} and B_h collapse reasonably well. A curve fit of the form shown in Equation 5.15 was fit to the data of the 1 mm, $B_h = 1$ case. The coefficients were found to be $p = 1.69$, $q = 0.206$, and $r = 5.07$.

$$\eta_c = \eta_c(s_0)\left(\text{erf}(p\xi_c{}^q)\right)^r \tag{5.15}$$

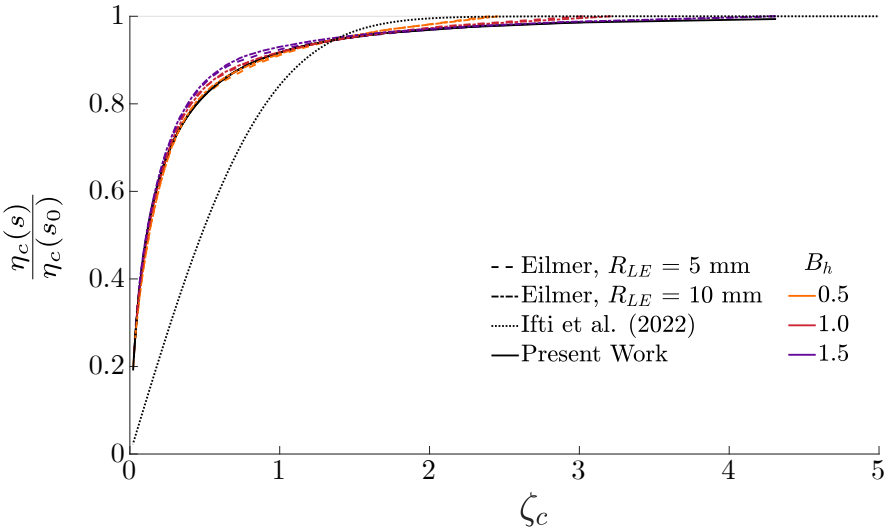


Figure 5.23: Concentration parameter versus film concentration efficiency for cases $R_{LE} = 5$, 10 mm.

Figure 5.24 shows the application of Equation 5.15 to predict the concentration efficiency in spatial coordinates. This prediction is compared to the CFD data for the 5 & 10 mm datasets. These results show that, as with flat plates, a modified advection-diffusion model remains valid for laminar film cooling downstream of a leading edge. To complete the surface concentration model, coolant concentration buildup over the injection surface would need to be modelled, which can also be used to inform the downstream concentration efficiency.

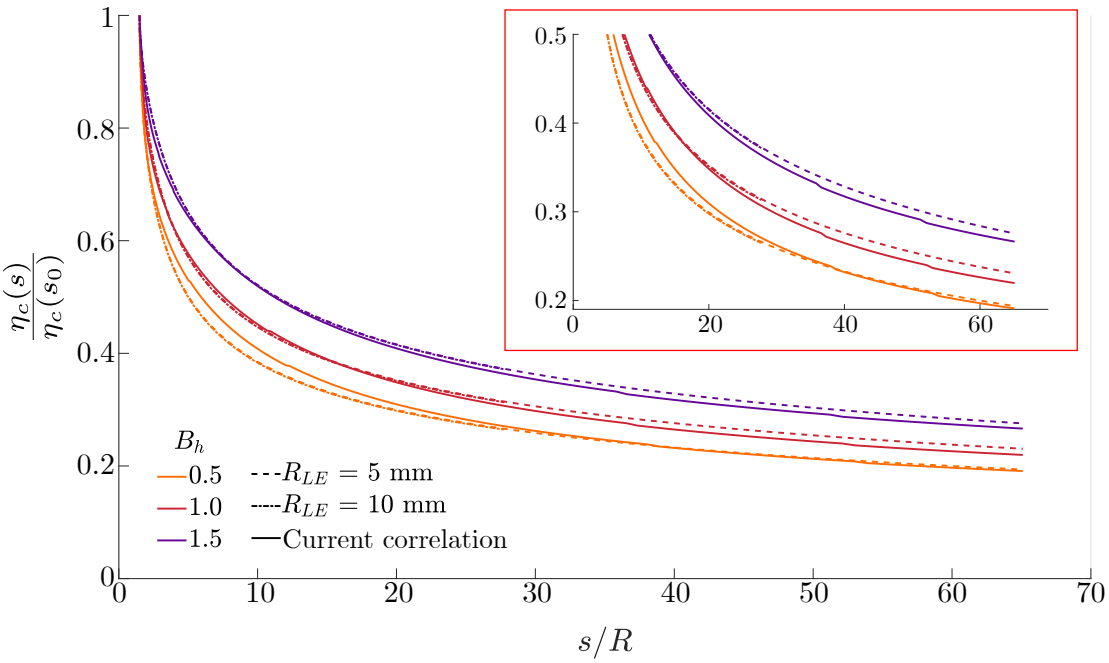


Figure 5.24: Film cooling concentration efficiency parameter versus surface coordinate for $R_{LE} = 5$, 10 mm.

5.5 Conclusion

Numerical simulations were carried out on a leading edge under hypersonic flow conditions with distributed transpiration cooling to model the trade-off between drag and cooling effects due to moderate blowing parameters and varying radii. Overall, the results indicate that transpiration cooling improves the survivability of sharper leading edges for sustained hypersonic flight by significantly reducing incoming heat flux without negating the aerodynamic advantage of the small radius, even for blowing conditions past the boundary layer blow-off parameter.

Simulation-informed correlations of heat flux reduction were formulated to predict the cooling performance for a range of freestream conditions, radii and coolant gases. Correlations for fundamental geometries (flat plates and stagnation points) were modified and extended for the leading edge injector.

A list of the adapted heat flux models is provided in Table 5.5, along with input parameters. Due to the normalisation of parameters, the calculation is carried out in a cascade, presented in row-order in the table. While the correlations

formulated in the table were formulated from the numerical results, they can be applied independent from CFD input[2].

Table 5.5: List of adapted models used in assembling a full heat flux model of leading edge transpiration cooling. SP: stagnation point, LE: leading edge, DS: downstream (of the injector).

Region	Cooling	Correlation	Inputs
SP	Uncooled	Fay-Riddell	M_∞, alt., R_{LE}, T_w
LE & DS	Uncooled	Lees	External geometry
SP	Cooled	Yoshikawa	$\dot{m}_{\text{inj},SP}$, coolant gas
LE	Cooled	Yoshikawa (extended)	$\dot{m}_{\text{inj}}(s)$
DS	Cooled	Heufer-Olivier: ξ_{th}	—

Figure 5.25 shows the full heat flux modelling implementation for select conditions. The modelled heat fluxes are within 9.8% of the numerical data over the leading edge. Downstream, errors rise to 20% for $s/R < 20$ and 30% for $s/R < 30$. By this point, the heat flux is already $< 4\%$ of that at the stagnation point: the most accurate part of the model is therefore in the regions of highest heat flux. The increasing downstream error reflects the cumulative effect of earlier correlation stages, each with local errors of 10–20%.

Since the correlations were focused on cooling toward the leading edge, the far downstream boundary layer thickening was not fully captured at high blowing parameters and at secondary freestream conditions. Further work may aim to incorporate the far downstream cooling behaviour into the modelling to account for these effects.

[2]The current calculation is independent of CFD data, however high fidelity CFD data may also be inserted at any stage to enhance accuracy.

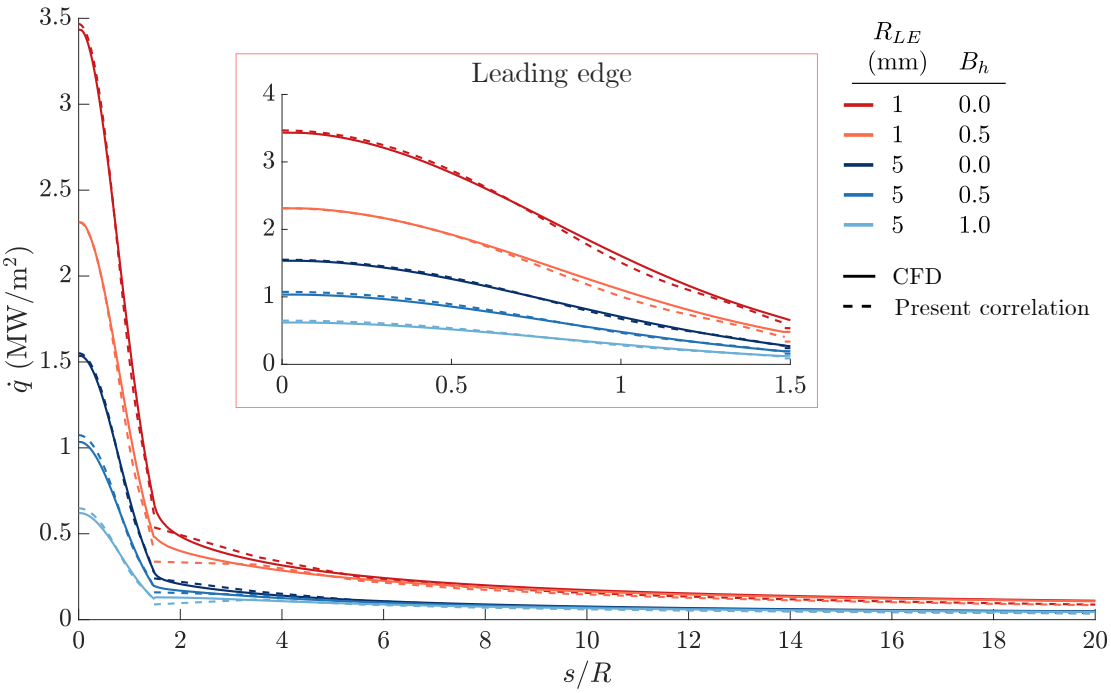


Figure 5.25: A comparison of modelled and CFD heat flux distributions of transpiration-cooled leading edges at freestream condition A with N_2 coolant. The semi-empirical models used are presented in Table 5.5.

Finally, the coolant concentration decay was modelled downstream of the injector. It was shown that the diffusion-advection model of coolant in a laminar flow was valid using correlation parameter ξ_c. However, further work is required to decouple the model from CFD data to obtain inputs for the coolant film velocity and height. The results showed that the coolant film linearly displaces the boundary layer, meaning that a control volume analysis may be applied to estimate the coolant layer height and velocity.

CHAPTER 6

Performance of a Transpiration Cooled Leading Edge

6.1 Introduction 151

6.2 Study Setup 158

6.3 Model Setup 163

6.4 Passive TPS Results 170

6.5 Transpiration Cooling Results 172

6.6 The Effect of Input Parameters 177

6.7 Further Constraints 183

6.8 Conclusion 188

Preface

The validated correlations and design tools developed in the previous chapters are brought together in the final results chapter of this thesis. A numerical tool was developed to assess the feasbility of employing leading edge transpiration cooling to a vehicle in steady flight. Aerothermal limits of the system were implemented to assess possible steady flight corridors, and the thermo-structural limits and coolant budgets are briefly discussed.

The majority of this chapter is comprised of a conference paper published at the International Conference on High-Speed Vehicle Science and Technology (HiSST) [53] and has since been revised with updated simulation and analysis methodology.

Author Contributions

- Raghul Ravichandran: Conceptualisation, numerical design, investigation, analysis, and writing.
- Luke Doherty: Supervision as secondary supervisor and funding assistance.
- Matthew McGilvray: Supervision as principal investigator and funding acquisition.

Acknowledgements

This work was funded by DSTL.

6.1 Introduction

6.1.1 Background

Mitigating intense surface heat fluxes and accumulated thermal loading is a key challenge in hypersonic vehicle design. At the same time, reducing leading edge bluntness to improve lift-to-drag ratio (L/D) for steady cruise [8], glide [12], and manned atmospheric entry [9] has been investigated. These aerodynamic improvements, however, come with increased thermal loads, as sharper leading edges significantly raise heat flux [17]. A TPS for sharp leading edges must therefore balance aerodynamic performance with thermal protection.

Figure 6.1 shows the cold wall stagnation point heat flux and heat load of historical missions, alongside estimates for a generic glide trajectory at varying R_{LE}. High heat flux, short-duration missions typically use ablative systems, which lack reusability and shape stability. Additionally, ablative TPS mass fraction increases linearly with heat load [18], reaching up to 50% for the Galileo probe. In contrast, low heat flux, long-duration missions favour passive systems. Silicon carbide ceramic matrix composite (C/C-SiC) is a passive TPS candidate material, due to its high heat capacity and operating temperature [8]. These systems are effective in steady flight, where the incoming heat flux can be balanced by re-radiation from the hot structure. However, active oxidation of the SiC matrix can lead to material degradation and loss of mechanical strength [63].

For applications where heat fluxes are too high for passive systems, and ablative systems cannot provide reusability or shape stability over the whole mission, an active TPS could be employed in a targeted manner. The volume, mass, and complexity penalties of active systems add further constraints to the existing aerodynamic and thermal trade-off.

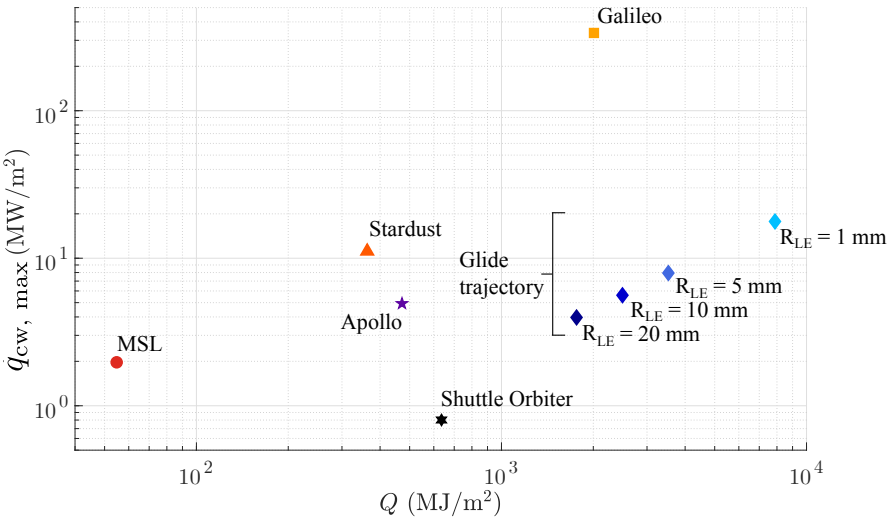


Figure 6.1: Peak cold wall stagnation point heat flux and heat loads of historical missions [17, 26–28] versus that of a generic glide trajectory [11] with different R_{LE} values.

Transpiration cooling is a promising candidate where coolant is injected through a permeable wall into the boundary layer, sketched for a leading edge in Figure 6.2. Protection is achieved via three simultaneous mechanisms:

1. Temperature reduction through internal convective heat transfer between the hot porous matrix and the coolant gas as it flows through the porous matrix.

2. As the coolant gas is swept downstream, the coolant film over the vehicle surface reduces thermal gradients and therefore heat flux.

3. The inert coolant film forms a chemical protection barrier, reducing catalytic wall heating effects and delaying material oxidation.

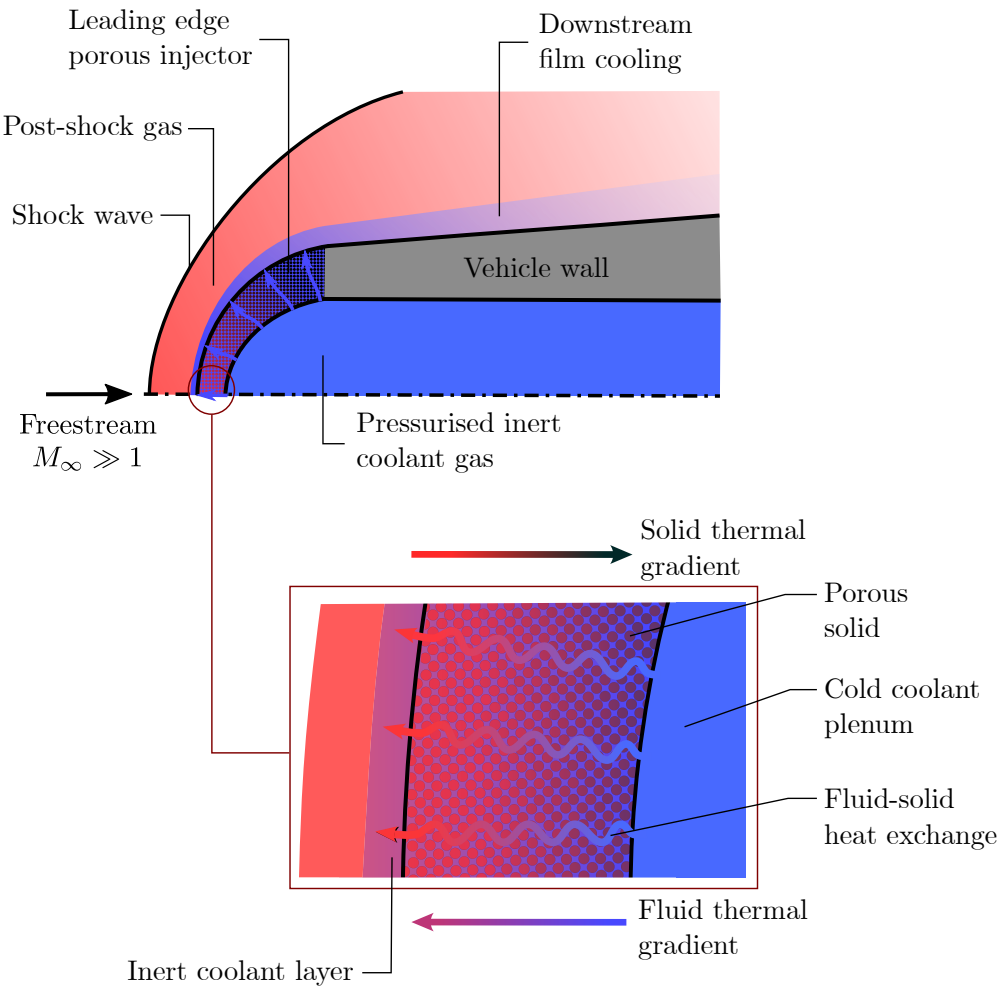


Figure 6.2: A sketch of a transpiration-cooled leading edge.

This study aims to model the combined effect of the first two of these mechanisms to understand how they may enable reusable or long duration cruise. This requires an understanding of the modelling of porous flows, internal convective heat transfer, and external heat flux blocking.

The flow of coolant through a fully saturated porous medium in one dimension is described by the Darcy-Forchheimer equation (Equation 6.1. The resistance of mass flux to the driving pressure is dictated by viscous ($\frac{\mu}{k_D}u$) and inertial ($\frac{\rho u}{k_F}u$) effects, where P, μ, ρu and u are the local coolant pressure, viscosity, mass flux and velocity respectively, and k_D and k_F are the Darcy and Forchheimer coefficients.

$$-p\frac{\mathrm{d}P}{\mathrm{d}x} = \frac{\mu}{k_D}u + \frac{\rho u}{k_F}u \tag{6.1}$$

This may be integrated from the internal to external surface for the isothermal case:

$$\frac{P_{\text{int}}^2 - P_{\text{ext}}^2}{2P_{\text{int}}L} = \frac{\mu_{\text{int}}}{k_D}u_{\text{int}} + \frac{\rho_{\text{int}}u_{\text{int}}}{k_F}u_{\text{int}} \tag{6.2}$$

In uniformly sintered porous materials, k_D and k_F may be treated as scalar values representing isotropic permeabilities [33]. Porous ceramic matrix composites (CMCs) often exhibit anisotropic permeabilities corresponding to fibre layup directions, leading to undesirable non-uniformities in the mass flux distribution [35, 36].

As the coolant flows through the hot porous matrix, thermal energy is transferred from solid to fluid which is characterised by the volumetric heat transfer coefficient, h_v. The temperature-dependent coolant viscosity, $\mu(T_c)$, in Equation 6.1 means that locally elevated coolant temperatures reduce local mass flux, a phenomenon known as *viscous blockage*. While an analytic solution for 1D non-isothermal flow was developed by Langener et al. under specific assumptions [38], the 2D case in this study is solved using a finite difference approach.

Previous work in Chapter 5 has developed a thermal model for heat flux reduction for a transpiration-cooled leading edge. This model estimates cooled and uncooled heat fluxes over the leading edge geometry using semi-empirical correlations derived from a sweep of numerical data, with the numerical method validated in high-speed wind tunnel tests. The model is discussed briefly below, detailed mathematically in Appendix C.3.

Cooling over the injector was correlated using the local non-dimensional mass flux parameter, B_h, which is defined as the ratio of uncooled Stanton number, St_0 to blowing ratio, F. These parameters are shown in Equations 6.3 to 6.5.

$$B_h = \frac{F}{St_0} \tag{6.3}$$

$$F = \frac{\rho_{inj}u_{inj}}{\rho_\infty u_\infty} \tag{6.4}$$

$$St_0 = \frac{\dot{q}_0}{\rho_\infty u_\infty (h_{aw} - h_w)} \tag{6.5}$$

The model uses correlations from Yoshikawa [29] and Heufer & Olivier [98], which have been employed for a range of other experimental and numerical transpiration cooling studies [31, 66, 70, 92, 93]. The model, detailed in Appendix C.3, was formulated using data for $B_h < 1.5B^*$ which was used as the system limits in this study. B^* is a *boundary layer blow-off* parameter, used to indicate where injected coolant displaces the boundary layer, changing the heat flux behaviour. Exceeding this parameter can lead to significant drag penalties [92] or boundary layer transition, but it has been shown that this does not necessarily occur at B^* exactly.

6.1.2 Distributed Mass Injection for Leading Edges

The spatial variation in heat flux along the leading edge requires a corresponding distribution of coolant mass flux, with maximum injection at the stagnation point where the heat flux is highest. Therefore, achieving a targeted mass flux distribution requires control of the porous flow.

Previous efforts to design leading edge injectors for achieving target mass flux distributions have been limited to numerical studies. Hermann et al. [87] used multiple plenums to reduce thermal stresses in ultra-high temperature ceramic (UHTC) leading edges, while Dickstein et al. [34] varied tungsten permeability to direct liquid water coolant toward high-flux regions. These studies considered 5-degree half angle wedges with leading edge radii $R_{LE} = 1$ to 10 mm, porous wall thicknesses from 0.4 to 2.8 mm, and material permeabilities of $k_D = 10^{-10}$ to 10^{-8} m^2, $k_F = 10^{-8}$ to 10^{-7} m.

6.1.3 Existing Systems Models

Although many transpiration cooling studies have investigated fundamental geometries, only two numerical tools have been developed to assess the performance of transpiration-cooled vehicles. These studies are described below, and compared to the present work in Table 6.1.

Böhrk et al. [49], developed a finite-difference code, HEATS, to calculate the mass flux requirements of a constant-thickness, transpiration-cooled flat plate

in the context of the flight experiment, SHEFEX-II [45]. The solid-fluid thermal exchange equations were formulated by Glass et al. [41] and solved in HEATS using a 2D finite difference formulation. When compared with the SHEFEX-II flight data, agreement of transient wall temperature was within 14%.

Hermann et al. [113] derived thermal impulse responses to the heat balance for rapid temperature calculations of blunt bodies and flat plates. The code, PIRATE, discretised the porous injector domain into slices to calculate the heat transfer and porous flow in 1D. For steady state calculations on a conical nosetip with radius $R_{LE} = 0.5$ m, transpiration cooling was shown to be beneficial for velocities of 5.5 to 8 km/s and altitudes of 30 to 55 km [57].

Both models employed semi-empirical correlations for aerodynamic heat flux, and for transpiration cooling. To avoid triggering boundary layer transition, they both also used the blowing ratio as a mass flux limit, detailed in the table below. PIRATE also implemented a limit $Re_{u,\infty} < 5 \cdot 10^5$ to avoid turbulent flow regimes. For flat plate calculations, both models considered porous flow in one dimension. For the blunt body calculations in [57], PIRATE prescribed the surface mass flux.

Previous studies have largely examined either system performance, or injector design, but not both simultaneously. This study aims to develop an injector design methodology to be used in a systems performance study. In sharp leading edges, the injector wall thickness is comparable to the radius, leading to non-negligible fluxes in the surface tangential (lateral) direction. Therefore, the heat transfer and porous flow must both be treated in 2D, and the injector architecture must be explicitly considered to distribute the coolant mass flux. To achieve this, a numerical finite-element tool: ***P****orous flow and* ***H****eat transfer* ***I****n* ***L****eading edges* (PHIL) was developed.

Table 6.1: Comparison of existing numerical tools for assessing transpiration-cooled vehicles, including the present work.

	HEATS [49]	PIRATE [113]	PHIL (Current work)
Solid and fluid temperature	Finite diff. (2D)	Impulse response (1D)	Finite elem. (2D)
Porous flow	1D	1D	2D
Geometries	Flat plate	Blunt body, flat plate	Blunt body
Heat flux	van Driest [111, 112]	van Driest [111, 112] Fay & Riddell [115] Lees [116]	Fay & Riddell [115] Lees [116]
Injector cooling	Conduction model	Kays [114]	Yoshikawa [29]
Film cooling	Goldstein [96]	Kutateladze [117]	Heufer & Olivier [98]
Injector geometry	Constant thickness	Constant thickness	Variable thickness
Flow conditions	Lam. & turb.	Lam. & turb.	Lam.
Blowing constraint	$F < 0.144$ [98]	$F < 0.04$	$B_h < 1.5B^*$
Validation datasets	[45–47]	[45, 46, 92, 167]	–

6.2 Study Setup

While vehicle design is a complex, multi-disciplinary design exercise, PHIL was confined to modelling the coolant flow and heat transfer within a simple geometry, subject to constraints on body temperature and blowing parameter. The solver is comprised of two coupled components: heat transfer and porous flow. The heat transfer solver computes the solid and fluid temperature fields (T_s, T_f) for a domain in local thermal non-equilibrium (LTNE), which requires accounting for the internal fluid-solid heat exchange. The porous flow component solves the 2D Darcy-Forchheimer equation to obtain the fluid velocity field $\mathbf{u}_f$. These two components are explicitly coupled: the velocity field $\mathbf{u}_f$ governs convective heat exchange, which raises the fluid temperature T_f; in turn, elevated T_f increases viscous resistance and reduces $\mathbf{u}_f$. The numerical implementation of PHIL to solve these coupled models is detailed in Section 6.3.

This work focuses on finding the operational corridor of a leading edge in steady flight for passive and actively cooled leading edges. PHIL was applied to consider altitudes of 10 to 60 km, velocities of $v_\infty = 1$ to 6 km/s, and leading edge radii of $R_{LE} = 1$ & 5 mm in a steady state study. The study investigated the required mass flux to bring the leading edge temperature down to the material operating temperature, T_{op}.

Transpiration cooling was deemed beneficial if it allowed the system to operate beyond the passively cooled case without requiring excessive mass flux that would compromise aerodynamic performance. More formally, this corridor was defined by the limits below.

- Lower limit: conditions where transpiration cooling was not required. This occurred when the temperature of a passively re-radiating leading edge was lower than the material's maximum allowable temperature[1].

- Upper limit: conditions where the required cooling was excessive. Large

[1]Due to differences in material and internal structure, the range of conditions where a passively re-radiating leading edge survives are not necessarily the same as where a porous leading edge does not require coolant.

blowing parameters have been shown to increase downstream drag and promote downstream boundary layer transition [67, 92]. The blowing limit was taken to be $B_{h,\max} = 1.5B^*$, to coincide with the limits of the transpiration cooling correlations employed.

A block diagram of the steps of the study and the inner optimisation loop of PHIL is shown in Figure 6.4, and is described here. Further details of the parameterisation and optimisation of the internal wall shape are provided in Appendix E.

For each steady-state condition, PHIL was employed to determine the mass flux and coolant pressure needed to reduce the incoming heat flux to survivable levels. Applying an untailored mass flux across all conditions would have been inefficient and risked exceeding the $B_{h,\max}$ limit; a tailored mass flux improved efficiency and helped to avoid the upper blowing limits. In Chapter 3, a single plenum injector with variable wall thickness was shown to be a viable methodology to produce highly tailored mass flux distributions. This methodology is employed again and shown in Figure 6.3. The constraints of the outer mould line mean that a variable wall thickness is achieved by contouring the internal wall shape.

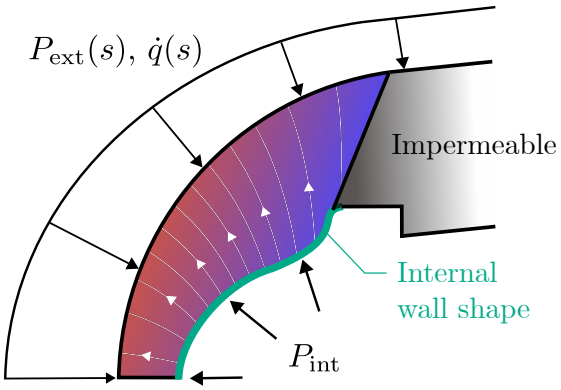


Figure 6.3: Sketch of the porous injector, with the internal wall contouring highlighted. An example of the fluid temperature distribution and velocity streamlines are overlaid.

These steps are repeated for each specified flight condition. Initial screening is carried out by calculating the thermal response of an uncooled leading edge to determine whether any mass flux is required, when $T_s > T_{\text{op}}$. If so, PHIL is applied

to determine the corresponding mass flux, plenum pressure, and injector geometry to reduce the temperature to T_{op} as efficiently as possible.

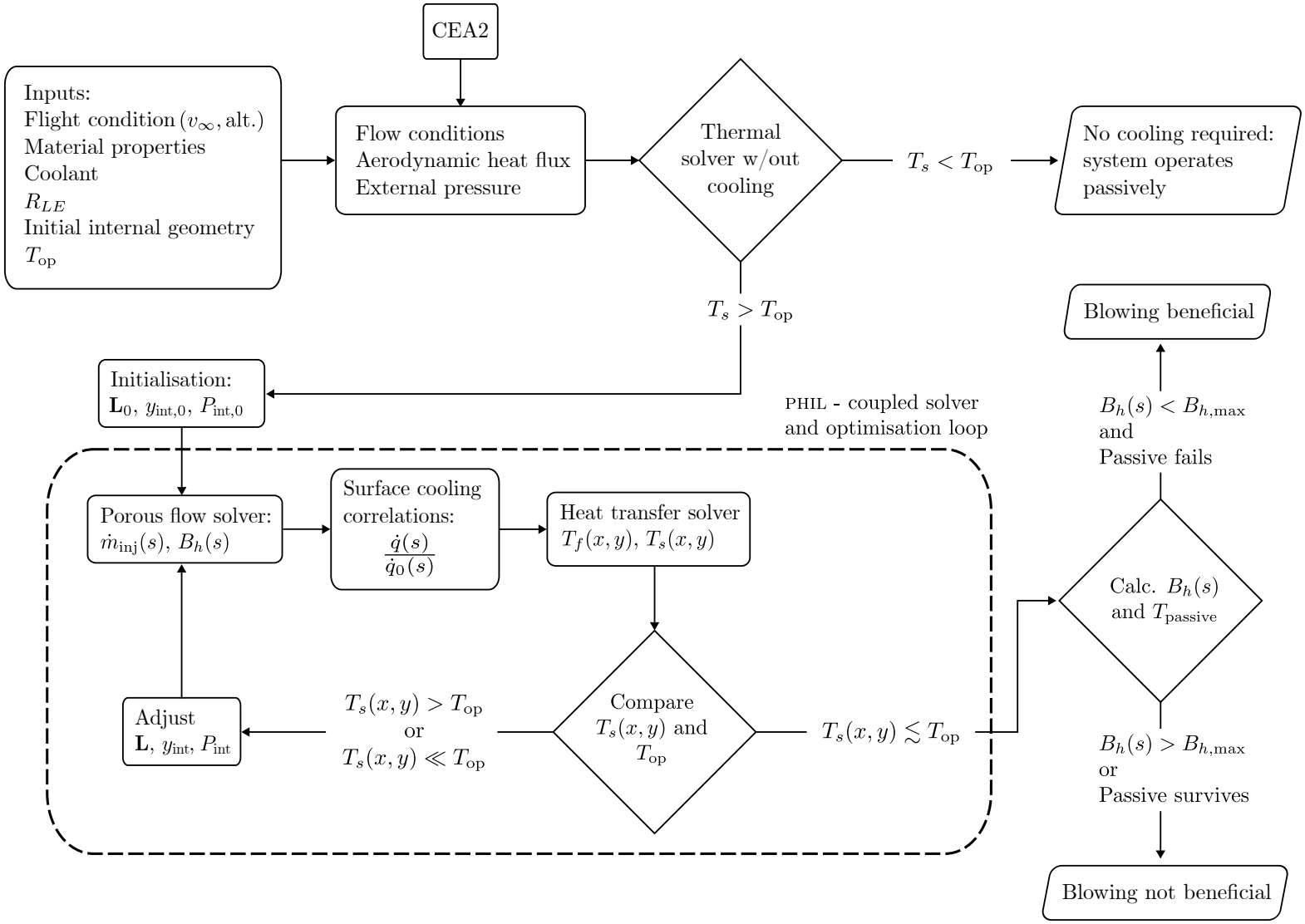


Figure 6.4: Flowchart of the steady state study to calculate the required mass injection and plenum pressure to cool to a target temperature. The optimisation steps are performed whenever $T_s > T_{\text{op}}$, independently of the the viability of the passive system. The optimisation variables: $\mathbf{L}$ and y_{int} are internal wall geometry input parameters, and P_{int} is the plenum pressure input.

6.2.1 Material and Coolant Properties

Two sintered leading edge materials (Inconel 625 and tungsten) with two coolants (nitrogen and helium) were compared against the performance of a passively re-radiating C/C-SiC leading edge. The thermal properties, porous matrix properties, and coolant gas properties used in the modelling are given in Tables 6.2 – 6.4. As before, T_{op} is the maximum material operating temperature throughout the solid domain, and was used as the target temperature for transpiration cooling optimisation.

Table 6.2: Solid material properties evaluated at 300 K [45, 54, 55]. Temperature dependence was accounted for by COMSOL through interpolation of high-temperature experimental data [168–170].

Material	T_{op} (K)	k_s (W/mK)	$C_{p,s}$ (J/kgK)	ρ (kg/m^3)	ε
Inconel 625	1600	9.75	411	8250	0.8
Tungsten	2000	175	132	19300	0.8
C/C-SiC	1950	17	1350	1900	0.8

Table 6.3: Assumed porous properties and surface emissivity. The values of h_v, k_D and k_F were selected from a range of experimental results in [33, 54, 71] for sintered materials.

ϕ	k_D (m^2)	k_F (m)	h_v (W/m^{3}K)
0.4	$6.4{\cdot}10^{-13}$	$2.1{\cdot}10^{-8}$	$2.5{\cdot}10^{5}$

Table 6.4: Coolant fluid properties evaluated at 300 K. Temperature dependence was again interpolated by COMSOL [170].

Coolant	k (W/mK)	$C_{p,f}$ (J/kgK)	ρ (kg/m^3)	μ (Pa·s)	W_f (g/mol)
Nitrogen	0.026	1040	1.15	$1.8{\cdot}10^{-5}$	28
Helium	0.15	5200	0.163	$2.1{\cdot}10^{-5}$	4
Argon	0.018	520.3	1.40	$2.2{\cdot}10^{-5}$	40

6.3 Model Setup

This section provides the implementation of PHIL, including the assumptions and governing equations.

The coupled porous flow and heat transfer calculations were performed using the finite element solver COMSOL MULTIPHYSICS[2]. Calculations of the flow conditions, and the injector optimisation algorithm were carried out in MATLAB and linked to the COMSOL model using the LIVELINK FOR MATLAB functionality. Figure 6.5 shows the flow of variables between the two software packages. To advance the optimiser, the temperature and mass flux outputs calculated in COMSOL are returned to MATLAB.

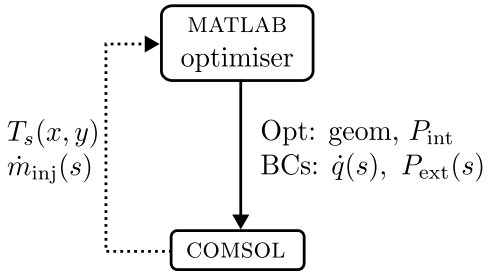


Figure 6.5: Flow of variables between the optimiser and the finite element simulation.

6.3.1 Key Assumptions

The governing equations of the heat transfer and porous flow processes were compiled based on the assumptions given in Table 6.5.

[2] COMSOL MULTIPHYSICS v6.1 using *Porous Media Flow* and *Heat Transfer* modules, with the *Local Thermal Non-Equilibrium* multiphysics coupling.

Table 6.5: Assumptions required by the coupled modelling used in PHIL.

Flow conditions	Steady-state The post-shock gas was in thermochemical equilibrium. Wall catalysis and material oxidation were not considered, nor mitigated by transpiration cooling. The blunted wedge was 2D planar at zero angle of attack. External flow was laminar and transition was not considered. The limit of $B_h < 1.5B^*$ was only considered at the stagnation point, where B^* has been correlated.
Porous flow	Surface pressure changes due to mass injection into the shock layer were negligible. The porous matrix had uniform isotropic permeability, was fully saturated, and had fully open porosity.
Heat transfer	Cooling correlations developed under cold coolant and injector assumptions are assumed to also be applicable to the hot NLTE domain. Heat transfer to the coolant was solely through internal fluid-solid heat exchange, characterised by h_v. Aerodynamic heat flux was not applied directly to the coolant. Aerodynamic heat flux was through convective heat transfer only. Radiative and catalytic heat fluxes were not considered. The thermal properties of the porous matrix (ρ, k, C_p) were calculated using Landauer's relation to account for the effect of material porosity [130]. The coolant temperature in the plenum was 300 K.

6.3.2 External Geometry

Aerodynamic heat flux and surface pressure boundary conditions were dictated by the external geometry and flight conditions. The leading edge geometry was a 2D cylindrically blunted wedge with leading edge radius of 1 or 5 mm, and half-angle 5°, shown in Figure 6.6. The domain was scaled with the radius such that $L_{\text{BASE}} = 100R_{LE}$. This ensured that the backside thermal boundary condition was sufficiently far away from the leading edge.

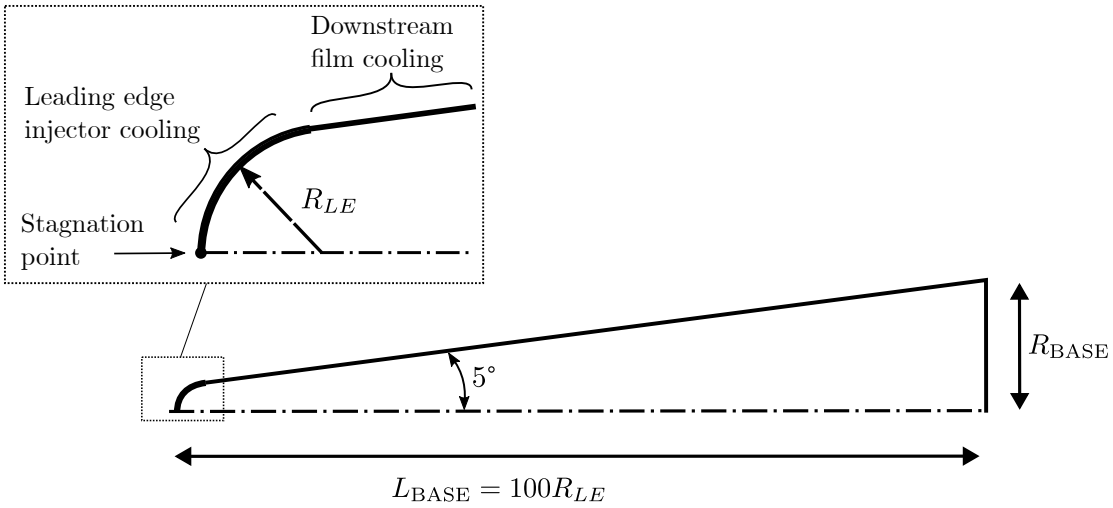


Figure 6.6: A sketch of the 2D outer mould line for external boundary conditions.

6.3.3 Internal Geometry

The internal wall contour was varied to control the 2D porous flow for a targeted mass flux distribution. The geometry was parameterised in MATLAB and fed into an optimisation loop for wall contouring. The conversion from a target temperature, to a target heat flux, to a target mass flux, to a geometry is a highly non-linear, simulation-driven optimisation problem. The flow of variables (Figure 6.5) meant that the COMSOL coupled solver would be a non-linear *black box* for the MATLAB-based optimiser. For such problems, derivative-free global methods are well-suited: a hybrid optimisation strategy using MATLAB's built-in particle swarm optimiser (PSO) and FMINCON was employed. Appendix E presents additional details of the

geometry parameterisation and the optimisation algorithm.

6.3.4 Governing Equations and Boundary Conditions

The porous leading edge and impermeable downstream wall were modelled as two separate domains, shown in Figure 6.7. In the porous injector (domain ①), the fluid and solid temperature fields (T_f, T_{s1}) were solved simultaneously with the porous flow velocity field, $\mathbf{u}$. In the solid wall (domain ②), the temperature field T_{s2} was computed separately, with a connecting thermal boundary between the two domains. The governing equations and boundary conditions are given in Tables 6.6 and 6.7 respectively. The terms of the governing equations within the coupled LTNE domain are described below. The fluid-solid exchange is characterised by the volumetric heat transfer coefficient, h_v.

$$\underbrace{k_s(1-\phi)\nabla^2 T_{s1}}_{\text{Conduction}} + \underbrace{h_v(T_{s1}-T_v)}_{\text{Solid–fluid exchange}} = 0 \tag{6.6}$$

$$\underbrace{\phi\rho_f C_{p,f}\frac{\mathbf{u}}{\phi}\cdot\nabla T_f}_{\text{Convection}} + \underbrace{h_v(T_f-T_{s1})}_{\text{Fluid–solid exchange}} = 0 \tag{6.7}$$

$$\nabla P = -\underbrace{\frac{\mu}{k_D}\mathbf{u}}_{\text{Viscous resistance}} - \underbrace{\frac{\rho_f}{k_F}|\mathbf{u}|\mathbf{u}}_{\text{Inertial resistance}} \tag{6.8}$$

External Boundary Conditions

At the external boundary, the incoming convective heat flux (reduced by hot-wall correction and transpiration cooling) is balanced by heat flux rejection through surface re-radiation. This thermal balance is given by Equation 6.9 and listed as the heat flux boundary condition in Table 6.7, relying on correlation-based calculations[3]. Both hot-wall corrections and thermal re-radiation require the surface temperature distribution, which is provided by the thermal solver.

[3]While semi-empirical correlations were employed for rapid calculations, high quality CFD or experimental data may also be used as an input to the external boundary conditions.

$$\dot{q}_{\text{in}} = \psi\gamma\dot{q}(s)_{\text{conv}} - \dot{q}_{\text{re-rad}} \tag{6.9}$$

Where:

- $\dot{q}(s)_{\text{conv}}$ is the convective heat flux, modelled by semi-analytical correlations for blunt bodies (Fay & Riddell [115] and Lees [116]), detailed in Appendix C.1.
- ψ is the heat flux reduction due to transpiration cooling, either leading edge injector cooling, or film cooling; both calculated through semi-empirical correlations.
- $\gamma = (1 - h_w/h_T)$ is the hot wall correction which scales aerodynamic heat flux at elevated wall temperatures, accounting for the driving enthalpy difference between the hot wall and hot flow.
- $\dot{q}_{\text{re-rad}} = \epsilon_{\text{ext}}\sigma\left(T_{\text{ext}}^4 - T_{\text{amb}}^4\right)$ is the heat flux rejection by re-radiation into the ambient atmosphere, calculated by the Stefan–Boltzmann law.

The external surface pressure on BC1 was required for the porous flow calculation, and was calculated using modified Newtonian theory.

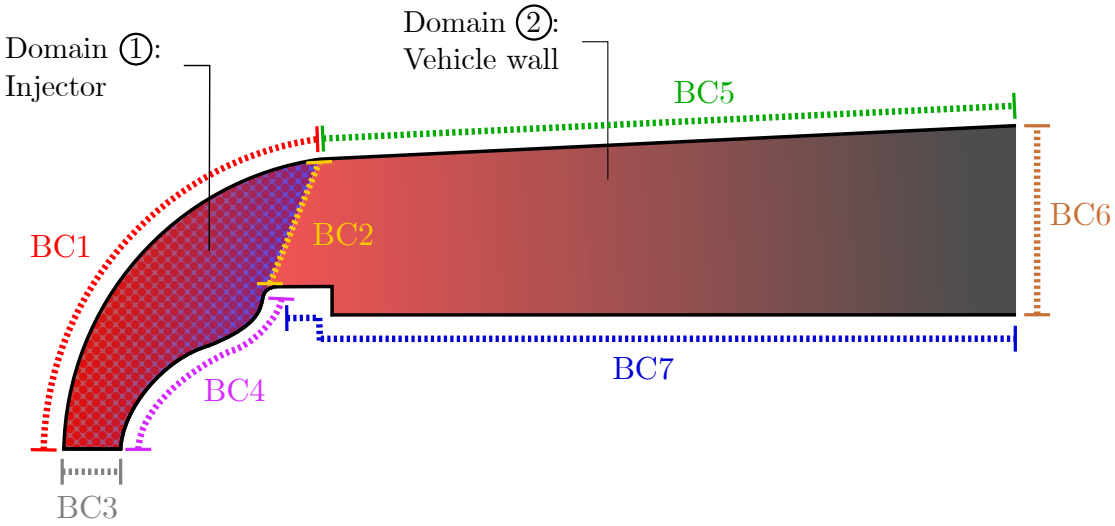


Figure 6.7: Annotated sketch of the domain and boundary conditions with descriptions provided in Tables 6.6 and 6.7. Not to scale.

Table 6.6: Governing equations of coupled heat transfer and porous flow processes in PHIL.

Domain	Description		Equations
①	Heat transfer	Solid:	$k_s(1-\phi)\nabla^2 T_{s1} + h_v(T_{s1} - T_f) = 0$
		Fluid:	$\phi\rho_f C_{p,f}\frac{\mathbf{u}}{\phi}\cdot\nabla T_f + h_v(T_f - T_{s1}) = 0$
	Porous flow		$\nabla P = -\frac{\mu}{k_D}\mathbf{u} - \frac{\rho_f}{k_F}\lvert\mathbf{u}\rvert\mathbf{u}$
②	Heat transfer		$k_s(1-\phi)\nabla^2 T_{s2} = 0$

Table 6.7: Heat transfer and porous flow boundary conditions in PHIL.

Physics	Boundary	Description	Equation
Porous flow	BC1	Outlet: pressure distribution	$P = P_{\text{ext}}(s)$
	BC2	No flow	$\rho u_n = 0$
	BC3	Symmetry	$\rho u_n = 0$
	BC4	Inlet: pressure	$P = P_{\text{int}}$
Heat transfer	BC1	Solid: heat flux + cooling + re-radiation	$\dot{q}_{\text{in},s1} = 0 = \psi\gamma\dot{q}(s)_{\text{conv},s1} - \dot{q}_{\text{re-rad},s1}$
		Fluid: Adiabatic outlet	$\dot{q}_f = 0$
	BC2	Solid: Thermal continuity	$T_{s1} = T_{s2}$
		Fluid: Adiabatic	$\dot{q}_f = 0$
	BC3	Solid: Symmetry	$\dot{q}_{s1} = 0$
		Fluid: Symmetry	$\dot{q}_f = 0$
	BC4	Solid: Backside re-radiation	$\dot{q}_{\text{out},s1} = \epsilon_{\text{int}}\sigma\left(T^4_{\text{int},s1} - T^4_{\text{int,amb}}\right)$
		Fluid: Temperature inlet	$T_f = T_{\text{int}};\ \dot{q}_f = 0$
	BC5	Heat flux + film cooling + re-radiation	$\dot{q}_{\text{in},s2} = 0 = \psi\gamma\dot{q}(s)_{\text{conv},s2} - \dot{q}_{\text{re-rad},s2}$
	BC6	Adiabatic	$\dot{q}_{s2} = 0$
	BC7	Backside re-radiation	$\dot{q}_{\text{out},s2} = \epsilon_{\text{int}}\sigma\left(T^4_{\text{int},s2} - T^4_{\text{int,amb}}\right)$

6.4 Passive TPS Results

6.4.1 Setup

In this study, the passive TPS was modelled as a re-radiating C/C-SiC, which has successfully been employed in flight experiments [8, 10]. Passive calculations were performed separately from the transpiration-cooled study, using identical freestream conditions to enable a direct comparison between the two during the post-processing phase. In this model, COMSOL was again employed, using the *Heat Transfer* module only. Thermal modelling of the passive system was carried out using the boundary conditions shown in Figure 6.8 and the C/C-SiC material properties in Table 6.2.

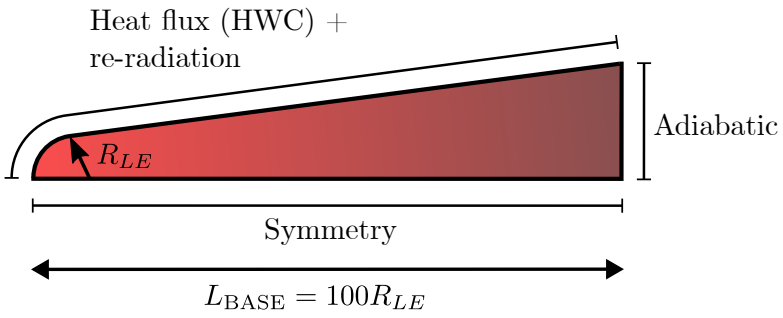


Figure 6.8: Passive TPS boundary conditions.

6.4.2 Results

At each condition, the maximum wall temperature occurs at the stagnation point of the leading edge, and is denoted T_{w0}. These values are plotted in the contour map in Figure 6.9. Flight conditions where T_{w0} exceeds the material operating temperature (T_{op}) indicate failure of the passive TPS and would therefore be considered for transpiration cooling. The boundary of this behaviour is demarcated by the overlaid line in the contour plot. The temperature field above the contour illustrates the temperature distribution within the C/C-SiC material for a selected condition.

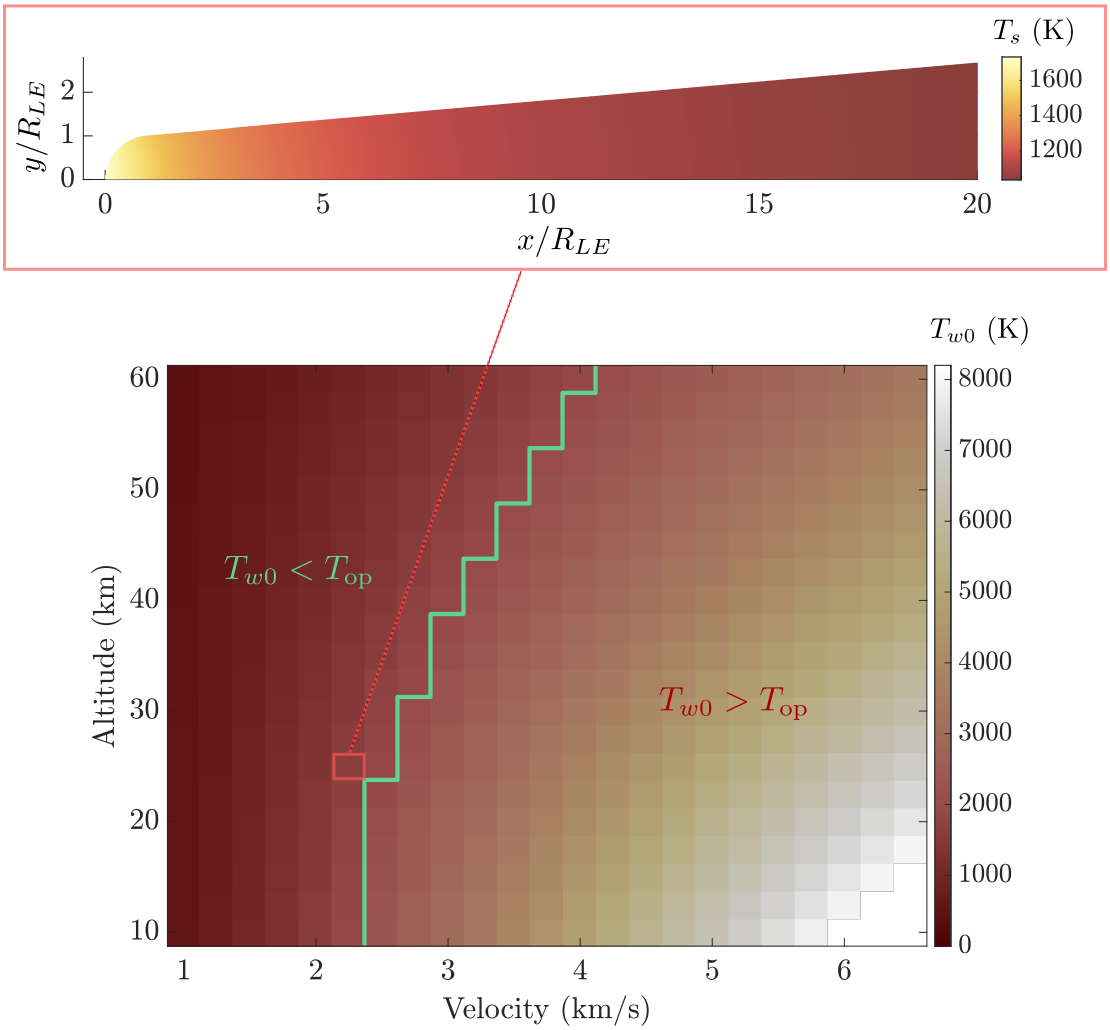


Figure 6.9: Stagnation point temperature contours T_{w0} across a matrix of flight conditions for a steady-state passive 1 mm C/C-SiC leading edge. The temperature field throughout the truncated domain is shown above for $v_\infty = 2.25$ km/s at 25 km altitude.

6.5 Transpiration Cooling Results

The results in this section are based on applying the algorithm in Figure 6.4 to each flight condition. When transpiration cooling is active, each condition is treated as an independent design point, reflecting a unique internal geometry and blowing condition to bring the material temperature down to T_{op}. Throughout this results section, transpiration cooling performance contours are expressed in terms of the normalised blowing parameter, B_h/B^*. Currently, B^* (and therefore B_h/B^*) is defined exclusively at the stagnation point, and all results should be interpreted as such. These values also represent the maximum B_h for along the surface, due to the highest heat flux.

The required B_h for each flight condition depends on a multi-dimensional set of input parameters in this study: R_{LE}, coolant gas, and T_{op} (material-specific). Figure 6.10 shows the performance map for one set of input parameters (Tungsten leading edge, $R_{LE} = 1$ mm, N_2 coolant).

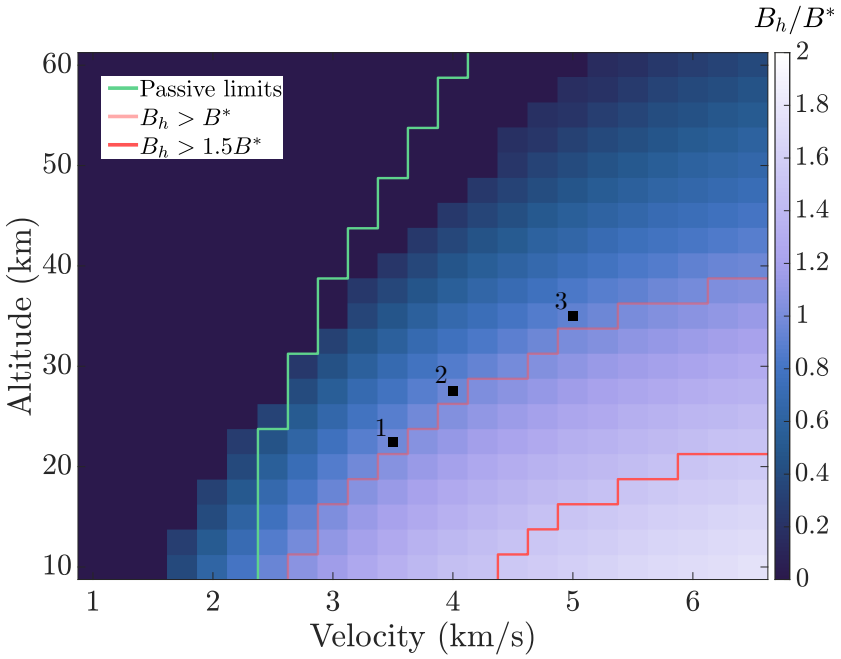


Figure 6.10: B_h-based performance map with regions of possible transpiration cooling deployment between the passive limits and $B_{h,\max} = 1.5B^*$. The results marked by the numbers box are analysed further below. The case presented in this graph is for a 1 mm tungsten leading edge with N_2 coolant.

The upper and lower limits of the operating corridor are overlaid, namely the blowing constraint $B_h > 1.5B^*$ and the passive system limits. The region of $B_h = B^*$ is included for reference. The results marked by the numbers box are discussed in detail further below.

Figure 6.11 shows the solid material temperature field, and the optimised shape of the internal injector wall. Figure 6.12 shows the corresponding coolant flow through the porous injector.

The solid material temperature is highest at the stagnation point, brought down to T_{op} as expected. Despite the high conductivity of tungsten, there are still large thermal gradients within the solid (180 K temperature drop over 10 mm axial distance). The effect of this is considerable thermal stress, which is quantified in Section 6.7.1. The solid temperature distribution along with the cooled and uncooled heat fluxes over the injector surface are shown in Figure 6.13a. The plenum shape has a pronounced eccentricity, as a consequence of the optimiser targeting the stagnation point heat flux with more coolant and the need to overcome the stagnation pressure. The surface mass flux and corresponding B_h along the injector are given in Figure 6.13b.

The result of targeting the highest temperature regions leads to significant drop-off in coolant velocities, v_f, from the stagnation point. At the stagnation point, $v_f = 1.1$ m/s, which drops to $v_f = 0.38$ m/s at $\theta = 45°$. Slower fluid resides in the hot porous matrix for a longer duration, leading to higher exit temperatures. At the injector outlet, from the stagnation point to 45°, the fluid temperature increases from 496 K to 874 K, reaching as high as 1205 K at the end of the injector.

A trade-off exists between blocking the external heat flux via B_h and cooling the injector through internal fluid-solid thermal exchange: higher velocities and mass fluxes enhance the former effect but weaken the latter one. Mitigation of this trade-off could be implemented by varying the h_v. Increasing h_v at the stagnation point improves thermal exchange but reduces permeability [40], adding extra coupling to the design. The effect of global changes to h_v are quantified in Section 6.6.4, however local optimisation of h_v is beyond the scope of this study.

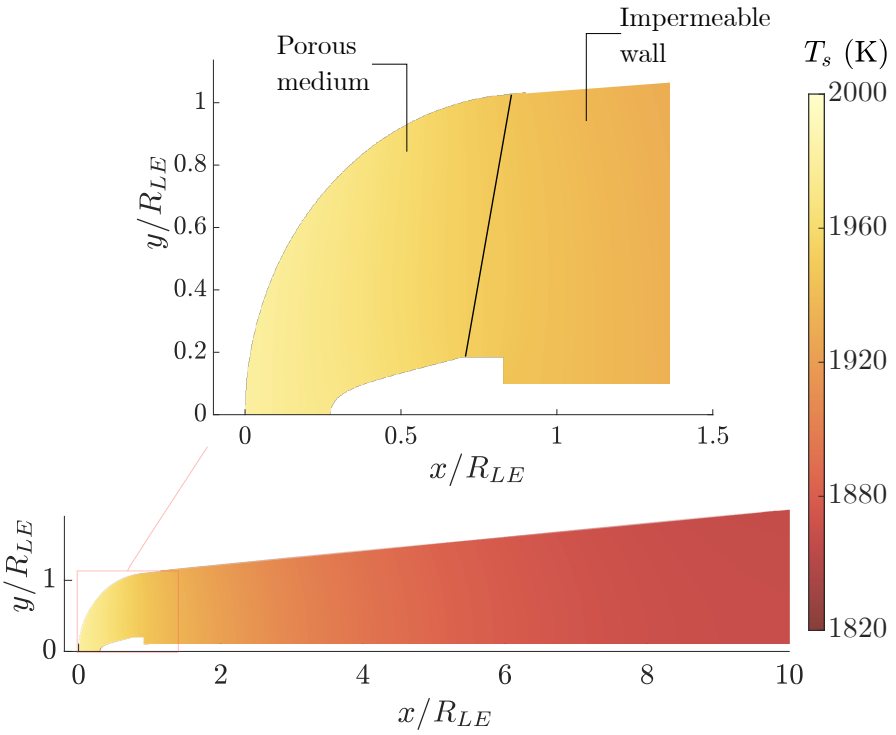
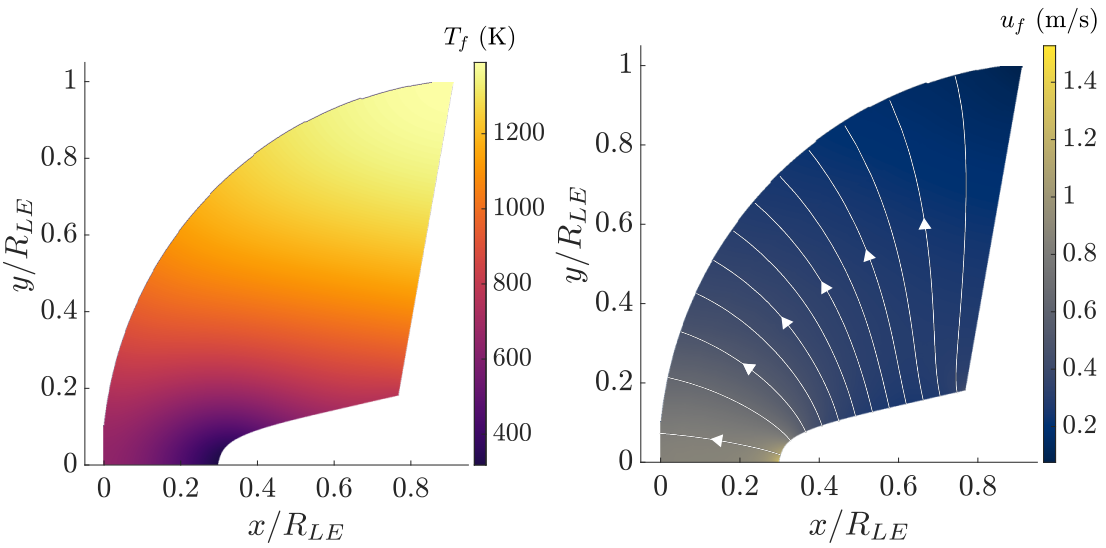


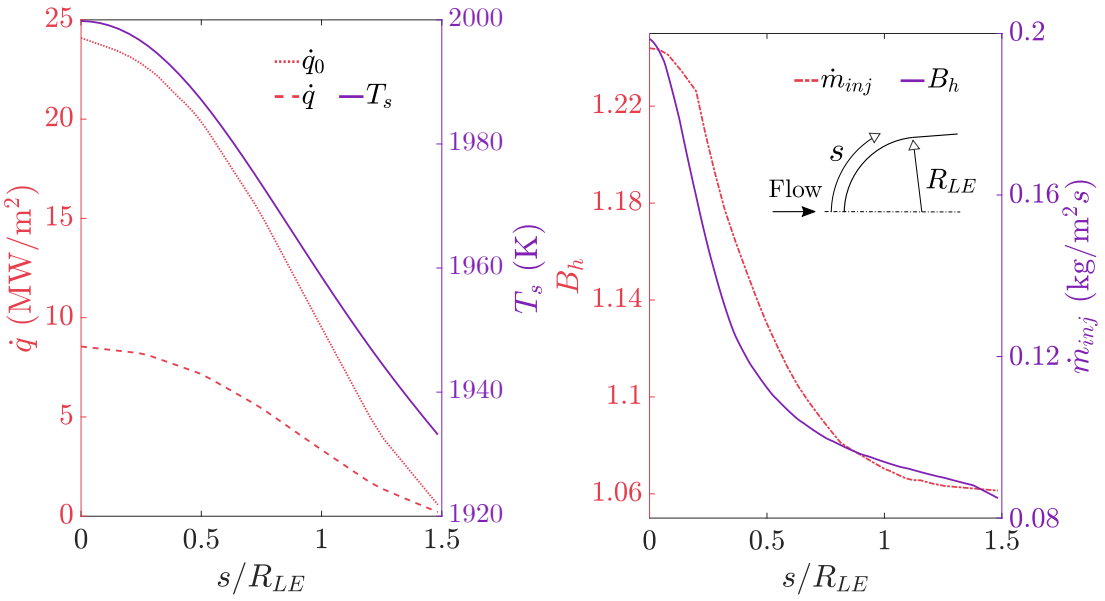
Figure 6.11: Temperature field T_s of the permeable leading edge and impermeable wall at $v_\infty = 3.5$ km/s, altitude = 22.5 km (point 1 in Figure 6.10). The injector internal wall contouring is also visible. This result required N_2 coolant at $P_{int} = 2.42$ bar for a tungsten leading edge.



(a) Fluid temperature, T_f.

(b) Fluid velocity, u_f.

Figure 6.12: Temperature and velocity fields of the N_2 coolant through the porous material at $v_\infty = 3.5$ km/s, altitude = 22.5 km, $P_{\text{int}} = 2.42$ bar (point 1 in Figure 6.10).



(a) Heat flux and temperature.

(b) Mass flux and blowing parameter.

Figure 6.13: Surface profiles of T_s, $\dot{q}$, B_h and $\dot{m}_{\text{inj}}$, for a 1 mm tungsten leading edge with nitrogen coolant at $v_\infty = 3.5$ km/s, altitude = 22.5 km. $P_{\text{int}} = 2.42$ bar (point 1 in Figure 6.10).

6.5.1 Plenum shape

The freestream conditions of the 3 marked points in Figure 6.10 all operate at similar B_h and B_h/B^* values, with uncooled heat fluxes within 15% of each other. Figure 6.14 shows the changes in optimised plenum shape at these conditions along lines of similar heat flux and blowing. The shapes are very similar, with small changes in height and radius of curvature at low θ.

Due to the decoupling from heat flux and blowing parameter variation, the plenum shape change between the three conditions is attributed to the change in surface pressure with freestream condition, where higher altitudes correspond to taller and more rounded plenums due to the relative change in influence from external pressure to heat flux.

It should be noted that in the shape optimisation process, the wall thickness along the stagnation line is fixed to be $0.3R_{LE}$ to appropriately constrain the optimisation. Plenum pressure is found according to the stagnation line conditions, and the rest of the shape is formed accordingly. Further details of this procedure

are described in Appendix E.

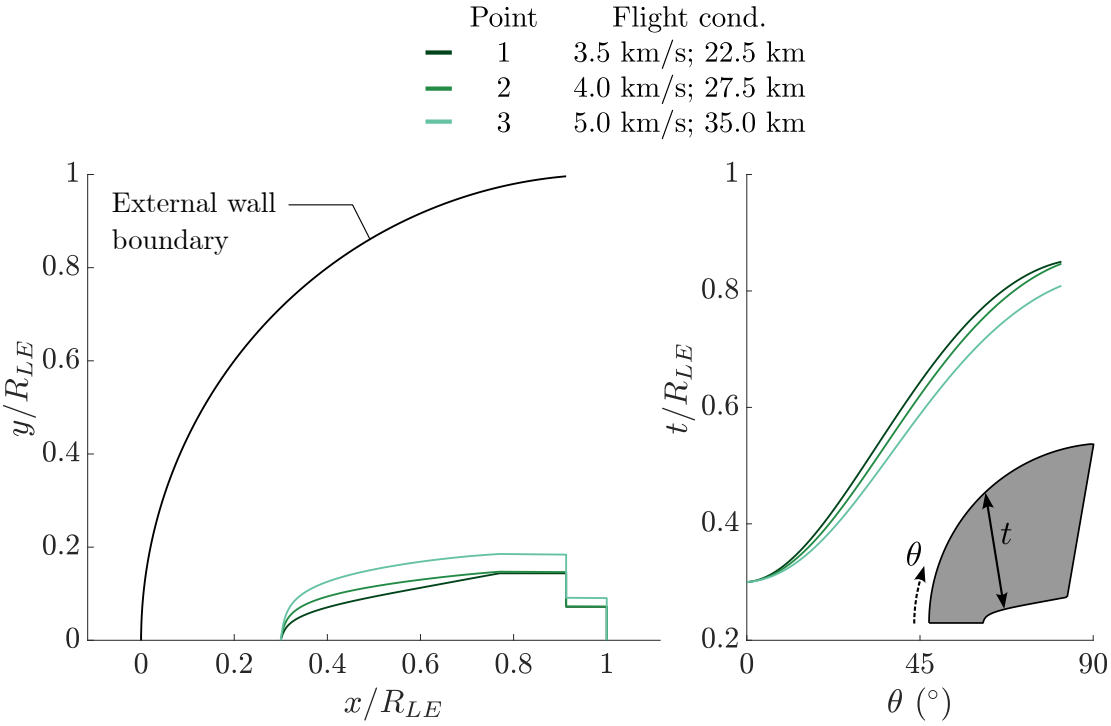


Figure 6.14: Porous wall shape (left) and thickness distribution (right) for three flight conditions at $B_h/B^* \approx 1$.

A preliminary conclusion may be formed by comparing Figures 6.9 and 6.10. The operating regime of a leading edge may be extended when employing transpiration cooling as a TPS rather than relying on passive cooling alone. This is based on the corridor formed between two constraints: the passive system limits and the maximum blowing parameter, $B_{h,\max} = 1.5B^*$. The next section discusses the effect of each of the different input parameters (radius, coolant, material) on the shape of this corridor is presented below. Additional contour plots and envelopes are presented in Appendix F including: heat flux reduction, surface temperature reduction and the effect of different gases on mass flow rate requirement.

6.6 The Effect of Input Parameters

The operation limits in this section are plotted as curves, connecting the cell centres that border the limits of the contours in previous section, resulting in some diagonal lines.

6.6.1 Material

Figure 6.15 compares the operation limits of actively cooled Inconel and tungsten leading edges with a passive C/C–SiC leading edge. Tungsten and C/C–SiC have similar maximum operating temperatures and perform similarly without coolant, though transpiration cooling further extends the survivable velocity range for tungsten. Inconel has a much lower operating temperature, corresponding to operating at much lower velocities. Active cooling provides only a modest extension beyond passive C/C–SiC. Material selection therefore remains critical: transpiration cooling cannot act as a complete substitute for high temperature materials.

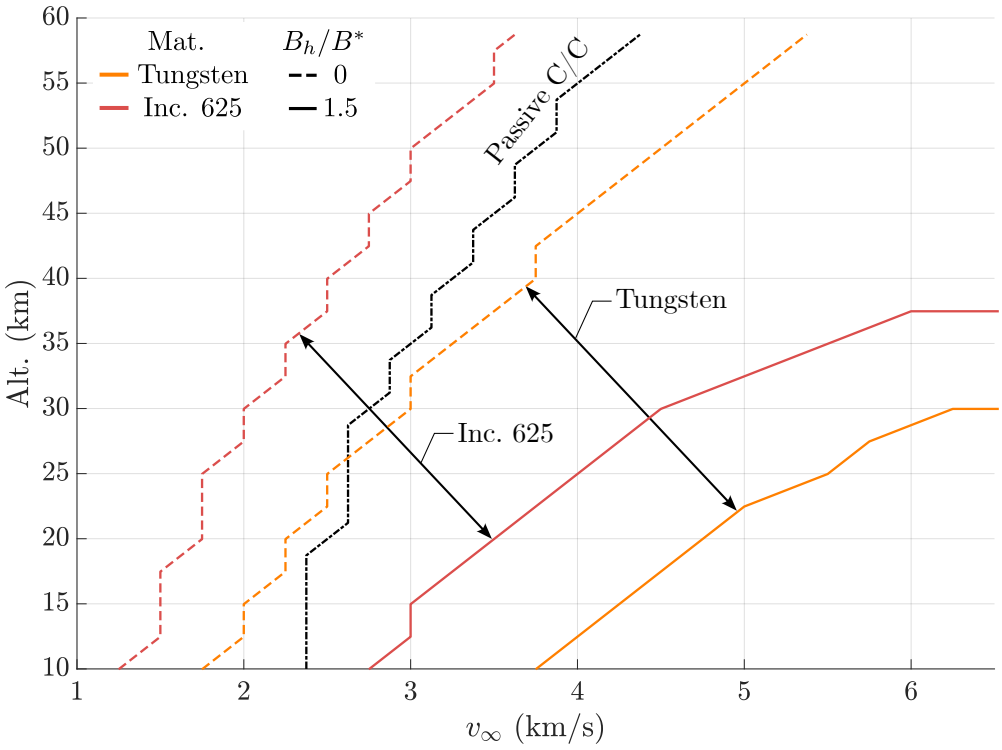


Figure 6.15: Effect of varying material. $R_{LE} = 1$ mm, coolant: N_2.

6.6.2 Coolant

Figure 6.16 presents the calculated system limits for a 1 mm tungsten leading edge employing three gases: helium, nitrogen and argon. Helium is often used as a candidate coolant in transpiration cooling studies as it has been demonstrated to be a more effective coolant per unit mass than nitrogen and argon due to its high heat capacity and low density [57, 85]. However, the figure suggests that there is a clear compromise between coolant mass efficiency and the system limits. The lower molecular weight of helium leads to a much lower B^* parameter and the B_h/B^* system limits are approached sooner[4]. The figure shows that nitrogen can operate at the widest velocity range at low altitudes among the three coolants.

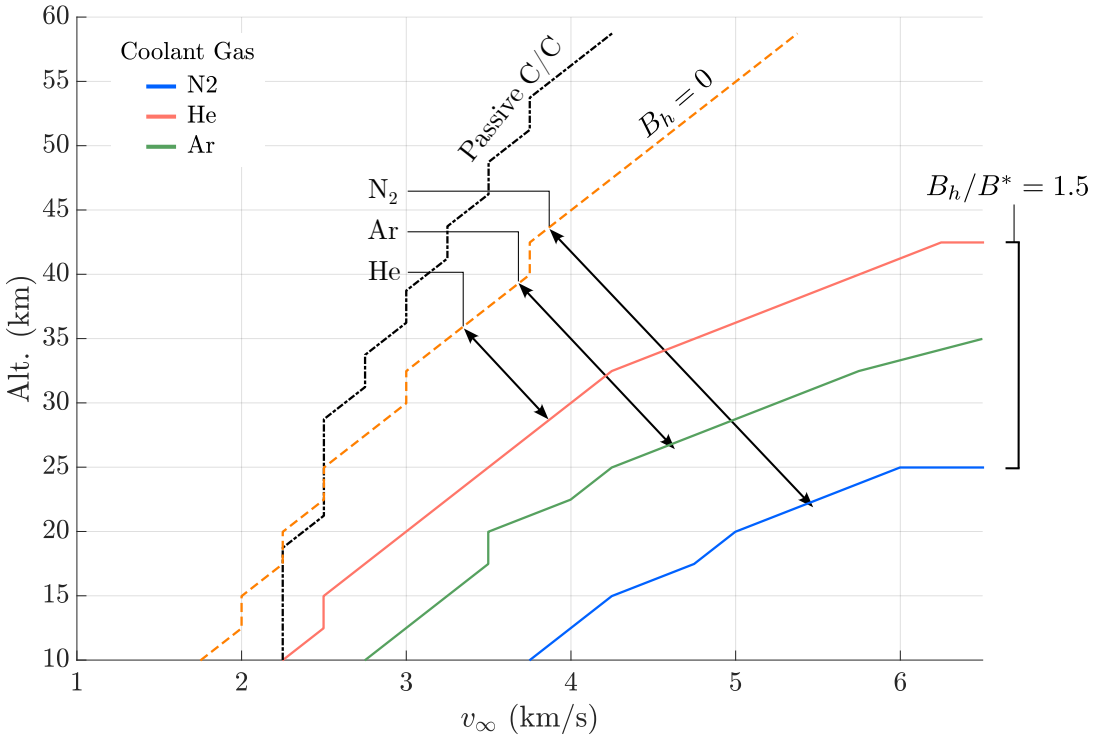


Figure 6.16: Effect of varying coolant. Material: tungsten, $R_{LE} = 1$ mm.

To understand this behaviour, Yoshikawa's correlation (which is employed at the heat flux boundary condition in PHIL) is plotted in Figure 6.17. The figure

[4]Obviously, a full vehicle-level design would include many other thermal, structural and aerodynamic system limits.

shows the heat flux reduction against B_h and demonstrates the source of the trade-off between mass efficiency and blowing limits.

The upper limit of the flight envelope is constrained where cooling curves intersect the $1.5B^*$ blowing limit. Helium has the best mass efficiency but reaches this limit earliest at $\Psi = 0.28$, reducing the incoming heat flux down to 28% before reaching the blowing limits. Argon tolerates the highest B_h before reaching this limit but the lower efficiency leads to a maximum Ψ of 0.13. Nitrogen provides the best compromise, achieving the lowest Ψ and therefore the widest operational range in Figure 6.16.

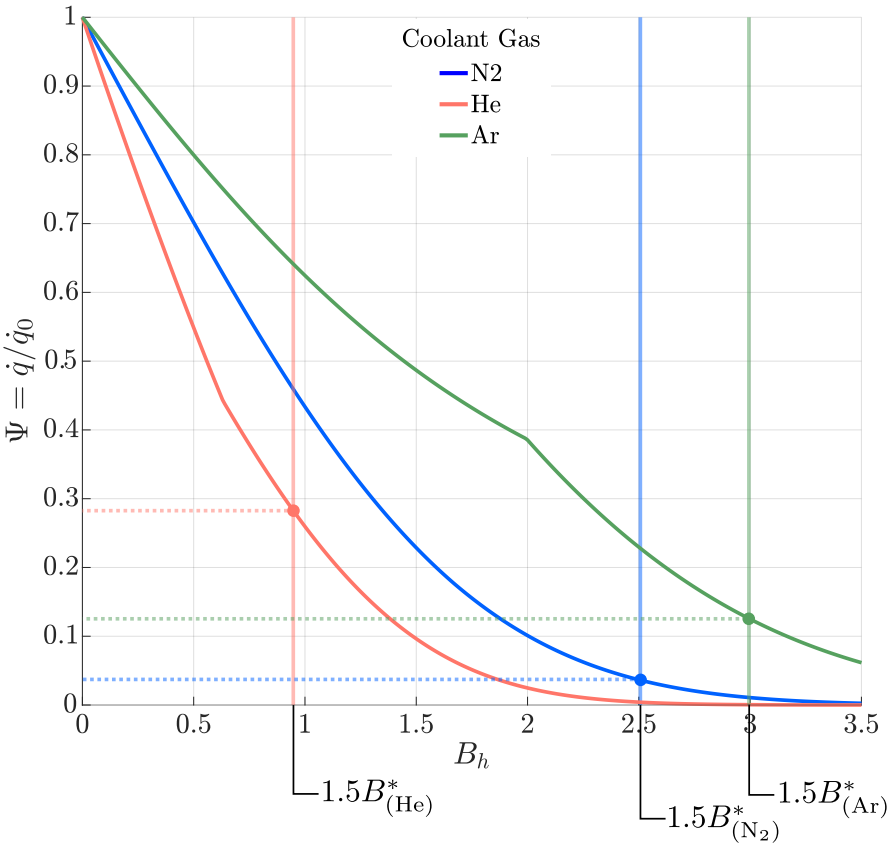


Figure 6.17: Heat flux reduction correlation by Yoshikawa [29] for the three gases considered. Note demarcated system limits at $B_h = 1.5B^*$. These cooling curves are presented for a 1 mm leading edge at $v_\infty = 2.1$ km/s at 30 km.

6.6.3 Radius

A decrease in R_{LE} is associated with an increase in convective heat flux and therefore increases the required B_h to reduce the surface temperature to within material limits. The effect of R_{LE} on B^* is very small, and so differences in B_h/B^* in radius effectively represents B_h.

In Figure 6.18, this is reflected by the 5 mm leading edge being able to operate at higher velocities for each B_h. At higher velocities, the active cooling requirements are very high ($> 90\%$ heat flux reduction), meaning the relative effect of radius in reducing heat flux becomes smaller. This is reflected in the 1 mm and 5 mm curves moving closer together in achievable velocities as the B_h requirements between the two radii begin to converge.

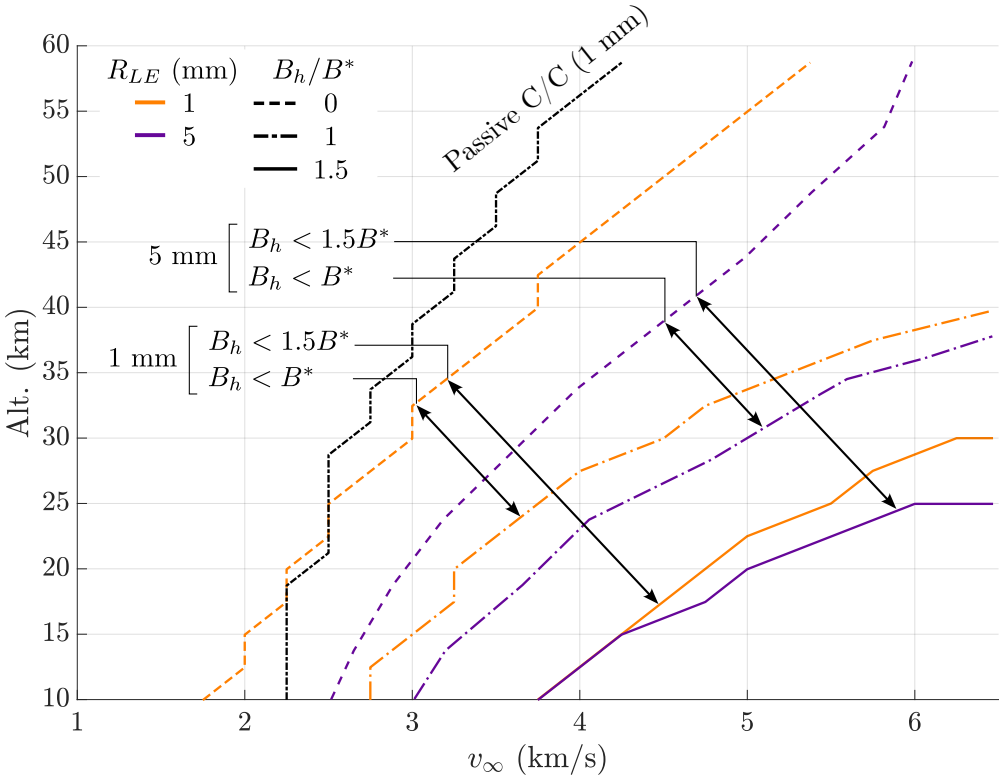


Figure 6.18: Effect of varying radius. Material: tungsten, coolant: nitrogen.

6.6.4 Volumetric Heat Transfer Coefficient

In the above results, the volumetric heat transfer coefficient was held constant at $h_v = 2.5 \cdot 10^5$ W/m^{3}K. To understand the effect of h_v on internal thermal exchange and viscous blockage, a range of values between $1 \cdot 10^5$ and $1 \cdot 10^6$ W/m^{3}K (within the nominal range of previous studies [33, 49, 57, 71]), were applied to the model. To isolate h_v, all other parameters: B_h, plenum pressure, geometry, and freestream conditions (condition 1: 3.5 km/s; 22.5 km), were held constant through a modification to the model for this test.

Figure 6.19 plots the fluid outlet temperatures, solid surface temperatures, and fluid surface mass fluxes for each test. As previously shown, targeting the mass flux toward the stagnation point reduces the thermal exchange to the fluid in that region due to the thinner material and higher coolant velocity, despite the higher solid temperature.

The coolant temperature was highly sensitive to h_v, however the corresponding changes in the solid temperature were comparatively moderate due to the high heat capacity of the porous matrix. Whilst the changes to T_s are modest, changes in h_v still violate the material's operational temperature limit if the design point is sufficiently close to T_{op}. Since h_v is governed by material microstructure, a vehicle designer must consider material processing tolerances when assessing thermal margins.

Figure 6.19 shows the outlet mass flux, where viscous blockage increases with higher T_f. Though not modelled here, the resulting mass flux reduction would lower B_h, increasing heat flux and reinforcing the viscous blockage in a feedback loop. Maintaining the required B_h would require a higher plenum pressure to compensate.

Overall, a higher h_v moderately reduces the temperature of the solid material at the cost of increased plenum pressure and therefore internal pressure loading.

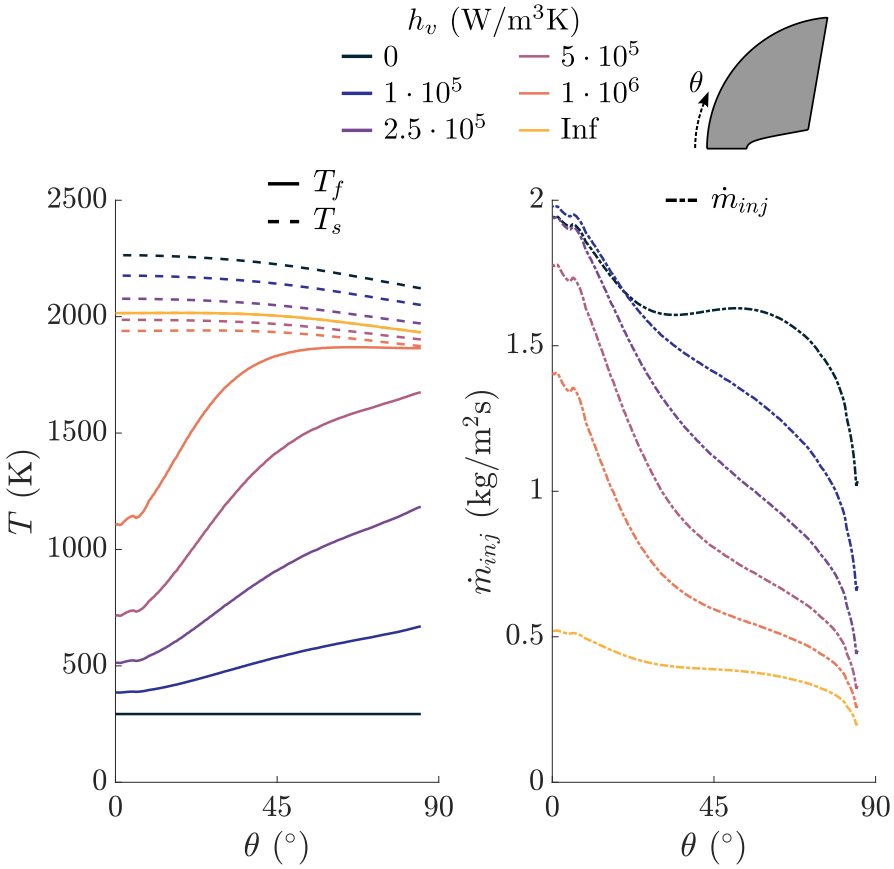


Figure 6.19: Effect of h_v on surface solid and fluid temperatures (left), and surface mass flux distribution (right). The plenum structure and pressure were designed at $h_v = 2.5 \cdot 10^5$ W/m^{3}K.

6.7 Further Constraints

The study so far has considered aerothermal constraints: passive operation and maximum blowing. This section performs first-cut calculations of mechanical stresses and coolant storage budgets to understand if the flight corridors presented in Section 6.5 would be narrowed by these additional considerations.

6.7.1 Stress Constraints

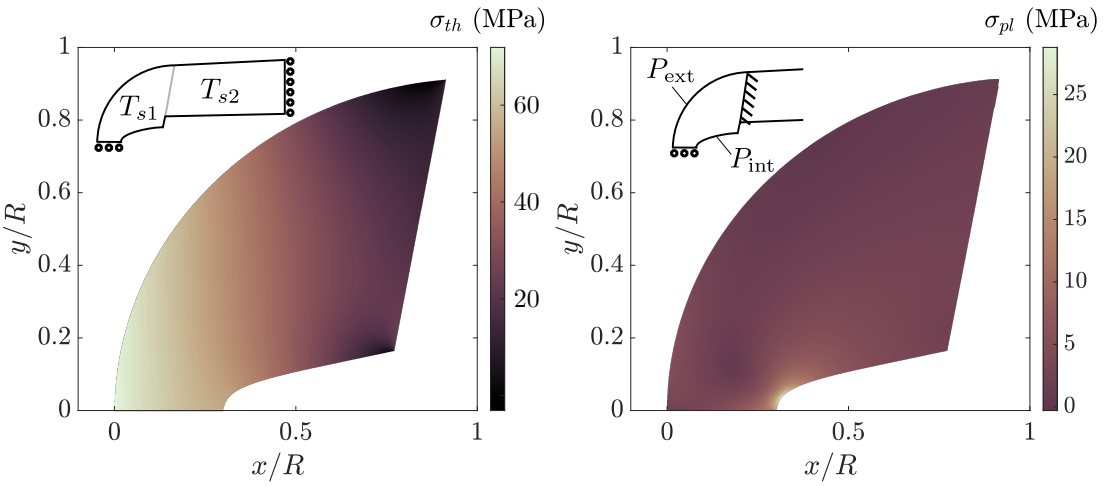
It has been noted in the literature [87] that thermal stress and mechanical loading due to the internal coolant pressure could impose structural constraints to the system. Thermal stresses, σ_{th}, arise due to non-uniform thermal gradients within the solid material. The thermal stresses are exacerbated by the discontinuity in thermal expansion properties between the porous and non-porous material. Pressure loading stresses, σ_{pl}, arise due to the pressure differential required to drive the porous flow. This was a constraint during the experimental work in Chapter 4, where the pressure differential limited the range of blowing conditions achievable by different gases. Contributions of these stresses are shown in Figure 6.20 for a single flight condition, calculated using linear elastic material modelling in COMSOL[5].

Thermal Stress

Temperature-dependent properties: thermal conductivity (k), thermal expansion coefficient (α), heat capacity (C_p), modulus (E), Poisson's ratio (ν) were all estimated using COMSOL's in-built material database, interpolating collections of experimental data of materials at high temperatures [168, 169].

For linear elastic modelling, the maximum σ_{th} of 73 MPa corresponded to a safety factor of 2.4 relative to the tensile strength of 172 MPa for tungsten at high temperatures [171]. σ_{th} showed low sensitivity to flight condition as the solid

[5]Stress calculations in COMSOL were deployed as a post-processing step, using the *Solid Mechanics* module with *Thermal Expansion* and *Poroelasticity* multiphysics interfaces.



(a) Thermal stress

(b) Isothermal pressure-loading stress

Figure 6.20: First principle linear stress contributions of the pressure-induced and thermal stresses on the porous leading edge. The applied mechanical boundary conditions are shown in the upper left of each figure. The yield strength of tungsten was taken to be 172 MPa at high temperatures [171]. The stress calculations were carried out for a 1 mm tungsten leading edge at condition 1 ($v_\infty = 3.5$ km/s, alt. = 22.5 km) using N_2 coolant at a plenum pressure of 4.2 bar.

temperature was limited to T_{op} by the optimisation routine: higher heat fluxes were compensated for by higher mass fluxes, driven by higher plenum pressures.

However, σ_{th} did show sensitivity to volumetric heat transfer coefficient: an increase in h_v from $2.5 \cdot 10^5$ to $1 \cdot 10^6$ W/m^{3}K reduced the peak stress from 73 MPa to 34 MPa. In the previous section, higher h_v required higher plenum pressures. Therefore, a vehicle designer may employ h_v as a design parameter to trade between thermal and pressure-induced stresses.

Pressure-Induced Stress

The effect of pressure-loading stress was heavily influenced by the material and gases under consideration. For condition 1, shown in Figure 6.20, helium and nitrogen are well within the $B_h = 1.5B^*$ blowing constraint. Table 6.8 shows the pressure requirements and associated stresses for both of these coolants. At this condition, helium required 33% less mass flux than nitrogen, but its lower molecular weight required around 1.6 times the plenum pressure and stress, within a 1.7 safety factor of yield. The effect of material permeability is included in Table 6.8, where

the lower permeability values are from samples used in other transpiration cooling experiments [33]. As expected, the material with lower permeability requires a higher plenum pressure for the same blowing condition. In the case of helium, this exceeds the yield stress of the material (172 MPa), and would lead to injector failure. Overall, the loading due to internal pressure may constrain the higher blowing rates, but are highly sensitive to permeability and coolant selection.

Table 6.8: List of internal plenum pressures and resulting mechanical stress for different coolant gases and permeabilities for cooling at $v_\infty = 3.5$ km/s, alt. = 30 km.

Permeability	k_D (m^2)	k_F (m)	Gas	P_{int} (bar)	σ_{pl} (MPa)
Nominal	$6.4 \cdot 10^{-13}$	$2.1 \cdot 10^{-8}$	N_2	4.2	55.8
			He	6.7	98.8
Lower	$3.4 \cdot 10^{-14}$	$1.6 \cdot 10^{-7}$	N_2	6.2	110
			He	14.1	266

6.7.2 Mass and Volume Budget

A vehicle designer may consider the relative constraints of the mass versus the volume budgets of the given calculations. For steady flight, the mass and volume budgets for a fixed-duration flight of 10 minutes were calculated for a 1 mm tungsten leading edge. The volume budget is calculated for an assumed coolant storage of 150 bar at 300 K, and is specified in terms of storage volume rather than expanded volume. Both results are per unit span normal to the simulation plane.

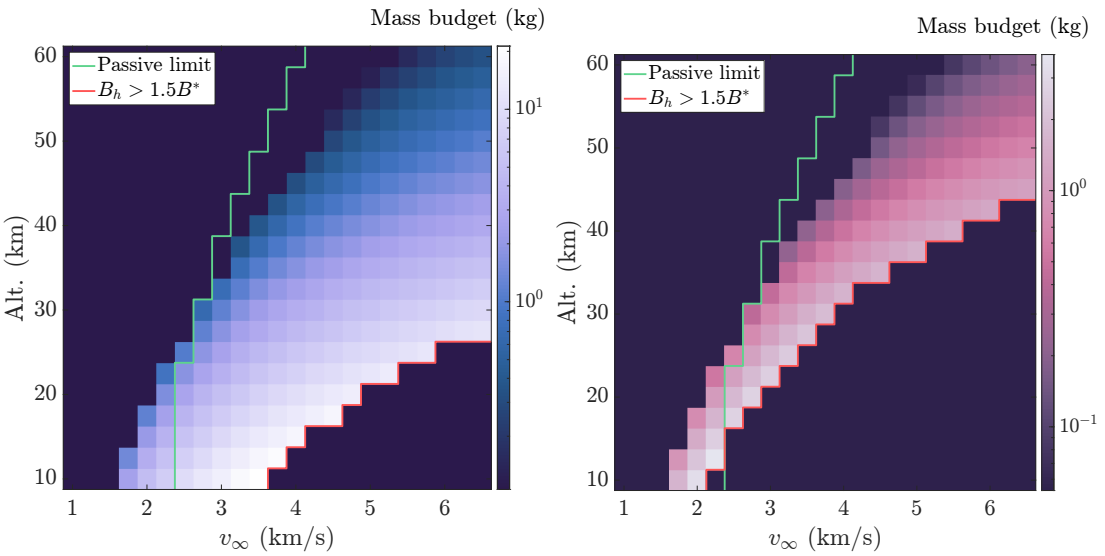
Comparing nitrogen and helium coolants, contours of coolant mass and volume budgets are shown in Figure 6.21 and 6.22 respectively. Conditions requiring no coolant, or exceeding the blowing parameter constraint were not shaded.

The contours reflect conclusions previously considered in this work, giving a clear indication of the different shapes of the steady-state flight corridor. Helium is a more mass-efficient coolant, requiring about 66% of the nitrogen mass flux and budget at the same flight condition. The density of helium means that the volume

budget of nitrogen is around 5 times lower than helium at the same conditions.

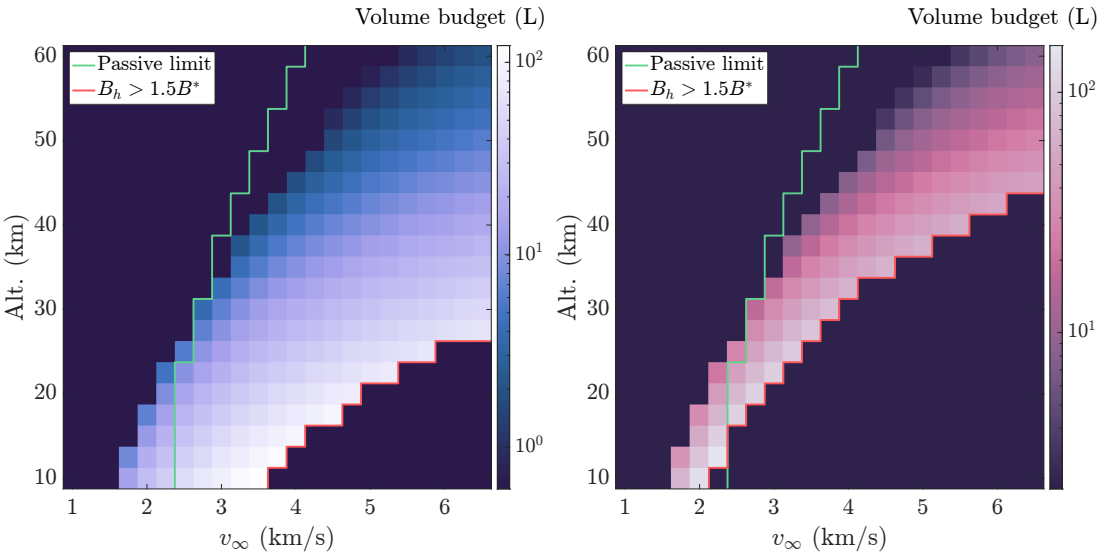
In Figure 6.21, the higher mass budgets are on the order of 10 kg (not including infrastructure), however under the assumed storage conditions, these volumes reach as high as 100 litres. While obviously this depends on the flight vehicle, volume constraints appear to be particularly restrictive.

At moderate conditions, such as at condition 1 (3.5 km/s, 22.5 km), a nitrogen coolant mass of 5.7 kg corresponds to a volume of 32 litres. A composite overwrapped pressure vessel (COPV) is typically used for gas storage on flight vehicles. At condition 1, the dry mass of an appropriate tank would be on the order of 10 kg [172, 173].



(a) Nitrogen (b) Helium

Figure 6.21: Mass budget for a 10 minute steady-state flight for a tungsten leading edge of radius 1 mm.



(a) Nitrogen (b) Helium

Figure 6.22: Volume budget for a 10 minute steady-state flight for a tungsten leading edge of radius 1 mm.

6.8 Conclusion

This study presents the first systems-level analysis that both quantifies the operational viability of transpiration cooling for sharp leading edges, and designs internal architectures that enable this operation.

This study developed a finite element numerical tool, PHIL, to simulate the two-dimensional coupled heat transfer and porous flow for a transpiration-cooled leading edge in flight. The tool employed semi-empirical correlations to model the transpiration cooling effects, augmenting the heat flux at the external boundary condition. The tool included an optimisation algorithm to control the coolant distribution via the injector geometry and plenum pressure, with the aim of reducing the leading edge temperature to a target value set by the leading edge material.

A study was conducted by applying PHIL to a matrix of steady state flight conditions to gain insight into where transpiration cooling may be beneficial over a C/C-SiC re-radiating TPS. A blowing constraint of $B_h < 1.5B^*$ was implemented to avoid aerodynamic penalties of excessive blowing. The study also compared the sensitivity of the operating corridors to different materials, gases and leading edge radii to understand their relative importance. The results showed that transpiration cooling increases the range of operable conditions with respect to a purely passive, re-radiating thermal protection system.

A final comparison in Figure 6.23 shows the steady-state contour map for a 1 mm tungsten leading edge for nitrogen cooling. Trajectories used in [57] and the limits of both nitrogen and helium coolants are overlaid. While the comparison of steady-state performance to transient trajectories is imperfect, it still offers some insight into where further investigation into the viability of transpiration cooling is possible. High-velocity, moderate altitude trajectories for lifting bodies (e.g. shuttle and IXV) fall within the blowing constraints of nitrogen and helium, whereas high-velocity, low-altitude ballistic trajectories may only be suitable for nitrogen coolants.

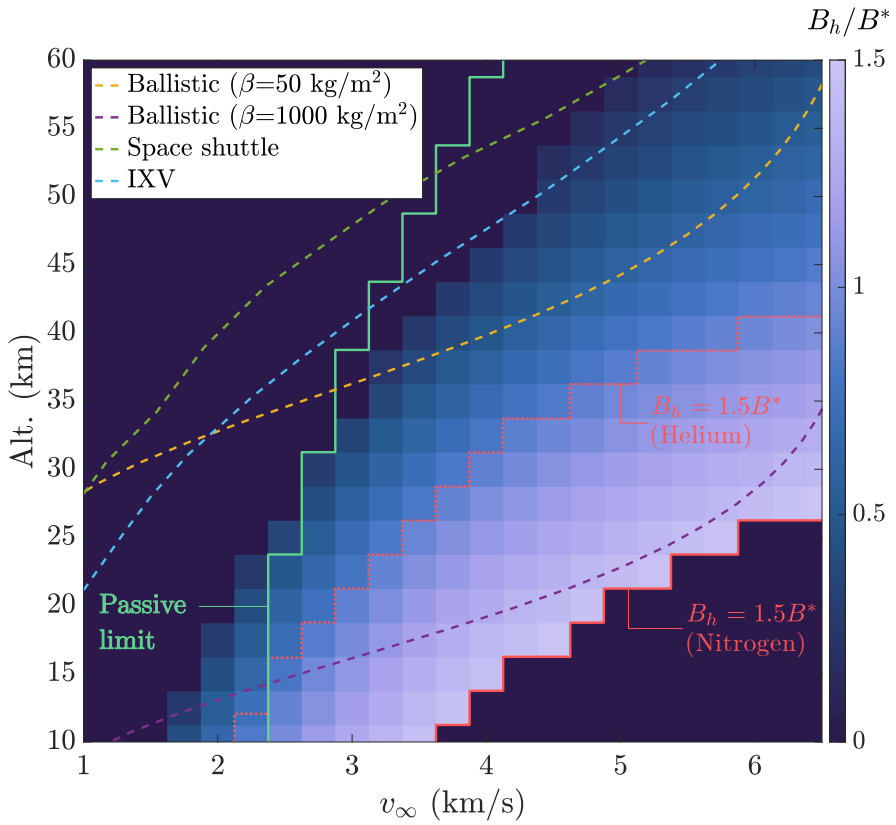


Figure 6.23: Contour of normalised blowing parameter across the range of viable conditions for a 1 mm tungsten leading edge using nitrogen coolant. Overlaid are blowing limits for helium and nitrogen, and trajectories from [57]. Ballistic trajectories assume an entry angle of 5°.

The performance and range of operable conditions is, however, highly dependent on the porous material and the selected coolant gases: a tungsten leading edge with nitrogen coolant was found to have the broadest range of operating conditions. The upper limit of survivable velocities were not particularly sensitive to radius, as blowing effects dominated the heat flux reduction, relative to thermal gains by increased bluntness.

Due to differences in heat capacity within the porous medium, the fluid temperature was significantly more sensitive to fluid-solid heat exchange than the solid temperature. Regions requiring higher coolant mass flux, such as the stagnation point, saw reduced thermal exchange due to wall contouring and increased fluid velocity. Effective utilisation of internal convection to reduce material temperatures would require optimising the porous material manufacturing to control

the distribution of h_v.

Post-processing of thermal and pressure-loading stresses gave a safety factor of around 2 for the selected material properties. Thermal stresses were alleviated by high conductivity and high h_v, but relatively insensitive to flight condition as the cooled target temperature was always the same for a given material. Pressure loading stresses were particularly sensitive to permeability and coolant gas. Nitrogen was once more the preferred coolant gas, as helium required significantly higher driving pressures to cool the leading edge to the same temperature.

Finally, a first-cut calculation on the volume and mass budgets for a 10 minute steady flight at 3.5 km/s at 22.5 km altitude revealed modest budgets of 5.7 kg of nitrogen requiring 32 L of storage, which is within current flight vehicle storage tank capabilities. While helium was a more mass-efficient coolant gas, the relative performance of nitrogen with respect to the blowing constraints, pressure-loading stresses, and volume efficiency makes it a more ideal coolant gas.

6.8.1 Further Work

Given the multi-faceted nature of vehicle design, future work may explore multiple distinct and intersecting paths.

The modelling could consider transient trajectories to further develop the applicability of transpiration cooling for high heat load, high heat flux trajectories. Transient analysis would involve assessing the off-design performance of the injectors, compared to the design exercise carried out under steady assumptions in this work. This approach could also provide a comparison against ablative TPSs, measuring where transpiration cooling outweighs the drag penalties from ablative surface recession, which is a highly transient process.

The constraints on flight corridors warrant further development. This work identified several key system constraints that could be refined to provide more robust operational envelopes. These include developing maximum blowing limits with greater confidence; stress limits incorporating nonlinear stress considerations; and material-specific oxidation response.

Additionally, this study revealed important design considerations, including the possibility to spatially distribute h_v and enhance fluid-solid thermal exchange at the stagnation point, and the need for appropriate permeability selection to manage internal pressure loading.

This study integrates validated correlations, optimised injector designs, and multi-constraint analysis to provide a design framework for sharp leading edge geometries that maintain aerodynamic performance while mitigating the associated severe heat fluxes.

CHAPTER 7

Conclusion and Final Remarks

7.1 Summary of Presented Work 193

7.2 Key Results 195

7.3 Further Work and Recommendations 197

7.4 Final Remarks 200

7.1 Summary of Presented Work

This thesis presents the first full-cycle approach to the design, testing, and application of transpiration-cooled leading edges for hypersonic flight. This represents the first complete development cycle carried out for a leading edge injector geometry. The work has bridged experimentation, numerical modelling, and flight-relevant performance analysis to build up a picture of how transpiration cooling on leading edges may be realised. To the author's knowledge, this work presents several firsts:

- The design and manufacture of a leading edge injector to enable highly tailored mass fluxes along the injector surface.
- The formulation of semi-empirical correlations for heat flux and coolant concentration specific to a transpiration-cooled leading edge, applicable across a range of flow conditions and bluntnesses.
- The experimental testing of a transpiration-cooled leading edge under hypersonic flow conditions; and the first additively manufactured porous injector, of any shape, tested in hypersonic flow.
- The formulation of a systems-level tool for the performance analysis of a sharp leading edge by simulating the tightly-coupled 2D porous flow and heat transfer.

These contributions were achieved through a systematic approach spanning design, experimentation, and analysis. The development and manufacture of porous leading edge injectors focused on delivering controlled, repeatable boundary conditions, evaluated by how well they matched the prescribed mass flux distribution and their uniformity. To achieve this, a novel leading edge fabrication process was developed, utilising additive manufacturing techniques for porous materials and bridging the gap between complex numerical designs and experimentally achievable injector geometries.

The injectors were tested under cold-flow hypersonic conditions in the High Density Tunnel. Optical diagnostics (infrared thermography and pressure-sensitive

paint) were used to measure heat flux, coolant concentration, and surface pressure on and downstream of the leading edge injector. The experimental data was used to validate the numerical methodology for simulating the same key parameters in Eilmer.

The numerical method was extended to model cooling performance at high-enthalpy flight conditions. Simulations investigated the influence of freestream conditions, geometry, and coolant gas on the trade-off between cooling and aerodynamic performance through drag. The resulting data was generalised through modified semi-empirical correlations for heat flux and concentration. A full semi-empirical model for heat flux distribution around the blunted wedge was developed, only requiring flight conditions, blowing conditions, and radius inputs. The correlations were intended to enable comparisons across a range of inputs to provide a foundation for low-order modelling.

For concentration modelling, the advection-diffusion model was shown to be viable via a modified correlation parameter. Additional work is required to decouple the correlation from CFD input data by developing a model for the coolant concentration build-up over the injection surface.

The heat flux correlations and injector design methodologies were then integrated into a multiphysics model, phil. The model was applied to a systems analysis study to design injector architectures and evaluate steady-state flight envelopes based on aerothermal limits, providing the link from fundamental research to flight-relevant performance assessment.

7.2 Key Results

Despite experimental blowing conditions operating beyond the boundary layer blow-off parameter, pressure drag penalties remained below 5%, and the boundary layer remained laminar throughout the measurement domain (220 mm long in the streamwise direction). These results are encouraging, as they suggest that effective thermal protection can be achieved with minimal aerodynamic penalties at the blowing conditions tested.

Manufacturing technique was a significant factor in obtaining high quality heat flux data. The CNC-machined injector showed 56% spanwise mass flux variation, corresponding to 38% in film cooling effectiveness. The additively manufactured injector demonstrated only 5% variation in mass flux, corresponding to 9% in film cooling. Despite identical design points and experimental conditions, the injectors exhibited different film cooling decay rates, confirming that manufacturing method is critical when designing experimental mass flux boundary conditions. The additively manufactured injector exhibited close agreement with CFD predictions (within 10%), successfully validating the numerical method by aligning numerical and experimental boundary conditions. However, conclusive validation will require a rigorous uncertainty analysis of the experimental data.

Numerical simulations at high enthalpy conditions revealed that drag penalties due to blowing were negligible, even beyond the boundary layer blow-off parameter (B^*). While surface pressure drag increased by 2-3.5%, this was offset by severe reductions in skin friction drag (30-40%), resulting in minimal net drag penalty. The pressure drag increase was geometry-dependent: 3.5% for a 1 mm leading edge decreasing to 1.5% for 5 mm at $B_h/B^* = 1.5$. This low sensitivity was attributed to the coolant layer displacing the boundary and shock layers from the stagnation point, causing only minor changes in effective bluntness and external flow.

The cooling performance demonstrated significant heat flux reduction capabilities. Just below the blow-off parameter ($B_h/B^* = 0.9$), stagnation point heat flux was reduced by 80%, increasing to 95% reduction beyond blow-off ($B_h/B^* = 1.5$).

A distinct behavioral shift occurred beyond the blow-off parameter, where the coolant layer began dominating the near-wall flowfield, driving heat flux toward a uniform distribution. Correlations based on this numerical data matched the heat flux to within 10% over the leading edge, decreasing to 30% by $s/R = 30$, at which point absolute heat flux was only 4% of the stagnation point value.

The multiphysics tool, PHIL, showed that transpiration cooling for sharp leading edges would be most viable at 2.5–6.5 km/s and 25–50 km, but was highly sensitive to material and coolant choice. The analysis revealed design challenges at the injector stagnation point, where minimal wall thickness severely limited internal heat exchange between solid and fluid. Optimal injector design therefore requires spatial tuning of thickness and volumetric heat transfer coefficient simultaneously to balance thermal exchange and flow resistance. Thermal stresses were below yield stress for tungsten at the condition where stress was considered, however this can increase with a less conductive material and higher heat flux conditions. Increasing volumetric HTC was also found to alleviate thermal stresses within the domain.

A blowing constraint of $1.5B^*$ was selected based on correlation limits and have been experimentally confirmed to avoid severe aerodynamic penalties. This limit meant that nitrogen enabled the widest flight envelope, predicted to survive around 1.3–1.7 times the velocity than a helium-cooled vehicle. As expected, helium provided the greatest mass efficiency, requiring around 66% of the mass flow rate at comparable conditions but 5 times more volume flow rate.

For practical implementation, a 10 minute steady flight at 30 km, 3.5 km/s would require a mass budget of 5.7 kg and a volume budget of 32 litres. At this condition, a 1 mm leading edge with low permeability required a plenum pressure of 6.2 bar for nitrogen and 14.1 bar for helium, leading to mechanical stress exceeding the material strength. Similar limitations were observed experimentally, where maximum achievable blowing was constrained by injector strength and was significantly lower for helium.

7.3 Further Work and Recommendations

There are a few clear methodological improvements that could lend greater confidence to the results. These are: a comprehensive error analysis on the experimental and numerical datasets; improvement on the semi-emperical correlations to encompass better capture the effect of freestream condition; confirmation that the numerical method validation holds at high enthalpy; and validation of the multiphyiscs tool, PHIL, using the present experimental results and historical datasets that were used for validation in [49, 113].

7.3.1 Scope

This work was carried out with the aim of modelling the performance of a transpiration-cooled leading edge. To achieve this, the approach required a cascade of information: low-cost systems modelling required correlations, which required simulations, which required experimental validation. The scope of the physics at each step was larger than that of the previous step. This is to be expected: *higher fidelity data means higher cost and smaller scope.*

Experiments were carried out in a cold flow facility at two freestream conditions for a single geometry for several blowing conditions. The numerical method and boundary condition were validated against this data. Correlations were formulated using high enthalpy, chemical non-equilibrium numerical data over 3 freestream conditions, assuming the validity of the numerical method held. The systems model extrapolated the correlations to apply them over a broader range of velocities and altitudes than the correlations were formed over. The scope of each study is sketched in an abstract space in Figure 7.1 to illustrate this point, and specific conditions and values are provided in Table 7.1.

Table 7.1: Span of conditions and assumptions for each of the three stages of investigation (experiment, numerical, systems), the envelope of which is sketched in Figure 7.1.

	Flow temp.	Wall temp.	Bluntness (mm)	Speed	Altitude (km)
Expt	Cold	Cold	3	$M_\infty = 7$	23, 27
Num	Hot	Cold	1, 5, 10	$M_\infty = 5, 7$	25, 35
Sys	Hot	Hot	1, 5	$v_\infty = 1.5\text{-}6.5$	10-60

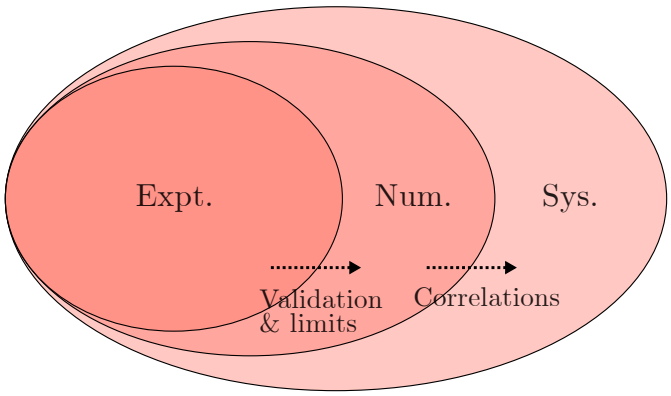


Figure 7.1: Abstract sketch of the set of conditions and assumptions spanned by each stage of the thesis, showing how each subsequent stage requires expansion of the results from the previous set. Specific conditions and values provided in Table 7.1.

The formulation of broader scope semi-empirical correlations require larger datasets. The current numerical set comprises 32 simulations across 3 geometries, 2 gases, 4 blowing levels, and 3 freestream conditions. This required 35,000 HPC core hours. In the systems study (where the correlations are applied), the range of velocities and altitudes is far more expansive, requiring significantly more simulations. The higher velocity conditions under consideration would also require confirmation on whether thermal non-equilibrium effects should be considered. While this is feasible, it would demand additional months and computing resources.

Validating simulations in a high-enthalpy facility is far more complex. While access to high-enthalpy hypersonic facilities is possible, substantial effort would be required to establish the necessary infrastructure (optical access and mass injection). Further development would be required to ensure the measurement

accuracy and response time of optical diagnostics in such flows. If the optics requirements cannot be met, the experimental model would need a full redesign to accommodate discrete sensors.

7.3.2 System Constraints

While the current study demonstrates the thermal benefits of transpiration cooling within defined limits, a complete feasibility assessment for flight vehicles requires the development of the model and the constraints. Many of these constraints have been either considered or assumed, however each one is a possible avenue to contribute to the performance assessment. The constraints listed below are not simple fixes within the modelling software, but would require additional numerical or experimental treatment to validate each approach.

- Aerodynamic penalties: Higher B_h beyond $1.5B^*$ may trigger transition or increase drag beyond acceptable levels. More experimental and numerical data on surface pressure is required at higher blowing parameters to further characterise the relationship between drag and blowing.

- Oxidation and catalysis: Oxidation models exist for both passive and transpiration-cooled TPS materials. Oxidation-blocking coolant concentration is correlated for limited geometries, but not yet completely over the leading edge. Oxidation constraints may narrow the flight envelope at high dynamic pressures but also extend it in the other direction where passive TPSs oxidise and transpiration cooling prevents oxidation. To implement this, coolant concentration must be correlated and then fed back into material response calculations.

- Structural stress: Thermal and pressure stresses remained within yield limits in some of the simulated cases. However, this was found to be highly material dependent, on some occasions exceeding yield stress of the materials considered. More robust assessments require complex high temperature

material modelling such as creep and nonlinear elasticity, and how these stresses may be relieved by local changes in volumetric HTC and permeability.

- Geometry: All data was collected at zero angle of attack and yaw. However, high L/D vehicles may pitch, bank, or feature swept leading edges. New experimental and numerical datasets would be required to deal with their behaviour for leading edge transpiration cooling, especially when a designed leading edge experiences off-design, transient pitch and roll manoeuvres.

Finally, the types of study conducted within PHIL could be improved. The geometries and results in Chapter 6 are optimised for each flight condition. However, a real trajectory would require operation in the off-design regime as well. Modelling off-design conditions, via transient trajectories or other steady conditions using a fixed geometry would be the next logical step to assess the viability of transpiration cooling.

7.4 Final Remarks

By establishing design tools, generating reproducible experimental data, and defining system-level performance limits, this research provides a foundation for the development and validation of actively cooled leading edges. As interest in hypersonic systems expands across both civilian and defence sectors, the ability to reliably model, manufacture, and test novel thermal protection systems becomes increasingly significant. The work presented here offers new technical insights and enables future advances in the design and experimental validation of reusable thermal protection systems.

References

[1] J. D. Anderson. "Hypersonic and High-Temperature Gas Dynamics, Third Edition". 2nd ed. AIAA Education Series. Reston, VA: American Institute of Aeronautics and Astronautics, (2006). ISBN: 978-1-56347-780-5.

[2] H. N. Kelly and M. L. Blosser. "Active Cooling from the Sixties to NASP". Tech. rep. NASA-TM-109079. Hampton, VA, United States: NASA Langley Research Center, (1994).

[3] U.S. Naval Institute Staff. "Report to Congress on Hypersonic Weapons". (2025). https://news.usni.org/2025/04/11/report-to-congress-on-hypersonic-weapons-18 (retrieved: 30/6/2025).

[4] University Consortium for Applied Hypersonics. "Home Page". (2025). https://hypersonics.tamu.edu/ (retrieved: 30/6/2025).

[5] T. Robinson. "On the Record with Mark Thomas, CEO, Reaction Engines". (2023). https://www.aerosociety.com/news/on-the-record-with-mark-thomas-ceo-reaction-engines/ (retrieved: 19/6/2025).

[6] J. Healey. "Development of Battle-Winning Hypersonic Technology Accelerated under New AUKUS Deal". (2024). https://www.gov.uk/government/news/development-of-battle-winning-hypersonic-technology-accelerated-under-new-aukus-deal (retrieved: 9/7/2025).

[7] L. F. Crabtree et al. "Estimation of Heat Transfer to Flat Plates, Cones and Blunt Bodies". Tech. rep. 3637. Ministry of Technology Aeronautical Research Council, (1970).

[8] C. W. Ohlhorst et al. "Development of X-43A Mach 10 Leading Edges". 56th International Astronautical Congress of the International Astronautical Federation, the International Academy of Astronautics, and the International Institute of Space Law. Fukuoka, Japan: American Institute of Aeronautics and Astronautics, (2005). DOI: https://doi.org/10.2514/6.IAC-05-D2.5.06.

[9] J. Reuther et al. "A Reusable Space Vehicle Design Study Exploring Sharp Leading Edges". AIAA Thermophysics Conference. Anaheim, CA, United States: American Institute of Aeronautics and Astronautics, (2001). DOI: https://doi.org/10.2514/6.2001-2884.

[10] H. Böhrk et al. "Sharp Leading Edge at Hypersonic Flight: Modeling and Flight Measurement". Journal of Spacecraft and Rockets 51.5 (2014), pp. 1753–1760. DOI: https://doi.org/10.2514/1.A32892.

[11] D. Hunter. "UK Hypersonic Glide Vehicle Concept and Performance Assessment". Portsdown West, (2019). https://www.aerosociety.com/media/12855/8-david-hunter.pdf (retrieved: 24/3/2025).

[12] W. F. N. Santos. "Bluntness Impact on Lift-to-Drag Ratio of Hypersonic Wedge Flow". Journal of Spacecraft and Rockets 46.2 (2009), pp. 329–339. DOI: https://doi.org/10.2514/1.41387.

[13] X.-q. Chen et al. “Bluntness Impact on Performance of Waverider”. Computers & Fluids 48.1 (2011), pp. 30–43. DOI: https://doi.org/10.1016/j.compfluid.2011.03.011.

[14] S. Li et al. “Aerodynamic Performance Investigation on Waverider with Variable Blunt Radius in Hypersonic Flows”. Acta Astronautica 137 (2017), pp. 362–372. DOI: https://doi.org/10.1016/j.actaastro.2017.05.001.

[15] J.-x. Liu et al. “Numerical and Experimental Study on Waverider with Blunt Leading Edge”. Computers & Fluids 84 (2013), pp. 203–217. DOI: https://doi.org/10.1016/j.compfluid.2013.06.005.

[16] S. Y. Chen. “The Longitudinal and Lateral Range of Hypersonic Glide Vehicles with Constant Bank Angle”. Tech. rep. RM-4630-PR. Santa Monica, CA: RAND Corporation, (1966).

[17] M. Wright and J. Dec. “Aerothermodynamic and Thermal Protection System Aspects of Entry System Design Workshop”. Thermal and Fluids Analysis Workshop. Pasadena, California: National Aeronautics and Space Administration, (2012).

[18] B. G. Laub and E. Venkatapathy. “Thermal Protection System Technology and Facility Needs for Demanding Future Planetary Missions”. Planetary Probe Atmospheric Entry and Descent Trajectory Analysis and Science. 544. Lisbon, Portugal: European Space Agency, (2003), pp. 239–247.

[19] A. Mitrea et al. “Time Resolved Heat-Flux Measurements on a CEV Candidate Shape at High Enthalpy”. AVT-200 Specialists’ Meeting on Hypersonic Laminar-Turbulent Transition. San Diego, CA., (2012).

[20] M. Bunn. “Technology of Ballistic Missile Reentry Vehicles”. Review of U.S. Military Research and Development. Ed. by K. Tsipis and P. Janeway. Massachusetts Institute of Technology, (1985), pp. 67–116. ISBN: 0-08-031622-0.

[21] J. M. Modlin. “Hypersonic Aerospace Vehicle Leading Edge Cooling Using Heat Pipe, Transpiration and Film Cooling Techniques”. PhD thesis. Georgia Institute of Technology, (1991).

[22] S. D. Kasen and H. N. G. Wadley. “Heat Pipe Thermal Management at Hypersonic Vehicle Leading Edges: A Low-Temperature Model Study”. Journal of Thermal Science and Engineering Applications 11.061001 (2019). DOI: https://doi.org/10.1115/1.4042988.

[23] T. Hermann et al. “Mixing Characteristics in a Hypersonic Flow around a Transpiration Cooled Flat Plate Model”. HiSST: International Conference on High-Speed Vehicle Science Technology. Moscow, Russia: Council of European Aerospace Societies, (2018).

[24] P. L. Collen. “Development of a High-Enthalpy Ground Test Facility for Shock-Layer Radiation”. DPhil Thesis. University of Oxford, (2021).

[25] R. N. Gupta et al. “A Review of Reaction Rates and Thermodynamic and Transport Properties for an 11-Species Air Model for Chemical and Thermal Nonequilibrium Calculations to 30000 K”. Tech. rep. NASA-RP-1232. (1990).

[26] S. Williams and D. M. Curry. “Assessing the Orbiter Thermal Environment Using Flight Data”. Journal of Spacecraft and Rockets 21.6 (1984), pp. 534–541. DOI: https://doi.org/10.2514/3.25692.

[27] M. J. Wright et al. “Sizing and Margins Assessment of Mars Science Laboratory Aeroshell Thermal Protection System”. Journal of Spacecraft and Rockets 51.4 (2014), pp. 1125–1138. DOI: https://doi.org/10.2514/1.A32579.

[28] F. S. Milos. “Galileo Probe Heat Shield Ablation Experiment”. Journal of Spacecraft and Rockets 34.6 (1997), pp. 705–713. DOI: https://doi.org/10.2514/2.3293.

[29] K. K. Yoshikawa. “Linearized Theory of Stagnation Point Heat and Mass Transfer at Hypersonic Speeds”. Tech. rep. NASA-TN-D-5246. (1969).

[30] T. A. Hermann et al. “Fluid-Solid Heat Exchange in Porous Media for Transpiration Cooling Systems”. AIAA Scitech 2019 Forum. San Diego, California: American Institute of Aeronautics and Astronautics, (2019). DOI: https://doi.org/10.2514/6.2019-0537.

[31] H. S. Ifti et al. “Laminar Transpiration Cooling Experiments in Hypersonic Flow”. Experiments in Fluids 63.6 (2022), p. 102. DOI: https://doi.org/10.1007/s00348-022-03446-1.

[32] M. Ewenz Rocher. “Application of Transpiration Cooling on Hypersonic Vehicles to Mitigate Material Oxidation”. DPhil Thesis. University of Oxford, (2021).

[33] H. S. Ifti et al. “Flow Characterization of Porous Ultra-High-Temperature Ceramics for Transpiration Cooling”. AIAA Journal 60.5 (2022), pp. 3286–3297. DOI: https://doi.org/10.2514/1.J061009.

[34] D. Dickstein et al. “Optimized Permeability of Microporous Foam for Transpiration Cooling in Hypersonic Leading Edge”. Journal of Thermophysics and Heat Transfer 36.4 (2022), pp. 907–919. DOI: https://doi.org/10.2514/1.T6475.

[35] S. Gulli and L. Maddalena. “Characterization of Complex Porous Structures for Reusable Thermal Protection Systems: Effective-Permeability Measurements”. Journal of Spacecraft and Rockets 51.6 (2014), pp. 1943–1953. DOI: https://doi.org/10.2514/1.A32980.

[36] C. Dittert et al. “Flowfield and Pressure Decay Analysis of Porous Cones”. AIAA Journal 55.3 (2017), pp. 874–882. DOI: https://doi.org/10.2514/1.J055298.

[37] V. König et al. “Numerical and Experimental Investigation of Transpiration Cooling with Carbon/Carbon Characteristic Outflow Distributions”. Journal of Thermophysics and Heat Transfer 33.2 (2019), pp. 449–461. DOI: https://doi.org/10.2514/1.T5457.

[38] T. Langener et al. “Experimental Investigations on Transpiration Cooling for Scramjet Applications Using Different Coolants”. AIAA Journal 49.7 (2011), pp. 1409–1419. DOI: https://doi.org/10.2514/1.J050698.

[39] D. Prokein et al. “Analysis of Anisotropy Effects for Transpiration Cooled CMC Leading Edges Using OpenFOAM”. 20th AIAA International Space Planes and Hypersonic Systems and Technologies Conference. Glasgow, Scotland: American Institute of Aeronautics and Astronautics, (2015). DOI: https://doi.org/10.2514/6.2015-3552.

[40] J. M. Baloyo and Y. and Zhao. “Permeability, Form Drag Coefficient and Heat Transfer Coefficient of Porous Copper”. Heat Transfer Engineering 42.8 (2021), pp. 670–682. DOI: https://doi.org/10.1080/01457632.2020.1723841.

[41] D. E. Glass et al. “Numerical Analysis of Convection / Transpiration Cooling”. Journal of Spacecraft and Rockets 38.1 (2001), pp. 15–20. DOI: https://doi.org/10.2514/2.3666.

[42] S. Schweikert et al. “Characterization of Actively Cooled Porous C/C Wall Segments According to Pressure Loss and Internal Temperature Distribution”. 7th European Workshop on Thermal Protection Systems & Hot Structures. Noordwijk, the Netherlands, (2013).

[43] M. Ewenz Rocher et al. “Pressure-Sensitive Paint Diagnostic to Measure Species Concentration on Transpiration-Cooled Walls”. Experiments in Fluids 63 (2022). DOI: https://doi.org/10.1007/s00348-021-03355-9.

[44] S. Loehle et al. “Measurement of Surface Heat Flux Distribution on a Transpiration Cooled Wedge in a Supersonic High-Enthalpy Air Flow”. AIAA Scitech 2019 Forum. San Diego, California: American Institute of Aeronautics and Astronautics, (2019). DOI: https://doi.org/10.2514/6.2019-1557.

[45] H. Böhrk. “Transpiration-Cooled Hypersonic Flight Experiment: Setup, Flight Measurement, and Reconstruction”. Journal of Spacecraft and Rockets 52.3 (2015), pp. 674–683. DOI: https://doi.org/10.2514/1.A33144.

[46] M. Kuhn and H. Hald. “Application of Transpiration Cooling for Hot Structures”. RESPACE – Key Technologies for Reusable Space Systems. Ed. by A. Gülhan. Berlin, Heidelberg: Springer Berlin Heidelberg, (2008), pp. 82–103. DOI: https://doi.org/10.1007/978-3-540-77819-6_6.

[47] H. Böhrk et al. “Shock Tube Testing of the Transpiration-Cooled Heat Shield Experiment AKTiV”. 18th AIAA/3AF International Space Planes and Hypersonic Systems and Technologies Conference. Tours, France: American Institute of Aeronautics and Astronautics, (2012). DOI: https://doi.org/10.2514/6.2012-5935.

[48] H. Tanno et al. “Transpiration Cooling Experiments in Free-Piston Shock Tunnel HIEST”. 8th European Workshop on Thermal Protection Systems and Hot Structures. Noordwijk, Niederlande, (2016).

[49] H. Böhrk et al. “Heat Balance of a Transpiration-Cooled Heat Shield”. Journal of Thermophysics and Heat Transfer 24.3 (2010), pp. 581–588. DOI: https://doi.org/10.2514/1.47172.

[50] L. T. Chauvin and H. S. Carter. “Exploratory Tests of Transpiration Cooling on a Porous 8 Degree Cone at M=2.05 Using Nitrogen Gas, Helium Gas and Water as the Coolants”. Tech. rep. NACA-RM-L55C29. Langley Field, VA: National Advisory Committee for Aeronautics, (1955).

[51] P. A. Libby and R. J. Cresci. “Experimental Investigation of the Downstream Influence of Stagnation-Point Mass Transfer”. Journal of the Aerospace Sciences 28.1 (1961), pp. 51–64. DOI: https://doi.org/10.2514/8.8852.

[52] P. J. Schneider et al. “Two-Dimensional Transpiration-Cooled Nosetip”. Journal of Spacecraft and Rockets 8.2 (1971), pp. 170–176. DOI: https://doi.org/10.2514/3.30239.

[53] R. Ravichandran et al. “Performance of a Transpiration-Cooled Sharp Leading Edge for Hypersonic Flight”. HiSST: International Conference on High-Speed Vehicle Science Technology. Busan, Korea: Council of European Aerospace Societies, (2024).

[54] C. Selcuk et al. “Porous Tungsten with Controlled Porosity by Low Temperature Sintering”. Powder Metallurgy 48.1 (2005), pp. 17–22. DOI: https://doi.org/10.1179/003258905X37648.

[55] R. Fusaro et al. “Liquid Metals Heat-Pipe Solution for Hypersonic Air-Intake Leading Edge: Conceptual Design, Numerical Analysis and Verification”. Acta Astronautica 197 (2022), pp. 336–352. DOI: https://doi.org/10.1016/j.actaastro.2022.05.034.

[56] J. Wang and L. J. Vandeperre. “Deformation and Hardness of UHTCs as a Function of Temperature”. Ultra-High Temperature Ceramics. John Wiley & Sons, Ltd, (2014). Chap. 10, pp. 236–266. ISBN: 978-1-118-70085-3. DOI: https://doi.org/10.1002/9781118700853.ch10.

[57] T. Hermann et al. “Performance of Transpiration-Cooled Heat Shields for Reentry Vehicles”. AIAA Journal 58.2 (2020), pp. 830–841. DOI: https://doi.org/10.2514/1.J058515.

[58] M. McGilvray et al. “Ultra-High Temperature Ceramics for Transpiration Cooling Applications in Hypersonic Vehicles”. ECI Symposium Series. Ultra-High Temperature Ceramics: Materials For Extreme Environment Applications V. (2022).

[59] R. Hedgecock and L. Vandeperre. “Porous UHTCs for Transpiration Cooling of Hypersonic Flight”. ECI Symposium Series. Ultra-High Temperature Ceramics: Materials For Extreme Environment Applications V. (2022).

[60] Y. Belrhiti et al. “Gel-Casting for Manufacturing Porous Alumina Ceramics with Complex Shapes for Transpiration Cooling”. Advances in Applied Ceramics 122.5-8 (2023), pp. 375–380. DOI: https://doi.org/10.1080/17436753.2023.2265204.

[61] Y. Belrhiti et al. “Brazing ZrB2 Ultra-High-Temperature Ceramics to Zr Metals for Hypersonic Thermal Protection Systems”. International Journal of Applied Ceramic Technology (2025). DOI: https://doi.org/10.1111/ijac.15161.

[62] M. Ewenz Rocher et al. “Testing a Transpiration Cooled Zirconium-Di-Boride Sample in the Plasma Tunnel at IRS”. AIAA Scitech 2019 Forum. San Diego, California: American Institute of Aeronautics and Astronautics, (2019). DOI: https://doi.org/10.2514/6.2019-1552.

[63] D. Glass. “Ceramic Matrix Composite (CMC) Thermal Protection Systems (TPS) and Hot Structures for Hypersonic Vehicles”. 15th AIAA International Space Planes and Hypersonic Systems and Technologies Conference. Dayton, Ohio: American Institute of Aeronautics and Astronautics, (2008). DOI: https://doi.org/10.2514/6.2008-2682.

[64] N. S. Jacobson and D. M. Curry. “Oxidation Microstructure Studies of Reinforced Carbon/Carbon”. Carbon 44.7 (2006), pp. 1142–1150. DOI: https://doi.org/10.1016/j.carbon.2005.11.013.

[65] M. M. Opeka et al. “Oxidation-Based Materials Selection for 2000°C + Hypersonic Aerosurfaces: Theoretical Considerations and Historical Experience”. Journal of Materials Science 39.19 (2004), pp. 5887–5904. DOI: https://doi.org/10.1023/B:JMSC.0000041686.21788.77.

[66] I. Naved et al. “Transpiration-Cooling Heat Transfer Experiments in Laminar and Turbulent Hypersonic Flows”. Journal of Thermophysics and Heat Transfer 37.2 (2023), pp. 281–295. DOI: https://doi.org/10.2514/1.T6626.

[67] P. Kerth et al. “Displacement of Hypersonic Boundary Layer Instability and Turbulence through Transpiration Cooling”. Physics of Fluids 36.3 (2024), p. 034102. DOI: https://doi.org/10.1063/5.0189321.

[68] W. J. Condren et al. “The Combined Effects of Large-Scale Roughness and Mass Injection in Hypersonic Flow”. HiSST: International Conference on High-Speed Vehicle Science Technology. Busan, Korea: Council of European Aerospace Societies, (2024).

[69] M. Ewenz Rocher et al. “Measuring the Concentration of Freestream Species on a Hypersonic Transpiration-Cooled Stagnation Point”. Journal of Spacecraft and Rockets 59.4 (2022), pp. 1380–1387. DOI: https://doi.org/10.2514/1.A35283.

[70] I. Naved et al. “Heat Transfer Measurements of a Transpiration-Cooled Stagnation Point in Transient Hypersonic Flow”. Journal of Thermophysics and Heat Transfer 37.2 (2023), pp. 296–308. DOI: https://doi.org/10.2514/1.T6610.

[71] K. Chakravarthy. “Multiparameter Optical Diagnostics for High-Speed Flow Applications”. PhD thesis. DPhil Thesis: University of Oxford, (2021).

[72] M. D. M. Innocentini et al. “Influence of Air Compressibility on the Permeability Evaluation of Refractory Castables”. Journal of the American Ceramic Society 83.6 (2000), pp. 1536–1538. DOI: https://doi.org/10.1111/j.1151-2916.2000.tb01426.x.

[73] S. Ergun. “Fluid Flow Through Packed Columns”. Chemical Engineering Progress 48.2 (1952), p. 89.

[74] J. Florio et al. “Characterization of Forced Convection Heat Transfer in Decomposing, Glass-Filled Polymer Composites”. Journal of Composite Materials 25.11 (1991), pp. 1515–1539. DOI: https://doi.org/10.1177/002199839102501108.

[75] P. Kerth. “Effect of Transpiration Cooling on Boundary Layer Transition for Hypersonic Flight”. DPhil Thesis. University of Oxford, (2023).

[76] F. Miró Miró et al. “Effect of Wall Blowing on Hypersonic Boundary-Layer Transition”. AIAA Journal 57.4 (2019), pp. 1567–1578. DOI: https://doi.org/10.2514/1.J057604.

[77] S. Gulli and L. Maddalena. “Arc-Jet Testing of a Variable-Transpiration-Cooled and Uncoated Carbon–Carbon Nose Cone”. Journal of Spacecraft and Rockets 56.3 (2019), pp. 780–788. DOI: https://doi.org/10.2514/1.A34176.

[78] A. Van Foreest et al. “Transpiration Cooling Using Liquid Water”. Journal of Thermophysics and Heat Transfer 23.4 (2009), pp. 693–702. DOI: https://doi.org/10.2514/1.39070.

[79] T. Reimer et al. “Arc Jet Testing of CMC Samples with Transpiration Cooling”. 44th AIAA Thermophysics Conference. San Diego, CA: American Institute of Aeronautics and Astronautics, (2013). DOI: https://doi.org/10.2514/6.2013-2904.

[80] L. Zhao et al. “An Experimental Investigation on Transpiration Cooling under Supersonic Condition Using a Nose Cone Model”. International Journal of Thermal Sciences 84 (2014), pp. 207–213. DOI: https://doi.org/10.1016/j.ijthermalsci.2014.05.019.

[81] C. C. Pappas and G. Lee. “Heat Transfer and Pressure on a Hypersonic Blunt Cone with Mass Addition”. AIAA Journal 8.5 (1970), pp. 954–956. DOI: https://doi.org/10.2514/3.5801.

[82] S. D. Brody. “Numerical Simulation of Stagnation Point Transpiration Cooling in Non-Equilibrium Hypersonic Flow”. DPhil Thesis. University of Oxford, (2025).

[83] J. C. Dunavant and P. E. Everhart. “Exploratory Heat-Transfer Measurements at Mach 10 on a 7.5 Deg Total-Angle Cone Downstream of a Region of Air and Helium Transpiration Cooling”. Tech. rep. NASA-TN-D-5554. Hampton, VA, United States: National Aeronautics and Space Administration, (1969).

[84] A. Gollnick. “An Experimental Study of Thermal Diffusion Effects on a Partially Porous Mass Transfer-Cooled Hemisphere”. International Journal of Heat and Mass Transfer 7.7 (1964), pp. 699–708. DOI: https://doi.org/10.1016/0017-9310(64)90001-8.

[85] A. Gülhan and S. Braun. “An Experimental Study on the Efficiency of Transpiration Cooling in Laminar and Turbulent Hypersonic Flows”. Experiments in Fluids 50.3 (2011), pp. 509–525. DOI: https://doi.org/10.1007/s00348-010-0945-6.

[86] H. S. Ifti et al. “Numerical Simulation of Transpiration Cooling in a Laminar Hypersonic Boundary Layer”. Journal of Spacecraft and Rockets 59.5 (2022), pp. 1726–1735. DOI: https://doi.org/10.2514/1.A35325.

[87] T. Hermann et al. “Design Principles for Transpiration Cooled Ceramic Sharp Leading Edges (In Review)” (2025).

[88] R. T. Swann and C. M. Pittman. “Numerical Analysis of the Transient Response of Advanced Thermal Protection Systems for Atmospheric Entry”. Tech. rep. NASA TN D-1379. NASA Langley Research Center, Hampton, VA, United States: National Aeronautics and Space Administration, (1962).

[89] J. G. Marvin and R. B. Pope. “Laminar Convective Heating and Ablation in the Mars Atmosphere.” AIAA Journal 5.2 (1967), pp. 240–248. DOI: https://doi.org/10.2514/3.3948.

[90] M. E. Tauber. “A Review of High-Speed, Convective, Heat-Transfer Computation Methods”. Tech. rep. NASA-TP-2914. NASA Ames Research Center, Moffett Field, CA, United States: National Aeronautics and Space Administration, (1989).

[91] H. T. Howe and Y. S. Sheaffer. “Mass Addition in the Stagnation Region for Velocity up to 50000 Feet per Second”. Tech. rep. NASA-TR-R-207. NASA Ames Research Centre, Moffett Field, CA, United States: National Aeronautics and Space Administration, (1964).

[92] G. E. Kaattari. “Effects of Mass Addition on Blunt-Body Boundary-Layer Transition and Heat Transfer”. Tech. rep. NASA-TP-1139. NASA Ames Research Center, Moffett Field, CA, United States: National Aeronautics and Space Administration, (1978).

[93] S. Brody et al. “Numerical Simulation of Transpiration Cooling on Stagnation Line in Thermochemical Non-Equilibrium”. AIAA SciTech 2024 Forum. Orlando, FL: American Institute of Aeronautics and Astronautics, (2024). DOI: https://doi.org/10.2514/6.2024-0648.

[94] E. R. G. Eckert et al. “Mass-Transfer Cooling of a Laminar Boundary Layer by Injection of a Light-Weight Foreign Gas”. Journal of Jet Propulsion 28.1 (1958), pp. 34–39. DOI: https://doi.org/10.2514/8.7218.

[95] W. Dahmen et al. “Numerical Simulation of Transpiration Cooling through Porous Material”. International Journal for Numerical Methods in Fluids 76.6 (2014), pp. 331–365. DOI: https://doi.org/10.1002/fld.3935.

[96] R. J. Goldstein. “Film Cooling”. Advances in Heat Transfer. Ed. by T. F. Irvine and J. P. Hartnett. 7. Elsevier, (1971), pp. 321–379. ISBN: 0065-2717. DOI: https://doi.org/10.1016/S0065-2717(08)70020-0.

[97] K. Fujiwara et al. “Review on Film Cooling in High-Speed Flows”. 31st International Symposium on Shock Waves 2. Ed. by A. Sasoh et al. Cham: Springer International Publishing, (2019), pp. 939–946. DOI: https://doi.org/10.1007/978-3-319-91017-8_118.

[98] K. A. Heufer and H. Olivier. “Experimental and Numerical Study of Cooling Gas Injection in Laminar Supersonic Flow”. AIAA Journal 46.11 (2008), pp. 2741–2751. DOI: https://doi.org/10.2514/1.34218.

[99] R. A. Hartunian and D. J. Spencer. “Experimental Results for Massive Blowing Studies.” AIAA Journal 5.8 (1967), pp. 1397–1401. DOI: https://doi.org/10.2514/3.4211.

[100] J. G. Marvin and C. M. Akin. “Combined Effects of Mass Addition and Nose Bluntness on Boundary-Layer Transition”. AIAA Journal 8.5 (1970), pp. 857–863. DOI: https://doi.org/10.2514/3.5778.

[101] C. R. Wimberly et al. “Transpiration and Film Cooling Effects for a Slender Cone in Hypersonic Flow”. AIAA Journal 8.6 (1970), pp. 1032–1038. DOI: https://doi.org/10.2514/3.5827.

[102] C. J. Stalmach Jr et al. “A Study of Boundary Layer Transition on Outgassing Cones in Hypersonic Flow”. Tech. rep. NASA-CR-1908. Dallas, TX, United States: Vought Aeronautics Company, (1971).

[103] C. Pappas and G. Lee. “Effects of Mass Addition of Various Gases on the Heat Transfer and Surface Pressures on a Blunt Cone in Hypersonic Flow.” 2nd Fluid and Plasma Dynamics Conference. San Francisco, CA, United States: American Institute of Aeronautics and Astronautics, (1969). DOI: https://doi.org/10.2514/6.1969-716.

[104] P.-X. Jiang et al. “Experimental Investigation of Combined Transpiration and Film Cooling for Sintered Metal Porous Struts”. International Journal of Heat and Mass Transfer 108 (2017), pp. 232–243. DOI: https://doi.org/10.1016/j.ijheatmasstransfer.2016.12.014.

[105] A. Brune et al. “Variable Transpiration Cooling Effectiveness in Laminar and Turbulent Flows for Hypersonic Vehicles”. AIAA Journal 53.1 (2015), pp. 176–189. DOI: https://doi.org/10.2514/1.J053053.

[106] L. Shen and J. Wang. “Numerical Investigation on the Optimization of Local Transpiration Cooling Effectiveness”. Applied Thermal Engineering 127 (2017), pp. 58–69. DOI: https://doi.org/10.1016/j.applthermaleng.2017.08.017.

[107] R. Ding et al. “Numerical Investigation on a Double Layer Combined Cooling Structure for Aerodynamic Heat Control of Hypersonic Vehicle Leading Edge”. Applied Thermal

Engineering 169 (2020), p. 114949. DOI: https://doi.org/10.1016/j.applthermaleng.2020.114949.

[108] J. Connolly. "Geometry Dependence of Transpiration Cooling for Hypersonic Systems". AIAA Scitech 2021 Forum. Online Event: American Institute of Aeronautics and Astronautics, (2021). DOI: https://doi.org/10.2514/6.2021-1519.

[109] M. Ewenz Rocher et al. "Correlation for Species Concentration on a Hypersonic Stagnation Point with Mass Injection". AIAA Journal 60.5 (2022), pp. 2798–2809. DOI: https://doi.org/10.2514/1.J061159.

[110] H. S. Ifti et al. "Analytical Model of Transpired-Coolant Concentration at Downstream Wall in High-Speed Laminar Flow". AIAA Journal 61.8 (2023), pp. 3541–3550. DOI: https://doi.org/10.2514/1.J062199.

[111] E. R. van Driest. "Investigation of Laminar Boundary Layer in Compressible Fluids Using the Crocco Method". Tech. rep. NACA-TN-2597. Washington D.C.: North American Aviation Inc., (1952).

[112] E. R. V. van Driest. "The Problem of Aerodynamic Heating". Aerodynamic Aspects Heating Session, National Summer Meeting. Los Angeles, CA, United States: Institute of the Aeronautical Sciences Los Angeles, (1956).

[113] T. Hermann et al. "Tool for Rapid Transient Transpiration-Cooled Reentry Simulation". AIAA Journal 58.2 (2020), pp. 842–853. DOI: https://doi.org/10.2514/1.J058516.

[114] W. M. Kays and M. E. Crawford. "Convective Heat and Mass Transfer". 3rd. New York, NY, United States: McGraw Hill, (1993). ISBN: 978-0-07-033721-3.

[115] J. A. Fay and F. R. Riddell. "Theory of Stagnation Point Heat Transfer in Dissociated Air". Journal of the Aerospace Sciences 25.2 (1958), pp. 73–85. DOI: https://doi.org/10.2514/8.7517.

[116] L. Lees. "Laminar Heat Transfer Over Blunt-Nosed Bodies at Hypersonic Flight Speeds". Journal of Jet Propulsion 26.4 (1956), pp. 259–269. DOI: https://doi.org/10.2514/8.6977.

[117] E. P. Volchkov et al. "Film Cooling by Injection into a Turbulent Boundary Layer". Journal of Applied Mechanics and Technical Physics 8.2 (1971), pp. 63–64. DOI: https://doi.org/10.1007/BF00918038.

[118] F. Hufgard et al. "Heat Flux Determination from Pressure Data for a Transpiration Cooling Environment". Heat Transfer Engineering 45.12-13 (2024), pp. 1106–1116. DOI: https://doi.org/10.1080/01457632.2023.2241178.

[119] I. Naved. "The Application of Transpiration Cooling as a Thermal Protection System for Hypersonic Vehicles". DPhil Thesis. University of Oxford, (2022).

[120] W. J. Condren et al. "A Method for IR Measurement of Large Scale Roughened Surfaces in Hypersonic Flow". AIAA SciTech 2023 Forum. National Harbor, MD & Online: American Institute of Aeronautics and Astronautics, (2023). DOI: https://doi.org/10.2514/6.2023-2443.

[121] H. D. Baehr and K. Stephan. "Heat and Mass Transfer". Berlin, Heidelberg: Springer Berlin Heidelberg, (2011). ISBN: 978-3-642-20020-5 978-3-642-20021-2. DOI: https://doi.org/10.1007/978-3-642-20021-2.

[122] J. Heikkila. “Geometric Camera Calibration Using Circular Control Points”. IEEE Transactions on Pattern Analysis and Machine Intelligence 22.10 (2000), pp. 1066–1077. DOI: https://doi.org/10.1109/34.879788.

[123] A. Watkins et al. “Development of next Generation Lifetime PSP Imaging Systems”. 20th International Congress on Instrumentation in Aerospace Simulation Facilities, 2003. Gottingen, Germany: IEEE, (2003), pp. 372–382. DOI: https://doi.org/10.1109/ICIASF.2003.1274889.

[124] ISSI. “TurboFIB-PSP-Datasheet”. (n.d.). https://innssi.com/wp-content/uploads/Pressure_Sensitive_Paint/TurboFIB/Documentation/TurboFIB-TF-XXX-PSP-Datasheet.pdf (retrieved: 23/2/2025).

[125] M. Kameda et al. “Adsorptive Pressure-Sensitive Coatings on Porous Anodized Aluminium”. Measurement Science and Technology 15.3 (2004), p. 489. DOI: https://doi.org/10.1088/0957-0233/15/3/001.

[126] M. K. Quinn et al. “Pressure-Sensitive Paint: Effect of Substrate”. Sensors 11.12 (2011), pp. 11649–11663. DOI: https://doi.org/10.3390/s111211649.

[127] R. Ravichandran et al. “Experiments on a Transpiration-Cooled Sharp Leading Edge in Hypersonic Flow”. HiSST: International Conference on High-Speed Vehicle Science Technology. Tours, France: Council of European Aerospace Societies, (2025).

[128] M. McGilvray et al. “The Oxford High Density Tunnel”. International Space Planes and Hypersonic Systems and Technologies Conferences. Glasgow, Scotland: American Institute of Aeronautics and Astronautics, (2015). DOI: https://doi.org/10.2514/6.2015-3548.

[129] J. Hillyer et al. “Commissioning of PALM: A New Mode of Operation Extending Test Times in Ludwieg Tunnels”. AIAA SciTech 2024 Forum. Orlando, FL: American Institute of Aeronautics and Astronautics, (2024). DOI: https://doi.org/10.2514/6.2024-2754.

[130] D. S. Smith et al. “Thermal Conductivity of Porous Materials”. Journal of Materials Research 28.17 (2013), pp. 2260–2272. DOI: https://doi.org/10.1557/jmr.2013.179.

[131] J. Schlacher et al. “Thermal Shock Resistant 3D-printed Ceramic Components through Spatially Tailored Porosity”. Additive Manufacturing 96 (2024), p. 104582. DOI: https://doi.org/10.1016/j.addma.2024.104582.

[132] S. Nohut et al. “Lithography-Based Additive Manufacturing of Porosity Graded Alumina”. Additive Manufacturing Letters 3 (2022), p. 100060. DOI: https://doi.org/10.1016/j.addlet.2022.100060.

[133] S. Nohut et al. “3D-printed Alumina-Based Ceramics with Spatially Resolved Porosity”. International Journal of Applied Ceramic Technology 21.1 (2024), pp. 89–104. DOI: https://doi.org/10.1111/ijac.14512.

[134] CMT Materials. “Metapor Machining Guide”. (n.d.). https://cmt.globecomposite.com/metapor-air-permeable-composites (retrieved: 27/12/2024).

[135] A. Ressler et al. “Cleaning Strategies for 3D-printed Porous Scaffolds Used for Bone Regeneration Fabricated via Ceramic Vat Photopolymerization”. Ceramics International 50.24, Part A (2024), pp. 53107–53119. DOI: https://doi.org/10.1016/j.ceramint.2024.10.160.

[136] R. Ravichandran et al. “Aerodynamic Effects and Heat Flux Augmentation of a Transpiration Cooled Hypersonic Sharp Leading Edge”. AIAA SciTech 2023 Forum. National Harbor, MD & Online: American Institute of Aeronautics and Astronautics, (2023). DOI: https://doi.org/10.2514/6.2023-0437.

[137] H H Bruun. “Hot-Wire Anemometry: Principles and Signal Analysis”. Measurement Science and Technology 7.10 (1996), p. 024. DOI: https://doi.org/10.1088/0957-0233/7/10/024.

[138] M. L. G. Oldfield. “Impulse Response Processing of Transient Heat Transfer Gauge Signals”. Journal of Turbomachinery 130.2 (2008), p. 021023. DOI: https://doi.org/10.1115/1.2752188.

[139] W. Ivison. “Quantifying the Effect of Protuberances and Interfaces from an Aero-Thermal-Structural Design Perspective”. DPhil Thesis. University of Oxford, (2024).

[140] W. Ivison et al. “Heat Flux Augmentation Caused by Surface Imperfections in Turbulent Boundary Layers”. HiSST: International Conference on High-Speed Vehicle Science Technology. Busan, Korea: Council of European Aerospace Societies, (2024).

[141] ISSI. “Painting Instructions For TurboFIB PSP”. (n.d.). https://innssi.com/wp-content/uploads/Pressure_Sensitive_Paint/TurboFIB/Documentation/Painting-Instructions-For-TurboFIB-PSP.pdf (retrieved: 16/1/2025).

[142] “U.S. Standard Atmosphere, 1976”. Tech. rep. NOAA-S/T-76-1562. (1976).

[143] J. Hillyer et al. “Enhancing the Test Time Performance of Ludwieg Tunnels”. AIAA SciTech 2024 Forum. Orlando, FL: American Institute of Aeronautics and Astronautics, (2024). DOI: https://doi.org/10.2514/6.2024-2754.

[144] R. Gollan and P. Jacobs. “About the Formulation, Verification and Validation of the Hypersonic Flow Solver Eilmer”. International Journal for Numerical Methods in Fluids 73.1 (2013), pp. 19–57. DOI: https://doi.org/10.1002/fld.3790.

[145] P. Jacobs and R. Gollan. “Implementation of a Compressible-Flow Simulation Code in the D Programming Language”. Applied Mechanics and Materials 846 (2016), pp. 54–60. DOI: https://doi.org/10.4028/www.scientific.net/AMM.846.54.

[146] K. A. Damm et al. “Application of a Jacobian-Free Newton-Krylov Method to the Simulation of Hypersonic Flows”. AIAA SciTech 2023 Forum. National Harbor, MD & Online: American Institute of Aeronautics and Astronautics, (2023). DOI: https://doi.org/10.2514/6.2023-2295.

[147] G. O. Roberts. “Computational Meshes for Boundary Layer Problems”. Second International Conference on Numerical Methods in Fluid Dynamics. Ed. by M. Holt. 8. Berlin: Springer Berlin, (1971), pp. 171–177. DOI: https://doi.org/10.1007/3-540-05407-3_27.

[148] J. Meinert et al. “Turbulent Boundary Layers with Foreign Gas Transpiration”. Journal of Spacecraft and Rockets 38.2 (2001), pp. 191–198. DOI: https://doi.org/10.2514/2.3693.

[149] K. K. Yoshikawa. “Linearized Theory of Stagnation Region Skin Friction and Mass Transfer at Hypersonic Speeds”. Tech. rep. NASA-TN-D-6262. NASA Ames Research Center, Moffett Field, CA, United States: National Aeronautics and Space Administration, (1971).

[150] C. C. Pappas and A. F. Okuno. "Measurements of Skin Friction of the Compressible Turbulent Boundary Layer on a Cone with Foreign Gas Injection". Journal of the Aerospace Sciences 27.5 (1960), pp. 321–333. DOI: https://doi.org/10.2514/8.8533.

[151] A. Richards. "University of Oxford Advanced Research Computing Facility" (2015). DOI: https://doi.org/10.5281/zenodo.22558.

[152] C. A. Steeves et al. "Feasibility of Metallic Structural Heat Pipes as Sharp Leading Edges for Hypersonic Vehicles". Journal of Applied Mechanics 76.3 (2009), p. 031014. DOI: https://doi.org/10.1115/1.3086440.

[153] H. S. Mickley et al. "Heat, Mass, and Momentum Transfer for Flow Over a Flat Plate With Blowing or Suction". Tech. rep. NACA-TN-3208. Massachusetts Institute of Technology, (1954).

[154] R. J. Cresci. "Theoretical Analysis of the Downstream Influence of Mass Transfer in a Stagnation Region". International Journal of Heat and Mass Transfer 5.9 (1962), pp. 837–857. DOI: https://doi.org/10.1016/0017-9310(62)90183-7.

[155] C. H. Lewis et al. "Effects of Mass Transfer and Chemical Nonequilibrium on Slender Blunted Cone Pressure and Pressure and Heat-Transfer Distributions at M = 13.2". Tech. rep. AEDC-TR-69-214. Arnold Air Force Station, TN, United States: Arnold Engineering Development Center, (1968).

[156] S. Luo et al. "Effects of Coolants of Double Layer Transpiration Cooling System in the Leading Edge of a Hypersonic Vehicle". Frontiers in Energy Research 9 (2021), p. 756820. DOI: https://doi.org/10.3389/fenrg.2021.756820.

[157] R. J. Goldstein et al. "Film Cooling With Normal Injection Into a Supersonic Flow". Journal of Engineering for Industry 90.4 (1968), pp. 584–588. DOI: https://doi.org/10.1115/1.3604692.

[158] M. Hombsch and H. Olivier. "Film Cooling in Laminar and Turbulent Supersonic Flows". Journal of Spacecraft and Rockets 50.4 (2013), pp. 742–753. DOI: https://doi.org/10.2514/1.A32346.

[159] E. Martelli et al. "Numerical Analysis of Film Cooling in Advanced Rocket Nozzles". AIAA Journal 47.11 (2009), pp. 2558–2566. DOI: https://doi.org/10.2514/1.39217.

[160] E. R. Eckert. "Survey on Heat Transfer at High Speeds". Tech. rep. ARL-189. Wright-Patterson Air Force Base: Aeronautical Research Laboratory, (1961).

[161] R. B. Bird et al. "Appendix E. Tables for Prediction of Transport Properties". Transport Phenomena. Revised 2nd Edition. New York, NY, United States: Wiley, (1960). ISBN: 978-0-470-11539-8.

[162] N. N. Gibbons et al. "Eilmer: An Open-Source Multi-Physics Hypersonic Flow Solver". Computer Physics Communications 282 (2023), p. 108551. DOI: https://doi.org/10.1016/j.cpc.2022.108551.

[163] "Gas Dynamics Toolkit". (n.d.). https://gdtk.uqcloud.net/ (retrieved: 15/3/2025).

[164] P. Jacobs et al. "Eilmer's Theory Book: Basic Models for Gas Dynamics and Thermochemistry". Tech. rep. Mechanical Engineering Report 2010/09. (2010).

[165] B. J. McBride et al. “NASA Glenn Coefficients for Calculating Thermodynamic Properties of Individual Species”. Tech. rep. TP-2002-211556. NASA Glenn Research Center: National Aeronautics and Space Administration, (2002).

[166] S. Gordon and B. J. McBride. “Computer Program for Calculation of Complex Chemical Equilibrium - I. Analysis”. Tech. rep. Cleveland, Ohio: National Aeronautics and Space Administration, (1996).

[167] R. Thompson and P. Gnoffo. “Implementation of a Blowing Boundary Condition in the LAURA Code”. 46th AIAA Aerospace Sciences Meeting and Exhibit. Reno, NV, United States: American Institute of Aeronautics and Astronautics, (2008). DOI: https://doi.org/10.2514/6.2008-1243.

[168] L. Binkele. “The High-Temperature Lorenz Number of Tungsten; an Analysis of Recent Results on the Thermal and Electrical Conductivity over the Temperature Range 300 to 1300 K”. High Temp. - High Pressures 15.5 (1983), pp. 525–531.

[169] C. Y. Ho et al. “Thermal Conductivity of the Elements”. Journal of Physical and Chemical Reference Data 1.2 (1972), pp. 279–421. DOI: https://doi.org/10.1063/1.3253100.

[170] COMSOL Inc. “Material Library User’s Guide”. (2024). https://doc.comsol.com/6.1/doc/com.comsol.help.matlib/MaterialLibraryUsersGuide.pdf (retrieved: 17/5/2025).

[171] M. Bauccio. “ASM Metals Reference Book”. ASM international, (1993). ISBN: 0-87170-478-1.

[172] J. Benton et al. “Design & Manufacture of a High Performance High Mass Efficient Gas Tank for the Vega Avum”. 43rd AIAA/ASME/SAE/ASEE Joint Propulsion Conference & Exhibit. American Institute of Aeronautics and Astronautics, (2007). DOI: https://doi.org/10.2514/6.2007-5500.

[173] D. M. Ray et al. “High Pressure Composite Overwrapped Pressure Vessel (COPV) Development Tests at Cryogenic Temperatures”. 49th AIAA/ASME/ASCE/AHS/ASC Structures, Structural Dynamics, and Materials Conference. New York, NY, United States: American Institute of Aeronautics and Astronautics, (2008). DOI: https://doi.org/10.2514/6.2008-1912.

[174] M. Zaccara et al. “A General Procedure for Infrared Thermography Heat Transfer Measurements in Hypersonic Wind Tunnels”. International Journal of Heat and Mass Transfer 163 (2020), p. 120419. DOI: https://doi.org/10.1016/j.ijheatmasstransfer.2020.120419.

[175] J. Taler and P. Duda. “Solving Direct and Inverse Heat Conduction Problems”. 1st ed. Springer Berlin, Heidelberg, (2006). ISBN: 978-3-540-33470-5. DOI: https://doi.org/10.1007/978-3-540-33471-2.

[176] R. B. Hetnarski, ed. “Encyclopedia of Thermal Stresses”. 1st ed. Springer Dordrecht, (2014). ISBN: 978-94-007-2738-0. DOI: https://doi.org/10.1007/978-94-007-2739-7.

[177] Schultz and Jones. “Heat Transfer Measurements In Short Duration Hypersonic Facilities”. Tech. rep. AGARD-AG-165. North Atlantic Treaty Organisation, (1973).

[178] Y. Wada and M.-S. Liou. “A Flux Splitting Scheme with High-Resolution and Robustness for Discontinuities”. 32nd Aerospace Sciences Meeting and Exhibit. Reno, NV, United

States: American Institute of Aeronautics and Astronautics, (1994). DOI: https://doi.org/10.2514/6.1994-83.

[179] Y. Wada and M.-S. Liou. "An Accurate and Robust Flux Splitting Scheme for Shock and Contact Discontinuities". SIAM Journal on Scientific Computing 18.3 (1997), pp. 633–657. DOI: https://doi.org/10.1137/S1064827595287626.

[180] G. D. van Albada et al. "A Comparative Study of Computational Methods in Cosmic Gas Dynamics". Upwind and High-Resolution Schemes. Ed. by M. Y. Hussaini et al. Berlin, Heidelberg: Springer Berlin Heidelberg, (1997), pp. 95–103. ISBN: 978-3-642-64452-8. DOI: https://doi.org/10.1007/978-3-642-60543-7_6.

[181] T. W. Drayna. "Design and Optimization of Hypersonic Inward-Turning Inlets". PhD thesis. University of Minnesota, (2011).

[182] A. Haselbacher and J. Blazek. "On the Accurate and Efficient Discretisation of the Navier-Stokes Equations on Mixed Grids". 14th Computational Fluid Dynamics Conference. Norfolk,VA, United States: American Institute of Aeronautics and Astronautics, (1999). DOI: https://doi.org/10.2514/6.1999-3363.

[183] K. A. Damm. "Adjoint-Based Aerodynamic Design Optimisation in Hypersonic Flow". PhD thesis. The University of Queensland, (2020). DOI: https://doi.org/10.14264/uql.2020.207.

[184] Y. Saad and M. H. Schultz. "GMRES: A Generalized Minimal Residual Algorithm for Solving Nonsymmetric Linear Systems". SIAM Journal on Scientific and Statistical Computing 7.3 (1986), pp. 856–869. DOI: https://doi.org/10.1137/0907058.

[185] N. N. Gibbons et al. "Flight Regime Limits of a Hypersonic Vehicle Using Electron Transpiration Cooling". AIAA Ascend 2021. Las Vegas, Nevada & Virtual: American Institute of Aeronautics and Astronautics, (2021). DOI: https://doi.org/10.2514/6.2021-4141.

[186] G. Simeonides. "Generalized Reference Enthalpy Formulations and Simulation of Viscous Effects in Hypersonic Flow". Shock Waves 8.3 (1998), pp. 161–172. DOI: https://doi.org/10.1007/s001930050109.

APPENDIX A

Supplementary Experimental Material

This appendix contains additional material pertinent to the experimental chapters—Chapters 3 and 4. It includes annotated photographs of the transpiration-cooled leading edge (TCLE) model and experimental setup during HDT testing, simulations of the outflow under off-design conditions, and details of the optical post-processing methodology.

A.1 Additional Leading Edge Outflow Simulations 216

A.2 Additional Experimental Photographs 218

A.3 Post-Processing of Experimental Optical Data 222

A.1 Additional Leading Edge Outflow Simulations

The following figures present simulations of the designed leading-edge architecture operating under freestream and blowing conditions different from the design conditions presented in Section 3.2. These simulations were performed to assess the off-design performance of the designed leading edge. These conditions correspond to cases that were subsequently tested experimentally in Chapter 4. Each parameter of the design condition (freestream Condition A in Table 4.2 with nitrogen coolant at B_h=1.2) was varied independently in the plots below, with changes specified in the figure captions.

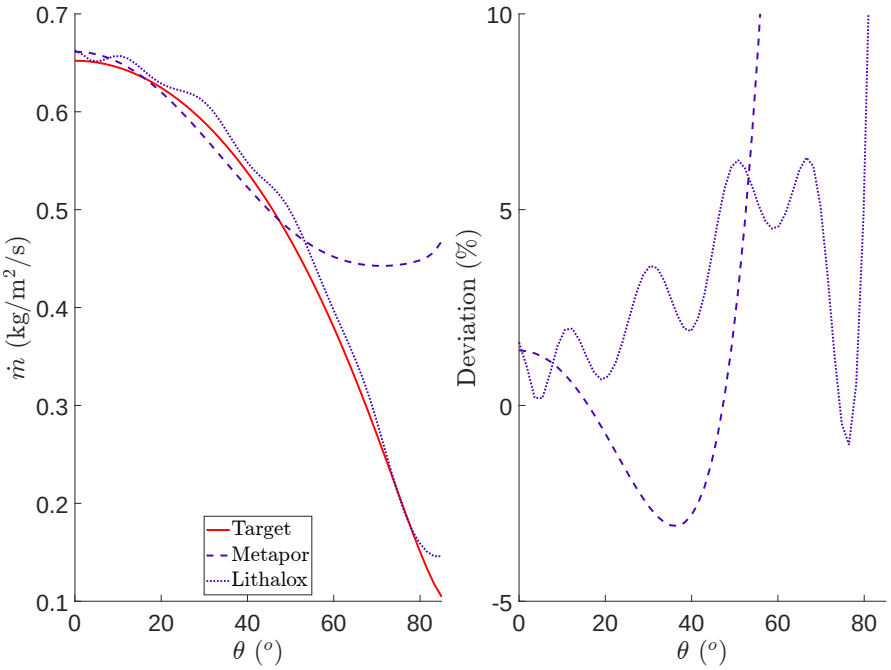


Figure A.1: Lower Reynolds number (Condition B in Table 4.2).

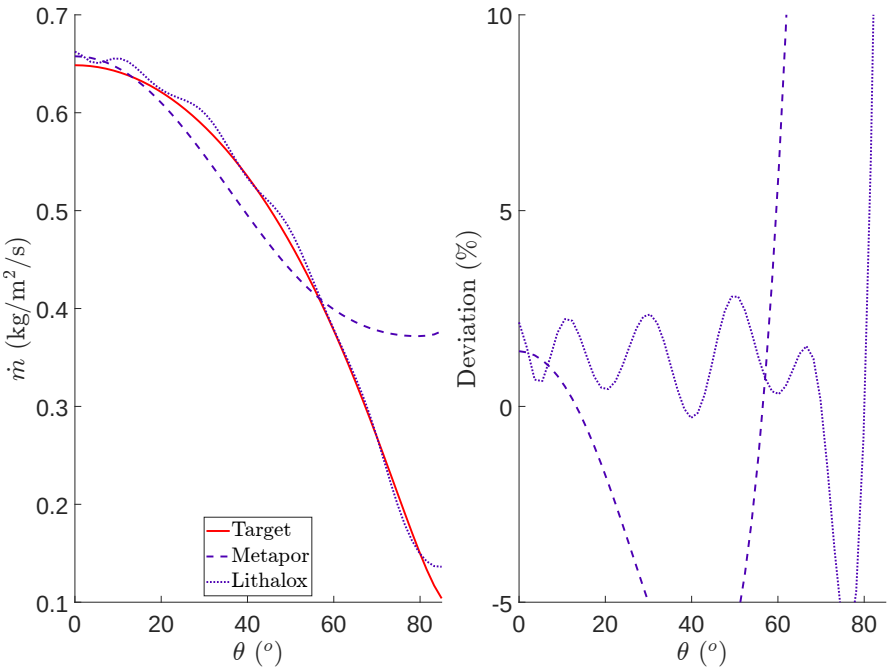


Figure A.2: Higher blowing (B_h=1.6) N_2 injection.

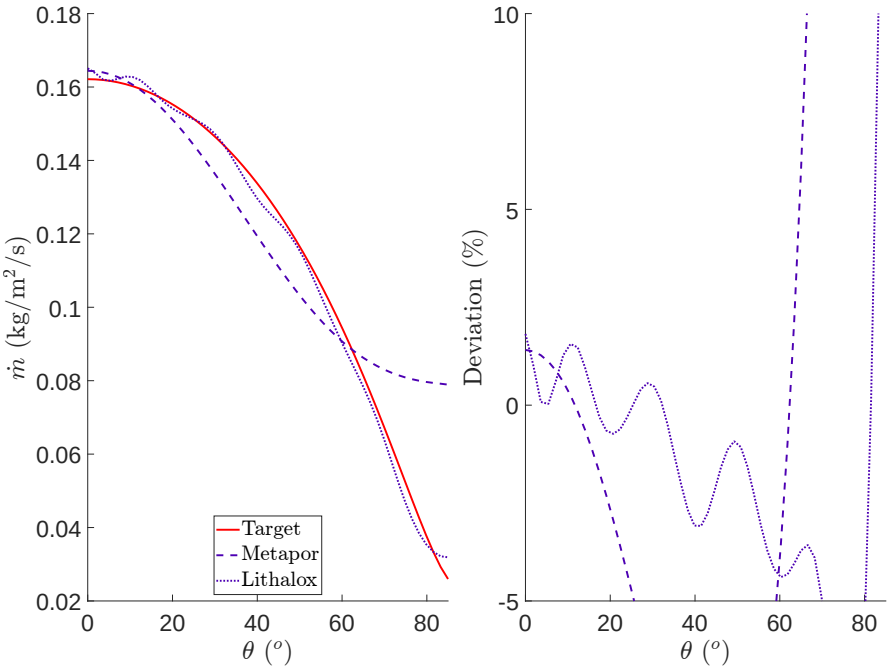


Figure A.3: Helium coolant (at $B_h = 0.4$)

A.2 Additional Experimental Photographs

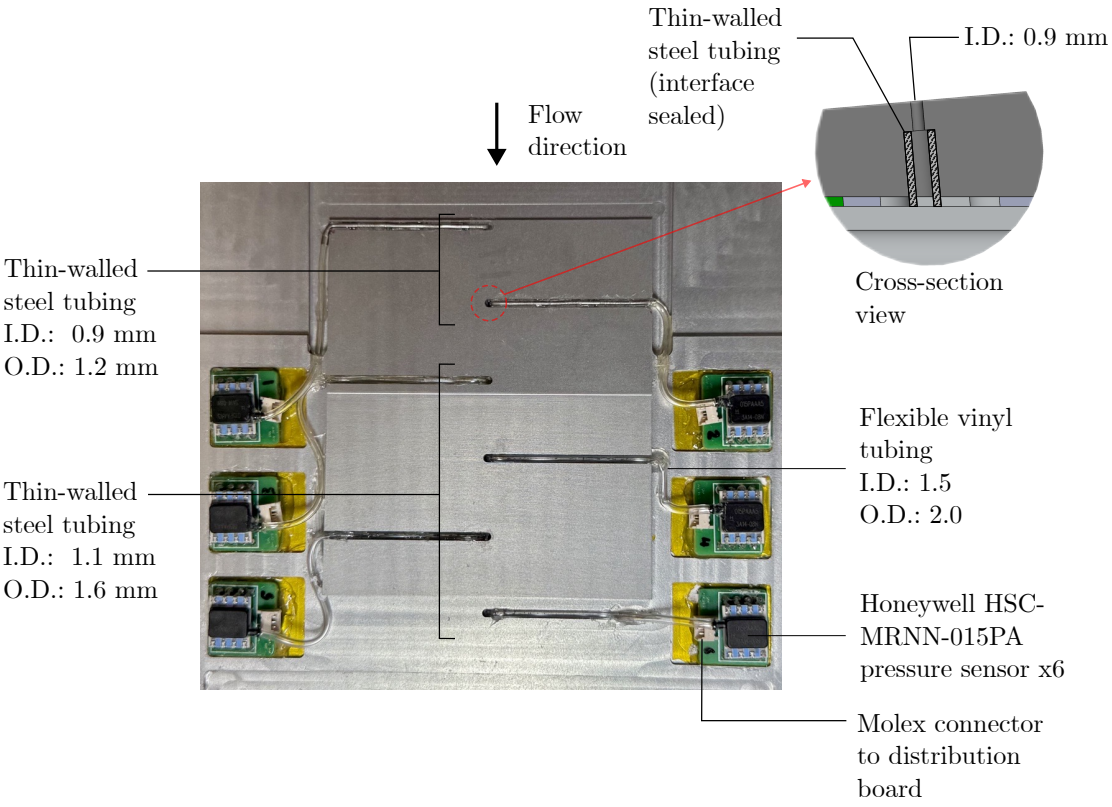


Figure A.4: Annotated photograph of the underside of the surface pressure tappings. Sensors were positioned laterally, as the model's centreline was occupied by the plenum. Thin-walled, small-diameter tubing connected the tapping holes to the sensors via channels in the plate. Tubing length was minimised to improve response time, and signal wiring was routed to a distribution board in the aftbody.

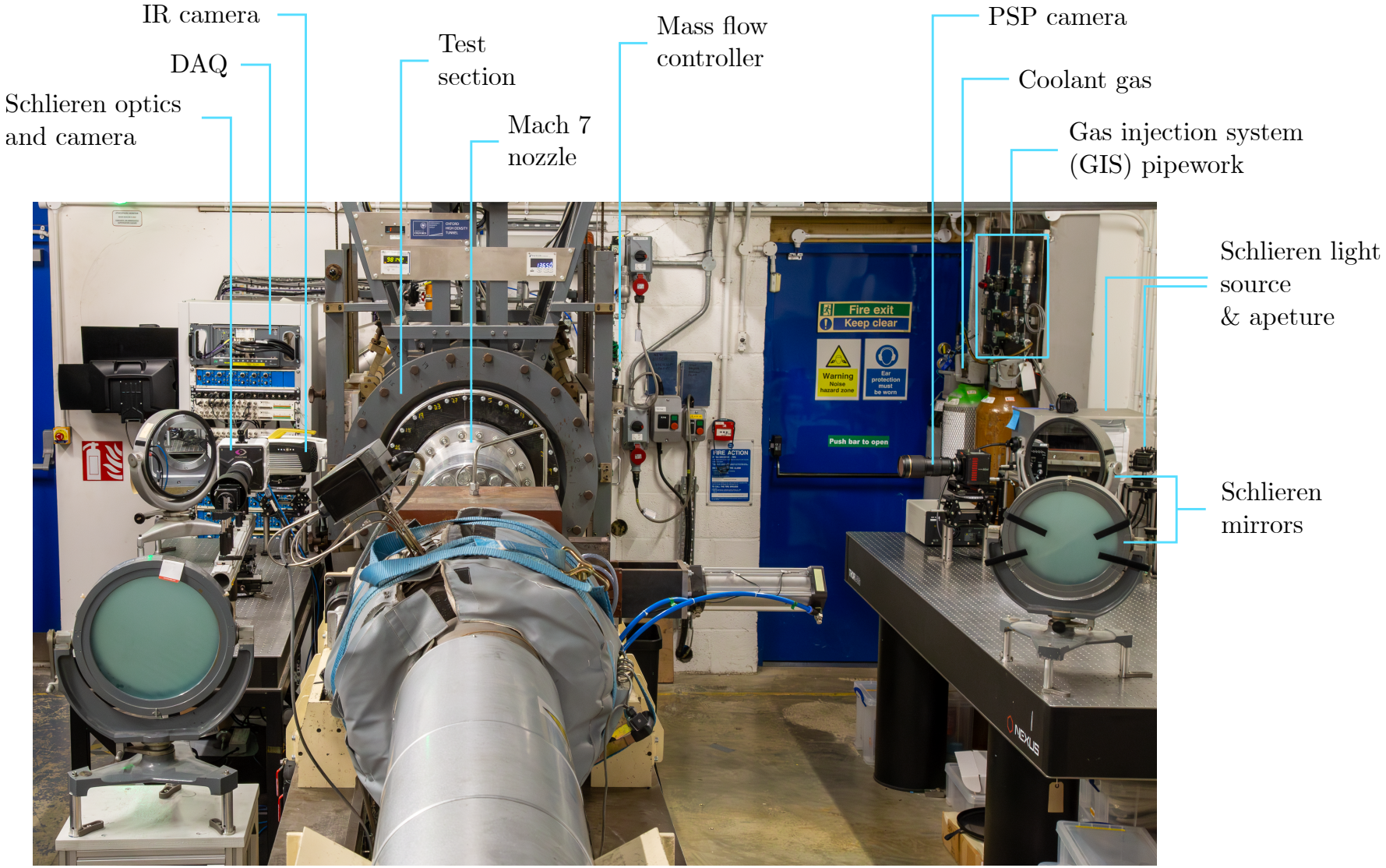


Figure A.5: Downstream view of the optical layout and infrastructure for HDT testing. During calibration and testing, the IR camera is covered by an optically opaque shroud to block ambient light, not pictured. The schlieren data collected is not presented in this work.

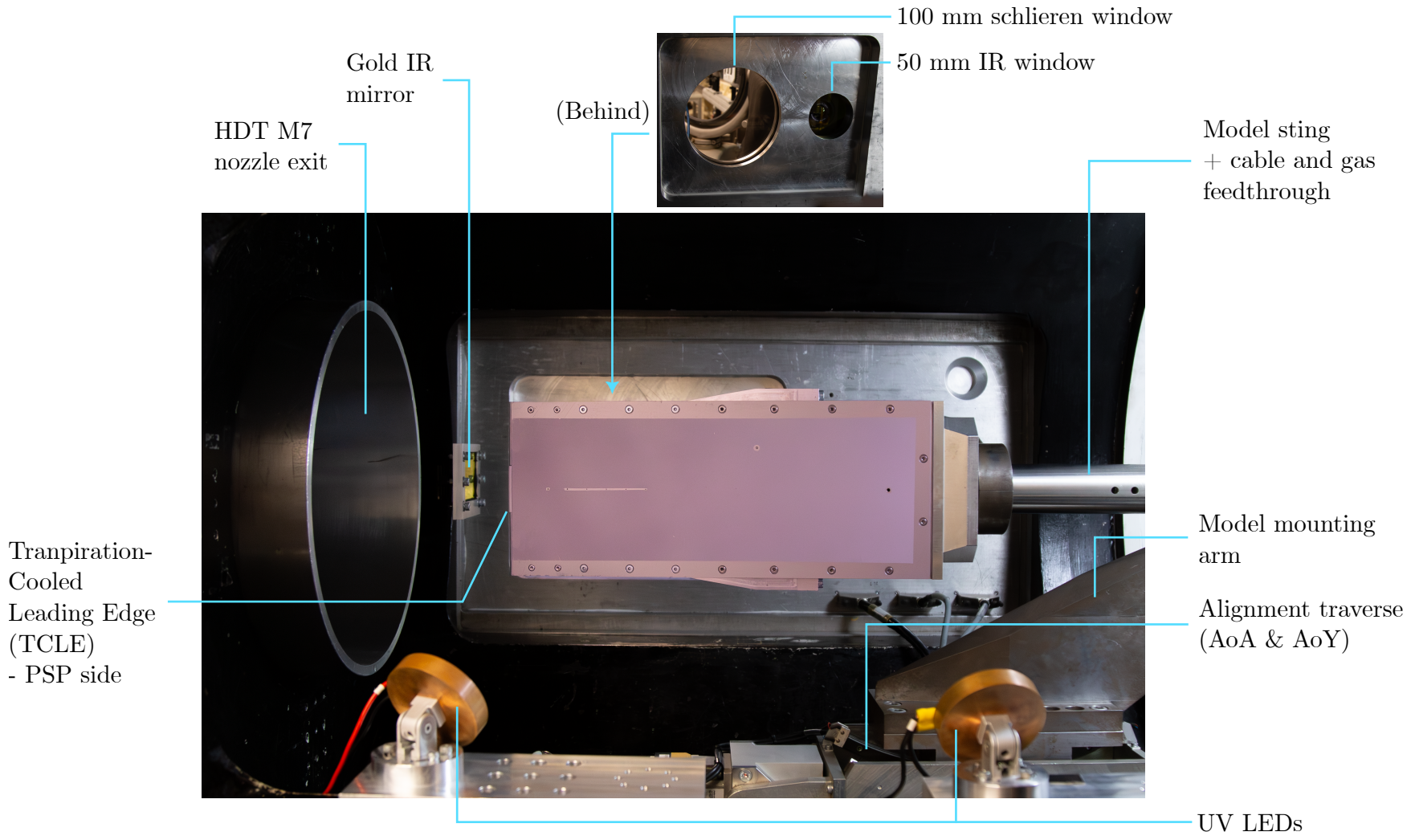


Figure A.6: Transpiration-cooled leading edge (TCLE) model in the HDT test section, with annotated optical setup components.



Figure A.7: TCLE model rotated by 90° in the HDT test section, showing the optical access windows behind. The PEEK heat transfer measurement surface is visible as the top surface of the model.

A.3 Post-Processing of Experimental Optical Data

Outlined in Chapter 4, optical measurement techniques during experiments were employed due to space constraints and resolution for the transpiration-cooled model. This section outlines the infrared (IR) thermography and the pressure-sensitive paint (PSP) processing to convert recorded frames into useful heat flux and concentration data.

A.3.1 IR Thermography

Previously mentioned, heat flux processing for IR thermography in the HDT has been developed and refined by several authors, including Naved et al. [66, 70], Ivison [140], and Condren [120]. Heat flux processing required thermal and emissivity parameters for each material measured, which are given in Table A.1.

Table A.1: Nominal thermal properties used for IR data processing. Values of the PEEK were provided in [119], measured by NETZSCH GmbH Application Laboratory. Values for the LithaLox were provided by Lithoz GmbH.

	LithaLox 1347	Victrex PEEK 450G
ρ (kg m^{-3})	3990	1310
k (W m^{-1} K^{-1})	29.0	0.25
C_p (J kg^{-1} K^{-1})	880	1201
$\alpha = \frac{k}{\rho C_p}$ (m^2 s^{-1})	$7.69 \cdot 10^{-6}$	$1.59 \cdot 10^{-7}$
$rrck = \sqrt{\rho C_p k}$ (J m^{-2} K^{-1} s$^{-0.5}$)	9735	627.1
ε	0.45	0.915

1. **Detection:** The Telops FAST M3k camera uses a 320×256 focal-plane array (FPA) detector sensitive to infra-red radiation of wavelengths between 1.5–5.4 μm. All physical bodies emit electromagnetic radiation over a range of wavelengths, with emission power described by Planck's Law (Equation A.1). Here, $I(\lambda, T)$ is the spectral intensity: the radiative power per unit power at a given wavelength, λ, and temperature, T. h is the Planck constant, c is the

speed of light in a vacuum, and k_B is the Boltzmann constant. Integrating across the range of MWIR wavelengths gives the detected intensity, expressed in Equation A.2.

$$I(\lambda, T) = \frac{2\pi hc^2}{\lambda^5} \left[\exp\left\{ \frac{hc}{\lambda k_B T} - 1 \right\} \right]^{-1} \tag{A.1}$$

$$U = R \left[\exp\left\{ \frac{B}{T} \right\} - F \right]^{-1} + G(T_{\text{amb}}) \tag{A.2}$$

The constants R, B, F are functions of the optical system. G is an additional term that accounts for non-experimental IR emissions and reflections incident on the sensor, that may originate from locations such as the optics windows and test section walls. This extraneous radiation is dependent on the ambient temperature, T_{amb}, which is measured by a thermocouple external to the test section. For each optical setup, the constants are empirically found on a per-pixel basis via an in-situ calibration procedure as proposed in [174], outlined below.

2. **Black Body Calibration:** The in-situ black body calibration was performed using a portable calibrator (CI-Systems SR-33-7). It was aligned to the model surface with a laser level and kept normal to the camera view to minimise directional emissivity errors. The calibration area was set to a range of temperatures, T_{cal}, with quoted spatial uniformity and setpoint accuracy of 0.01 K and 0.05 K, respectively. For wide-angle measurements, calibration was repeated at three streamwise locations to cover the full field of view, and the results were stitched together. Contours of the pixel-wise calibration coefficients B, F, R, and $G(T_{\text{amb, cal}})$ are shown in Figures A.14 and A.15 for the two IR viewing configurations. As the calibration was performed in-situ, it was valid only for the specific optical setup and acquisition settings used during calibration, which were kept fixed thereafter.

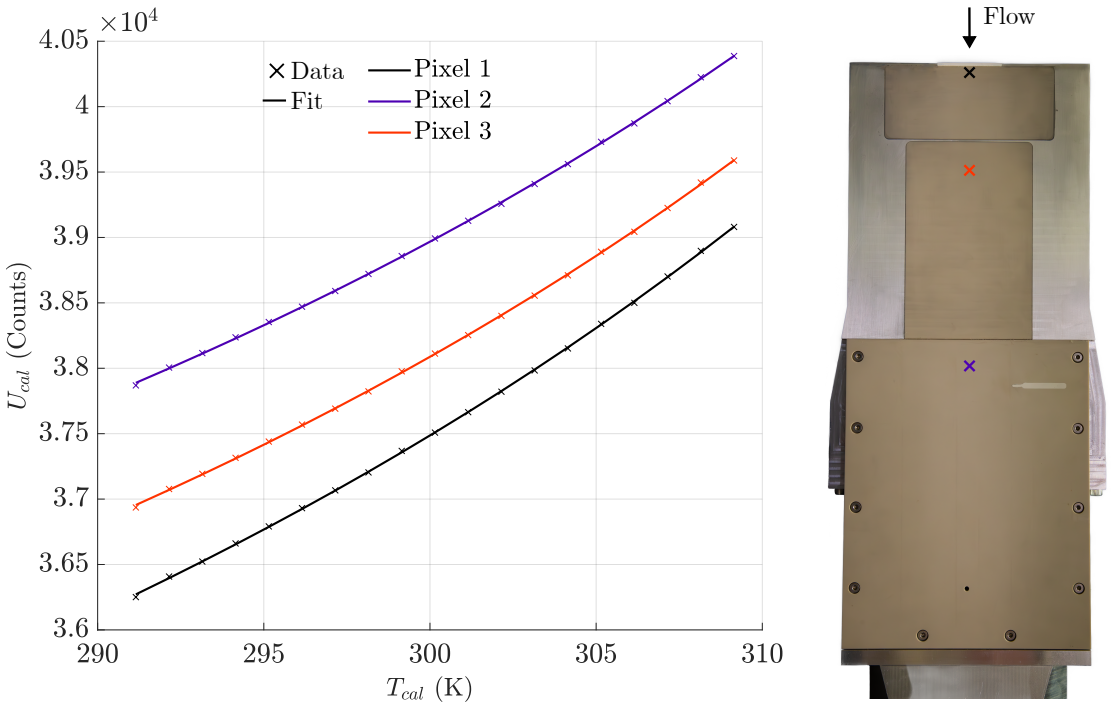


Figure A.8: IR calibration data points and curve fits for 3 pixels along the model centreline. The calibration curves are fitted to Equation A.2, and pixel locations are marked in the photograph of the model on the right. The variability in the fitted lines is due to sensor non-uniformities, corrected by the calibration.

3. **Calibration corrections:** Additional corrections were required to account for differences between calibration and experiment in ambient gas material emissivity (ε), transmissivity (τ), and ambient temperature (T_{amb}). The calibrator has a quoted emissivity of $\varepsilon = 0.98$, and the emissivities of the two model materials are listed in Table A.1. Calibrations were performed under atmospheric conditions, where IR absorption by carbon dioxide and water vapour is present. To avoid this during tests, each shot in the HDT used dry synthetic air (oxygen and nitrogen only), supplied by BOC Ltd. The transmissivity values, τ, for both conditions were calculated by Ivison [140], and the combined change in emissivity and transmissivity is represented by the correction ratio C.

$$C = \frac{\varepsilon_{\text{expt}}\tau_{\text{expt}}}{\varepsilon_{\text{cal}}\tau_{\text{cal}}} \tag{A.3}$$

The change in ambient temperature was accounted for by using $G(T_{\text{amb, cal}})$ in the calibration curve fits (Figure A.8), and applying $G(T_{\text{amb}})$ during

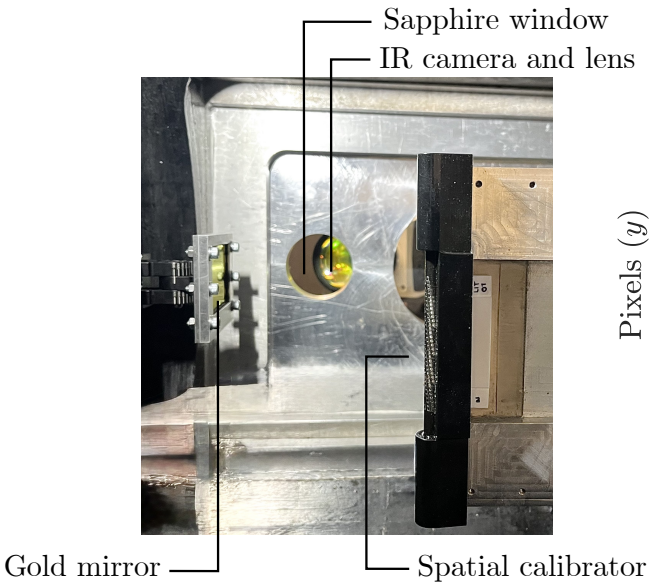
the experiment by rearranging Equation A.2 using pre-flow counts $U_{\text{pre-flow}}$, assuming ambient temperature remains constant over the test duration.

$$G(T_{\text{amb, expt}}) = U_{\text{pre-flow}} - CR\left[\exp\left\{\frac{B}{T_{\text{amb, expt}}}\right\} - F\right]^{-1} \tag{A.4}$$

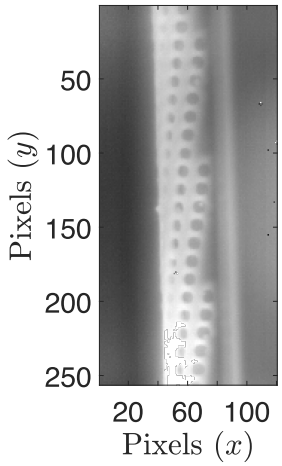
4. **Directional emissivity correction (leading edge view):** IR measurements of the leading edge were captured over a highly curved surface. The effect of view angle on the measured emissivity is known as *directional emissivity* and is well-documented [121]. The relationship between the effective emissivity of a material and the viewing angle, θ_v, is given below, where n is the material refractive index.

$$\varepsilon(\theta_v) = \frac{2\cos(\theta_v)\cdot\sqrt{n^2-\sin^2(\theta_v)}}{\left(\cos(\theta_v)+\sqrt{n^2-\sin^2(\theta_v)}\right)^2}\left[1+\frac{n^2}{\left(\cos(\theta_v)\cdot\sqrt{n^2-\sin^2(\theta_v)}+\sin^2(\theta_v)\right)^2}\right] \tag{A.5}$$

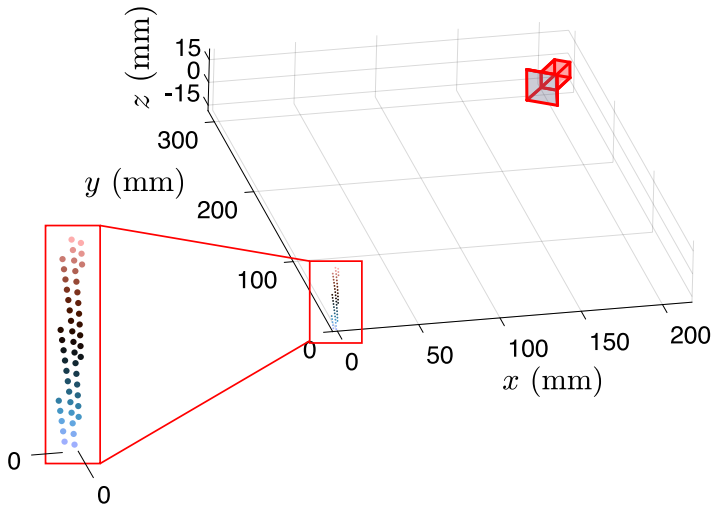
The calibration of highly curved models for IR measurements in the HDT is documented by Condren [120], based on the geometric camera calibration approach of Heikkilä [122]. This procedure was followed in the present work, where the global camera position in 3D space was determined from a series of calibration images mapped to the 2D image plane. The steps of this calibration process are illustrated in Figure A.9, resulting in a transformation from global camera coordinates to the model surface, enabling viewing angle determination at each pixel. The optical configuration for leading edge viewing provided a view of half of the leading edge surface: from stagnation point to a short section of the PEEK downstream of the injector (PEEK length $\sim$ 10 mm).



(a) Annotated photograph of spatial calibration of leading edge



(b) View of calibrator in IR camera



(c) Detected points and camera projected onto global position map

Figure A.9: Images of the spatial calibration procedure for directional emissivity correction for leading edge heat flux measurements. A 3D printed spatial calibrator with a precisely-defined array of holes was used to map pixel coordinates to model surface coordinates. A combination of the extrinsic calibration and intrinsic camera calibration to find the angle between the optical path and the surface normal, and hence find directional emissivity of each pixel.

5. **Temperature:** The temperature of the model during an experiment is finally found by re-arranging Equation A.2 by applying the calibration and background count terms. The camera trigger is synchronised with the DAQ to produce a pixel-wise time-accurate temperature trace.

$$T = B\left[\ln\left\{\frac{CR}{U_{\text{flow}} - G(T_{\text{amb, expt}})}\right\} + F\right]^{-1} \tag{A.6}$$

6. **Internal heat transfer correction (leading edge view):** Heat flux processing of the leading edge injector must take into account the unsteady expansion of coolant gas into the injection plenum that leads to a change in gas temperature, affecting the backside thermal boundary condition of the injector. Following the procedure outlined by Naved [66], the heat transfer from coolant to solid is assumed to be a linear time-invariant process. This effect is accounted for by measuring the transient temperature profile during injection into an evacuated test section without freestream flow. This baseline profile is then temporally aligned with, and subtracted from, the actual test data to isolate the temperature rise due to cross-flow heating alone.

7. **Spatial calibration and dewarping:** Spatial calibrators with precisely defined cutouts and locating features were placed directly over the imaged surfaces. This enabled correction of the fish-eye distortion caused by the wide-angle 13 mm lens, and conversion of pixel coordinates to model surface coordinates for both optical layouts.

8. **Heat flux calculation:** Converting measured surface temperature history to transient heat flux is an ill-posed heat transfer problem. In short-duration hypersonic ground testing, a common simplification is the one-dimensional semi-infinite assumption: heat transfer into the material is assumed one-dimensional (so each pixel may be processed independently), and the backside of the material does not experience a temperature rise over the test duration (i.e., the material behaves as effectively semi-infinite). The validity of this assumption is governed by the *thermal penetration depth*, defined as the

material depth, d, at which the temperature rise over time t does not exceed 0.5% [175, 176]. This critical thickness is expressed in Equation A.7, with material properties given in Table A.1. For downstream measurements, the PEEK inserts were machined to satisfy this condition for test durations up to 0.5 s. However, the thin wall of the porous leading edge meant the semi-infinite assumption could not be satisfied for any quasi-steady HDT plateaus. Instead, a finite-element reconstruction method was formulated. Both methods are described below.

$$d = 4\sqrt{\frac{kt}{\rho C_p}} \tag{A.7}$$

(a) **Downstream:** The transient heat flux on the PEEK surface was calculated using Equation A.8 [177], which is solved using the impulse response method of Oldfield [138]. The impulse response processing is carried out on a per-pixel basis, providing a 2D map of the surface heat flux.

$$\dot{q}(t) = \sqrt{\frac{\rho C_p k}{\pi t}}\,(T(t) - T(0)) \tag{A.8}$$

(b) **Leading edge:** The finite element reconstruction (FER) method used imported CAD geometry and a finite element solver to determine the heat flux required to produce the experimentally measured temperature rise. COMSOL's heat transfer module was coupled to a Nelder-Mead optimisation routine using the LIVELINK FOR MATLAB functionality. At each timestep, the solver iteratively adjusted the input heat flux until modelled surface temperatures matched experimental measurements across both the leading edge and downstream PEEK within the field of view (PEEK length ∼10 mm). The heat flux distribution was parameterised as a Bézier curve with 4 uniformly distributed control points on the leading edge and 4 on the PEEK to produce a smooth, continuous curve. Each subsequent timestep used the previous in-depth temperature field solution. Figure A.13 shows this routine.

The internal support lattice introduced a highly three-dimensional backside boundary condition, requiring 3D geometry and mesh. However, the periodic nature of the lattice meant that only a representative slice was needed. Figure A.10 shows the geometry and boundary conditions. Despite the backside variation, the external surface temperature was highly spanwise-uniform, permitting a 1D approach for noise reduction and faster processing. Experimental surface temperatures were averaged across the injector span, yielding the transient 1D temperature distribution shown in Figure A.11. This was compared to the spanwise-averaged FEM surface temperature (Figure A.12), allowing the optimiser to target a 1D heat flux distribution rather than a 2D surface.

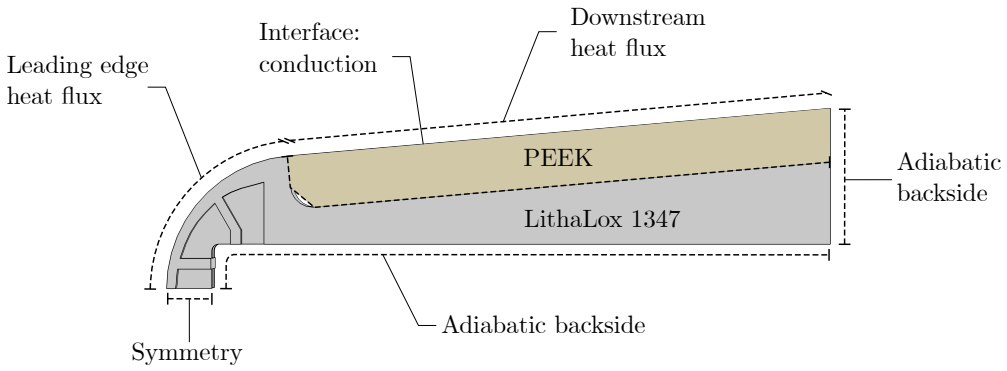


Figure A.10: Annotated diagram of the boundary conditions used by the FER method.

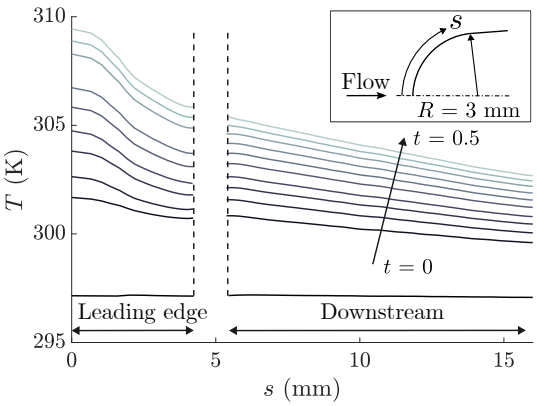


Figure A.11: Surface temperature distributions measured by IR thermography, used as a transient input to the FER model. The gap between the leading edge and PEEK region corresponds to the adhesive interface, where reliable temperature data could not be obtained.

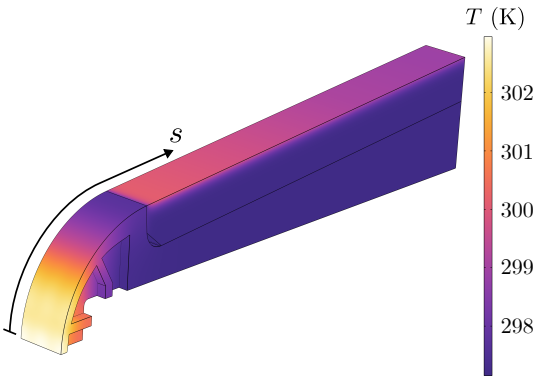


Figure A.12: 3D temperature field of the FER model at $t = 0.1$ s. For each timestep, the heat flux distribution input is optimised until the spanwise-average surface temperature distribution matches that of the experiment (Figure A.11).

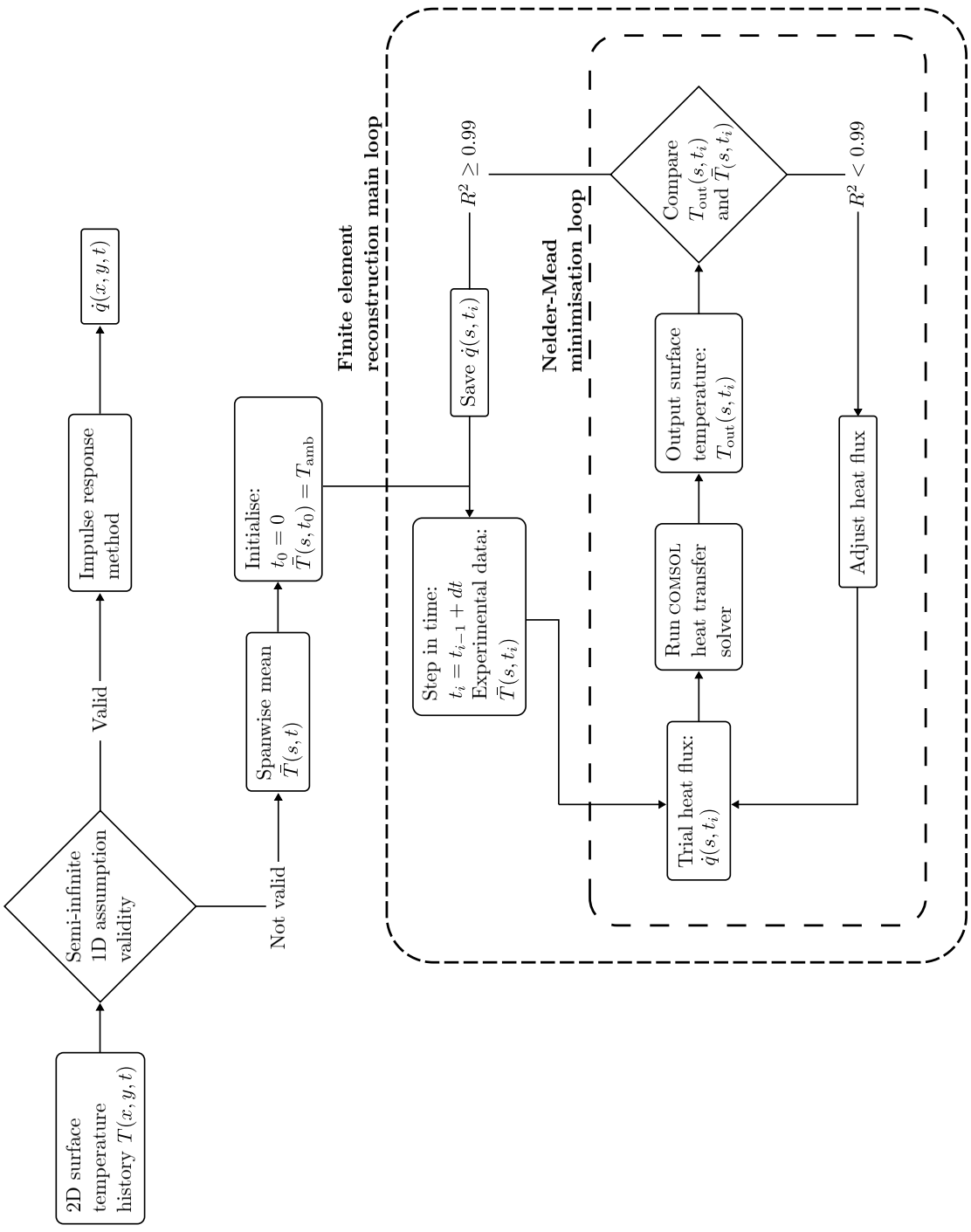


Figure A.13: Flowchart of heat flux processing of the experiments. The finite element reconstruction method is summarised by a series of two loops: the time-stepping and the optimisation loop for each time-step.

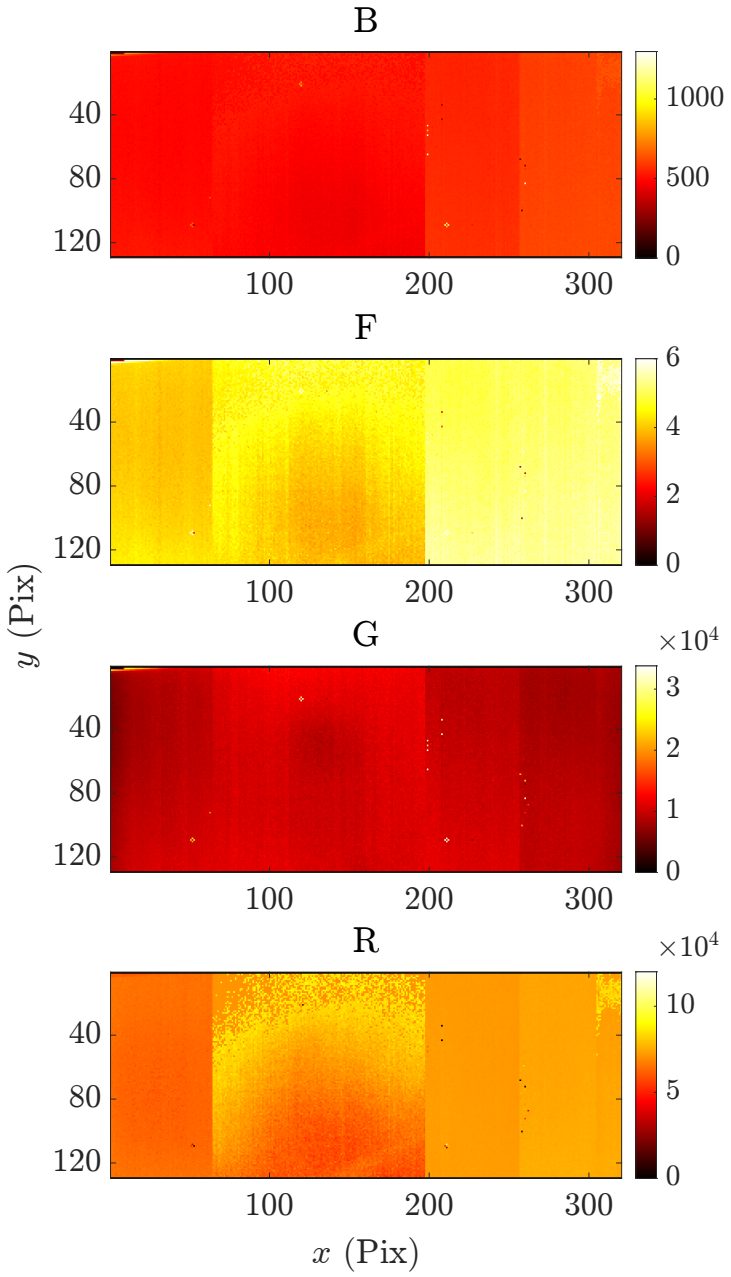


Figure A.14: Contour plots of the IR calibration curve coefficients for the downstream measurements using the 13 mm focal length lens. The calibration requires the black body calibrator to be placed at three locations to cover the wide-angle field of view, and the per-pixel coefficient fields are stitched together.

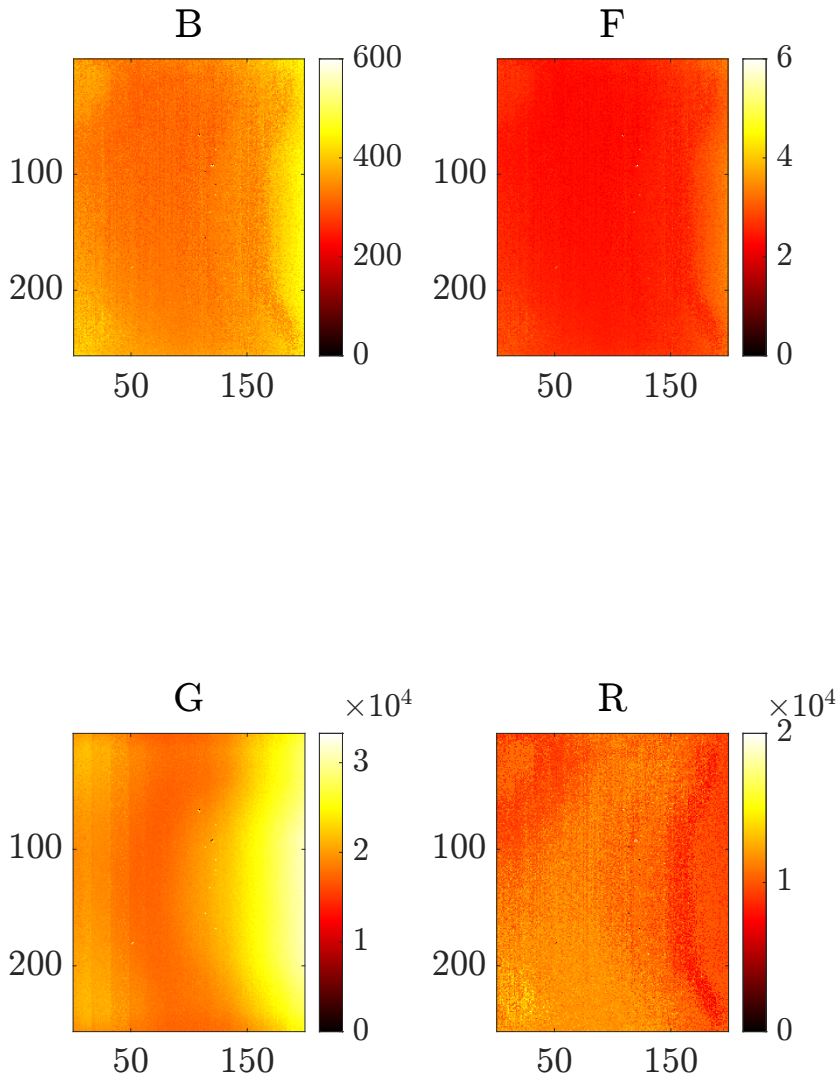


Figure A.15: Contour plots of the IR calibration curve coefficients for the leading edge measurements using the 100 mm focal length lens.

A.3.2 Pressure-Sensitive Paint

PSP processing for surface coolant concentration and pressure follows nearly identical procedures. Following photoexcitation of the PSP luminophore, emission intensity is inversely proportional to surface oxygen partial pressure (pO_2), which in turn is affected by both static pressure and the local concentration of oxygen. Higher static pressure increases pO_2 and reduces intensity, while foreign gas reduces local oxygen concentration, decreasing pO_2 and increasing intensity. These effects cannot easily be disentangled, requiring separate experiments to isolate each phenomenon. Both experiments employ identical optical arrangements, require air as the freestream gas, and use a common processing framework:

For coolant concentration measurements, moderate blowing parameters ($B_h \leq 1.5B^*$) of foreign gases were tested. This work has shown that moderate blowing does not significantly augment surface static pressure, therefore isolating changes in pO_2 to changes in oxygen concentration. The absence of oxygen at the surface is used to infer the presence of foreign gas coolant.

For pressure measurements, air was used as the coolant gas, maintaining constant surface oxygen concentration between tests with and without injection, therefore isolating changes in pO_2 to changes in surface pressure. These high blowing parameter tests enabled PSP measurement of 2D surface pressure immediately downstream of the leading edge, with tapping measurements providing pressure data verification further downstream.

1. **Detection:** The strength of luminophore molecule emission is measured by the camera as intensity, I, for each pixel. The luminophores are chosen to exploit oxygen quenching mechanisms whereby an excited luminophore molecule is deactivated by oxygen collisions without photon emission. At higher pO_2, quenching occurs at a higher rate, decreasing the measured intensity. This relationship is described by the Stern-Volmer equation, shown below, where A, n, and B are calibration constants, and ref represents

conditions at a reference condition.

$$\frac{I}{I_{\text{ref}}} = A\left(\frac{pO_{2,\text{ref}}}{pO_2}\right)^n + B \tag{A.9}$$

2. **Intensity Calibration:** The PSP is calibrated in situ by allowing the evacuated wind tunnel test section to rise to atmospheric pressure over several seconds. A surface-mounted Kulite transducer is synchronised with the camera to generate a time-resolved trace of intensity ratio versus pressure ratio for each pixel. It is assumed that the oxygen concentration remains constant throughout the pressure increase. The reference condition is taken as the final frame before the test section begins to pressurise.

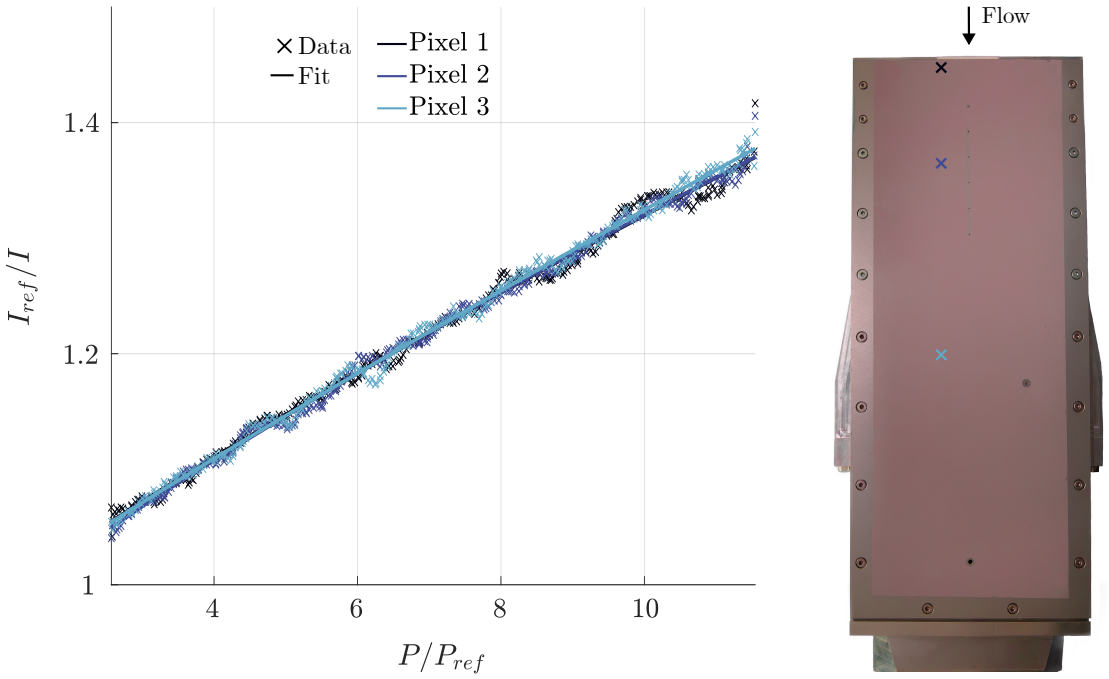


Figure A.16: PSP calibration data points and curve fits for 3 pixels, 20 mm off the centreline, with locations marked in the photograph of the model. The calibration curves are fitted to Equation A.9.

3. **Spatial calibration:** As with the IR thermography processing, a machined plate with precisely-defined features was placed over the downstream surface such that the pixel coordinates could be mapped to model surface coordinates.

4. **Partial pressure calculation:** During an experiment, the test section is initially evacuated, taken as the reference condition. Once the camera is triggered by flow arrival, a 2D time-accurate intensity map is produced. The calibration curve for each pixel is applied to yield $p\mathrm{O}_2$.

5. **Conversion to concentration or pressure:** Processing of coolant concentration and surface pressure diverges here:

   (a) **Surface coolant concentration:** Partial pressure of oxygen is converted to coolant concentration by employing the ideal gas law and Dalton's law of partial pressures, arranged in Equation A.10. The ratio of measured oxygen partial pressure to surface static pressure yields the mole fraction of oxygen, $\chi(\mathrm{O}_2)$

   $$\frac{p\mathrm{O}_2}{P_{\mathrm{surf}}} = \frac{N(\mathrm{O}_2)}{N_{\mathrm{tot}}} = \chi(\mathrm{O}_2) \tag{A.10}$$

   Due to the assumption of an unmodified surface pressure, P_{surf} is directly measured by the PSP without coolant injection. The only gases in the experiment are the oxygen-free coolant and the freestream air (of which oxygen is a component). Since the mole fractions of gases in a mixture must sum to unity, the mole fraction of coolant gas, $\chi(c)$, at the model surface may be expressed as below, where subscript 0 indicates the uncooled measurement.

   $$\chi(c) = 1 - \frac{p\mathrm{O}_2}{p\mathrm{O}_{2,0}} \tag{A.11}$$

   (b) **Surface pressure augmentation:** When the coolant gas used is air, the surface pressure is found by multiplying the measured $p\mathrm{O}_2$ field by the mole fraction of oxygen in synthetic air, taken to be 0.21. The pressure tappings and reference Kulite on the model surface were used as reference gauges to verify the pressure measurement.

Figure A.17 shows the calibration coefficient maps used for the Stern-Volmer

equation. When generating calibration data, the quality of the curve fit to the calibration data is measured using the coefficient of determination, R^2, determined by the following equation:

$$R^2 = 1 - \frac{\sum_i (y_i - f_i)^2}{\sum_i (y_i - \overline{y})^2} \tag{A.12}$$

Here, y_i is each discrete dependent variable, either intensity ratio (PSP) or counts (IR thermography); f_i is the fitted curve, and $\overline{y}$ is the mean of the acquired data. Each of the calibration curves are fitted using a nonlinear least-squares algorithm.

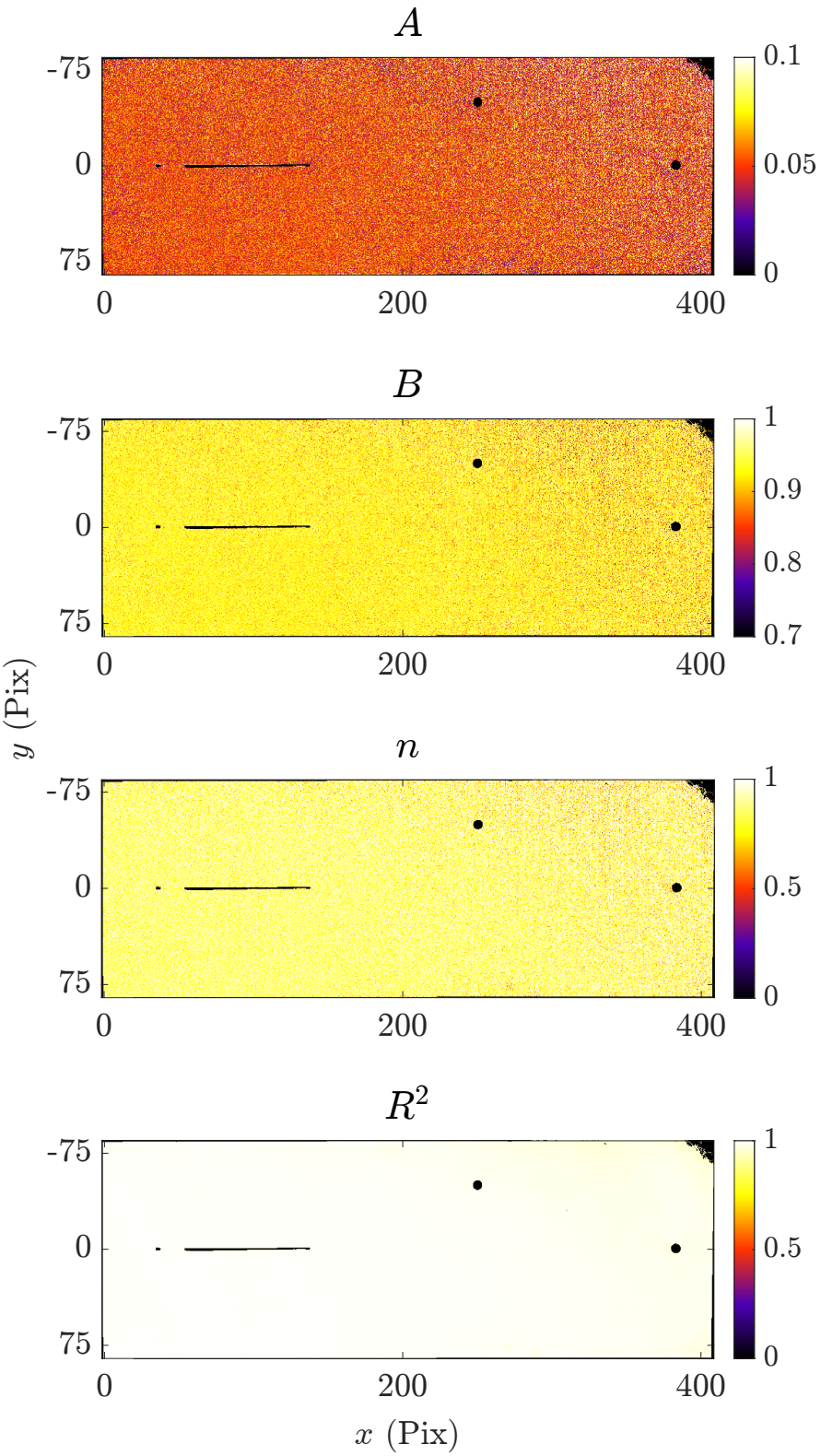


Figure A.17: Contour plots of the PSP calibration curve coefficients.

APPENDIX B

Eilmer Simulation Setup

The following description of Eilmer (Sections B.1.1 – B.1.3 only) was contributed by K. Damm as a co-author for the conference publication 'Aerodynamic Effects and Heat Flux Augmentation of a Transpiration Cooled Hypersonic Sharp Leading Edge' [136]. The remainder of this Chapter (Sections B.1.4 – B.2: mass flux boundary condition, mesh independence study) is the author's own work.

B.1 Solver Description 240

B.2 Mesh Independence Study 244

B.1 Solver Description

B.1.1 Governing Equations

The flow in this study is modelled using the compressible Navier-Stokes equations, which assume continuum flow and Newtonian behaviour of the fluid. The Navier-Stokes equations in their integral form are written as follows,

$$\frac{\partial}{\partial t}\int_V \boldsymbol{U} dV = -\oint_S (\boldsymbol{F_c} - \boldsymbol{F_v}) \cdot \hat{\boldsymbol{n}} dA + \int_V \boldsymbol{Q} dV, \tag{B.1}$$

where $\boldsymbol{U}$ is the vector of conserved variables (mass, momentum, energy), t is time, V is volume, dA is area, $\boldsymbol{F_c}$ is the convective flux vector, $\boldsymbol{F_v}$ is the viscous flux vector, and $\boldsymbol{Q}$ is the source term vector.

B.1.2 Spatial Discretisation

Eilmer employs a cell-centered finite volume method to discretise Equation B.1. This gives the semi-discrete form of the governing equations,

$$\frac{\partial \boldsymbol{U}}{\partial t} = -\frac{1}{V}\sum_{faces} (\mathbf{F}_c - \mathbf{F}_v) \cdot \hat{\mathbf{n}}\ dA + \mathbf{Q}, \tag{B.2}$$

where $\boldsymbol{U}$ and $\boldsymbol{Q}$ now represent cell-average values, dA is a face area, and $\sum_{faces}$ denotes summation over the cell faces. In this work, the convective fluxes ($\boldsymbol{F}_c$) are computed using an adaptive calculator that selects the AUSMDV scheme by Wada and Liou [178] away from shocks and Hänel's method [179] near shocks. The switching between the two flux calculators is governed by a shock detector that is a simple measure of the relative change in normal velocity at interfaces. Second-order spatial accuracy for the convective fluxes is achieved by reconstructing the primitive flow state variables within the finite-volumes using a piecewise-parabolic scheme. To ensure stability when reconstructing the flow state in finite-volumes near shocks, the limiter by van Albada et al. [180] is employed. In regions with very strong gradients, further dissipation is added by multiplying the standard

limiter value by the heuristic pressure-based limiter value outlined in the work by Drayna [181]. The spatial gradients for computing the viscous fluxes ($\mathbf{F}_v$) are computed using a cell-centered weighted least-squares method and the face-tangent augmented face-gradient method [182].

B.1.3 Steady-State Accelerator

This work is interested in the steady-state solutions to the governing equations. A fully-implicit scheme is favourable for solving such problems. To derive the update scheme, the right-hand side terms in Equation B.2 are collected in into a vector a residual:

$$\frac{\partial \mathbf{U}}{\partial t} = \mathbf{R}(\mathbf{U}). \tag{B.3}$$

Using a backward difference to discretise the time derivative, recovers the fully discrete form of the governing equations as follows,

$$\frac{\Delta \mathbf{U}^k}{\Delta t} = \mathbf{R}(\mathbf{U}^{k+1}).$$

This is implicit since $\boldsymbol{U}^{k+1}$ are unknowns, and is approximated using the known state $\boldsymbol{U}^k$ and a first order linearisation of the residual vector,

$$\frac{\Delta \mathbf{U}^k}{\Delta t} = \mathbf{R}(\mathbf{U}^k) + \frac{\partial \mathbf{R}(\mathbf{U}^k)}{\partial \mathbf{U}^k}\Delta \mathbf{U}^k. \tag{B.4}$$

This can then be rearranged to recover the implicit-Euler time marching iterate,

$$\left[\frac{1}{\Delta t}\mathbf{I} - \frac{\partial \mathbf{R}(\mathbf{U}^k)}{\partial \mathbf{U}^k}\right]\Delta \mathbf{U}^k = \mathbf{R}(\mathbf{U}^k), \quad \mathbf{U}^{k+1} = \mathbf{U}^k + \Delta \mathbf{U}^k. \tag{B.5}$$

A globalised Newton-Krylov method is used to accelerate convergence to the steady-state solution [183]. Specifically, Newton's method is used to solve for $\boldsymbol{R}(\boldsymbol{U}) = 0$, where the linear system of equations arising at each nonlinear step (i.e. Equation B.5) is solved iteratively via a preconditioned GMRES method

[184]. Noting that as the pseudo-transient term $1/\Delta t$ approaches 0 in Equation B.5 (i.e. for very large Δt), Newton's method is recovered. Robust preconditioning is achieved by an incomplete LU factorization of an approximate flow Jacobian constructed by only considering a nearest-face-neighbour stencil. To reduce the computational cost of constructing the preconditioner matrix, the Jacobian is frozen for a user-selectable number of iterations.

B.1.4 Transpiration Cooling Boundary Condition

The transpiration cooling boundary condition imposed the mass flux distribution prescriptively rather than determinatively. The mass flux distribution was pre-calculated for each cooled simulation, and described by means of a smooth polynomial fit against the subtended body surface angle, as presented in the main thesis body. In this work, the mass flux boundary is implemented using Eilmer's user-defined function (UDF) boundary condition, as set out by Ewenz Rocher [109]. The UDF uses 'ghost cells' along with mass and species continuity equations to calculate flow properties at the surface interface (the injector outlet). This is shown in Figure B.1.

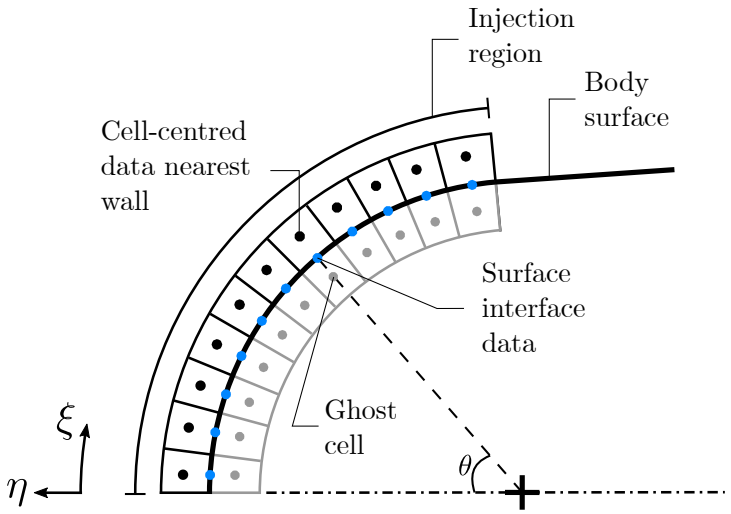


Figure B.1: Sketch of the transpiration cooling boundary condition in Eilmer. Primary data in Eilmer is stored in cell centres [144].

The concentration c_w and coolant velocity v_{inj} at the injector outlet (surface

interface) are found using the following procedure:

- The mass flux distribution at the wall is prescribed by a sixth order polynomial in terms of subtended angle, θ.
- The solutions for the pressure, temperature and velocity in the wall-adjacent cells are propagated through the flow solver.
- Pressure continuity and a fixed coolant wall temperature set the interface and ghost cell temperatures and pressures. Ghost cell properties are updated during the inviscid solution phase, and the surface interface is set during the viscous update.
- Coolant concentration is solved by discretising Equation B.6 [109] and solving for c_w; where v_w is the wall normal velocity, the concentration gradient is found using the wall-adjacent cell data, and D_{12} is the computed binary diffusion coefficient. The diffusion coefficient is evaluated for each coolant gas using the properties found listed by Bird [161].

$$\left(\frac{\partial c}{\partial y}\right)_w = (c_w - 1)\frac{v_w}{D_{12}} \tag{B.6}$$

B.2 Mesh Independence Study

A mesh independence study was carried out to ensure that the domain was sufficiently discretised to capture the flow physics. The study aimed to establish the appropriate resolution where converged simulations did not depend on the level of mesh refinement, while avoiding excessive refinement that would lead to unnecessary computational cost. Surface heat flux was selected as the quantity of interest in this study. Grids were deemed sufficiently resolved when the surface heat flux distribution did not differ from the finest grid by more than 0.1%.

Recalling that the domain size linearly scaled with R_{LE}, but did not vary significantly with other input parameters, a study was conducted for each R_{LE}. The study was conducted at the highest $Re_{u,\infty}$ in the study (Condition B), and without mass injection.

Each grid was constructed using Eilmer's in-built mesh generation functionality. For each domain, five mesh settings were tested, shown in Table B.1. The number of cells in the radial (η), and tangential (ξ) directions were increased together by a factor of 1.5 for each subsequent mesh. Cells were clustered using the in-built stretching function devised by Roberts [147], with stretching parameters β also provided in Table B.1. Symmetric clustering was applied to the body surface and the shock-fitted boundary, and weaker clustering was applied to the stagnation / symmetry line, as shown in Figure B.2.

Each grid in the study (and subsequent simulations in the main study) was run on 48 high performance computing cores at the University of Oxford's Advanced Research Computing service [151]. Simulations were run until a convergence criteria for the global residual was satisfied: $\boldsymbol{R}(\boldsymbol{U}) < 10^{-13}$, or until the maximum wall clock run time of 12 hours was exceeded (approx. 750 CPU hours per simulation).

Table B.1: Key parameters for the mesh independence study. Parameter β controls cell clustering density, which increases as β approaches 1. Cell stretching was applied symmetrically in η.

Grid No.	n_{cells} (×1E3)	n_η	n_ξ	β_η	β_ξ
1	40	200	200	1.001	1.1
2	90	300	300	1.001	1.1
3	203	450	450	1.001	1.1
4	457	676	676	1.001	1.1
5	1028	1014	1014	1.001	1.1

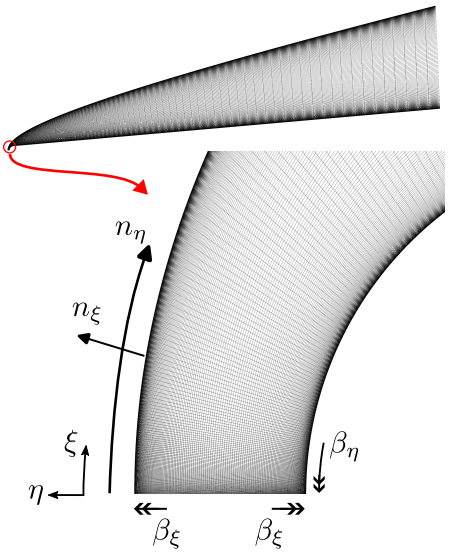


Figure B.2: Diagram of grid for mesh independence study, with cell number and clustering directions represented by arrows. R_{LE} = 5 mm, grid number: 3.

The heat flux distributions for each of the five grids are shown for the $R_{LE} = 1$ mm domain in Figures B.3. Figure B.4 shows the asymptotic behaviour of stagnation point heat flux with increasing grid resolution. A common benchmark parameter for blunt body heat transfer simulations is the Reynolds number based on the cell height at the wall, Re_c, defined below [185]. A typical Re_c on the order of 1 is required for resolving the boundary layer. Distributions for Re_c are shown in Figure B.5. The selected grids for each domain size is shown in Table B.2.

$$Re_c = \frac{\rho_w a_w y_c}{\mu_w} \tag{B.7}$$

Where ρ_w, a_w and μ_w are the density, local speed of sound, and viscosity at the wall, and y is the cell height in the wall-normal direction.

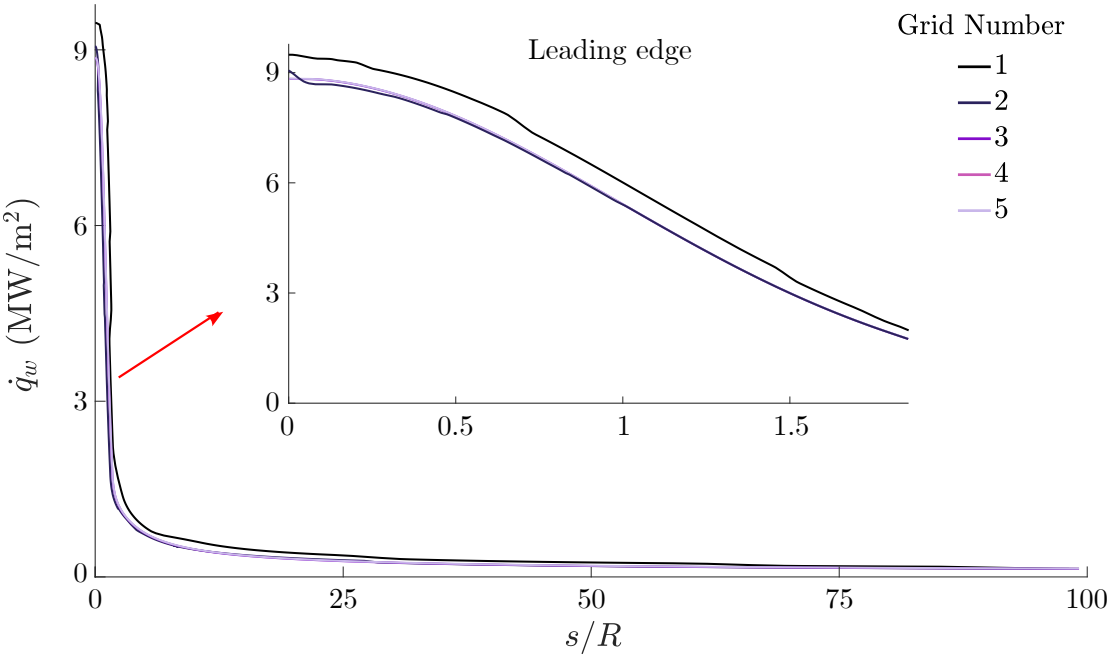


Figure B.3: Surface heat flux distribution for each level of grid refinement for the $R_{LE} = 1$ mm domain. The distributions correspond to freestream Condition B without mass injection.

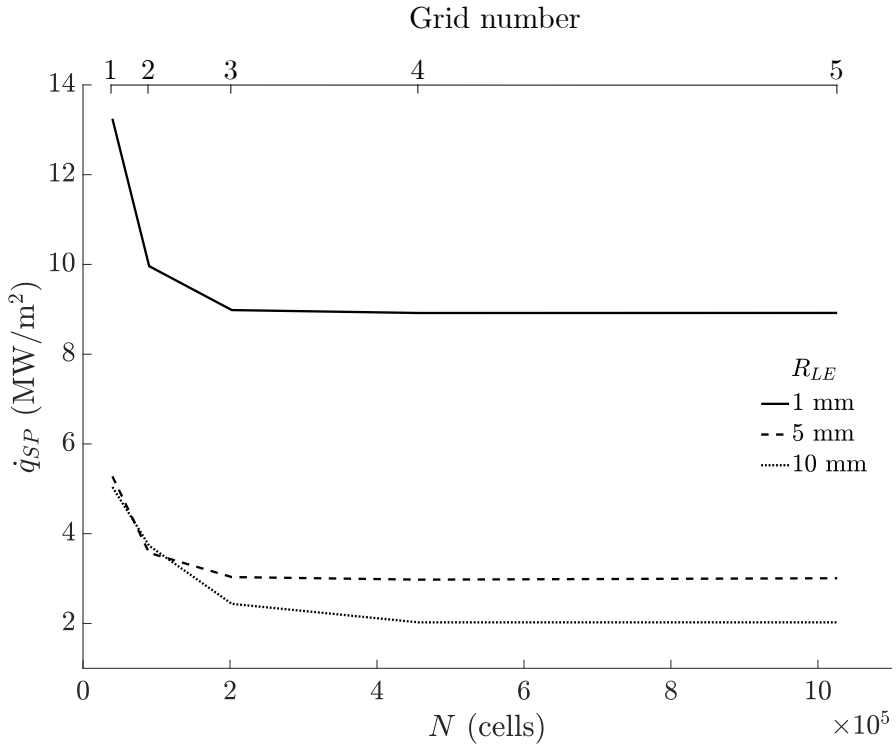


Figure B.4: Stagnation point surface heat flux convergence for all three R_{LE} domains.

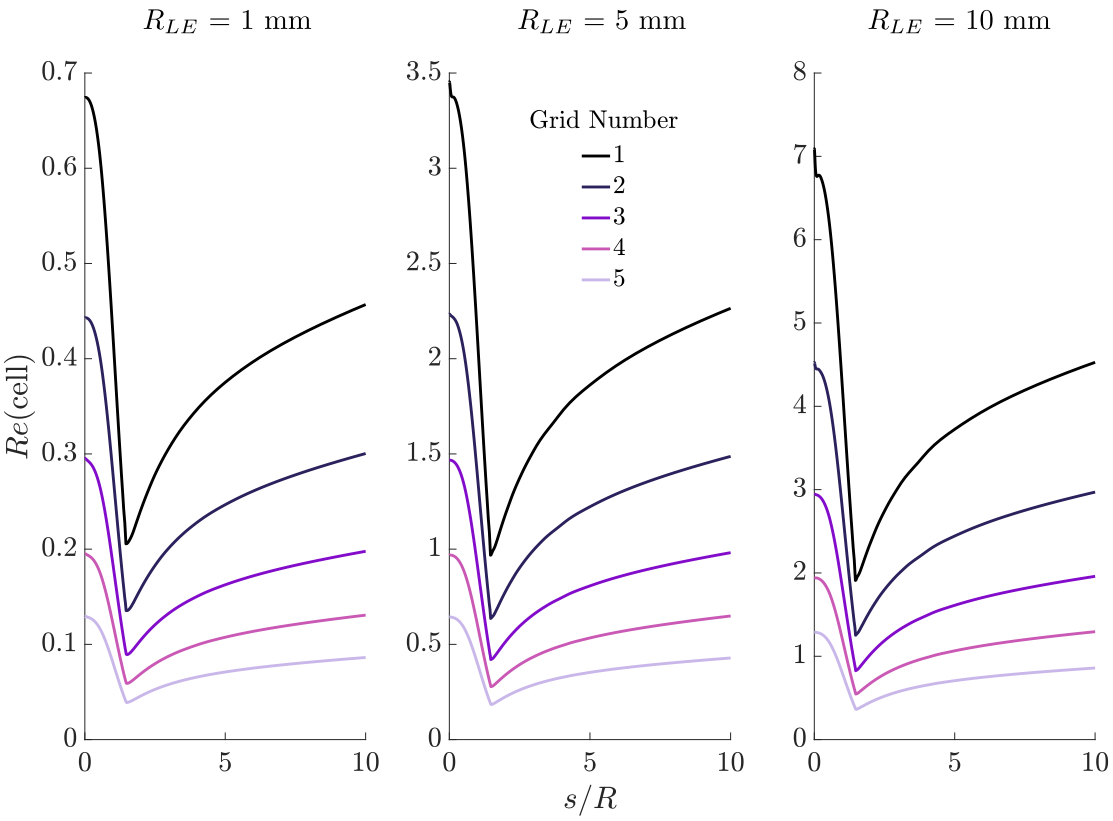


Figure B.5: Distributions of Re_c for $s/R < 10$. Values on the order of 1 are generally considered to have appropriate resolution for blunt body heat transfer.

Table B.2: Selected mesh resolution parameters following the mesh independence study.

R_{LE} (mm)	n_{cells}	n_η	n_ξ	β_η	β_ξ
1	203k	450	450	1.001	1.01
5	203k	450	450	1.001	1.01
10	457k	676	676	1.001	1.01

APPENDIX C

Heat Flux Modelling

This Appendix outlines the implementation of well-known semi-analytic correlations for heat flux around the leading edge, the adaptation of film cooling correlations to the leading edge geometry, and a detailed outline of the semi-empirical model, all developed in Chapter 5 and employed throughout Chapter 6.

C.1 Uncooled Heat Flux Modelling 249

C.2 Film Cooling Correlation Formulation 252

C.3 Semi-empirical Transpiration Cooling Model 254

C.1 Uncooled Heat Flux Modelling

C.1.1 Stagnation Point

The leading edges in this work were considered to be 2D planar at zero angle of attack. The uncooled heat flux at the stagnation point may be modelled using the Fay-Riddell correlation [115], modified for a 2D planar geometry [7], shown in Equation C.1.

$$\dot{q}_{FR}(0) = \frac{0.438}{Pr_w^{0.6}}(\rho_e\mu_e)^{0.42}(\rho_w\mu_w)^{0.08}(h_{T,e} - h_w)\left(1 + (Le^{0.52} - 1)\frac{h_d}{h_{0,e}}\right)\left(\frac{dv_e}{dx}\right)^{0.5} \tag{C.1}$$

Properties ρ, μ and h are density, viscosity and enthalpy. Subscripts e and w refer to properties at the boundary layer edge and wall respectively. $h_{T,e}$ is the total enthalpy at the boundary layer edge, and the term $(h_{T,e} - h_w)$ accounts for the driving enthalpy difference between the hot post-shock gas and a vehicle's hot wall. For a sharp leading edge stagnation point, boundary layer edge properties were treated as the post-shock properties. The velocity gradient, $\frac{\mathrm{d}v_e}{\mathrm{d}x}$ was estimated from Newtonian theory, shown in Equation C.2.

$$\frac{dv_e}{dx} = \frac{1}{R_{LE}}\sqrt{\frac{2(P_e - P_\infty)}{\rho_e}} \tag{C.2}$$

The modelling in this thesis required two inputs: geometry and flight condition. The freestream static flow conditions were calculated according to the 1976 U.S. Standard atmosphere [142], and total flow conditions were calculated using isentropic relations. Post-shock flow conditions were calculated using a MATLAB wrapper of NASA's CEA2: a Fortran-based code for computing thermodynamic properties and chemical equilibrium compositions of high-temperature gas mixtures. A shock problem was run to compute the flow properties immediately behind the normal shock, and a $P - T$ problem was run to compute flow properties at the hot wall. The gas compositions from CEA2 also provide the necessary information to calculate dissociation enthalpies of air, h_d. The CEA2 and Fay-Riddell

calculations assumed non-ionised flow in thermochemical equilibrium, and do not account for radiative heat flux into the body.

C.1.2 Blunt Body Distribution

The heat flux distribution around the body was estimated using Lees' method [116], adapted for the blunted wedge. The distribution is a geometry-dependent distribution that scales linearly with stagnation point heat flux, $\dot{q}(0)$. In Equation C.3, θ is the subtended surface angle from the stagnation point, θ_w is the wedge half-angle, and α_w is the wedge surface inclination. In this work, the shape was always fixed to $\theta_w = 5°$ and $\alpha_w = 85°$. The distribution is split into two parts: the cylindrically blunted leading edge ($\theta \leq \alpha_w$) and the downstream region ($\theta > \alpha_w$).

$$\dot{q}(s) = \begin{cases} \dot{q}(0) \cdot D^{-0.5} \left[2\theta \sin(\theta)[(1 - K_\infty)\cos^2(\theta) + K_\infty\right] & \theta \leq \alpha_w \\ \dot{q}(0) \cdot A \frac{(s'/R_{LE})}{\sqrt{B + (s'/R_{LE})^3}} & \theta > \alpha_w \end{cases} \tag{C.3}$$

$$D = (1 - K_\infty)\left(\theta^2 - \frac{\theta \sin(4\theta)}{2} + \frac{1 - \cos(4\theta)}{8}\right) + 4K_\infty\left(\theta^2 - \theta\sin(2\theta) + \frac{1 - \cos(2\theta)}{2}\right) \tag{C.3a}$$

$$s' = R_{LE}\left[\cot(\theta_w) + \frac{s}{R_{LE}} - (\alpha_w)\right] \tag{C.3b}$$

$$A = \frac{\sqrt{3}}{2}\sqrt{(1 - K_\infty)\sin^2(\alpha_w) + K_\infty}\sqrt{\alpha_w} \tag{C.3c}$$

$$B = \frac{3}{16}\left[\sin^2(\theta_w)(1 - K_\infty)\sin^2(\theta_w) + K_\infty\right]^{-1} \frac{D\Big|_{\theta=\alpha_w}}{\alpha_w} - \cot^3(\theta_w) \tag{C.3d}$$

$$K_\infty = \frac{1}{\gamma_\infty M_\infty^2} \tag{C.3e}$$

$$\alpha_w = \frac{\pi}{2} - \theta_w \tag{C.3f}$$

C.1.3 Comparison to Laminar CFD

The heat flux profiles above were compared to the laminar CFD simulations run in Chapter 5, and are shown below.

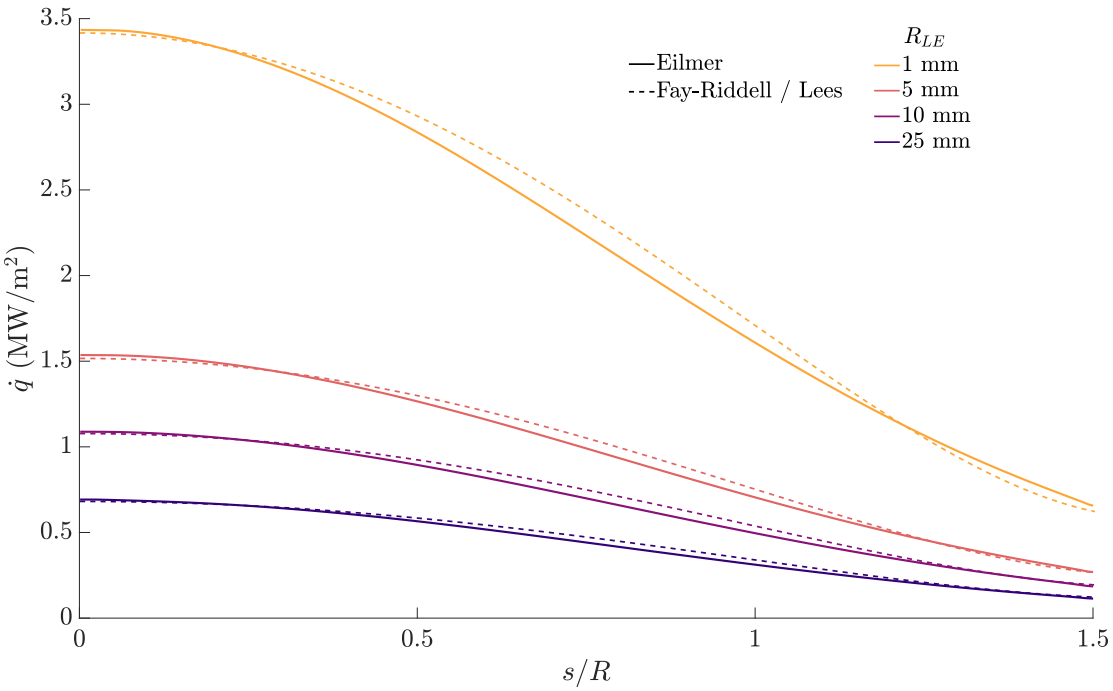


Figure C.1: Comparison of theoretical and numerical heat flux distributions for leading edges with different radii. The freestream conditions used for both methods correspond to $M_\infty = 7$ at 35 km altitude.

C.2 Film Cooling Correlation Formulation

The geometry downstream of the injector was considered as an inclined flat plate. The flat plate film cooling correlation developed by Hombsch & Olivier [98] and adapted by Ifti [110] used a correlation parameter, $\xi_{th,FP}$, to fit a power law correlation for η_{th}.

$$\eta_{th,FP} = \frac{St}{St_0} = f(\xi_{th,FP}) \tag{C.4}$$

$$\xi_{th,FP} = \frac{1}{Fl}\sqrt{\frac{x - x_0}{x_{\text{ref}}}\frac{C^* x}{Re_u}} \tag{C.5}$$

This was adapted for the leading edge injector to produce a heat flux correlation that could be applied directly to a low-cost model without the need for CFD input as follows:

- The streamwise coordinates, x, were substituted for body surface coordinates, s. The nature of the injection beginning at $s = 0$ meant that the injector length is also the distance from the leading edge that film cooling occurs: $l = s_0$. The updated coordinates are shown in Figure C.2.

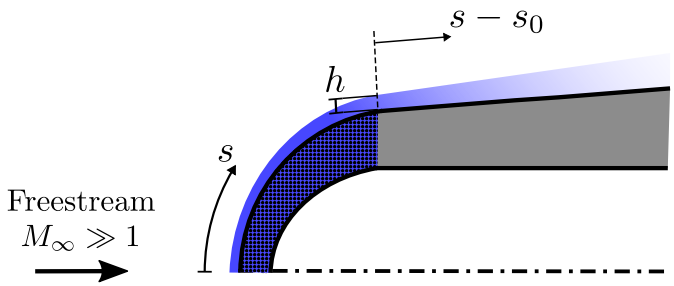


Figure C.2: Leading edge coordinate system used when adapting the flat plate film cooling correlation to the leading edge.

- The mass flux distribution and therefore the blowing ratio, F, was not constant along the injector surface. In the correlation parameter, $\overline{F}$ was

defined as a mean blowing ratio. The term Fl was therefore replaced by $\overline{F}s_0$.

$$\overline{F}s_0 = \frac{\int_0^{s_0} \rho_c u_c \mathrm{d}s}{\rho_\infty u_\infty} \tag{C.6}$$

- In the original correlation, x_{ref} was an empirical factor to account for the boundary layer growth upstream of injector, taken as $x_0^{1.16}$, where x_0 was the distance from leading edge to either the slot injector, or the end of the porous injector (for transpiration cooling). The leading edge case is different in three ways: there is no boundary layer formation prior to injection; the boundary layer over the injection region is subject to positive pressure gradients and viscous interaction effects; and the boundary layer size changes considerably with different R_{LE}. As such, the factor was empirically adjusted to accommodate the change in geometry using $s_{\text{ref}} = s_0^{1.21}$, and was found to compensate for the effect of changing injector size for $R_{LE} = 1$ – 25 mm.

- The Chapman-Rubesin factor evaluated at Eckert's reference temperature, C^* [160, 186], accounts for the effect of temperature and viscosity profiles within the boundary layer. This formulation requires boundary layer edge parameters, which are very challenging to model near the leading edge without CFD. Using the current CFD data, the cold-wall formulation of the study meant that $C^* \approx 1$, allowing the term to be removed for the low-cost correlation.

- Lastly, the effect of Stanton number was incorporated by introducing the B_h parameter. This is introduced using an empirical formulation, $f(B_h) = k_1 {B_h}^2 + k_2 B_h + k_3$ where for this case, $k_1 = 1.44$, $k_2 = -3.6027$, and $k_3 = 3.9149$.

The updated correlation parameter is given below in Equation C.7.

$$\xi_{th} = \frac{f(B_h)}{\overline{F}w} \sqrt{\frac{s - s_0}{s_{\text{ref}}} \frac{s}{Re_{u,\infty}}} \tag{C.7}$$

C.3 Semi-empirical Transpiration Cooling Model

Following the results from Chapter 5, the full model for heat flux reduction using modifications of existing semi-empirical correlations is presented below.

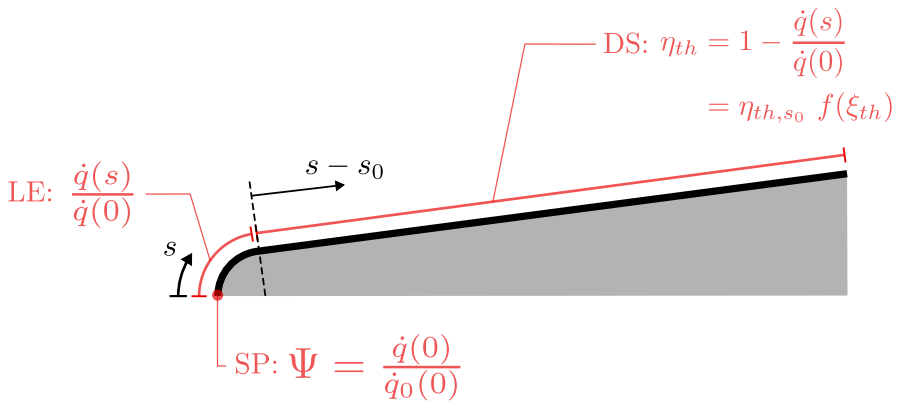


Figure C.3: Leading edge boundaries and coordinates for semi-empirical heat flux correlations. SP: stagnation point. LE: leading edge. DS: downstream (film cooling).

C.3.1 Leading Edge (LE)

Yoshikawa's [29] correlation for a stagnation point was shown to be valid over the entire injector surface, s. Here, the blowing parameter,B_h, is the ratio of uncooled local Stanton number, St_0, to the blowing ratio, F. h_{aw} and h_w are the adiabatic wall enthalpy and the wall enthalpy, $\dot{m}_{\text{inj}}(s)$ is the surface coolant mass flux distribution, $\dot{q}_0(s)$ is the uncooled heat flux distribution – estimated using the correlations in Appendix C.1. The subscripts c, ∞, and 0 refer to injected coolant, freestream, and uncooled quantities respectively. $N_c = 1$ or $5/9$ for diatomic or monatomic coolant gases respectively; k_b is a shape factor equal to unity for axisymmetric stagnation points; and W is molecular weight.

$$\Psi(s) = \frac{\dot{q}(s)}{\dot{q}_0(s)} = \sqrt{\pi\Lambda}\frac{\exp\{-\Lambda B_h(s)^2\}}{1+\mathrm{erf}\{\Lambda\}^{0.5}B_h(s)} \tag{C.8}$$

$$\Lambda = \begin{cases} \frac{1}{\pi}\frac{\Delta}{\Delta_0}\lambda^{B_h(s)/B^*} & (B_h(s) \leq B^*) \\ \frac{1}{\pi}\frac{\Delta}{\Delta_0}\lambda & (B_h(s) > B^*) \end{cases} \tag{C.8a}$$

$$B_h(s) = \frac{F(s)}{St_0(s)} = \frac{\dot{m}_{\mathrm{inj}}(s)\cdot(h_{aw}(s)-h_w)}{\dot{q}_0(s)} \tag{C.8b}$$

$$B^* = 1.82\frac{\sqrt{\pi\epsilon(W_c/W_\infty)}}{k_b(\chi'_w)^*} \tag{C.8c}$$

$$(\chi'_w)^* = \frac{1.187\sqrt{(8\epsilon(1-\epsilon)}}{(1+\sqrt{8/3\epsilon})-\epsilon)(1+0.225\sqrt{\epsilon})} \tag{C.8d}$$

$$\lambda = \sqrt{\frac{W_\infty}{W_c}}N_c \tag{C.8e}$$

$$\frac{\Delta}{\Delta_0} = 1 + k_b\sqrt{\frac{1}{\epsilon}\frac{W_\infty}{W_c}}F(s) \tag{C.8f}$$

$$\epsilon = \frac{\rho_\infty}{\rho_1} \tag{C.8g}$$

C.3.2 Downstream Film Cooling (DS)

The correlation by Heufer & Olivier was adapted for film cooling downstream of a porous leading edge injector. The adapted correlation requires the heat flux reduction at the end of the injector as an input, in turn predicted using Equation C.8 for $s = s_0$, with s_0 defined in Figure C.3. The film cooling correlation is given below. For the case of a 5-degree wedge at zero angle of attack and yaw $a = 2.05$, $b = 0.0476$, $c = -0.907$; and $k_1 = 1.44$, $k_2 = -3.6027$, $k_3 = 3.9149$.

$$\eta_{th}(s) = 1 - \frac{\dot{q}(s)}{\dot{q}_0(s)} \tag{C.9a}$$

$$= \eta_{th}(s_0)\ [1 + a\xi_{th}]^c + b \tag{C.9}$$

$$\xi_{th} = \frac{f(B_h)}{\overline{F}w}\sqrt{\frac{s - s_0}{s_{\text{ref}}}\frac{s}{Re_{u,\infty}}} \tag{C.9b}$$

$$\overline{F}w = \frac{\int_0^{s_0} \rho_c u_c \mathrm{d}s}{\rho_\infty u_\infty} \tag{C.9c}$$

$$f(B_h) = k_1 {B_h}^2 + k_2 B_h + k_3 \tag{C.9d}$$

APPENDIX D

Supplementary CFD Data

This appendix consists of supplementary plots to Chapter 5. In the main chapter, data points were selected for clarity and brevity. This appendix contains data with additional freestream conditions, coolant gases, and leading edge radii. The additional plots are split into three: input parameters, drag effects, and film cooling data.

D.1 Effect of Input Parameter on Blowing 258

D.2 Drag Augmentation 260

D.3 Boundary and Shock Layer Augmentation 261

D.4 Heat Flux Reduction 263

D.1 Effect of Input Parameter on Blowing

This section contains plots examining the effects of the different input parameters on predicted transpiration cooling performance. Using Yoshikawa's correlation (Equation 5.4), Figure D.1 shows the predicted heat flux reduction on a stagnation point injector for a range of coolants and conditions. A baseline case is highlighted, and each input parameter is independently varied to show the effect on the cooling response. The most significant change in curve shape occurs with molecular weight of coolant gas. Altitude, freestream Mach number, and radius all have weaker effects on the cooling efficiency curves in Figure 5.3. Altitude and Mach number have minor effects on B^* but radius have none.

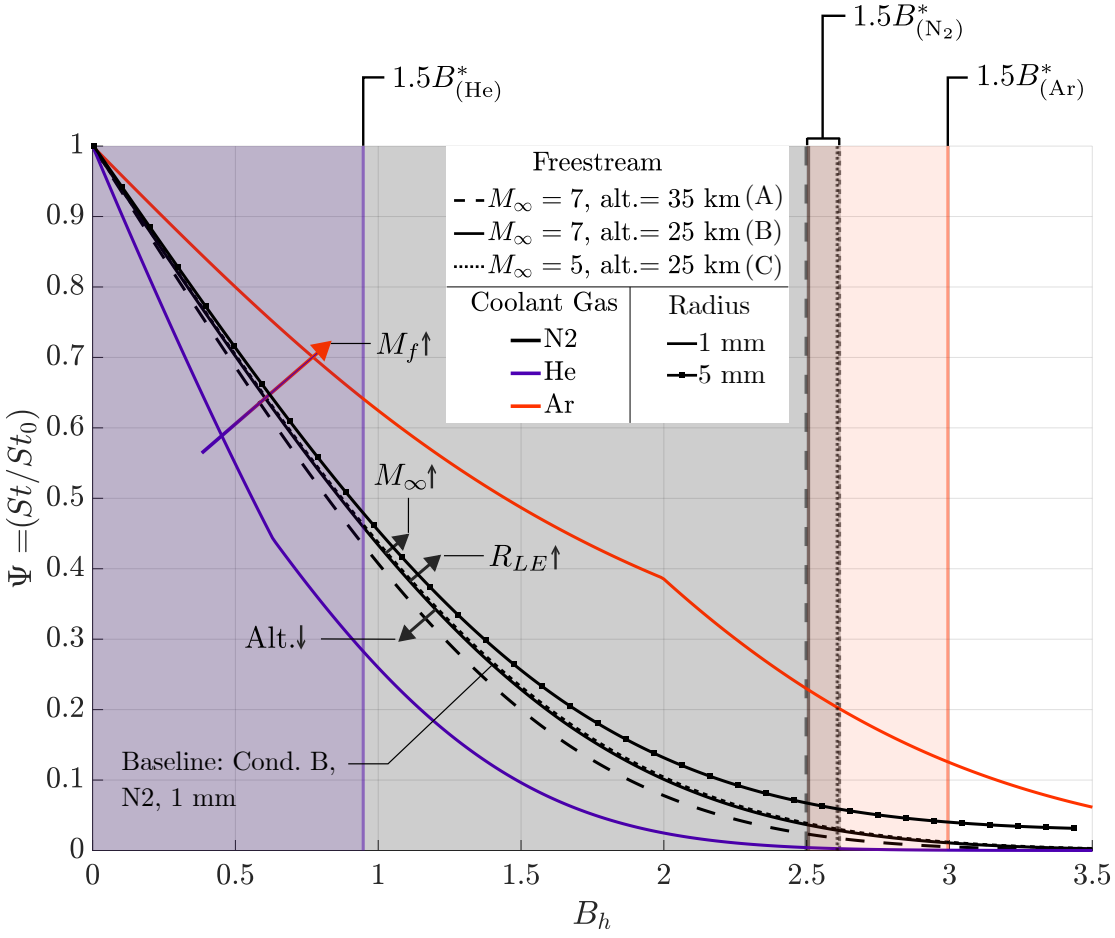


Figure D.1: Curves of predicted stagnation point heat flux reduction, Ψ, against B_h for a selection of the conditions and gases. The shaded regions bounded by vertical lines indicate the range of conditions that satisfy $B_h < 1.5B^*$.

A baseline example uncooled heat flux and corresponding calculated mass flux distribution are shown in Figure D.2. Also shown is the effect of independently changing each of the input parameters: M_∞, altitude, B_h, and R_{LE} on mass flux distribution. The effect of individually changing B_h, altitude, M_∞ and R_{LE} are highlighted. Mapping of B_h to mass flux distribution is independent of the coolant gas.

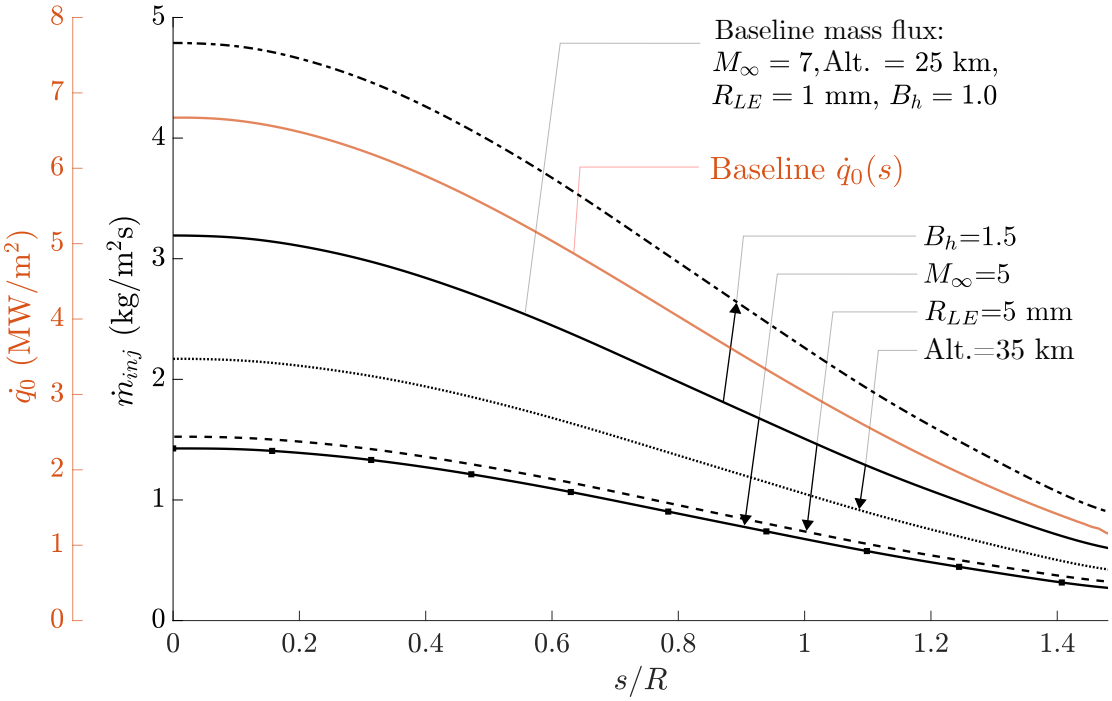


Figure D.2: Mass flux distributions calculated from the results of the uncooled simulations. The effect of individually changing B_h, altitude, M_∞ and R_{LE} are highlighted. Mapping of B_h to mass flux distribution is independent of the coolant gas.

D.2 Drag Augmentation

Figure D.3 shows the shock and boundary layer position for a sweep of blowing parameters. Figure D.4 plots the drag contribution changes due to blowing for all four radii tested, showing the linear trends in pressure and skin friction drag changes, and their sensitivity to radius.

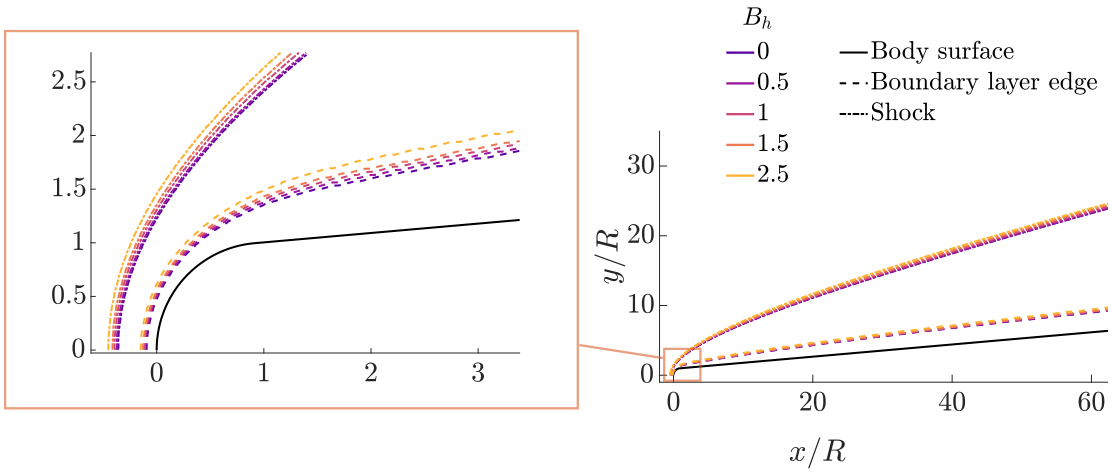


Figure D.3: Detected shock and boundary layer shape over the surface for different blowing parameters. Plot to scale. $R_{LE} = 1$ mm, Cond. A, coolant: N_2.

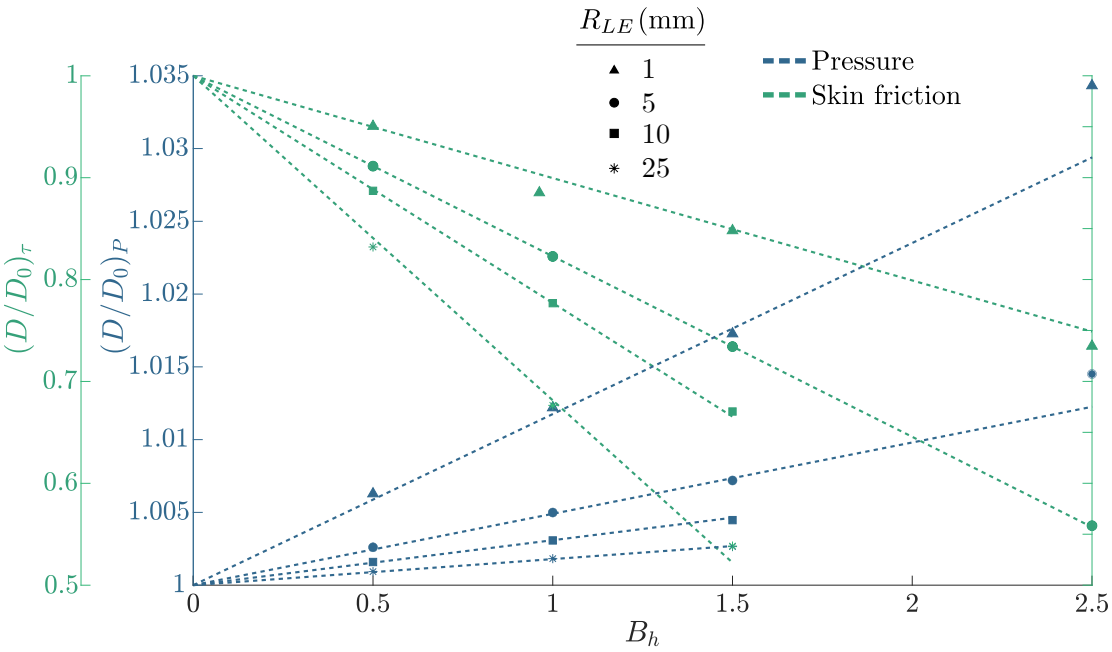


Figure D.4: Effect of B_h on drag contributions: cooled drag normalised by uncooled drag for pressure and skin friction. Condition A, N_2 coolant.

D.3 Boundary and Shock Layer Augmentation

The boundary layer and shock layer thicknesses, measured normal to the surface, are shown in Figures D.5 and D.6 for a range of conditions. Boundary layer thickness, δ, increases with radius and blowing parameter as expected. Normalising by the laminar compressible boundary layer growth rate factor: $\sqrt{Re_s}/M_\infty$, shows that the boundary layer growth rate is increased by a constant factor proportional to B_h and independent of radius. The effect of blowing on the shock layer thickness, Δ, is small as shown in Figure D.6. The stagnation line shock standoff augmentation, $\Delta_{SP}/\Delta_{SP,0}$, is compared to the theoretical prediction of Δ/Δ_0 in Equation 5.4.

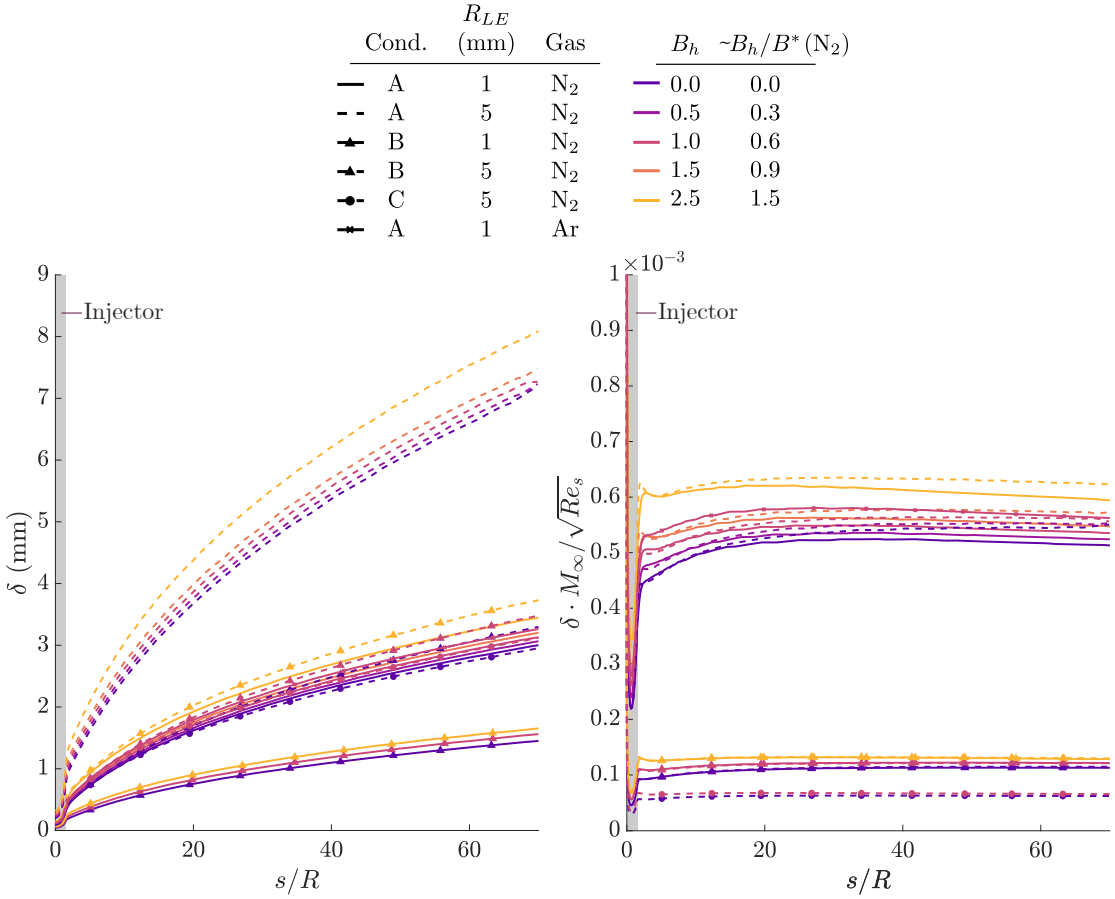


Figure D.5: Boundary layer thickness distributions for $R_{LE} = 1$ and 5 mm for a range of conditions and coolants. Left: absolute BL thickness. Right: BL thickness normalised by freestream laminar growth factor.

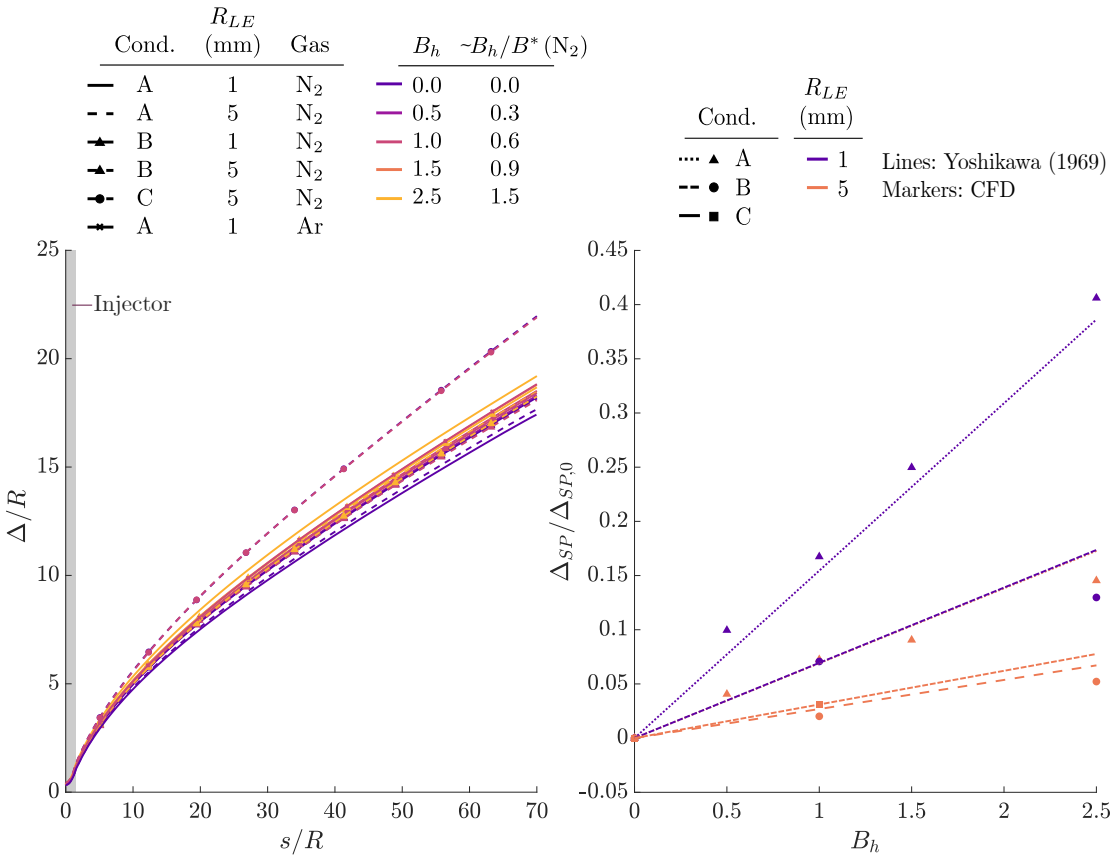


Figure D.6: Shock layer thickness augmentation for $R_{LE} = 1$ and 5 mm for a range of conditions and coolants. Left: SL thickness normalised by leading edge radius. Right: stagnation point standoff augmentation versus semi-analytical theory.

D.4 Heat Flux Reduction

Figure D.7 shows how the cooled-uncooled heat flux ratio is effectively constant for a constant blowing parameter along the injector surface (for $B_h < B^*$). Larger radii exhibit slight deviation from this trend, where cooling increases along the injector surface, likely due to a larger area for film cooling build-up. However, this relationship breaks down for $B_h > B^*$, where the absolute heat flux (rather than heat flux ratio) is constant along the surface.

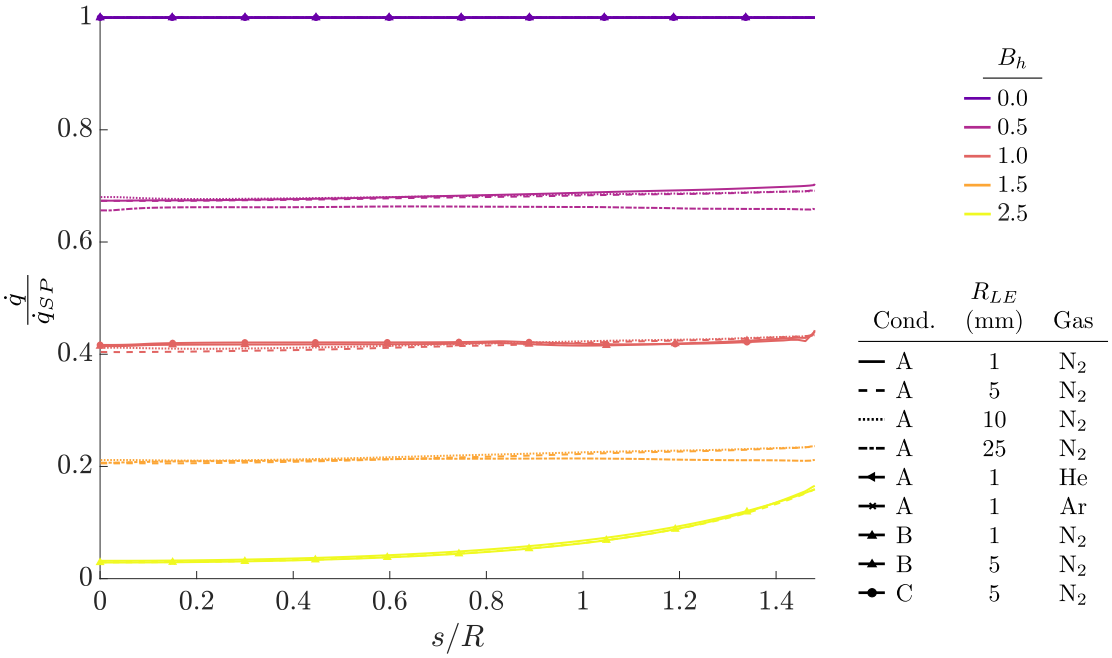
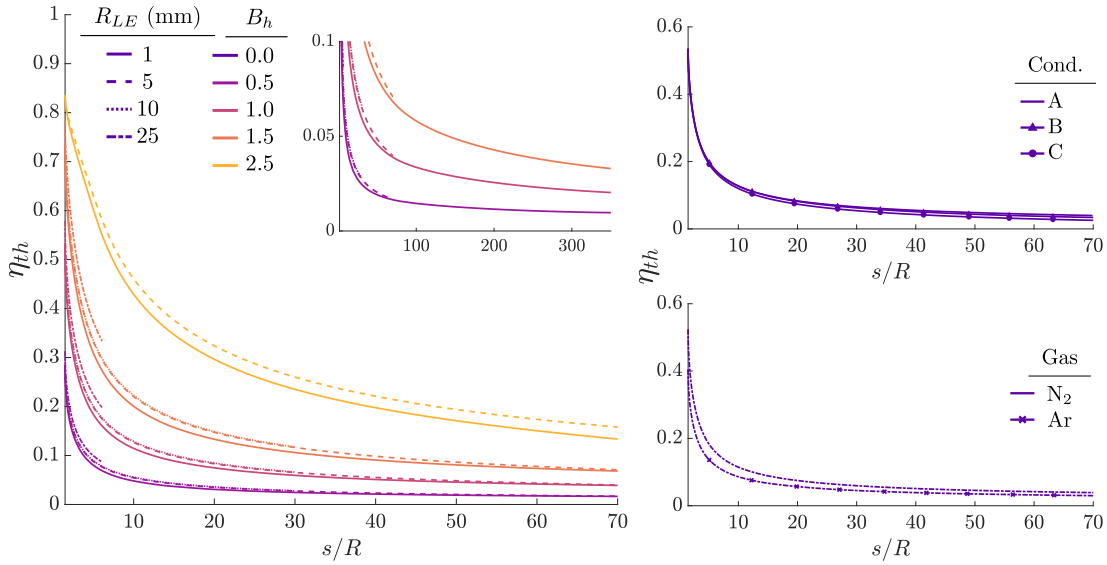


Figure D.7: Heat flux reduction along the leading edge injector for constant B_h mass flux distributions.

Figure D.8 shows the effect of different input parameters on film cooling. In subfigure **(a)**, the 10 and 25 mm curves are slightly truncated due to the domain setup in Figure 5.4, and the inset plot in subfigure shows the film cooling persistence for the full domain of $s/R \leq 350$ for $R_{LE} = 1$ mm at moderate B_h.

Freestream condition has a relatively small effect on the film cooling decay, whereby cooling at higher Reynolds numbers diminishes more quickly due to higher advection rates. The choice of coolant has a slightly greater effect: the cooling performance of argon can be seen to diminish more quickly than nitrogen at the

same conditions and mass flux, which is consistent with argon's higher binary diffusion coefficient and lower volumetric flux.



(a) Effect of radius and B_h. Condition A, N_2 coolant.

(b) Effect of freestream condition and coolant gas. $R_{LE} = 5$ mm, $B_h = 1$.

Figure D.8: Downstream heat flux reduction.

Figure D.9 shows the film cooling distributions based on the predictive correlation in Equation 5.13, compared to the CFD data. The correlation was fit to the dataset $R_{LE} = 1$ mm, $B_h = 1$, N_2 coolant, freestream condition A. The plot contains data for a range of leading edge radii, B_h values and two coolant gases.

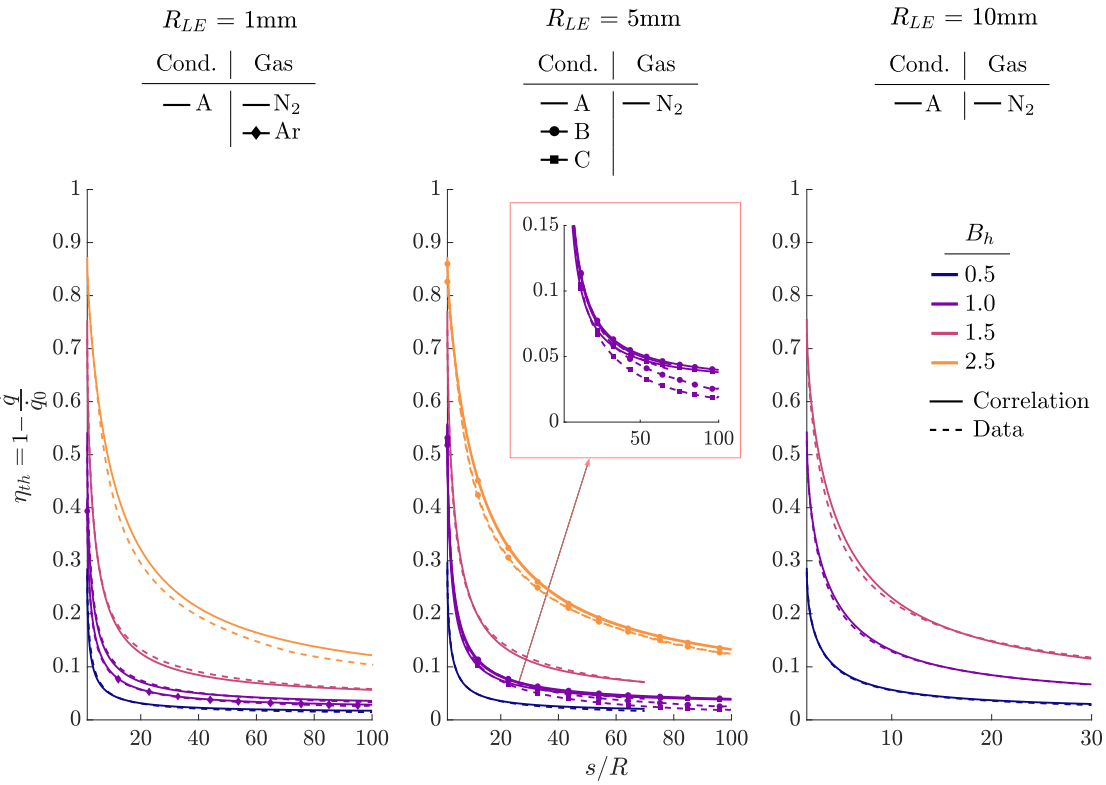


Figure D.9: Film cooling spatial distributions for a range of conditions, comparing the correlation prediction versus the CFD data.

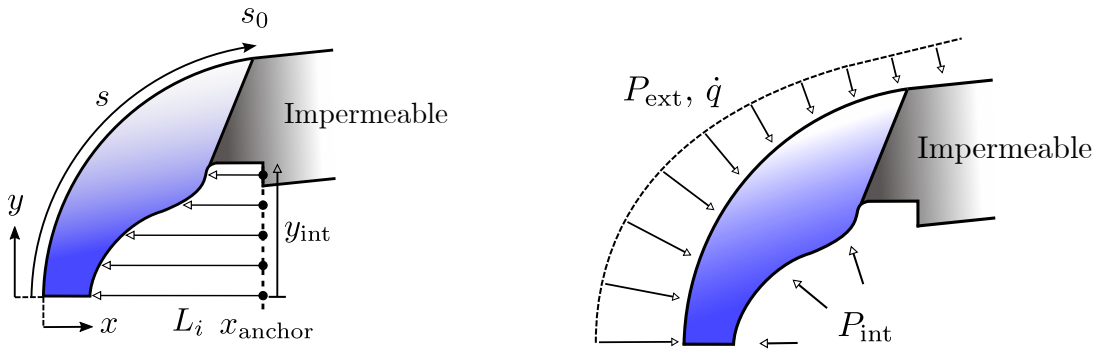
APPENDIX E

Internal Geometry Optimisation

At various stages, this thesis investigates the design and additive manufacture of a porous leading edge injector. This appendix provides details on the parameterisation and optimisation algorithm used to generate the injector architecture. The algorithm presented here corresponds to that used in Chapter 6, while a simpler version, tailored to an isothermal mass flux target, was applied in Chapter 3.

Conversion from a target temperature to a geometry via porous flow and heat transfer is a highly non-linear, simulation-driven optimisation problem. The MATLAB-based optimisation program therefore saw the COMSOL coupled solver as a non-linear *black box*, as sketched in Figure E.2. For such problems, derivative-free global methods are well suited. A hybrid optimisation strategy was employed using MATLAB's built-in particle swarm optimiser (PSO) to perform a global sweep and provide an initial solution, and FMINCON to refine the result. The Sequential Quadratic Programming (SQP) algorithm in FMINCON was chosen due to its efficiency in handling nonlinear constraints, and the function's feasibility mode was enabled to more confidently guarantee constraint satisfaction.

The internal geometry was constructed using a Bezier curve, where $n = 5$ control points were distributed evenly across $y = 0$ to y_{int} and in the x direction by a series of lengths, L_i spanning from $x = x_{\text{anchor}} = R_{LE}$. A target mass flux distribution was achieved through variation of the input parameters: $\mathbf{L}$, P_{int}, and y_{int} (where $\mathbf{L} = L_1, \ldots, L_n$).



(a) Geometry parameterisation.

(b) Heat flux and pressure sketch.

Figure E.1: Internal geometry parameterisation and boundary conditions for injector architecture optimisation.

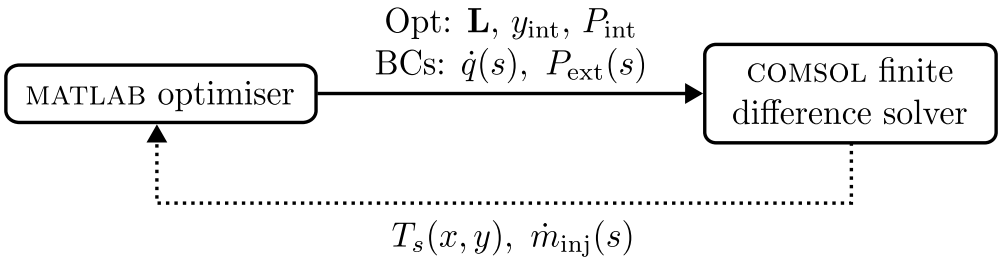


Figure E.2: Flow of variables between software packages during the geometry optimisation loop. The conversion of input variables to output variables within COMSOL is a driven by physical processes, but is also a highly nonlinear 'black-box' for the MATLAB optimiser.

The optimisation problem is defined in Equation E.1. The first constraint was the primary means by which the target temperature was achieved. The next four constraints were upper and lower bounds for the (x, y) coordinates of the Bezier curve, to prevent self-intersection or intersection with the external geometry The final two constraints increased the speed of convergence. Specifiying the wall thickness on the stagnation line, L_1, prevented problem overdetermination by setting P_{int} based on the stagnation line problem and proceeding with the rest of the geometry thereafter.

$$
\begin{aligned}
\underset{(\mathbf{L},\ y_{\text{int}},\ P_{\text{int}})}{\text{minimize}} \quad & \dot{m}_{\text{tot}} = \int_0^{s_0} \rho_{\text{inj}} u_{\text{inj}}\, ds \\
\text{subject to} \quad & T_s(x, y) \leq T_{\text{op}}, \\
& y_{\text{int}} \leq y_{\text{surf}}\big|_{x=x_{\text{anchor}}}, \\
& y_{\text{int}} \geq 0, \\
& L_i \geq 0 \qquad\qquad i = 1, \ldots, n, \\
& L_i \leq x_{\text{anchor}} - x_{\text{surf}}\big|_{y=y_i} \qquad i = 1, \ldots, n, \\
& L_1 = 0.3 R_{LE}, \\
& L_i \leq L_{i-1} \qquad\qquad i = 1, \ldots, n
\end{aligned}
\tag{E.1}
$$

APPENDIX F

Steady-State Systems Analysis Data

The following appendix chapter shows contours of the results from the steady-state systems study conducted in Chapter 6. Flight conditions are represented as x-y coordinates corresponding to velocity and altitude pairs. These contours show analysis for operating limits, surface heat flux and temperature reduction and mass flux requirements.

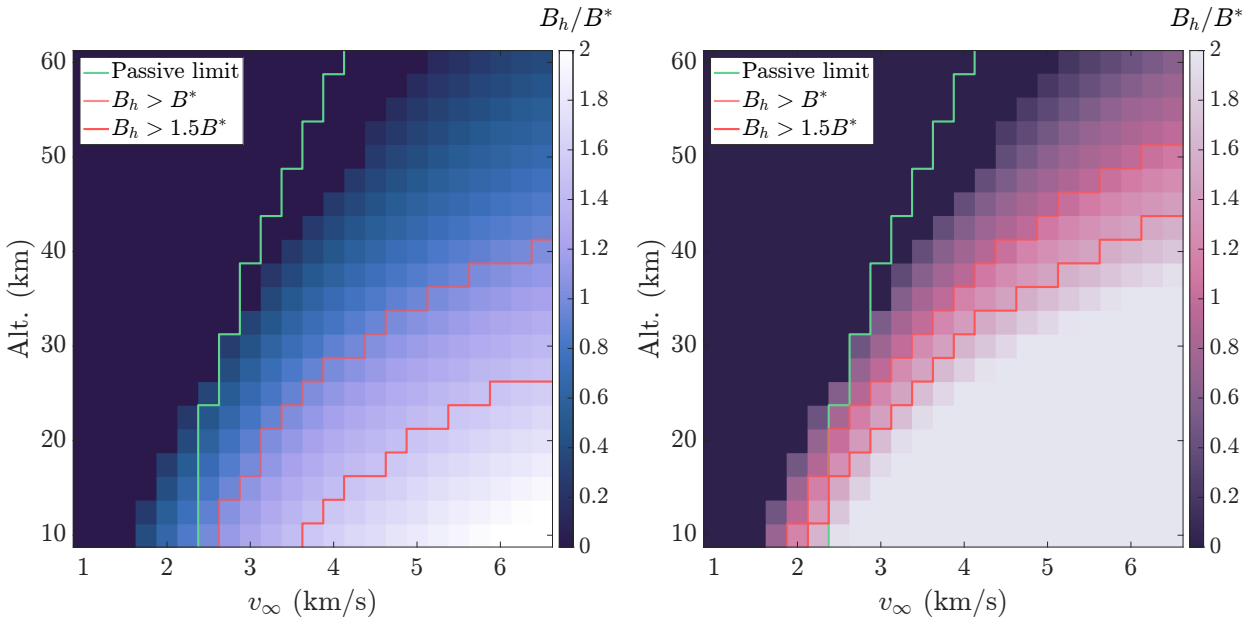
F.1 Operating Limits 270

F.2 Surface Heat Flux and Temperature Reduction 271

F.3 Mass Flux 272

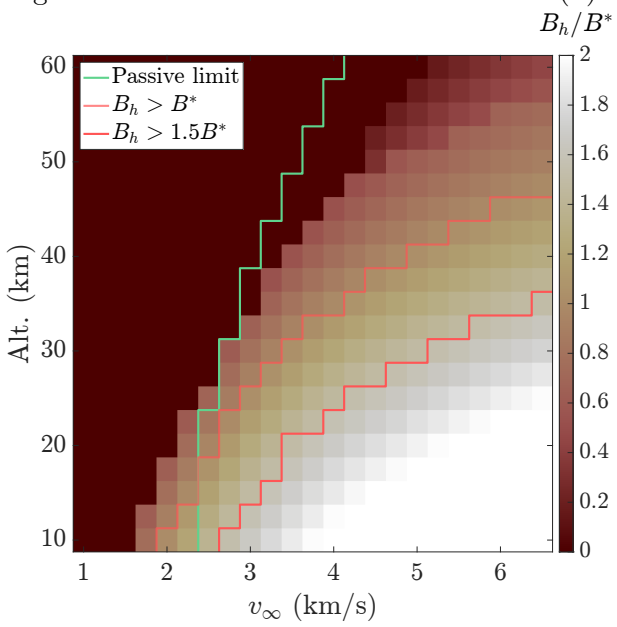
F.1 Operating Limits

The following contours show B_h/B^* for three coolant gases, showing limits of the passive system, as well as the blowing parameter-based system limits.



(a) Nitrogen

(b) Helium



(c) Argon

Figure F.1: B_h/B^* for different coolant gases. 1mm Tungsten.

F.2 Surface Heat Flux and Temperature Reduction

The following contours show the stagnation point surface heat flux and temperature. This data represents nitrogen cooling on a 1 mm tungsten leading edge.

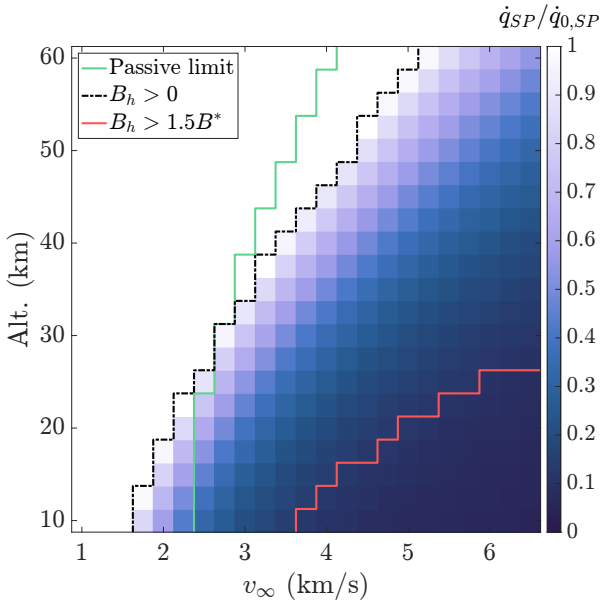


Figure F.2: Heat flux reduction at the stagnation point due to blowing, where $q/q_0 = 1$ indicates no transpiration cooling required.

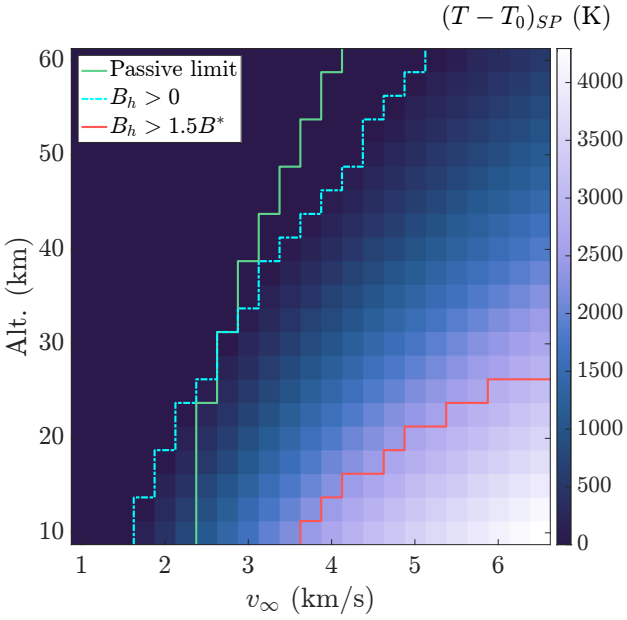


Figure F.3: Temperature reduction at the stagnation point due to blowing.

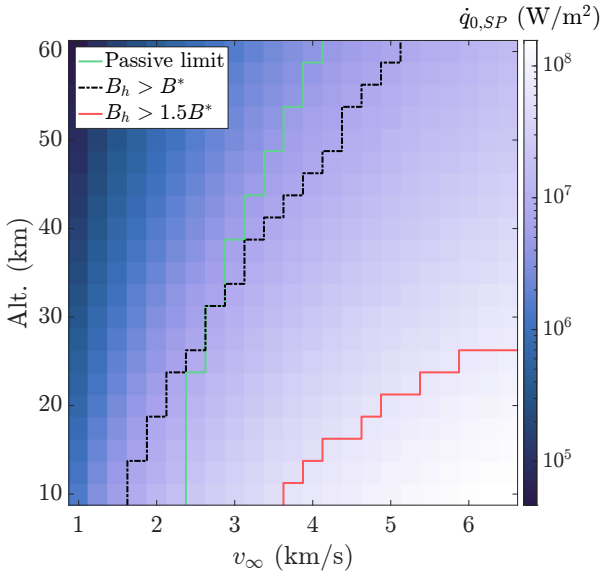


Figure F.4: Uncooled stagnation point heat flux. Note: colourmap is log scale.

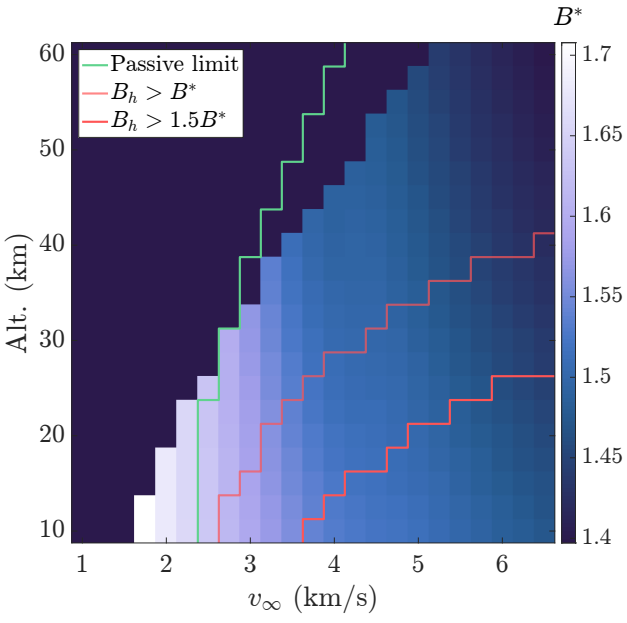
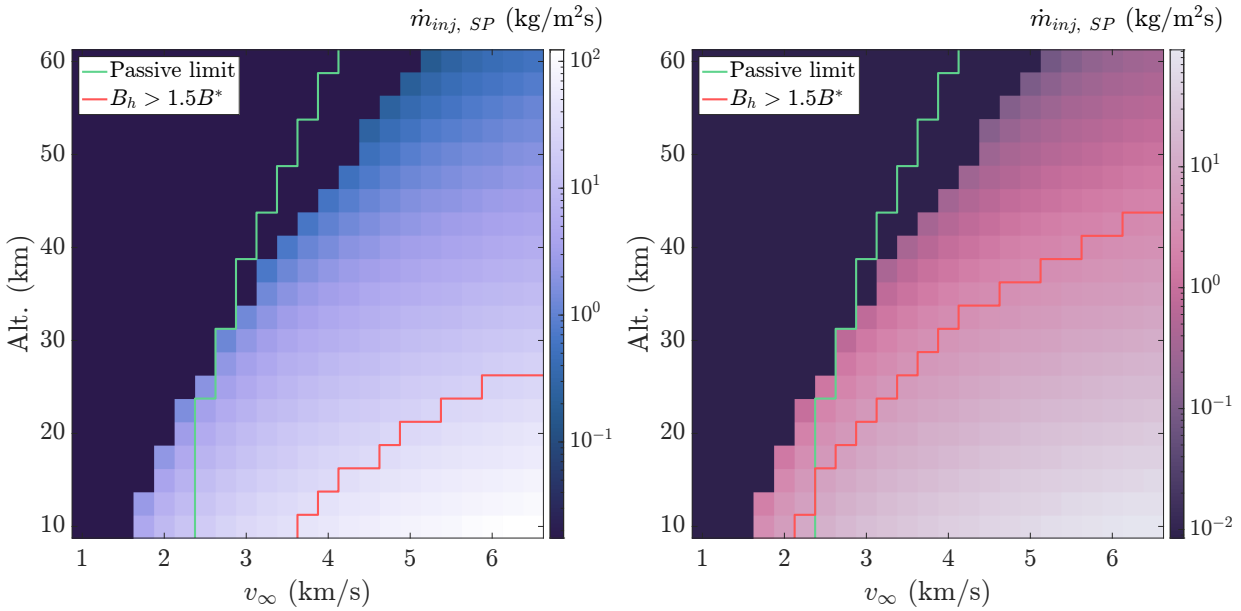


Figure F.5: Contour of B^*, used as the system limit parameter, shows some variation with conditions.

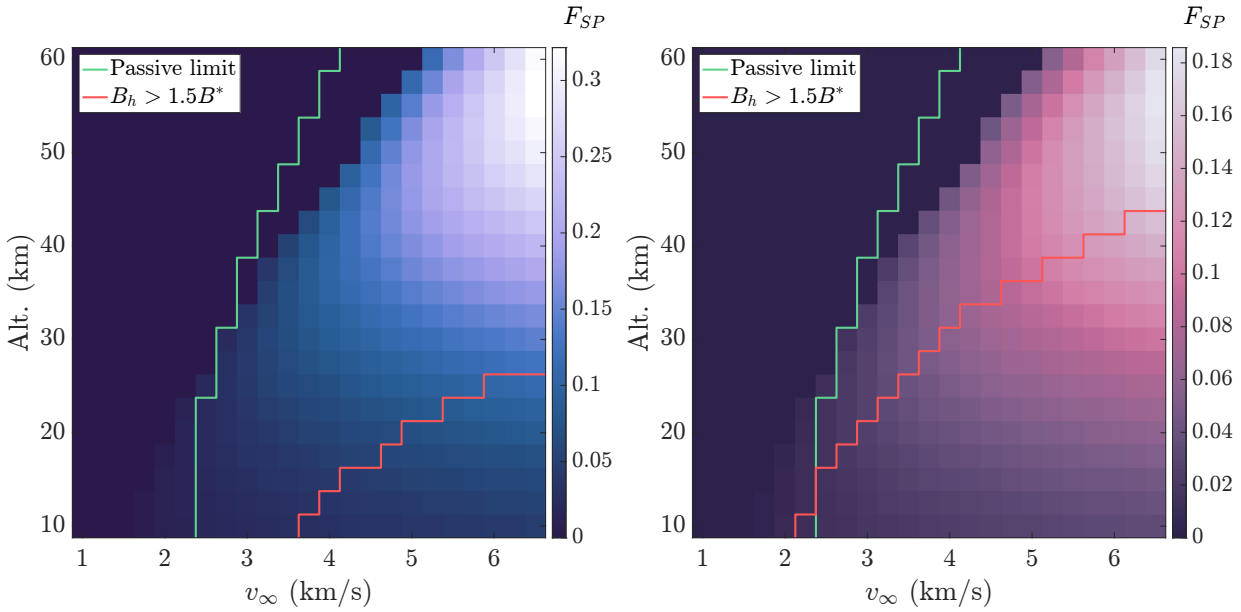
F.3 Mass Flux

The mass flux and blowing ratio contours for helium and nitrogen, showing the mass flux demands for a 1 mm tungsten leading edge.



(a) Nitrogen (b) Helium

Figure F.6: Mass flux at the stagnation point. Note colourmap is log scale.



(a) Nitrogen (b) Helium

Figure F.7: F at the stagnation point.